

**UNIVERSITY OF CALIFORNIA**  
**Santa Barbara**

**Design, Fabrication and Characterization  
of High-Speed Intra-Cavity Contacted  
Vertical-Cavity Lasers**

**A dissertation submitted in partial satisfaction  
of the requirements of the degree of**

**Doctor of Philosophy**  
**in**  
**Electrical and Computer Engineering**  
**by**  
**Jeffrey Winfield Scott**

**Committee Members:**

**Professor Larry A. Coldren, Chairperson**

**Professor Herbert Kroemer**

**Professor Evelyn L. Hu**

**Professor Mark Rodwell**

**ECE Technical Report #95-06**  
**June 1995**

**UMI Number: 9542051**

**Copyright 1995 by  
Scott, Jeffrey Winfield  
All rights reserved.**

---

**UMI Microform 9542051  
Copyright 1995, by UMI Company. All rights reserved.**

**This microform edition is protected against unauthorized  
copying under Title 17, United States Code.**

---

**UMI**

**300 North Zeeb Road  
Ann Arbor, MI 48103**

This is an authorized facsimile, made from the microfilm master copy of the original dissertation or master thesis published by UMI.

The bibliographic information for this thesis is contained in UMI's Dissertation Abstracts database, the only central source for accessing almost every doctoral dissertation accepted in North America since 1861.

**UMI** Dissertation  
Services

A Bell & Howell Company

300 North Zeeb Road  
P.O. Box 1346  
Ann Arbor, Michigan 48106-1346  
1-800-521-0600 734-761-4700  
<http://www.bellhowell.inforlearning.com>

Printed in 2000 by digital xerographic process  
on acid-free paper

DPGT

**12**

**THIS PAGE BLANK (USPTO)**



## **INFORMATION TO USERS**

**This manuscript has been reproduced from the microfilm master. UMI films the text directly from the original or copy submitted. Thus, some thesis and dissertation copies are in typewriter face, while others may be from any type of computer printer.**

**The quality of this reproduction is dependent upon the quality of the copy submitted. Broken or indistinct print, colored or poor quality illustrations and photographs, print bleedthrough, substandard margins, and improper alignment can adversely affect reproduction.**

**In the unlikely event that the author did not send UMI a complete manuscript and there are missing pages, these will be noted. Also, if unauthorized copyright material had to be removed, a note will indicate the deletion.**

**Oversize materials (e.g., maps, drawings, charts) are reproduced by sectioning the original, beginning at the upper left-hand corner and continuing from left to right in equal sections with small overlaps. Each original is also photographed in one exposure and is included in reduced form at the back of the book.**

**Photographs included in the original manuscript have been reproduced xerographically in this copy. Higher quality 6" x 9" black and white photographic prints are available for any photographs or illustrations appearing in this copy for an additional charge. Contact UMI directly to order.**

# **UMI**

**A Bell & Howell Information Company  
300 North Zeeb Road, Ann Arbor, MI 48106-1346 USA  
313/761-4700 800/521-0600**

**THIS PAGE BLANK (USPTO)**

This dissertation of Jeffrey Winfield Scott  
is approved:



---

Professor Herbert Kroemer



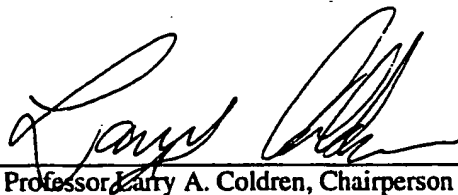
---

Professor Evelyn L. Hu



---

Professor Mark Rodwell



---

Professor Larry A. Coldren, Chairperson

June 1995

**Design, Fabrication and Characterization of High-Speed  
Intra-Cavity Contacted Vertical-Cavity Lasers**

**Copyright © by  
Jeffrey Winfield Scott  
All rights reserved  
June 1995**

**Department of Electrical and Computer Engineering  
University of California, Santa Barbara  
Santa Barbara, CA 93106**

### **Acknowledgments**

Santa Barbara is a wonderful place to live and learn in. Most impressive is the collaborative atmosphere. Over 100 solid state students and 12 faculty members focused on compound semiconductor devices share common laboratories and research ideas. I have always felt welcome in other professors offices and laboratories. The lack of politics has made it possible to overcome the technical challenges and has given me a first rate graduate education. The entire faculty deserves much credit for this unique and exciting environment. Most importantly, I am indebted to Professor Larry Coldren for teaching me the theory of semiconductor lasers and guiding my research.

In the area of device modeling, I am indebted to Professor Herbert Kroemer for introducing me to numerical modeling, Dubravko Bahic and Scott Corzine for guiding me through the details of numerical techniques and G. Ronald Hadley for teaching me the ADI technique for current flow analysis. In the field of device fabrication, I would like to thank Professor Evelyn Hu for her insight and encouragement in developing the dry etch processes, G. Allan Vawter for introducing me to optoelectronic processing, and Gerry. R. Robinson for developing much needed photolithographic techniques. Countless assistance from Jack Whaley, Brian Carralajo and Ernie Canie kept the processing equipment up and running. I am particularly grateful to Professor John Bowers, Professor Mark Rodwell and Rahda Nagarajan for their valuable insight into high speed lasers and Cathal Mahon, Frank Peters and Dan Cohen for their assistance in the measurement lab.

The development of vertical cavity laser technology has been a collaborative effort in our group. I strongly benefited from the interaction with and work of fellow graduate students Randy Geels and Scott Corzine. Graduate students Bruce Young, Brian Thilbeault and Matt Peters have contributed many important ideas and have worked hard to provide vertical cavity laser material.

My research has consistently been funded by ARPA, more recently via the Optoelectronics Technology Center. I am truly grateful for the years of support.

**Dedicated to:**

**My parents for all the years of love and care  
and  
Linda my wife for her patience and support.**

## Vita

October 24, 1961: Born in Pasadena, California  
December 1983: B.A., Physics, UC Berkeley  
1984-January 1987: Process Engineer, Harris Microwave Semiconductor  
December 1989: M.S., Electrical Engineering, UC Santa Barbara  
December 1994: Ph.D., Electrical Engineering, UC Santa Barbara

## Publications

1. R.G. Geels, R.H. Yan, J.W. Scott, S.W. Corzine, R.J. Simes, and L.A. Coldren. "Analysis and Design of a Novel Parallel Driven MQW-DBR Surface-Emitting Laser" in *CLEO '88*, 1988. Anaheim, CA.
2. S.W. Corzine, R.S. Geels, J.W. Scott, R.-H. Yan, and L.A. Coldren. "Design of Fabry-Perot surface-emitting lasers with a periodic gain structure" *IEEE Journal of Quantum Electronics*, **25** (6) pp. 1513-24. (1989)
3. S.W. Corzine, R.S. Geels, R.H. Yan, J.W. Scott, L.A. Coldren, and P.L. Gourley. "Efficient, narrow-linewidth distributed-Bragg-reflector surface-emitting laser with periodic gain." *IEEE Photonics Tech. Lett.*, **1** (3) pp. 52-4. (1989)
4. P.L. Gourley, T.M. Brennan, B.E. Hammons, S.W. Corzine, R.G. Geels, R.H. Yan, J.W. Scott, and L.A. Coldren, "High Efficiency TEM(0) Continuous-Wave (Al,Ga)As Epitaxial Surface-Emitting Lasers and Reduced Threshold with Half-Wave Periodic Gain" *Appl. Phys. Lett.*, **54** (13) pp. 1209. (1989)
5. R.S. Geels, S.W. Corzine, J.W. Scott, D.B. Young, and L.A. Coldren. "Low threshold planarized vertical-cavity surface-emitting lasers." *IEEE Photonics Tech. Lett.*, **2** (4) pp. 234-6. (1990)
6. L.A. Coldren, S.W. Corzine, R.S. Geels, A.C. Gossard, K.-K. Law, J.L. Merz, J.W. Scott, R.J. Simes, and R.H. Yan. "High-efficiency vertical cavity lasers and modulators" in *Proceedings of the SPIE - The International Society for Optical Engineering*, 1991.
7. C.C. Barron, M. Whitehead, K.-K. Law, J.W. Scott, M.E. Heimbuch, and L.A. Coldren. "K-band operation of asymmetric Fabry-Perot modulators" *IEEE Photonics Technology Letters*, **4** (5) pp. 459-61. (1992)

8. Z.M. Chuang, J.W. Scott, D.B. Young, and L.A. Coldren. "Strained InGaAs/GaAs quantum well constricted-mesa lasers and application in a vertical-twin-guide tunable laser." *IEEE Photonics Tech. Lett.*, **4** (4) pp. 315-18. (1992)
9. L.A. Coldren, R.S. Geels, S.W. Corzine, and J.W. Scott, "Efficient vertical-cavity lasers" *Optical and Quantum Electronics*, **24** (2) pp. S105-19. (1992)
10. R.S. Geels, B.J. Thibeault, S.W. Corzine, J.W. Scott, and L.A. Coldren. "Design and characterization of In<sub>0.2</sub>Ga<sub>0.8</sub> MQW vertical-cavity surface-emitting lasers" *IEEE Journal of Quantum Electronics*, **29** (12) pp. 2977-87. (1993)
11. M.K. Kilcoyne, J.W. Scott, and J. Plombon. "Packaging of optical interconnect arrays for optical signal processing and computing." in *Proceedings of the SPIE - The International Society for Optical Engineering*, 1993.
12. F.H. Peters, M.J. Majewski, M.G. Peters, J.W. Scott, B.J. Thibeault, D.B. Young, and L.A. Coldren. "Vertical cavity surface emitting laser technology" in *Proceedings of the SPIE - The International Society for Optical Engineering*, 1993.
13. F.H. Peters, M.G. Peters, D.B. Young, J.W. Scott, B.J. Thibeault, S.W. Corzine, and L.A. Coldren, "High-power vertical-cavity surface-emitting lasers" *Electronics Letters*, **29** (2) pp. 200-1. (1993)
14. M.G. Peters, F.H. Peters, D.B. Young, J.W. Scott, B.J. Thibeault, and L.A. Coldren, "High wallplug efficiency vertical-cavity surface-emitting lasers using lower barrier DBR mirrors" *Electronics Letters*, **29** (2) pp. 170-2. (1993)
15. M.G. Peters, B.J. Thibeault, D.B. Young, J.W. Scott, F.H. Peters, A.C. Gossard, and L.A. Coldren, "Band-gap engineered digital alloy interfaces for lower resistance vertical-cavity surface-emitting lasers" *Applied Physics Letters*, **63** (25) pp. 3411-13. (1993)
16. J.W. Scott, S.W. Corzine, D.B. Young, and L.A. Coldren, "Modeling the current to light characteristics of index-guided vertical-cavity surface-emitting lasers" *Applied Physics Letters*, **62** (10) pp. 1050-2. (1993)
17. J.W. Scott, R.S. Geels, S.W. Corzine, and L.A. Coldren. "Modeling temperature effects and spatial hole burning to optimize vertical-cavity surface-emitting laser performance" *IEEE Journal of Quantum Electronics*, **29** (5) pp. 1295-308. (1993)
18. B.J. Thibeault, J.W. Scott, M.G. Peters, F.H. Peters, D.B. Young, and L.A. Coldren, "Integrable InGaAs/GaAs vertical-cavity surface-emitting lasers" *Electronics Letters*, **29** (25) pp. 2197-9. (1993)



19. D.B. Young, J.W. Scott, F.H. Peters, M.G. Peters, M.L. Majewski, B.J. Thibeault, S.W. Corzine, and L.A. Coldren, "Enhanced performance of offset-gain high-barrier vertical-cavity surface-emitting lasers" *IEEE Journal of Quantum Electronics*, **29** (6) pp. 2013-22. (1993)
20. D.B. Young, J.W. Scott, F.H. Peters, B.J. Thibeault, S.W. Corzine, M.G. Peters, S.-L. Lee, and L.A. Coldren, "High-power temperature-insensitive gain-offset InGaAs/GaAs vertical-cavity surface-emitting lasers" *IEEE Photonics Tech. Lett.*, **5** (2) pp. 129-32. (1993)
21. M.G. Peters, D.B. Young, F.H. Peters, J.W. Scott, B.J. Thibeault, and L.A. Coldren, "17.3% peak wall plug efficiency vertical-cavity surface-emitting lasers using lower barrier mirrors" *IEEE Photonics Tech. Lett.*, **6** (1) pp. 31-3. (1994)
22. J.W. Scott, F.H. Peters, B.J. Thibeault, D.B. Young, L.A. Coldren, and F.H. Peters, "2.488 Gbit/s optical data transmission with linear arrays of intra-cavity contacted vertical cavity lasers" in *European Conference on Optical Communications*, 1994. Geneva, Switzerland.
23. J.W. Scott, B.J. Thibeault, S.W. Corzine, and L.A. Coldren, "Advances and Opportunities in the Design and Modeling of Vertical-Cavity Surface-Emitting Lasers" in *3rd International Workshop on Computational Electronics*, 1994. Portland, Oregon.
24. J.W. Scott, B.J. Thibeault, C.J. Mahon, L.A. Coldren, and F.H. Peters, "High Modulation Efficiency of Intra-Cavity Contacted Vertical Cavity Lasers" *Applied Physics Letters*, **65** (12) pp. 1483-1485. (1994)
25. J.W. Scott, B.J. Thibeault, C.J. Mahon, F.H. Peters, D.B. Young, and L.A. Coldren, "Intra-cavity contacted vertical cavity laser arrays optimized for low current, high speed interconnects" in *14th IEEE Int. Semiconductor Laser Conference*, 1994. Maui, Hawaii, USA.
26. J.W. Scott, B.J. Thibeault, D.B. Young, and L.A. Coldren, "High Efficiency Sub-Milliamp Vertical Cavity Lasers With Intra-Cavity Contacts" *IEEE Photonics Tech. Lett.*, **6** (6) pp. 678-680. (1994)
27. D.B. Young, A. Kapila, J.W. Scott, V. Malhotra, and L.A. Coldren, "Reduced threshold vertical-cavity surface-emitting lasers." *Electronics Letters*, **30** (3) pp. 233-5. (1994)

## **Abstract**

### **Design, Fabrication and Characterization of High-Speed Intra-Cavity Contacted Vertical-Cavity Lasers**

by

Jeffrey Winfield Scott

This dissertation has two main goals. One is to present models which predict the terminal characteristics of vertical-cavity lasers. This involves modeling the current flow into the active region, the conversion of current into light, and the emission of light from the optical cavity. The second goal is to present the design and realization of an index-guided vertical cavity laser which uses contacting layers within the optical cavity to supply current to the active region.

The models are presented in succession from the one dimensional optical analysis of the vertical cavity, to the two dimensional calculations of the active region's current-to-light conversion, to the three dimensional calculation of current flow into the active region from ring contacts. Thermal effects and non-uniform transverse-optical-mode profiles are included. The quantum mechanics of the conversion of current into light on a microscopic scale is a dissertation topic in itself. This dissertation builds upon previous work, using an established gain model for the microscopic active region properties. The above models form a set of tools which connect the microscopic active region properties to the measured current-to-light characteristics of actual devices. These tools are used to design and analyze index-guided intra-cavity contacted vertical-cavity lasers.

With both contacts within the optical cavity, the substrate can be made from semi-insulating GaAs resulting in a low parasitic capacitance. The index-guided design allows the fabrication of very small, sub-milliamp threshold lasers which have high bandwidths at low currents due to the small modal volume. These properties make the lasers ideal for high-speed applications. Data is presented on both the small signal response and the bit error rate characteristics at multi-Gigabit data rates, showing good agreement with theory.

# Table of Contents

<b>Chapter 1: Overview and Background .....</b>	<b>1</b>
1.0 Introduction .....	1
1.1 Historical Background .....	2
1.2 Intra-Cavity Contacted Vertical-Cavity Lasers .....	12
1.3 Dissertation Overview .....	19
References .....	22
 <b>Chapter 2: Current-to-Light Simulation .....</b>	 <b>26</b>
2.0 Introduction .....	26
2.1 Formulation of Equations .....	30
2.2 Thermal Model .....	36
2.3 Numerical Algorithm .....	38
2.4 Internal Parameters .....	42
2.5 Predicted Current-to-Light Characteristics .....	52
2.5.1 Temperature sensitivity .....	52
2.5.2 Power conversion efficiency .....	54
2.5.3 Reduced threshold current .....	56
2.6 Spatial Hole Burning .....	60
References .....	67
 <b>Chapter 3: Intra-Cavity Design .....</b>	 <b>70</b>
3.0 Chapter Overview .....	70
3.1 Analytical Analysis .....	71
3.1.1 Current crowding .....	71
3.1.2 Current leveling .....	77
3.1.3 Analytic design curves .....	80
3.2 Numerical Analysis .....	87
3.2.1 Model formulation .....	88

3.2.2 Grids and convergence .....	92
3.2.3 Comparison of analytic and numerical solutions .....	97
3.2.4 Effect of current leveling on laser performance .....	102
References .....	106
<b>Chapter 4: <i>In-Situ</i> Control and Laser Fabrication .....</b>	<b>108</b>
4.0 Chapter Overview .....	108
4.1 Growth Control .....	109
4.2 Structure Formation .....	115
4.3 Contacts and Interconnects .....	124
References .....	131
<b>Chapter 5: Intra-Cavity Laser Characteristics .....</b>	<b>133</b>
5.0 Chapter Overview .....	133
5.1 Device Structure .....	134
5.2 CW Characteristics .....	138
5.3 Pulsed Characteristics .....	146
5.4 Microwave Response .....	150
5.5 Digital Data Transmission .....	161
References .....	166
<b>Chapter 6: Laser Analysis and Improved Designs .....</b>	<b>168</b>
6.0 Chapter Overview .....	168
6.1 Analyzing the Intra-Cavity Lasers .....	168
6.1.1 Summary of the Analysis .....	168
6.1.2 Current-injection Simulation .....	169
6.1.3 Current-to-Light Simulation .....	174
6.2 Major Improvements for Minor Changes .....	177
6.3 Current-Apertured Design .....	178
6.4 Conclusion .....	186
References .....	188

<b>Appendix A: Refractive Index of <math>\text{Al}_x\text{Ga}_{1-x}\text{As}</math> .....</b>	<b>189</b>
References .....	191
<b>Appendix B: Quantum Well Model .....</b>	<b>193</b>
B.1 Quantum Well Active Regions .....	193
B.2 Temperature and carrier dependence of the gain spectrum .....	196
B.3 Numerical gain calculations and curve fits .....	202
References .....	211
<b>Appendix C: Laser Fabrication Process .....</b>	<b>213</b>
<b>Appendix D: Vertical-Cavity Design .....</b>	<b>224</b>
D.1 Appendix Overview .....	224
D.2 Introduction to Vertical-Cavity Laser Design .....	225
D.3 Transmission Matrix Analysis .....	234
D.3.1 Waves in conducting medium .....	235
D.3.2 Transmission matrix derivation .....	238
D.3.3 Longitudinal enhancement factor .....	244
D.4 Distributed Bragg Reflectors .....	252
D.5 Round-trip Cavity Parameters .....	261
D.6 Energy Storage, Quality Factor and Photon Lifetime .....	268
References .....	272
<b>Appendix E: Thermal and Electrical Properties of AlGaAs .....</b>	<b>274</b>
References .....	280

## List of Figures

Fig. 1.1 In-plane laser schematic .....	3
Fig. 1.2 Early vertical cavity laser schematic .....	4
Fig. 1.3 Early vertical cavity lasers at UCSB .....	5
Fig. 1.4 Early intra-cavity laser $L-I$ .....	7
Fig. 1.5 $L-I$ model schematic .....	9
Fig. 1.6 Threshold current vs. stage temperature .....	10
Fig. 1.7 SEM of RIE etched two step mesa .....	11
Fig. 1.8 Schematic of intra-cavity contacted laser .....	13
Fig. 1.9 Calculated intra-cavity $I_{th}$ vs. Size .....	14
Fig. 1.10 $L-I$ characteristics of intra-cavity contacted lasers .....	16
Fig. 1.11 SEM of an intra-cavity contacted laser .....	19
Fig. 1.12 Schematic of the various models used .....	20
Fig. 2.1 $L-I$ characteristics for broad area and 7 $\mu\text{m}$ lasers .....	27
Fig. 2.2 $L-I$ model schematic .....	30
Fig. 2.3 Diagram of the quantum well and leakage currents .....	33
Fig. 2.4 Grid and areas used for numerical $L-I$ calculations .....	39
Fig. 2.5 Algorithm used for $L-I$ calculation .....	41
Fig. 2.6 Calculated and measured $L-I$ .....	48
Fig. 2.7 Calculated and measured $I_{th}$ vs. $T_{sub}$ .....	48
Fig. 2.8 Varying surface recombination velocity .....	49
Fig. 2.9 Varying diffusion constant .....	49
Fig. 2.10 Sensitivity to leakage coefficient value .....	50
Fig. 2.11 Sensitivity to Auger coefficient value .....	50
Fig. 2.12 $L-I$ characteristics for laser A for varying temperature .....	51
Fig. 2.13 $L-I$ characteristics for laser B for varying temperature .....	51
Fig. 2.14 $I_{th}$ vs. $T_{sub}$ for varying gain offset .....	53
Fig. 2.15 $I_{th}$ vs. $T_{sub}$ for varying threshold gain .....	53

Fig. 2.16 $L$ - $P$ characteristics for varying drive voltages .....	55
Fig. 2.17 $I_{th}$ vs. $T_{sub}$ for varying number of wells .....	57
Fig. 2.18 $L$ - $I$ characteristics for varying number of wells .....	58
Fig. 2.19 Effect of varying boundary conditions on $I_{th}$ .....	59
Fig. 2.20 Carrier density profiles for Laser $B$ .....	61
Fig. 2.21 Transverse optical modes for cylindrical waveguide .....	62
Fig. 2.22 Modal gain for Laser $B$ during $L$ - $I$ curve .....	63
Fig. 2.23 Carrier density profiles for current apertured laser .....	64
Fig. 2.24 $L$ - $I$ characteristics of current apertured laser .....	65
Fig. 2.25 Modal gain curve of current apertured laser .....	66
Fig. 3.1 Current crowding network.....	71
Fig. 3.2 Current leveling network .....	77
Fig. 3.3 Current crowded and leveled profiles, log scale .....	81
Fig. 3.4 Current crowded and leveled profiles, linear scale .....	82
Fig. 3.5 Current leveled intra-cavity network.....	83
Fig. 3.6 Analytic intra-cavity design curves .....	85
Fig. 3.7 Detail of experimental intra-cavity design .....	86
Fig. 3.8 Grid and areas used for numerical $I$ - $V$ calculations .....	88
Fig. 3.9 Sample structure for numerical analysis .....	93
Fig. 3.10 Current density profiles for varying grids .....	94
Fig. 3.11 Convergence of ADI technique .....	96
Fig. 3.12 Current density profile for varying ideality factor .....	98
Fig. 3.13 Comparison of analytic and numerical profiles .....	98
Fig. 3.14 Current density profile for varying leveling resistance .....	99
Fig. 3.15 Current crowding in a ring contacted structure .....	101
Fig. 3.16 Effect of leveling layer on current profiles .....	102
Fig. 3.17 $L$ - $I$ characteristics for varying leveling resistance.....	103
Fig. 3.18 Modal gain curves for varying leveling resistance .....	104
Fig. 4.1 White light <i>in-situ</i> growth monitoring setup .....	111

Fig. 4.2 Measured and calculated DBR spectra .....	112
Fig. 4.3 Measured and calculated vertical cavity spectra .....	113
Fig. 4.4 Reflectivity and PL spectra for 931006b .....	114
Fig. 4.5 Intra-cavity structure and layers .....	116
Fig. 4.6 Two step mesa process schematic .....	118
Fig. 4.7 HeNe laser <i>in-situ</i> etch monitoring setup .....	119
Fig. 4.8 <i>In-situ</i> laser monitor signal vs. time .....	120
Fig. 4.9 Undercut etch process schematic .....	120
Fig. 4.10 SEM of undercut test structures .....	121
Fig. 4.11 SEM of two step mesa structure .....	122
Fig. 4.12 SEM showing breakdown of etch selectivity .....	123
Fig. 4.13 SEM of intra-cavity laser after n ohmic .....	124
Fig. 4.14 Dielectric via process schematic .....	125
Fig. 4.15 SEM of intra-cavity laser after dielectric via .....	126
Fig. 4.16 P-ohmic metal process schematic.....	127
Fig. 4.17 Interconnect metal process schematic .....	128
Fig. 4.18 SEM of high density intra cavity contacted laser arrays .....	129
Fig. 4.19 SEM showing close view of completed laser .....	130
Fig. 4.20 SEM of the high speed laser arrays .....	130
Fig. 5.1 Schematic of the intra-cavity contacted laser .....	135
Fig. 5.2 Detail of experimental intra-cavity design .....	136
Fig. 5.3 CW <i>L-I</i> characteristics of 20 nm offset lasers .....	138
Fig. 5.4 CW <i>L-I</i> characteristics of 10 nm offset lasers .....	139
Fig. 5.5 CW <i>I-V</i> characteristics of 10 nm offset lasers .....	140
Fig. 5.6 CW Power conversion efficiency .....	141
Fig. 5.7 CW <i>L-I</i> characteristics scaled by area .....	142
Fig. 5.8 Optical spectra for the four laser sizes .....	143
Fig. 5.9 Wavelength shift with temperature .....	145
Fig. 5.10 Determination of the thermal conductivity .....	145
Fig. 5.11 Pulsed <i>L-I</i> characteristics of 10 nm offset lasers .....	147



Fig. 5.12 Pulsed $L$ - $I$ characteristics scaled by area .....	148
Fig. 5.13 Pulsed $I$ - $V$ characteristics of 10 nm offset lasers .....	149
Fig. 5.14 Microwave probing setup .....	150
Fig. 5.15 $ S_{11} $ for the four laser diameters.....	151
Fig. 5.16 $S_{11}$ for the 7 $\mu$ m laser in Smith chart format.....	153
Fig. 5.17 Small signal equivalent circuit for 7 $\mu$ m laser.....	154
Fig. 5.18 Normalized modulation response of the 7 $\mu$ m laser .....	155
Fig. 5.19 Bandwidth of the four lasers vs. drive current .....	158
Fig. 5.20 Modulation Current Efficiency Factor vs. diameter .....	160
Fig. 5.21 Experimental setup for bit error rate measurements .....	161
Fig. 5.22 2.488 Gbit/s BER curves for the four laser diameters .....	162
Fig. 5.23 Eye diagram for the 5 $\mu$ m laser at 2.488 Gbit/s.....	164
Fig. 5.24 1.6 Gbit/s on/off modulation at varying temperatures .....	165
Fig. 5.25 Variation in received signal power for $10^{-9}$ BER.....	166
Fig. 6.1 Intra-cavity structure for simulation .....	169
Fig. 6.2 Calculated pulsed $I$ - $V$ curves for four laser diameters .....	170
Fig. 6.3 Calculated CW $I$ - $V$ curves for four laser diameters .....	171
Fig. 6.4 Calculated current profiles for 5 $\mu$ m laser .....	172
Fig. 6.5 Calculated current profiles for 15 $\mu$ m laser .....	173
Fig. 6.6 Comparison of calculated and measured $L$ - $I$ .....	175
Fig. 6.7 Calculated multimode $L$ - $I$ curve for 10 $\mu$ m laser .....	176
Fig. 6.8 Predicted $L$ - $I$ curves for improved 7 $\mu$ m laser.....	178
Fig. 6.9 Current-apertured structure for simulation .....	179
Fig. 6.10 Current density profiles for varying designs .....	181
Fig. 6.11 Current density profiles multiplied by radius .....	182
Fig. 6.12 Voltage distribution in structure at 8 mA bias .....	183
Fig. 6.13 Predicted $I$ - $V$ and current density profiles .....	183
Fig. 6.14 Predicted $L$ - $I$ characteristics of current-apertured design.....	184
Fig. 6.15 Calculated modal gain curves for the 7 $\mu$ m laser .....	185
Fig. 6.16 Predicted modal gain curve of current-apertured design.....	186

Fig. A.1 AlGaAs index of refraction .....	191
Fig. B.1 Gain vs. current schematic .....	194
Fig. B.2 P-I-N junction band diagram .....	195
Fig. B.3 Fermi-Dirac functions and density of states .....	197
Fig. B.4 Calculated quantum well gain curve and spectrum .....	200
Fig. B.5 Schematic of the curve fit model .....	203
Fig. B.6 Peak gain: comparison of model and calculation .....	205
Fig. B.7 Gain spectra: comparison of model and calculation .....	206
Fig. B.8 $N_{th}$ vs. $T_{jcr}$ : varying gain offset .....	207
Fig. B.9 $N_{th}$ vs. $T_{jcr}$ : varying threshold gain .....	208
Fig. B.10 Recombination current density vs. carrier density .....	209
Fig. D.1 Typical semiconductor vertical cavity .....	226
Fig. D.2 Optical power flow : in-plane and vertical cavities .....	227
Fig. D.3 Mode spacing for in-plane and vertical cavities .....	230
Fig. D.4 Coordinate system for transmission matrix analysis .....	236
Fig. D.5 Layer numbering for transmission matrix analysis .....	239
Fig. D.6 Transmitted and reflected waves from gain medium .....	249
Fig. D.7 Longitudinal enhancement factor .....	252
Fig. D.8 Phase diagram for a distributed Bragg reflector .....	253
Fig. D.9 Phase diagram for substrate and air terminations .....	254
Fig. D.10 Phase diagram for metal termination .....	255
Fig. D.11 Reflectivity spectra for varying mirror periods .....	257
Fig. D.12 Reflectivity phase for a distributed Bragg reflector .....	259
Fig. D.13 Reflectivity spectra for varying index steps .....	260
Fig. D.14 Typical optical cavity design with doping .....	263
Fig. D.15 Axial standing wave pattern in cavity .....	266
Fig. D.16 Determination of the quality factor .....	271

Fig. E.1 Thermal impedance of AlGaAs .....	274
Fig. E.2 Donor activation in AlGaAs digital alloys.....	276
Fig. E.3 Structure of three intra cavity designs .....	278
Fig. E.4 <i>J-V</i> of three intra cavity designs.....	279

## Chapter 1: Overview and Background

### 1.0 Introduction

This dissertation presents my work towards developing the vertical-cavity surface-emitting laser. From the outset, my original proposal was to make a vertical-cavity laser with lateral injection and all-semiconductor distributed Bragg reflectors [1]. My initial experimental attempts, however, produced lasers with performance far below my expectations. It became clear that the structure's complexity called for device models to explore and optimize the design. Chapters 2 and 3 present the models which are capable of simulating the terminal characteristics of the lasers. The modeling showed the need for careful control of the epitaxial growth and for precise formation of multiple mesas. The *in-situ* controlled growth and device fabrication processes I developed are presented in Chapter 4. The resulting intra-cavity contacted lasers showed excellent characteristics including sub-milliamp threshold currents, high quantum efficiency and record modulation-current-efficiency-factors. The measured laser characteristics are presented in Chapter 5.

The interplay between model and experiment has been a central theme in my work. I have continuously developed models to design better devices and used experimental confirmation to refine the models. My first major contribution to the field was the development of a current-to-light model for etched-post vertical-cavity lasers with uniform current injection. The model was able to simulate the output characteristics for varying size and temperature, including a wide variety of physical effects [2]. The next major contribution was the identification of the importance of a gain-offset design with high carrier confinement for producing stable, high-operating-temperature vertical-cavity lasers [3]. I then demonstrated the improvements by designing and fabricating etched-post lasers with dramatic improvements in performance [4, 5].

With the active region design now optimized, the next major contribution was the development of the intra-cavity contacted device models for non-uniform

current injection and the introduction of a current-leveled design which limits current crowding effects [2]. This structure had the advantage of a dielectric current constriction for current confinement, removing the etched active-region boundaries from the region of current injection, while maintaining strong index-guiding for tight optical confinement. The next major contribution was the demonstration of intra-cavity contacted lasers which show good agreement with the theoretical models including sub-milliamp threshold currents [6]. I fabricated the intra-cavity contacted vertical-cavity lasers on semi-insulating substrates with coplanar transmission lines. This low-parasitic-capacitance contacting scheme made it possible to make high-speed measurements on-wafer. Analysis of the microwave measurements showed that these were the first vertical-cavity lasers to behave in agreement with theory and demonstrated the importance of tight optical confinement for high-frequency operation at low bias currents [7].

Chapter 6 first presents a comparison of the experimental data with the laser models and then presents the projected performance of improved designs. Using only excess optical losses as a fitting parameter, the model shows good agreement with the data. My last major contribution to the field is the introduction of the current-apertured design. The current-apertured design restricts the region of current injection to a diameter less than that of the transverse optical mode. The result is a stabilized single-mode operation while simultaneously increasing the laser efficiency [2,8]. Such highly efficient, stable single-mode operation vertical-cavity lasers can be expected to play an important role in telecommunications, laser printing and sensor applications.

## 1.1 Historical Background

At the beginning of my thesis work, nearly all semiconductor lasers were made using an in-plane cavity configuration as shown in Fig. 1.1. Light propagates in the plane of the surface, both guided and amplified by a thin layer sandwiched between p-type and n-type doped layers on either side. Typically, the ends of the crystal are cleaved to form parallel mirrors which reflect part of the light back on itself. As current is driven through the diode, electrons and holes are

trapped in the thin central layer producing a population inversion. For a range of photon energies near the bandgap, the probability of downward stimulated emission exceeds absorption and thus the central layer provides optical gain. An increase in the injected current results in an increase in the population inversion and the optical gain until a threshold current level is reached.

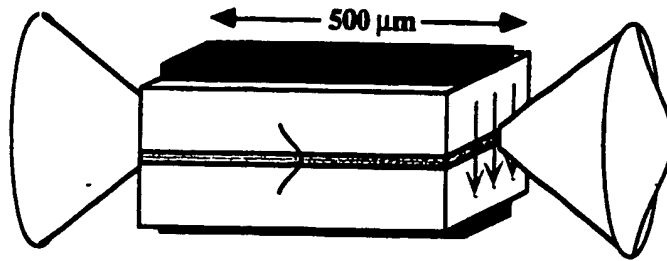


**Fig. 1.1.** Schematic of an in-plane semiconductor laser. Current is shown as gray arrows while the transverse optical mode is shown propagating between the two mirror facets.

Once the gain equals a resonant mode's optical losses due to scattering, free carrier absorption and transmission out the facets, the carrier population and gain stays essentially fixed. Instead, the optical power in the resonant mode with the highest gain increases linearly as the current is increased above the threshold current.

One group under the leadership of Kenichi Iga at Tokyo Institute of Technology had been struggling to produce a semiconductor laser with a radically different configuration [9]. This vertical cavity configuration is detailed in Fig. 1.2. Here, light propagates normal to the surface. Since the cavity length is quite short, very high reflectivities are required. Technically this design proved to be very challenging, and the majority of their publications covered the theoretical analysis of this device structure and attempts to achieve lasing under pulsed electrical excitation.

The advantages of the vertical-cavity laser are closely related to the different geometry. Emission from the surface removes the need for cleaving, allowing automated wafer-level testing and opening the possibility of two-dimensional laser

#### 4 Section 1.1 Historical Background

arrays. Another advantage is that the beam is emitted from an aperture many wavelengths across, resulting in a low divergence beam and thereby relaxing packaging tolerances compared to the highly stigmatic, diverging beam of the in-plane design. Yet another advantage is that the small area makes it theoretically possible to produce very low threshold currents. In addition, the short cavity length means that the Fabry-Perot modes are widely spaced. The large energy separation between longitudinal modes makes it possible to realize a single mode laser without the complicated grating process used for in-plane lasers.

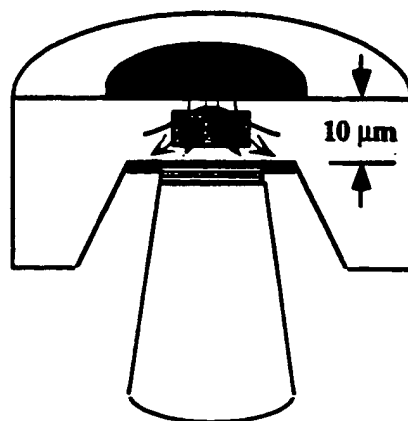


**Fig. 1.2.** Schematic of a surface emitting semiconductor laser. The active region and current are confined by regrowth techniques. Mirrors are made from combinations of metals and multi-layer dielectrics.

In 1984 Iga's group achieved room temperature pulsed operation of a surface emitting laser [10]. By 1988 they had achieved room temperature continuous wave (CW) operation [11]. The laser had a threshold current of 32 mA and an external quantum efficiency (the ratio of photons emitted to injected electrons) of 10%. At this point I had joined Prof. Coldren's group and was searching for a research topic. Graduate students Ran Hon Yan and Rob Simes were developing Fabry-Perot reflection modulator using epitaxially grown distributed Bragg reflectors. Looking at their device structure, I proposed that a vertical-cavity laser could be made using the same technology. Along with

graduate students Randy Geels and Scott Corzine, we began working on a vertical-cavity laser with epitaxial semiconductor mirrors. Our initial designs were based on a n-i-p-i structure to allow multiple active regions [12] which were capable of lasing with reflectivities on the order of 95%. Geels worked on growth and the optical cavity design [1]. I worked on the electrical design and pursued diffusion techniques to contact these multiple diode devices while Corzine made optical pumping experiments to study the devices without the complications of fabrication [13]. Our group, however, was not the only lab pursuing a vertical-cavity laser with semiconductor mirrors; it was an idea whose time had come.

In 1989 Jewell *et al.* at AT&T reported on the lasing operation of a vertical-cavity lasers using a single pin active region [14, 15]. This proved that the mirrors were capable of providing reflectivities in excess of 99.5% and opened the possibility of simpler device designs. At that point our work at UCSB became focused on two distinct designs. Randy Geels strove to improve on Jack Jewell's bottom emission, etched pillar design. I began working on a top emission, intra-cavity contacted design. These early device structures are shown in Fig. 1.3.

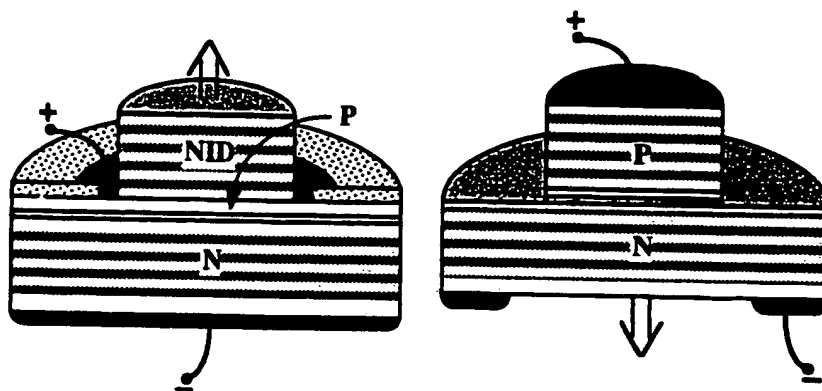


Fig. 1.3. Two laser structures with single active regions. On the left, a top-surface-emitting laser with one intra-cavity contact to the p-side of the diode. On the right, the bottom-emission vertically-contacted structure.



My initial goals were to provide low resistance by bypassing the p-type mirror stack and to emit light out the top surface for ease of testing and freedom to choose the operating wavelength.

Early in 1990, Yoo *et al.* reported [16, 17] on a similar structure using a heterojunction bipolar transistor process and an oxygen implant for electrical isolation under the p ring contact. They reported a 6 mA threshold and a linewidth of 5 Å under pulsed operation. Their claim of lasing seemed suspect as the 5 Å linewidth roughly matches the cold cavity resonance that would filter the broadband spontaneous emission, while spectral measurements on other vertical-cavity lasers had shown spectrometer limited linewidths below 1 Å. In addition, the current-to-light ( $L-I$ ) characteristics, given in arbitrary units, were highly non-linear. Their measured current-to-light curve was similar to the response of a spontaneous emission source coupled to a saturable absorber, such as the central unpumped region of their 25 μm diameter ring-contacted device. They have not made any additional publications on that device structure.

Optical pumping measurements by Scott Corzine on my first wafer had indicated threshold currents on the order of 4 mA with external efficiencies in the range of 20%. The  $L-I$  characteristics of my first working device in May of 1990 are shown in Fig. 1.4. The continuous wave measurements shown in the inset were initial cause for excitement, but the low power levels and the nonlinear characteristics, similar to Yoo's results, were suspicious. Under pulsed current excitation the lasers showed very different characteristics. The threshold current was closer to 22 mA while the external efficiency was about 2%. This confirmed the saturable absorber theory, but was far poorer performance than predicted by the optical pumping experiments. What had gone wrong?

Returning to the intra-cavity device structure of Fig. 1.3, the most obvious problem is the lack of current confinement. By observing the spontaneous emission below threshold, it appeared that I was pumping a diameter ~2.5 times larger than my device. This shunt path would lead to a seven fold increase in the threshold current and an equivalent reduction in the external efficiency. The hypothesis that a shunt path was responsible for the poor performance made sense,

yet implied a more complex structure was required. There were other clues apparent in the device characteristics. The lasers only worked when pulsed, not under continuous wave (CW) operation. To make the measurements without heating I used 50 ns pulses. Longer pulses showed a dramatic drop off in output power at the tail of the pulse. I became convinced that the proper alignment of the cavity mode with the gain peak was a critical parameter.

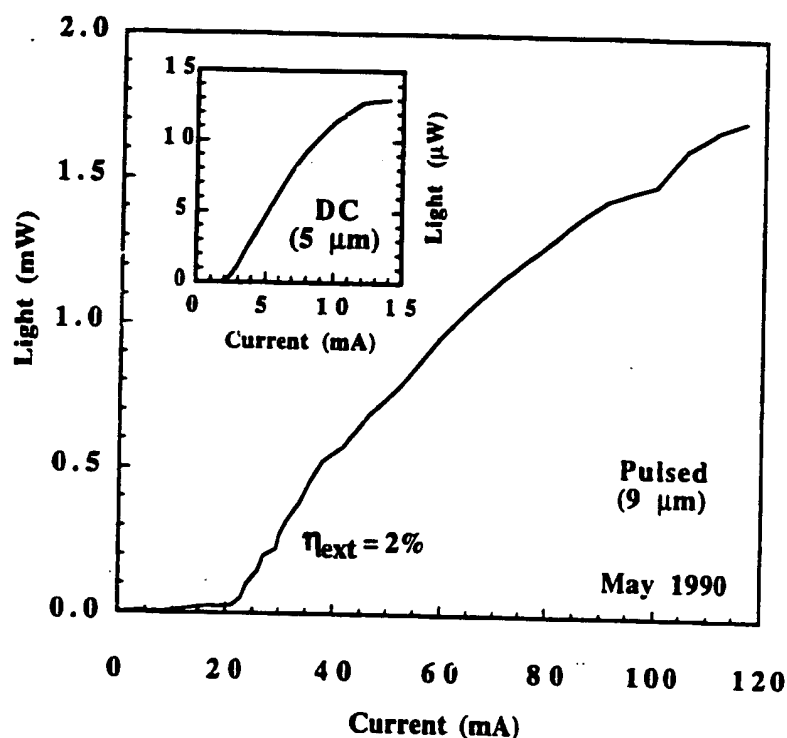


Fig. 1.4. Initial current-to-light ( $L$ - $I$ ) results for the intra-cavity laser shown in Fig. 1.3

Even under operation with very short pulses, the laser showed non-linear current-to-light characteristics. If this saturation of output power was not due to heating, then where was it coming from? Again considering the ring contact

configuration, I suspected that the current was crowding near the contact where the optical mode was weak and not penetrating under the central waveguide. I hypothesized that as the diode became forward biased its dynamic resistance became low in comparison with the spreading resistance of the contact layer and thus the additional current was not distributed under the waveguide. Further reflection and calculations lead me to believe that it would be necessary to introduce some resistance between the heavily doped contact layer and the p-i-n junction if one desired milliwatts of output power.

All these measurements indicated changes in the design of the laser. Yet as with all engineering problems, there are tradeoffs to be made. Lacking quantitative tools to optimize the design, I was at a loss. For the next two years, my work was concentrated on developing numerical models with predictive power. Chapters 2 and 3 describe these models. Soon after my initial results, Geels successfully fabricated the bottom emission design [18]. He took a wealth of data. The simple device structure of this bottom emission laser was ideal for modeling. I began applying my models to his experimental results, extracting internal parameters. I further encouraged him to make temperature dependent measurements as well, as I have always found that the temperature dependence of a device reveals its underlying physics. My goal was to develop a simulation of the laser's current-to-light characteristics that could be used to explore the performance of the more complicated intra-cavity designs.

At the same time Corzine, with considerable effort, had developed a first principle gain model for the strained quantum wells. Measurements on in-plane lasers indicated an excellent agreement with his theory. Using cylindrical coordinates to reduce the simulation to one dimension, I combined the results of his quantum well gain calculations with equations for the various other physical effects in the device as shown in Fig. 1.5. The carrier density is found in each cell so that current continuity is satisfied. Included are the effects of carrier diffusion, surface recombination, spontaneous and stimulated emission, spatial hole burning, Auger recombination and carrier leakage [2]. In modeling the temperature dependence of the threshold current, it became clear that the relative position of the

gain peak to the cavity mode was an essential and sensitive parameter. Changing the lasing wavelength by 10 nm, a 1% change in the growth rate, would have a significant effect on the current-to-light characteristics.

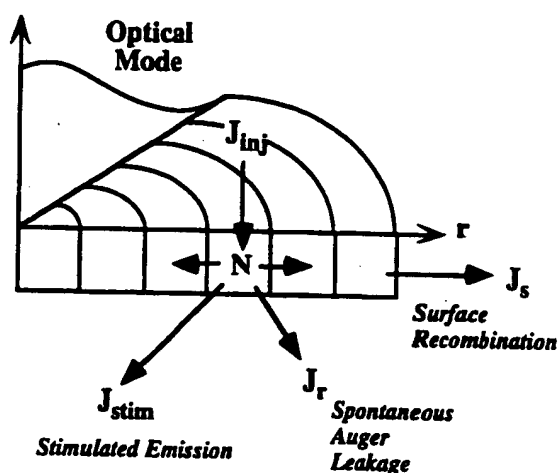


Fig. 1.5. Schematic of the numerical current-to-light model. The strong variation of the optical mode results in spatial hole burning effects.

During this period from 1990-1992, my modeling efforts were intensified by the high frequency of down time on the molecular beam epitaxy (MBE) growth system which produced our wafers. At the end of this period, our understanding of the laser's physics had greatly improved due to the modeling, and I designed an improved version of the bottom emission device with better carrier confinement and lower optical losses. Graduate students Bruce Young, Brian Thilbeault and Matt Peters were active members of the group, replacing the now graduated Randy Geels as the principle growers. Collectively we tried several versions of my redesign of Geels' device, varying the output mirror reflectivity and the gain offset. Bruce Young grew a wafer with a +25 nm gain offset (determined by subtracting the cavity mode wavelength  $\lambda_c$  from the room temperature photoluminescence peak  $\lambda_{pl}$ ). Using an improved process that eucapsulated the etched surfaces with silicon dioxide, I fabricated the material into vertical-cavity

lasers which proved to have record performance and very high temperature operation [4]. Even more interesting, however, was the broad range of temperature-stabilized operation.

Realizing temperature-stabilized operation represents an important advancement in semiconductor laser sources. Most high-speed laser modules use a thermoelectric cooler to control the laser temperature. An alternative is the hybrid integration of a monitor detector on the backside facet along with bias control circuitry to adjust the drive conditions. In either case, considerable complexity and cost is introduced into the final laser module. A temperature-stabilized, low-threshold-current laser no longer needs these kinds of controls. In the case of packaged laser arrays, this simplicity is even more important. The possibility of a threshold minimum for the vertical-cavity design was originally discussed by Gourley [19]. Tell *et al.* [20] reported experimental measurements showing a minimum in threshold for vertical-cavity lasers at very low temperatures.

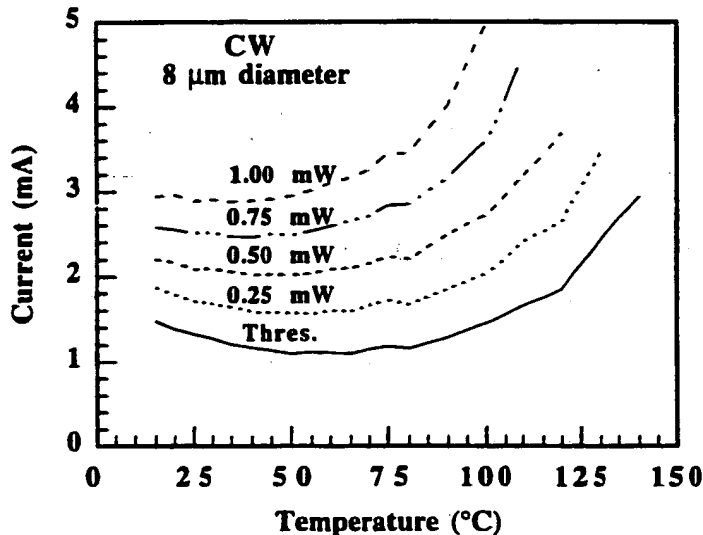
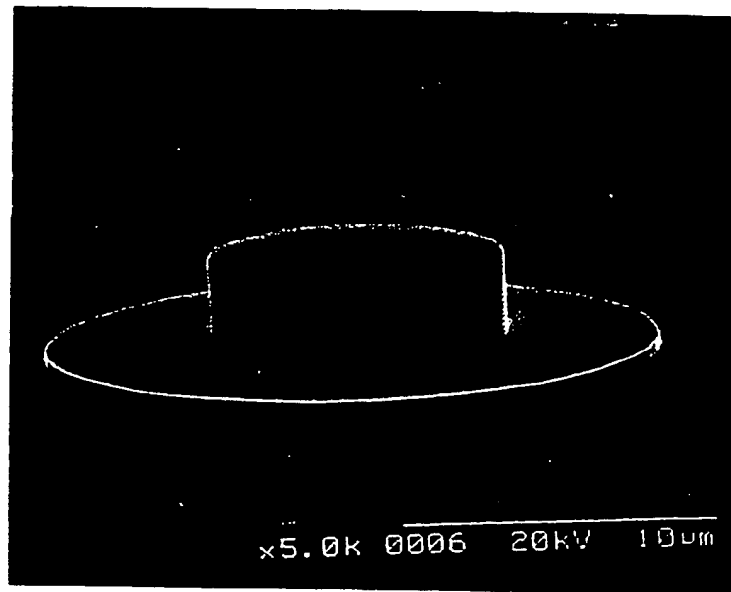


Fig. 1.6. Plot of the current needed to maintain a fixed output power for a gain offset designed bottom emission pillar type vertical-cavity laser.

The bottom surface emitting lasers grown by Young that I had designed and fabricated showed a minimum at elevated temperatures [3]. We took extensive data on their characteristics. A plot of the current required to maintain a given output power is shown in Fig. 1.6 [5]. This property has the potential to dramatically reduce the costs of high speed laser modules and is entirely dependent on the cavity design and growth control. Since 1992, we have been able to consistently produce working vertical-cavity laser material.

With the material growth under control, the device models verified and an excellent active region design I set about developing the design and fabrication technology for these intra-cavity contacted vertical-cavity lasers. The two are not independent as the fabrication technologies limit the tolerances and materials needed in the epitaxial design.



**Fig. 1.7.** Scanning electron micrograph of the two-mesa structure produced in a single reactive ion etch step. The field is n-type, the ring mesa is p-type while the undoped center pillar is both a reflector and a waveguide.

One of the earliest processes I developed at UCSB was the incorporation of an *in-situ* optical reflectivity monitor on the Cl reactive ion etcher. This process allowed the etching several microns of material and stopping within 500Å of the target. Using an *in-situ* monitoring scheme turned out to be a highly useful technique. Many devices and a number of dissertations have relied on this technique for accurate, controlled etching. Building on this control I developed a two-mesa process which uses a sacrificial Si mask to repeatably produce the mesa structure shown in Fig. 1.7. Several intra-cavity optoelectronic devices have been fabricated with this technique [21-23]. Using this structure it would be possible to produce contacts to both p and n type layers within the optical cavity.

During this period, however, the field was continuing to advance. Work by Matt Peters in our group [24] and Lear *et al.* at Sandia [25] had reduced the drive voltage of vertical-cavity lasers with current injection through the mirror stacks to less than 3V. Scherer *et al.* [26] and Choquette *et al.* [27] had both fabricated vertical-cavity lasers with one intra-cavity contact, although their performance was not as good as the vertically contacted pillar structures. Both ~10 µm diameter lasers had threshold currents near 4 mA with external quantum efficiencies in the range of 4 to 12% and maximum output powers below 1.5 mW. With these developments in mind, it was important to redefine the advantages and goals of my work on the intra-cavity contacted vertical-cavity lasers. I choose to take full advantage of the design by using two intra-cavity contacts on a semi-insulating substrate. This low capacitance, current-constricted design is discussed in the next section.

## 1.2 Intra-Cavity Contacted Vertical-Cavity Lasers

Most vertical-cavity laser structures under investigation can be divided into two classes; index-guided and gain-guided. Index-guided structures confine the current and optical mode using an index discontinuity in the structure which results in predictable transverse modes determined by the waveguide dimensions. The gain-guided structures use proton implantation to confine the region of current

injection. In gain-guided structures thermal lensing and spatial hole burning have important effects on the transverse mode profile due to the lack of strong index discontinuities [28]. In either case, the current is generally injected into the active region after passing through the distributed Bragg reflector (DBR) mirror stacks.

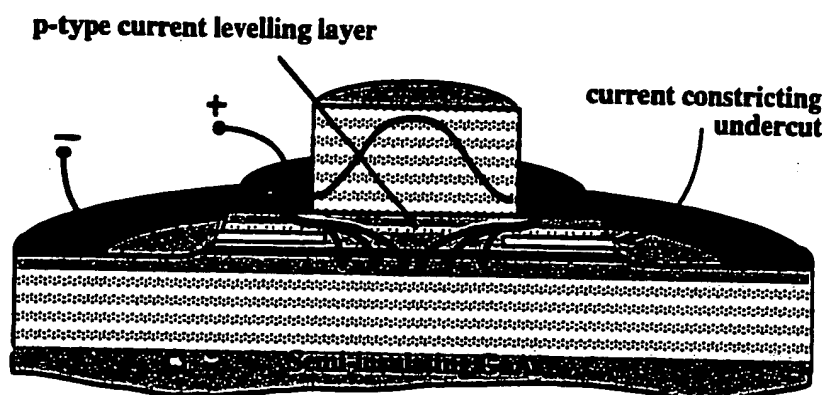


**Fig. 1.8.** Schematic of the redesigned intra-cavity contacted structure including a current constriction to avoid shunt paths and a resistive current leveling layer to minimize current crowding.

In order to reduce the drive voltage and improve the laser's power conversion efficiency, much effort has been made to improve the DBR conductivity by tailoring the bandgap and doping profiles of the heterointerfaces [24, 25, 29]. Along with these efforts, however, come other difficulties. The dopants cause free carrier optical losses, and the graded DBR interfaces result in deeper optical penetration depths which also increase the optical losses. In addition, the ternary alloys used in the graded regions can have thermal impedances as much as ten times that of the binary materials due to increased phonon scattering. The top-surface-emission intra-cavity contacted structure shown schematically in Fig. 1.8 avoids the above difficulties by separating the electrical contact design from the DBR reflector design. The current is distributed by two doped layers on either side of the active region while the mirror stacks and substrate are undoped. The lateral index-guide is determined by the smallest



diameter index discontinuity. In these devices the dielectric current constriction formed by wet etching an AlAs layer provides the lateral index-guide.

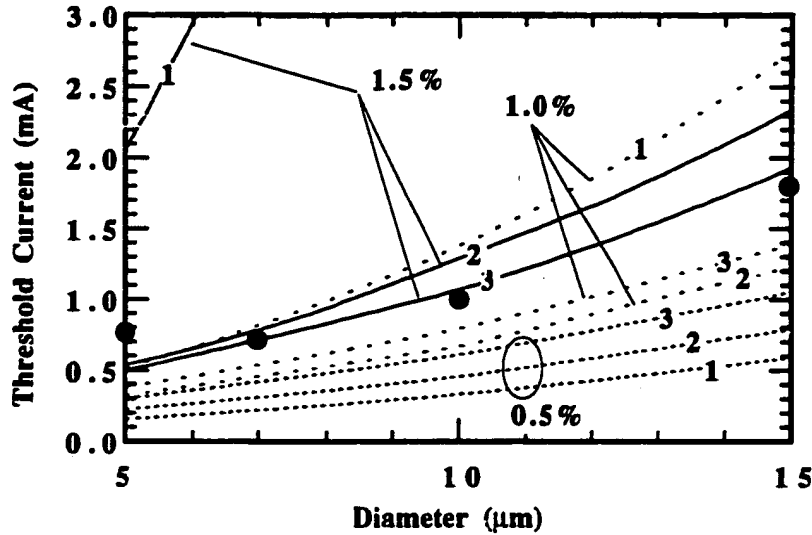


Fig. 1.9. Calculated threshold current for varying constriction diameter. The curves are calculated for round-trip gain levels of 1.5, 1.0 and 0.5% for 1, 2 and 3 quantum wells. The carriers are allowed to diffuse out to an etched surface 5  $\mu\text{m}$  beyond the constriction/mode radius. The gray dots are experimental results.

Low threshold in-plane lasers have been produced using either regrowth or disordering processes. Such advanced processes have not yet produced high performance vertical-cavity lasers due to the requirements of high planarity for the distributed Bragg reflectors. A simple current constriction is able to produce the low threshold currents required for array applications. Calculations using the current-to-light model of Chapter 2 showing the potential of the design to produce low threshold lasers are presented in Fig. 1.9. Using the parameters listed in Table 6.1, the threshold current as a function of laser diameter is plotted for several round-trip threshold gain levels. For each gain level, the threshold current is calculated using one, two and three quantum wells, each well presumed to be 80Å

thick with 80Å GaAs barriers. The calculation assumes that the cavity mode is offset 4 nm longer than the gain peak at a carrier density of  $4 \times 10^{18} \text{ cm}^{-3}$ , as was the case in the experimental devices presented in Chapter 5. The radial carrier diffusion out from the current constriction in the quantum well is included, assuming an ambipolar diffusion coefficient of 40 cm/s. The threshold current becomes smaller as the laser diameter is reduced as long as the threshold gain remains constant. In practice, increased optical scattering and diffraction losses increase the threshold gain levels for the smaller lasers.

The optimal number of quantum wells to use depends on the required gain level. Three round-trip gain levels are shown. The highest is representative of the lasers presented in Chapter 5. The middle level represents a design with lower external efficiency, but still quite practical. The lowest level has a threshold gain level just slightly higher than the internal losses, so that the optical losses of the cavity would need to be improved to make this design practical. At a round-trip gain of 1.5%, the threshold current increases as the number of wells is reduced, indicating that the quantum well gain is saturating. At a round-trip gain of 0.5%, the situation is reversed with the threshold current dropping as the number of wells is reduced. Even with the outward diffusion of carriers, very low threshold currents can be expected for this current-constricted design. The lasers fabricated in this work had a mirror transmission of 0.87% and round-trip internal losses of 0.45%. Additional scattering losses of 0.15% bring the required threshold gain of the 7  $\mu\text{m}$  diameter laser to nearly 1.5%. From the plot the threshold current is predicted to be 0.71 mA, in good agreement with the 0.72 mA measured. The laser had an external quantum efficiency of 38%. If a lower efficiency was acceptable, the mirror transmission could be reduced and the threshold current could easily be brought below 0.5 mA. While even lower threshold currents could be achieved with fewer quantum wells, the differential gain and hence speed would also be reduced.

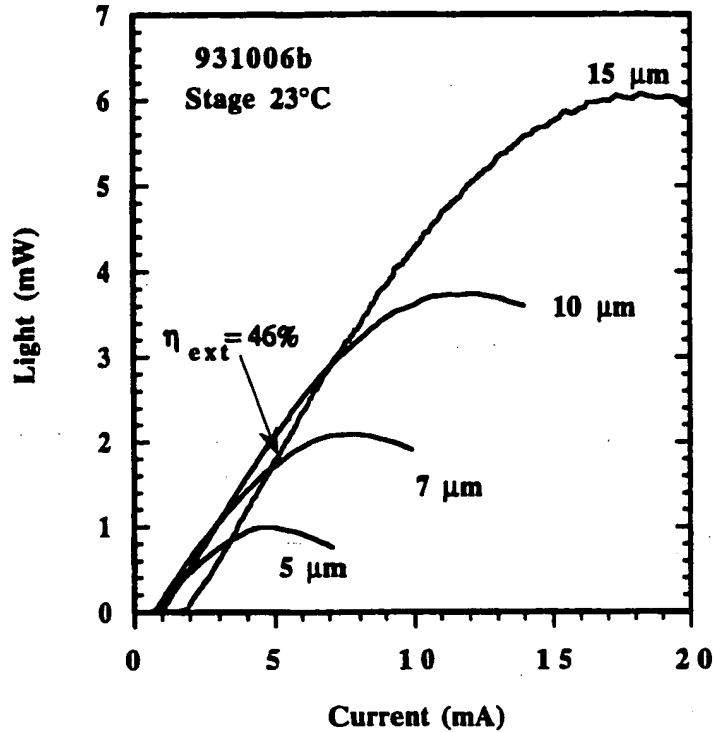


Fig. 1.10. Measured  $L-I$  characteristics of the intra-cavity contacted lasers shown in Fig. 1.8. Sub-milliamp thresholds and high external quantum efficiency are observed for these lasers with a 4nm gain offset.

To span the range from single mode to multimode operation, lasers with diameters of 5, 7, 10 and 15  $\mu\text{m}$  were fabricated. The experimental threshold currents are shown as gray dots in Fig. 1.9. The threshold current follows the theoretical curve for the three quantum well active region used except for the smallest device. The threshold current for the 5  $\mu\text{m}$  laser is higher because excess optical losses have increased the threshold round-trip gain to 2%. The corresponding current-to-light characteristics for these intra-cavity contacted vertical-cavity lasers are shown in Fig. 1.10 [6]. Threshold currents are as low as 0.7 mA for the 7  $\mu\text{m}$  diameter laser which has a maximum output power of 2 mW.

The external quantum efficiency of the 15  $\mu\text{m}$  laser is 46%. Drive voltages were near 3V at threshold and below 4V at peak power for all four device diameters, indicating considerable room for improvement as discussed in Chapter 6. Surface scattering and spatial hole burning have competing effects, resulting in a wide range of spectral properties. The 5  $\mu\text{m}$  device lases with a side mode suppression ratio (MSR) in excess of 40dB while the 15  $\mu\text{m}$  device has four competing transverse modes. These device characteristics are discussed in detail in Chapter 5 and modeled in Chapter 6.

In addition to the potential for reduced thermal impedance and optical losses of the intra-cavity design, the two ring contacts on the top surface allow the substrate to be made of semi-insulating material. Interconnect lines can be routed without introducing stray capacitance. All of the high speed microwave design and characterization techniques developed for monolithic microwave integrated circuits become applicable. On-wafer probing of lasers contacted by coplanar transmission lines can be used to make scattering parameter measurements. Using a fiber-optic probe, high-speed device characterization can be made on wafer. Digital data transmission experiments at multi Gigabit/s rates can be made without any device packaging! The same 7  $\mu\text{m}$  diameter laser has a modulation bandwidth in excess of 8 GHz at a bias of only 4 mA [7]. The results of the high speed measurements are discussed in Chapter 5.

Another advantage of the intra-cavity design is its ability to be used to produce current apertured designs. A current apertured design restricts the carrier injection to a diameter less than that of the optical mode. The improved overlap of the optical mode with the carriers has two major benefits. First, the laser is more efficient with a 20 - 30% increase in the external quantum efficiency [2]. The second benefit is a stabilization of fundamental mode operation, first analyzed by Moriki *et al.* in 1987 [30] for a similar gain apertured design. While the short cavity length results in a wide frequency spacing of the longitudinal modes, the strong lateral index-guide supports many closely spaced transverse modes. The fundamental transverse mode is peaked at the center of the device and tends to deplete the carriers in the center. This spatial hole burning increases the gain of the

higher order transverse modes, resulting in multimode operation at elevated output powers. By restricting the injection carriers to the central region of the waveguide, multimode operation can be suppressed.

While simple in principle, this design has been elusive due to a lacking technology. The requirement is that the current injection or active region must be constricted without constricting the optical mode. The conventional techniques of ion implantation or diffusion have been successfully applied for such tasks in in-plane lasers [31], but the thick upper mirror stack has precluded their use on vertical-cavity lasers with semiconductor mirrors. The ring contacted intra-cavity design shown in Fig. 1.8 does not use the upper mirror for conduction. It could also be a dielectric mirror deposited after the fabrication was complete, allowing the use of conventional techniques. The  $L-I$  characteristics shown in Fig. 1.10 demonstrate that these ring contact designs can produce high performance vertical-cavity lasers. In combination with a current apertured design, their future looks very bright indeed. These advanced designs will be discussed in greater detail in Chapter 6.

Finally, the intra-cavity design has the potential for a high yield, nearly planar fabrication process. The fabrication sequence discussed in Chapter 4 became relatively complex due to requirements of providing isolated ring contacts around the base of a  $3\text{ }\mu\text{m}$  tall waveguide / mirror with a clear top as shown in Fig. 1.11. The fabrication required many masking steps with a combination of image reversal resist and self aligned dry etch and deposition processes. From a developmental view, this structure was ideal as it represents the minimum number of changes from the bottom-emission etched-post laser. Now that the intra-cavity designs have been proven viable, the next step is to make them easier to fabricate. Replacing the upper waveguide with a dielectric mirror deposited after the fabrication is complete greatly simplifies the fabrication sequence. Conventional photolithographic techniques can be used on the nearly planar structure. While the results presented in Chapter 5 represent state-of-the-art semiconductor lasers, combining the intra-cavity designs developed in this dissertation with dielectric

mirrors and a current-apertured process will produce very high performance, manufacturable single-mode vertical-cavity lasers arrays.

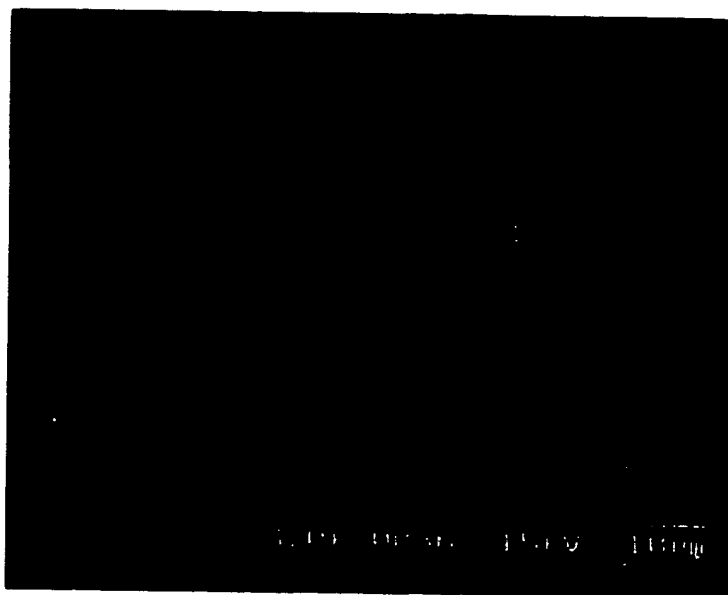


**Fig. 1.11.** Scanning electron micrograph of a 10  $\mu\text{m}$  diameter intra-cavity contacted vertical-cavity laser. Corresponding schematic and characteristics are shown in Fig. 1.8 and Fig. 1.10 respectively.

### 1.3 Dissertation Overview

The dissertation has two main parts. Chapters 2 and 3 develop the design tools needed to simulate the terminal characteristics of intra-cavity contacted vertical-cavity lasers. Chapters 4 and 5 present the technology needed to realize the designs and the experimental characteristics of the lasers. Chapter 6 uses the experimental data to confirm the models and then predicts the performance of improved laser designs.

Many different effects must be included to accurately describe the laser's continuous wave (CW) properties. The collection of models used are outlined in Fig. 1.12. An optical model, active region model, thermal model, electrical model and current-to-light model must be combined together. Appendices B and D

discuss the active region model and the cavity's optical model respectively. Chapters 2 and 3 combine these models with thermal, electrical, transverse optical and current-to-light models to enable simulation of a wide variety of device structures.

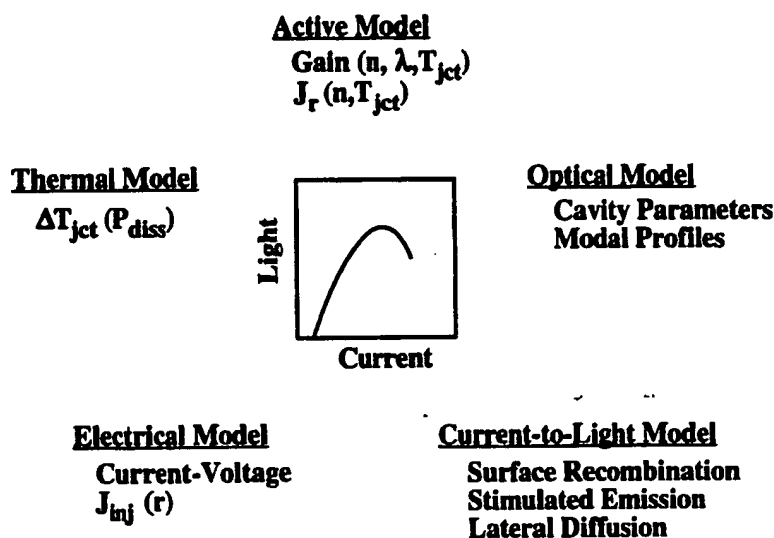


Fig. 1.12. The collection of device models needed to simulate the lasers' characteristics.

Chapter 2 develops the current-to-light model including two dimensional effects. Starting from the round-trip cavity parameters derived in Appendix D, the chapter begins with a qualitative discussion to introduce the effects of spatial hole burning, carrier diffusion, surface recombination and gain offset. Next, the numerical equations which describe these effects are developed. The simulations for single-mode operation are applied to experimental data, extracting internal parameters and clarifying the device physics. An attempt is made to emphasize the various measurements that can be made to separate out the different physical effects. Finally, the model is used to investigate the potential performance of various laser designs.

Chapter 3 considers the effect of non-uniform current injection and the design of the intra-cavity contact layers. The chapter begins with an analytical analysis of current crowding and current leveling effects. Next, the numerical model for current flow in cylindrical coordinates is developed which includes the nonlinear diode properties. The current model is compared with the analytic formulas and then combined with the current-to-light model from Chapter 2 to predict the performance of intra-cavity contacted lasers, showing the advantage of introducing a limited leveling resistance between the contacting layer and the active region.

Chapter 4 presents the fabrication technology developed to realize the intra-cavity design. The fabrication sequence is complex, and thus reliable, repeatable processes were needed for a high probability of success (even today, good material is difficult to come by.) Emphasis was made on dry etching and self-aligned processes. *In-situ* control for both the wafer growth and the reactive ion etching was introduced to provide repeatable results. The fabrication process is covered in general terms, the step-by-step details left to Appendix C.

Chapter 5 shows the experimental measurements made on the laser arrays. DC and pulsed  $L-I$ ,  $I-V$  and spectral characteristics are shown and discussed. One of the major advantages of the laser design is that both contacts are on and emission is from the top surface of a semi-insulating substrate. This convenient, low capacitance design is ideal for making various high-speed measurements without any device packaging. Accurate microwave characterization is possible, including the variation of modulation response with varying laser diameter and temperature. The data represents the first experimental confirmation of the theory for vertical-cavity laser modulation response. Along with the microwave measurements, bit error rate measurements at Gbit/s data rates have been made, showing that the lasers do not introduce power penalties associated with anomalous large-signal modulation response.

Chapter 6 looks at future directions for intra-cavity contacted lasers. First, all the various details learned by fabricating and testing these first generation lasers point out some dramatic improvements in the laser characteristics are possible for



relatively little work. Using the models developed in the dissertation, the intra-cavity contacted lasers are analyzed and then realistic predictions are made for these improved lasers. These designs are then extended assuming the development of a current apertured technology. The results indicate that intra-cavity contacted vertical-cavity lasers can be expected to become an important very high-speed low-current single-mode coherent light source.

### References

1. R.G. Geels, R.H. Yan, J.W. Scott, S.W. Corzine, R.J. Simes, and L.A. Coldren, "Analysis and Design of a Novel Parallel Driven MQW-DBR Surface-Emitting Laser" in *CLEO '88*, 1988. Anaheim, CA.
2. J.W. Scott, R.S. Geels, S.W. Corzine, and L.A. Coldren, "Modeling temperature effects and spatial hole burning to optimize vertical-cavity surface-emitting laser performance." *IEEE Journal of Quantum Electronics*, **29** (5) pp. 1295-308. 1993
3. J.W. Scott, S.W. Corzine, D.B. Young, and L.A. Coldren, "Modeling the current to light characteristics of index-guided vertical-cavity surface-emitting lasers." *Applied Physics Letters*, **62** (10) pp. 1050-2. 1993
4. D.B. Young, J.W. Scott, F.H. Peters, B.J. Thibeault, S.W. Corzine, M.G. Peters, S.-L. Lee, and L.A. Coldren, "High-power temperature-insensitive gain-offset InGaAs/GaAs vertical-cavity surface-emitting lasers." *IEEE Photonics Technology Letters*, **5** (2) pp. 129-32. 1993
5. D.B. Young, J.W. Scott, F.H. Peters, M.G. Peters, M.L. Majewski, B.J. Thibeault, S.W. Corzine, and L.A. Coldren, "Enhanced performance of offset-gain high-barrier vertical-cavity surface-emitting lasers." *IEEE Journal of Quantum Electronics*, **29** (6) pp. 2013-22. 1993
6. J.W. Scott, B.J. Thibeault, D.B. Young, and L.A. Coldren, "High Efficiency Sub-Milliwatt Vertical Cavity Lasers With Intra-Cavity Contacts" *IEEE Photonics Technology Letters*, **6** (6) pp. 678-680. 1994
7. J.W. Scott, B.J. Thibeault, C.J. Mahon, L.A. Coldren, and F.H. Peters, "High Modulation Efficiency of Intra-Cavity Contacted Vertical Cavity Lasers" *Applied Physics Letters*, **65** (12) pp. 1483-1485. 1994

8. J.W. Scott, D.B. Young, B.J. Thibeault, M.G. Peters, and L.A. Coldren, "Design of Index-Guided Vertical-Cavity Lasers for Low Temperature Sensitivity, Sub-Milliamp Thresholds and Single Mode Operation." *IEEE Journal of Quant. Elec.*, to be published June, 1995
9. K. Iga, F. Koyama, and S. Kinoshita, "Surface emitting semiconductor lasers." *IEEE Journal of Quantum Electronics*, **24** (9) pp. 1845-55. 1988
10. K. Iga, S. Ishikawa, S. Ohkouchi, and T. Nishimura, "Room-temperature pulsed oscillation of GaAlAs/GaAs surface emitting injection laser." *Applied Physics Letters*, **45** (4) pp. 348-50. 1984
11. F. Koyama, S. Kinoshita, and K. Iga, "Room temperature CW operation of GaAs vertical cavity surface emitting laser." *Transactions of the Institute of Electronics, Information and Communication Engineers E*, **E71**, (11) pp. 1089-90. 1988
12. S.W. Corzine, R.S. Geels, J.W. Scott, R.-H. Yan, and L.A. Coldren, "Design of Fabry-Perot surface-emitting lasers with a periodic gain structure." *IEEE Journal of Quantum Electronics*, **25** (6) pp. 1513-24. 1989
13. S.W. Corzine, R.S. Geels, R.H. Yan, J.W. Scott, L.A. Coldren, and P.L. Gourley, "Efficient, narrow-linewidth distributed-Bragg-reflector surface-emitting laser with periodic gain." *IEEE Photonics Technology Letters*, **1** (3) pp. 52-4. 1989
14. J.L. Jewell, K.F. Huang, K. Tai, Y.H. Lee, R.J. Fischer, S.L. McCall, and A.Y. Cho, "Vertical cavity single quantum well laser." *Applied Physics Letters*, **55** (5) pp. 424-6. 1989
15. J.L. Jewell, A. Scherer, S.L. McCall, Y.H. Lee, S. Walker, J.P. Harbison, and L.T. Florez, "Low-threshold electrically pumped vertical-cavity surface-emitting microlasers." *Electronics Letters*, **25** (17) pp. 1123-4. 1989
16. H.-J. Yoo, J.R. Hayes, N. Andreadakis, E.G. Paek, J.P. Harbison, L.T. Florez, and Y.-S. Kwon, "Fabrication of vertical cavity front surfaces emitting laser diode (FSELD) using HBT process." *Extended Abstracts of the 22nd (1990 International) Conference on Solid State Devices and Materials*, pp. 769-72. 1990
17. H.-J. Yoo, J.R. Hayes, N. Andreadakis, E.G. Paek, J.P. Harbison, L.T. Florez, and Y.-S. Kwon, "Fabrication of vertical-cavity front-surface-emitting laser diode (FSELD) using a heterojunction bipolar transistor process." *Japanese Journal of Applied Physics, Part 2 (Letters)*, **30** (3B) pp. L492-4. 1991

18. R.S. Geels, S.W. Corzine, J.W. Scott, D.B. Young, and L.A. Coldren, "Low threshold planarized vertical-cavity surface-emitting lasers." *IEEE Photonics Technology Letters*, 2 (4) pp. 234-6. 1990
19. P.L. Gourley, S.K. Lyo, T.M. Brennan, B.E. Hammons, C.F. Schaus, and S. Sun, "Lasing threshold in quantum well surface-emitting lasers: many-body effects and temperature dependence." *Applied Physics Letters*, 55 (26) pp. 2698-700. 1989
20. B. Tell, K.F. Brown-Goebeler, R.E. Leibenguth, F.M. Baez, and Y.H. Lee, "Temperature dependence of GaAs-AlGaAs vertical cavity surface emitting lasers." *Applied Physics Letters*, 60 (6) pp. 683-5. 1992
21. C.C. Barron, M. Whitehead, K.-K. Law, J.W. Scott, M.E. Heimbuch, and L.A. Coldren, "K-band operation of asymmetric Fabry-Perot modulators." *IEEE Photonics Technology Letters*, 4 (5) pp. 459-61. 1992
22. Z.M. Chuang, J.W. Scott, D.B. Young, and L.A. Coldren, "Strained InGaAs/GaAs quantum well constricted-mesa lasers and application in a vertical-twin-guide tunable laser." *IEEE Photonics Technology Letters*, 4 (4) pp. 315-18. 1992
23. B.J. Thibeault, J.W. Scott, M.G. Peters, F.H. Peters, D.B. Young, and L.A. Coldren, "Integrable InGaAs/GaAs vertical-cavity surface-emitting lasers" *Electronics Letters*, 29 (25) pp. 2197-9. 1993
24. M.G. Peters, B.J. Thibeault, D.B. Young, J.W. Scott, F.H. Peters, A.C. Gossard, and L.A. Coldren, "Band-gap engineered digital alloy interfaces for lower resistance vertical-cavity surface-emitting lasers." *Applied Physics Letters*, 63 (25) pp. 3411-13. 1993
25. K.L. Lear, S.A. Chalmers, and K.P. Killeen, "Low threshold voltage vertical cavity surface-emitting laser." *Electronics Letters*, 29 (7) pp. 584-6. 1993
26. A. Scherer, J.L. Jewell, M. Walther, J.P. Harbison, and L.T. Florez, "Fabrication of low threshold voltage microlasers." *Electronics Letters*, 28 (13) pp. 1224-6. 1992
27. K.D. Choquette, G. Hasnain, J.P. Mannaerts, J.D. Wynn, R.C. Wetzel, M. Hong, R.S. Freund, and R.E. Leibenguth, "Vertical-cavity surface-emitting lasers fabricated by vacuum integrated processing." *IEEE Photonics Technology Letters*, 4 (9) pp. 951-4. 1992

28. R. Michalzik and K.J. Ebeling, "Modeling and design of proton-implanted ultralow-threshold vertical-cavity laser diodes." *IEEE Journal of Quantum Electronics*, **29** (6) pp. 1963-74. 1993
29. K. Kojima, R.A. Morgan, T. Mullaly, G.D. Guth, M.W. Focht, R.E. Leibenguth, and M.T. Asom, "Reduction of p-doped mirror electrical resistance of GaAs/AlGaAs vertical-cavity surface-emitting lasers by delta doping" *Electronics Letters*, **29** (20) pp. 1771-2. 1993
30. K. Moriki, H. Nakahara, T. Hattori, and K. Iga, "[Single transverse mode condition of surface-emitting injection lasers]." *Electronics and Communications in Japan, Part 2 (Electronics)*, **71** (1) pp. 81-90. 1988
31. A.G. Vawter, D.R. Myers, T.M. Brennan, and B.E. Hammons, "Low threshold current implanted-planar buried-heterostructure graded-index separate confinement heterostructure laser in GaAs/AlGaAs." *Applied Physics Letters*, **56** (20) pp. 1945-7. 1990

## Chapter 2: Current-to-Light Simulation

### 2.0 Introduction

One of the major advantages of a vertical-cavity laser is the ability to make arrays of very small lasers. Their small size, however, makes thermal and edge effects important. This chapter presents the current-to-light ( $L-I$ ) simulations that I have developed which include thermal effects, gain offset design and various lateral effects. The model is then used to examine various designs, showing the directions for improved vertical-cavity laser performance. The thermal effects considered include temperature and carrier density driven shifts of the peak gain and gain spectrum relative to a more slowly shifting cavity mode. The lateral effects include radially varying current injection, spatial hole burning, surface recombination and ambipolar carrier diffusion within the quantum wells. The gain offset, realized by growing the structure to place the cavity mode on the long wavelength side of the gain peak, is an important device parameter which can result in temperature stabilized operation. The effect of varying gain offset is analyzed in detail.

Three important assumptions have been made which keep the program simple and efficient. First, cylindrical symmetry is assumed to reduce the problem to a one dimensional radial calculation. Second, the structure is assumed to be strongly index guided so that the optical modes are determined by the waveguide dimensions. Third, the temperature rise of the junction is calculated using an analytic function. In this way the transverse optical mode, electrical injection and thermal profile calculations are decoupled from the current-to-light simulation.

To highlight the importance of these thermal and lateral effects, consider Fig. 2.1. The  $L-I$  characteristics of two bottom emission vertical-cavity lasers are shown, both fabricated from the same material. One is the continuous wave (CW) characteristics of a  $7\text{ }\mu\text{m}$  square single mode device while the other is the pulsed  $L-I$  curve for a  $60\text{ }\mu\text{m}$  diameter multimode device that has been scaled down to an equivalent size by multiplying the current and light scales by the

relative areas, that is,  $(7^2) / (\pi 30^2)$ . From the comparison of the two experimental characteristics, it is clear that the single mode structures are not simply scaled down versions of the broad area lasers. The output power,  $P_{out}$ , as a function of current is given by

$$P_{out} = \frac{h\nu}{q} \eta_{inj} \eta_{opt} (I - I_{th}) \quad (2.1)$$

where  $h\nu$  is the photon energy,  $q$  is the electron charge,  $\eta_{inj}$  is the injection efficiency,  $\eta_{opt}$  is the optical efficiency and  $I_{th}$  is the threshold current.

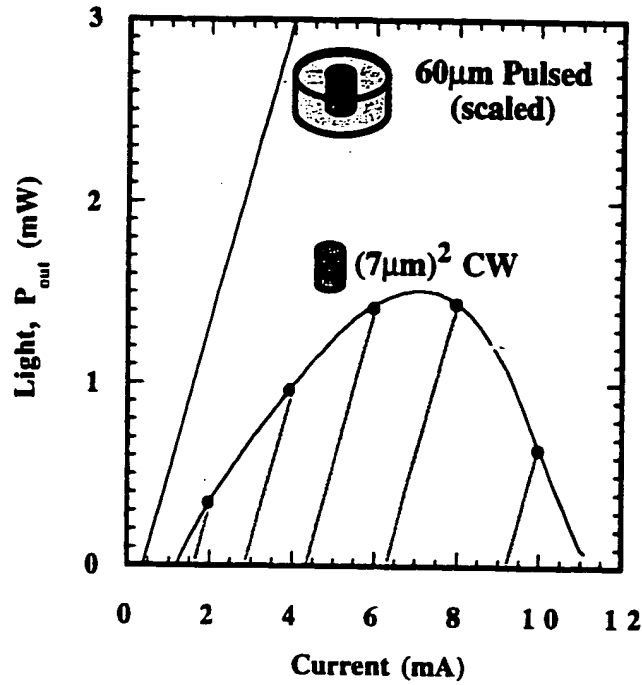


Fig. 2.1. Current-to-light characteristics for two bottom emission devices made from the same material. The pulsed  $L$ - $I$  curve of the broad area laser has been scaled by the relative areas. The intersection of the diagonal gray lines with the axis show that the effective threshold current is changing with bias current.

The injection efficiency  $\eta_{inj}$  is presumed to be constant and due to recombination in the undoped confinement regions where the carriers are not interacting with the optical field. First consider the broad area laser characteristics. Since the measurements are pulsed, the junction temperature is constant. Its highly multimode lasing operation allows the optical field to be treated as uniform laterally while the large diameter means that the edge effect of surface recombination is minimal. The broad area device, then, represents the one dimensional analysis of Appendix D. Clearly there is much more happening in the small area devices. The threshold current density of the small laser is double that of the broad area laser, primarily due to surface recombination. One way to understand the  $L$ - $I$  characteristics of the small devices is to define an "effective" threshold current which changes with bias as shown by the gray lines in Fig. 2.1. Here we have defined the threshold current as the current required to maintain the modal gain at the threshold level.

Using Eqn. (2.1) the output power can be calculated if the threshold current is known. As can be seen from the figure, this threshold current can vary dramatically in vertical-cavity lasers. To explore this idea further, we take the derivative of Eqn. (2.1) yielding a local, current dependent external differential quantum efficiency

$$\eta_{ext}(I) = \frac{q}{h\nu} \frac{dP_{out}}{dI} = \eta_{inj} \eta_{opt} \left( 1 - \frac{dI_{th}}{dI} \right) = \eta_i \eta_{opt}, \quad (2.2)$$

with the definition that

$$\eta_i = \eta_{inj} \left( 1 - \frac{dI_{th}}{dI} \right) \quad (2.3)$$

where  $\eta_i$  is the internal differential efficiency. If the changes in effective threshold current with bias is expanded, we can identify the effects driving the change in threshold current,

$$\frac{dI_{th}}{dI} = \frac{\partial I_{th}}{\partial T_{jct}} \frac{dT_{jct}}{dI} + \frac{\partial I_{th}}{\partial I}. \quad (2.4)$$

The first term on the right is related to a shift of the gain peak relative to the cavity mode driven by Joule heating. This causes a rise in the carrier density and an increase in threshold current. This term can become so large that the differential efficiency becomes negative and the output "rolls over" as shown in Fig. 2.1. The second term in Eqn. (2.4) is a spatial hole burning effect associated with single mode devices and can be clearly observed even under pulsed operation where the junction temperature  $T_{jct}$  is essentially constant. The spatial hole burning effect is due to a poor overlap of the optical mode with the active region and is similar to a leakage path shunting the active region. Essentially, the electric field at the perimeter is so weak that it cannot effectively stimulate the carriers into the optical mode and the carriers are lost to other recombination currents, reducing the internal efficiency. This chapter presents the tools needed to quantitatively investigate these effects and allow the determination of optimal designs.

The chapter is organized as follows. First, the equations to be used are formulated. Next, the thermal models are discussed including the shifts in optical cavity parameters with temperature. The numerical algorithm for their solution is presented and then the simulation is applied to some experimental devices to extract the internal device parameters used in the model. Finally, the numerical model is used to calculate the current-to-light characteristics for various designs and to determine the conditions necessary for single transverse mode operation. Throughout this chapter, the current injection into the active region is assumed to be uniform, although the model is formulated for use with any current injection profile so that it can be used to investigate the effects on non-uniform injection in the intra-cavity contacted designs in Chapter 3.



## 2.1 Formulation of Equations

The equations to be solved are the current continuity equation and the steady state photon and electron rate equations. Although the large diameter devices lase in many modes, as the laser diameter of our index-guided structure is reduced to  $\sim 10 \mu\text{m}$  the optical modes become restricted. For a cylindrical dielectric waveguide the fundamental mode is the  $\text{HE}_{11}$  mode [1]. The field is cosine like and is nearly zero near the edges of the vertical waveguide due to the large semiconductor-air index discontinuity. Since the stimulated emission rate is proportional to the product of the gain and the modal energy density, the current conversion into photons is not uniform across the device diameter. Thus, lateral carrier densities are not uniform, recombination and leakage currents vary radially and there are lateral diffusion currents. Near the perimeter, where the mode is weak, stimulated recombination is small and the carrier density rises. The current near the perimeter is lost to bulk and surface recombination instead of being converted into light, even if the junction is at room temperature.

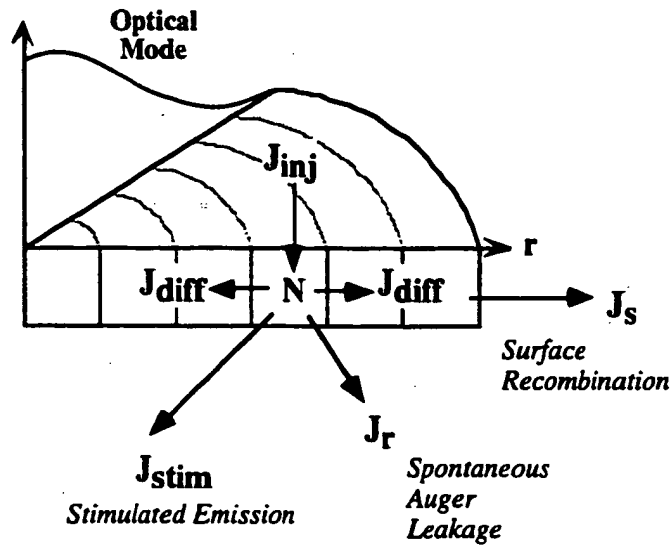


Fig. 2.2. Schematic of the current-to-light model showing the various currents.

A schematic of the finite difference model used and the various currents considered is shown in Fig. 2.2. To reduce the calculation to one dimension, cylindrical coordinates have been used and I have assumed azimuthal symmetry. Because of the high injection condition, all electron and hole currents are assumed to be equal. The fundamental relation to be solved in the active region is the steady state continuity equation. The injected current is considered as an independent variable, and the stimulated emission, diffusion, and recombination currents are assumed to be dependent on the local carrier density. The steady state continuity equation for lateral currents inside the active region is

$$\nabla \cdot \mathbf{J} = G_{en} - R_{ec}, \quad (2.5)$$

where  $G_{en}$  is the generation rate of carriers per unit volume and  $R_{ec}$  is the rate of total loss of carriers per unit volume due to both stimulated and non-stimulated recombination. Because of the high levels of injection, charge neutrality will be assumed, and so the lateral currents are presumed to result from ambipolar diffusion. In this case the continuity equation becomes

$$\nabla \cdot \mathbf{J}_{diff} = \left( \frac{\eta_{inj} J_{inj}}{l_{act}} \right) - \left( \frac{J_{stim} + J_{rec} + J_{leak}}{l_{act}} \right)$$

or

$$l_{act} (\nabla \cdot \mathbf{J}_{diff}) = \eta_{inj} J_{inj} - J_{stim} + J_{rec} + J_{leak} \quad (2.6)$$

where  $\mathbf{J}_{diff} = -qD_a \nabla n$ . For simplicity, the ambipolar diffusion constant,  $D_a$ , inside the quantum well is assumed to be independent of carrier density. This differential equation will be written as a difference equation in cylindrical coordinates in the next section.

In order to solve for the carrier density profile, all currents must be expressed as a function of the carrier density. The injected current density is treated as the input variable from which the various other parameters are

calculated. The recombination currents for each quantum well are shown in Fig. B.10 of Appendix B. They are

$$J_{rec}(n) = (\#_{wells}) (J_{spon}(n) + J_{barr}(n) + J_{Auger}(n)). \quad (2.7)$$

Assuming that the respective carrier densities in each band of the multiple wells are in thermal equilibrium, the total recombination current is scaled by the number of wells.

The spontaneous emission in the well,  $J_{spon}$  and in the barriers,  $J_{barr}$ , are calculated from the bandstructure and quasi-Fermi levels by the QWGain program [2]. The Auger recombination,  $J_{Auger}$ , is calculated using a  $C_A n^3$  dependence. To approximate the leakage current, shown in Fig. 2.3, the functional form of a homojunction diode is used [3] where the applied voltage is replaced with the quasi Fermi level separation,  $\Delta E_{fcv}$ , in the active region

$$J_{leak} = J_o \exp \left( - \frac{(E_{gB} - \Delta E_{fcv}(n, T_{jct}))}{kT_{jct}} \right). \quad (2.8)$$

In this way the leakage current is dependent on the local carrier density. This is important because the carrier density is not simply a function of the injected current density. Lateral carrier diffusion, surface recombination and variations in the stimulated transition rate can cause large radial variations in the carrier density. The constant prefactor  $J_o$  is fitted to the measured data and  $E_{gB}$  is the bandgap of the confinement layers. The relation between  $\Delta E_{fcv}$  and the carrier density is calculated using from the bandstructure model.

The last current needed to complete Eqn. (2.6) is the stimulated current  $J_{stim}(n)$ . The continuity equation including the stimulated current is interesting as all the local carrier densities are coupled together globally by the optical mode which extends over the entire active region. A higher stimulated emission in one

area increases the field strength which, in turn, increases the stimulated emission everywhere.

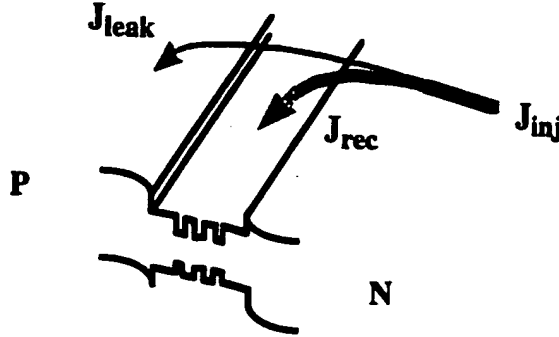


Fig. 2.3. Schematic showing the recombination currents in the wells and the leakage into the cladding regions.

Solving this system of equations requires an iterative approach as discussed in the next section. In all equations that follow the optical mode intensity profile  $E^2(r)$  is assumed to be normalized such that

$$\int E^2(r) dA = 1. \quad (2.9)$$

The intensity profile  $E^2(r)$  therefore has units of 1/area. The derivation of  $J_{stim}$  begins by noting that the steady state photon rate equation is satisfied when the round trip modal gain is equal to the threshold gain,

$$G_m = G_{th}, \quad (2.10)$$

where  $G_{th} = L+T$  and noting that the modal gain is defined as

$$G_m \equiv \int_{act} G(n) E^2(r) dA \quad (2.11)$$

#### 34 Section 2.1 Formulation of Equations

where  $G(n) = 2\xi_{enh}g_{ma}(n)l_{act}$  as defined in Eqns (D.4) and (D.19) of Appendix D. The output power is given by

$$P_{out} = \frac{h\nu}{q} \eta_{opt} I_{stim} \quad (2.12)$$

where the stimulated current is found by integrating the stimulated current density over the active region

$$I_{stim} = \int_{act} J_{stim} dA. \quad (2.13)$$

The local stimulated emission rate is proportional to the product of the gain and the squared electric field. To obtain the proportionality constant for  $J_{stim}(n)$ , the above equations can be combined. First multiply both sides of Eqn. (2.10) by  $I_{stim}$  and then substitute Eqns. (2.11) and (2.13) as follows:

$$G_{th} I_{stim} = I_{stim} G_m; \quad (2.14)$$

$$G_{th} \int_{act} J_{stim} dA = I_{stim} \int_{act} G(n) E^2(r) dA. \quad (2.15)$$

Finally, dividing both sides by  $G_{th}$  and requiring the equality to hold on a per unit area basis yields the stimulated transition rate with the correct normalization constants

$$J_{stim}(n) = I_{stim} E^2(r) \frac{G(n)}{G_{th}}. \quad (2.16)$$

Equation (2.16) expresses both the equation for stimulated emission at each point and, when integrated over the active region, the threshold condition that the

modal gain be equal to the threshold gain. Using this expression for  $J_{stim}$ , Eqns. (2.6) and (2.13) together satisfy both the continuity equation and the steady state carrier and photon rate equations. The final conditions necessary to uniquely determine a solution of Eqn. (2.6) are the boundary conditions for the carrier density at the center and edge of the active region shown in Fig. 2.2. No current can flow into the center since it is the symmetry point,

$$\left. \frac{dn}{dr} \right|_{r=0} = 0, \quad (2.17)$$

while at the perimeter, surface recombination current must be supplied by diffusion

$$-qD_a \left. \frac{dn}{dr} \right|_{edge} = qnS_r \quad (2.18)$$

where  $S_r$  is the surface recombination velocity. The above system of nonlinear equations describe the various recombination currents, stimulated emission and diffusion currents within the active region all as a function of the carrier density. They are written into finite difference form in the next section.

Extension of the above equations to multimode operation is made simply by adding additional terms:

$$J_{stim} \Rightarrow \sum_i J_{stim}^i; \quad (2.19)$$

$$P_{out} = \frac{h\nu}{q} \sum_i \eta_{opt}^i I_{stim}^i \quad (2.20)$$

where the round trip losses  $L^i$  and hence optical efficiency can be different for the higher order modes due to surface scattering losses, diffraction losses or other

losses which vary for different transverse modes. Each optical mode is considered independent without interaction except through the common pool of carriers. The simulated current densities in Eqn. (2.19) are defined as

$$J_{stim}^i(n) = I_{stim}^i E_i^2(r) \frac{G(n)}{G_{th}^i} \quad (2.21)$$

where the threshold gain of each mode is different due to the different losses. The total current converted into each mode is given by

$$I_{stim}^i = \left( \beta^i \int_{act} J_{spont}^i dA \right) + \int_{act} J_{stim}^i dA \quad (2.22)$$

where the term in parenthesis is the fraction of spontaneous emission radiated into the mode. The spontaneous emission term is important for calculating the transition from below to above threshold. For multimode equations where some are below threshold and some are above, accurate calculation of the various mode strengths requires the inclusion of the spontaneous emission term. The main penalty for including multiple optical modes is that the convergence is much slower. We have made such calculations but the results do not add significantly to the understanding gained from a single mode calculation. For the remainder of the chapter I will restrict my calculations to the single mode case above threshold. In this case the spontaneous emission term can be ignored. Overlap integrals showing the gain of higher order modes and the implications for stabilized single mode operation will be presented later in this chapter. Some multimode calculation are shown in Chapter 6.

## 2.2 Thermal Model

Before making numerical calculations we must consider the inclusion of temperature effects in the model. The effects to be included are the changes in optical parameters and the changes in the gain characteristics. To estimate the

average junction temperature rise,  $\Delta T_{jct}$ , of a surface emitting laser the formula for a constant temperature disk on the surface of a semi-infinite substrate of can be used [4, 5]

$$\Delta T_{jct} = \frac{(P_{elec} - P_{opt})}{4r\sigma_{th}} \quad (2.23)$$

where  $P_{elec}$  is the input power,  $P_{opt}$  is the light output,  $r$  is the laser radius and  $\sigma_{th}$  is the effective thermal impedance of the substrate. Using Eqn. (2.23) and the thermal conductivity of GaAs, 0.044 W/cm°C, gives a thermal impedance of 1.1°C/mW for a 10μm-diameter laser. Although crude, this analytic approximation is attractive for its simplicity and has proven to be sufficient to model the lasers optical properties. A better approximation is to assume a constant profile which is higher in the center than the edges, with the average value given by Eqn. (2.23). The profile used is based on numerical simulation and is discussed in section 2.4. To maintain reasonable accuracy, the effective thermal conductivity in Eqn. (2.23) for a given structure is measured experimentally as discussed in the next section. For the calculations within this chapter, it is assumed that the current density-voltage ( $J$ - $V$ ) characteristics are known so that the input power for any given area and current can be calculated. In practice, I have used the measured  $J$ - $V$  characteristics for the experimental devices, concentrating my modeling on the active region properties and intra-cavity design.

The temperature dependence of the gain curves, both peak gain, wavelength and spectrum, are discussed in detail in Appendix B including the model to be used. The essential points are that the peak gain decreases with increasing temperature and that the peak wavelength shifts to longer wavelengths with either increasing temperature or carrier density. The relative position of the cavity mode to the gain peak can therefore be used to stabilize the laser threshold with a gain offset design. It is important, then, to know how the cavity's optical



parameters shift with temperature. The major effect is a shift of the cavity mode to longer wavelengths with increasing temperature. The cavity mode shift is due to the change in index with temperature. In GaAs, this index shift is  $4 \times 10^{-4} / ^\circ\text{C}$ . For this work, the cavity mode shift with temperature is measured experimentally and is on the order of 0.6 to 0.8  $\text{\AA}/^\circ\text{C}$ .

In summary, the average temperature rise of the active region is calculated using Eqn. (2.23), the experimental  $J$ - $V$  characteristics and the measured effective thermal conductivity of the layer structure. This temperature rise is used to determine the changes in the resonant cavity wavelength. Using an analytical form for the radial variation, the temperature rise across the active region is included into the quantum well gain model discussed in Appendix B, resulting in lower peak gain and a shift in the peak wavelength due to bandgap shrinkage. The gain peak shifts towards longer wavelengths at a rate 4-5 times faster than the cavity mode, and hence the offset varies with temperature. By placing the room temperature cavity mode on the long wavelength side of the gain peak, temperature compensated operation is achieved at the price of a higher threshold current. The analysis of these gain offset designs require the inclusion of the above thermal effects. With all the inputs quantified, we are ready to turn to the numerical calculations.

### 2.3 Numerical Algorithm

In section 2.1 the differential equations to be solved were presented. In this section they are converted to difference equations and then the numerical algorithm used to solve them is presented. Various internal parameters such as surface recombination velocity, ambipolar diffusion coefficient, Auger coefficient and leakage current coefficient are deduced from a variety of experimental measurements. Once the internal active region parameters are known, the model will be used to explore the  $L$ - $I$  characteristics of various structures in section 2.5.

First a grid is needed for the calculation. Figure 2.4 shows a part of the grid shown in Fig. 2.2. The grid is defined by the radial points  $r_i$ . Cell

boundaries are taken to bisect between the grid points. The "generation" and "recombination" current densities in Eqns (2.5) and (2.6) such as  $J_{inj}$ ,  $J_{rec}$ ,  $J_{leak}$  and  $J_{stim}$ , are multiplied by the area of an annulus defined by the cell boundaries as shown in the figure.

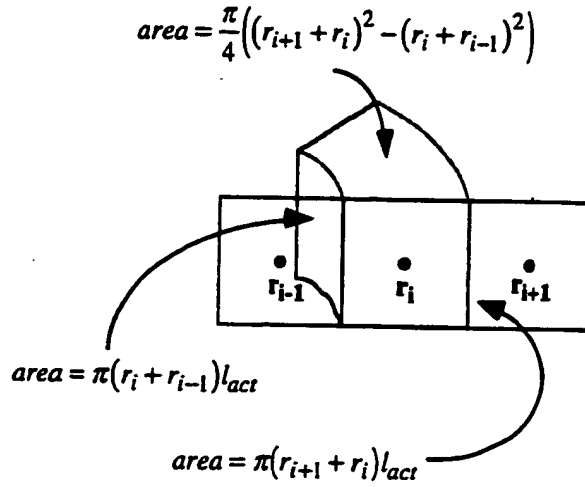


Fig. 2.4. The grid and areas used for the calculations are shown for a general grid point. The active region thickness is  $l_{act}$ .

The diffusion and surface recombination currents are calculated by multiplying the diffusion current density with the cross sectional boundary, shown for the inner and outer boundaries in the figure. The diffusion current density from the cell<sub>i+1</sub> into cell<sub>i</sub> is approximated using the carrier densities at the cell centers

$$J_{diff}^{i+1 \rightarrow i} = qD_a \frac{n_{i+1} - n_i}{r_{i+1} - r_i}. \quad (2.24)$$

The total current into cell<sub>i</sub> must balance

$$\begin{aligned}
& \left( \pi(r_{i+1} + r_i) l_{act} \right) \left( q D_a \frac{n_{i+1} - n_i}{r_{i+1} - r_i} \right) - \left( \pi(r_i + r_{i-1}) l_{act} \right) \left( q D_a \frac{n_i - n_{i-1}}{r_i - r_{i-1}} \right) \\
& + \left( \frac{\pi}{4} \left( (r_{i+1} + r_i)^2 - (r_i + r_{i-1})^2 \right) \right) (J_{inj} - J_{stim} - J_{rec} - J_{leak}) = 0
\end{aligned} \tag{2.25}$$

For the innermost cell, cell<sub>1</sub>, the diffusion current into the center is eliminated. For the outermost cell, cell<sub>n</sub>, the diffusion current into the cell from the boundary is replaced with a surface recombination current,

$$J_{diff}^{n+1 \rightarrow n} \Rightarrow -q S_r n_n, \tag{2.26}$$

so that there is a flow of current out of the cell. The description of the system of equations to be solved is complete. There remains, however, a question of how to solve this system of equations. It must be kept in mind that while the current densities depend on the local carrier density within the cell, they also depend on temperature and, in the case of the stimulated emission current, on the total stimulated emission across the active region. Thus each cell is connected by diffusion to each neighbor in Eqn. (2.25) and connected to all the other cells by the temperature rise in Eqn. (2.23) and the stimulated emission rate in Eqns. (2.13) and (2.16).

I have found a two pass, self consistent iterative approach is highly convergent and stable. The first pass calculates the stimulated emission from the cells holding the diffusion currents,  $J_{diff}$ , constant, decoupling the calculation for each cell from its neighbor. The second pass calculates the diffusion currents holding the stimulated emission current,  $J_{stim}$ , constant, removing the global optical coupling of all cells. Each pass calculates the carrier density in each cell so that current continuity, Eqn. (2.25), is satisfied except the respective current densities are held constant. The procedure is outlined in Fig. 2.5. In the first pass, an initial guess for the total stimulated current,  $I_{stim}$ , is used in Eqn. (2.16) allowing the carrier density in each cell to be determined, balancing the net

incoming diffusion currents and injected current with the outgoing stimulated emission and various recombination currents. The stimulated emission currents are added to give a new value for  $I_{stim}$  and the cycle is repeated until the value for  $I_{stim}$  has converged. The calculated values for  $J_{stim}$  in each cell are then used in the second pass.

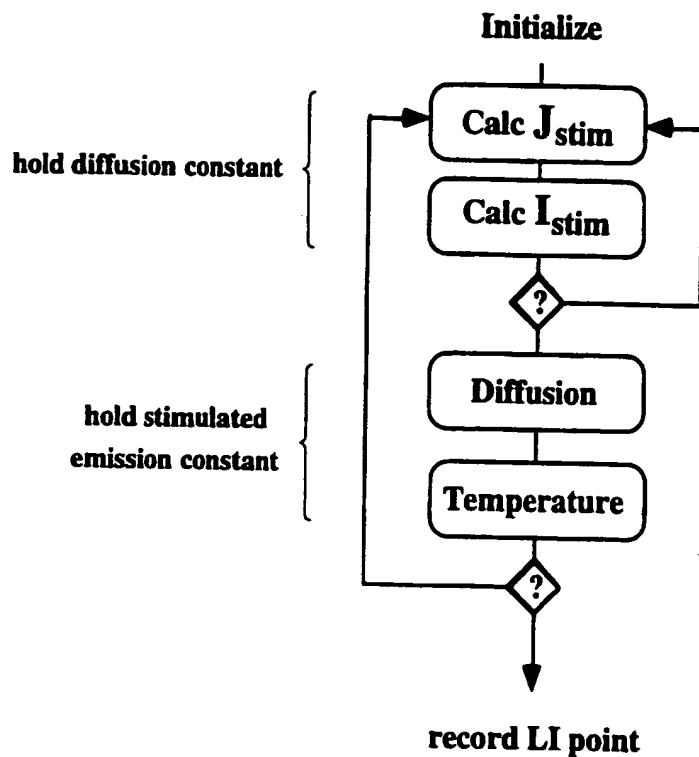


Fig. 2.5. The two pass self consistent iteration algorithm used to calculate the stimulated emission and carrier density profiles in the active region.

The second pass calculates the carrier density in each cell so that current continuity in each cell is satisfied, including the boundary conditions Eqns. (2.17) and (2.18). The diffusion current couples each cell together, so that there is only one solution. The procedure is to guess a carrier density in the first cell,

and then balancing the injected current less the stimulated current with the various recombination currents by diffusion from the neighboring cell, producing the neighboring cell's carrier density. This process is repeated, propagating the carrier density to the outer boundary where the current imbalance in the final cell is calculated, including surface recombination. Depending on the sign of the imbalance, the initial guess was too high or low. Using bisection on the carrier density in the first cell, the carrier density profile can be calculated with procedure which satisfies Eqn. (2.25) quite rapidly. The diffusion currents for the self consistent solution are then returned to the first pass and the entire cycle repeated. Before returning to the first pass, however, the output power is calculated using Eqn. (2.12) which is used in Eqn (2.23) to recalculate the junction temperature as shown in Fig. 2.5. The entire two pass iteration is repeated until the carrier density profile and output power have converged. The result is a point on an  $L-I$  curve. The injected current is increased, and the algorithm is repeated to determine the next  $L-I$  point. In this manner an  $L-I$  characteristic is calculated. To simulate pulsed operation, an identical procedure is used except the temperature is held constant.

#### 2.4 Internal Parameters

Before using the model, various internal device parameters must be chosen. These are based on experimental measurements whenever possible. To determine the injection efficiency, measurements on in-plane lasers using an identical three  $\text{In}_{0.2}\text{Ga}_{0.8}\text{As}$  quantum wells have been made. By measuring lasers of varying length and plotting the inverse external efficiency vs. length the intercept yields an injection efficiency  $\eta_{inj} = 0.8$  [6]. To determine the surface recombination velocity, the threshold current density for a wide range of bottom emission vertical-cavity laser diameters was plotted vs. the perimeter to area ratio. The slope yields a surface recombination velocity of  $2 \times 10^5$  cm/s [6].

The determination of the diffusion coefficient for carrier motion within the plane of the strained quantum wells is a difficult problem. Since all recombination currents in the active region require an electron and a hole, it is

assumed that the electron and hole fluxes are equal. This means that a built in field develops to balance the different diffusion coefficients of the two types of carriers. In addition, the high carrier densities makes it reasonable to assume that the electron and hole densities are the same, only very small differences are required to produce the built in field. With these assumptions, one can derive the ambipolar diffusion coefficient,  $D_a$ , in terms of the values for each carrier:

$$D_a = \frac{\mu_n D_p + \mu_p D_n}{\mu_n + \mu_p} \approx \frac{2D_p D_n}{D_p + D_n} \quad (2.27)$$

where the subscripts denote the carrier type p for holes, n for electrons and  $\mu$  is the mobility and  $D$  is the diffusion constant. The approximate form in Eqn. (2.27) is derived using the Einstein relation  $D/\mu = k_B T_{jct}/q$  which is not an accurate approximation at these high carrier densities but is qualitatively useful. If the two diffusion constants are nearly equal, the ambipolar constant is the average value. If the electron diffusion coefficient is much larger, as is usually the case, the ambipolar diffusion constant becomes twice that of the holes due to the built-in electric field. To determine the ambipolar diffusion constant, in-plane InGaAs/AlGaAs quantum well lasers of varying widths were fabricated and then the threshold current dependence on well width was fitted using an ambipolar diffusion model. Hu's calculations [7] extract an ambipolar diffusion coefficient of 22 cm<sup>2</sup>/s. In my work, I have found a value of 40 cm<sup>2</sup>/s shows the best agreement with our experimental data.

The thermal model requires the use of an effective thermal conductivity for the layer structure. While the value can be approximated using the geometric mean of the mirror layers, we have found it fairly simple to measure experimentally. First a laser is biased above threshold on a temperature controlled stage. The lasing wavelength is measured as the stage temperature is varied so that the wavelength shift with temperature,  $d\lambda_c/dT_{jct}$ , is known. The stage temperature is then held constant and the laser drive current is varied while the lasing wavelength is again monitored. Taking the difference of the input

electrical power with the output light power produces the dissipated power in the device. From the slope of the wavelength shift vs. the dissipated power and the measured  $d\lambda_c/dT_{jct}$  the junction temperature rise vs. dissipated power is known. The thermal impedance is thus calculated and the effective thermal conductivity can be found using Eqn. (2.23). We have found the same value of thermal conductivity in Eqn. (2.23) describes the thermal impedance for varying laser diameters  $\leq 15 \mu\text{m}$ . The experimental values range from  $0.045 \text{ mW}/^\circ\text{C}\mu\text{m}$  [6] for lasers with  $\text{Al}_{0.2}\text{Ga}_{0.8}\text{As}$  cladding in the cavity to a lower  $0.039 \text{ mW}/^\circ\text{C}\mu\text{m}$  [8] for lasers with  $\text{Al}_{0.5}\text{Ga}_{0.5}\text{As}$  cladding layers in the cavity. The value for GaAs is  $0.044 \text{ mW}/^\circ\text{C}\mu\text{m}$ . Considering the thermal impedance plotted in Fig. 2.27 the above values are reasonable for the above  $1\lambda$  thick cavity materials embedded in AlAs/GaAs mirrors. In the calculations that follow these experimental values are used to determine the average junction temperature rise used to determine the shifts in cavity mode with temperature.

To determine the model parameters, two types of measurements were made on two vertical-cavity laser structures. One measurement is the continuous wave (CW) current to light characteristic. The other measurement is the threshold current,  $I_{th}$ , vs. stage temperature,  $T_{sub}$ , under pulsed operation. The  $I_{th}$  vs.  $T_{sub}$  measurement provides the effective threshold current shown in Fig. 2.1. Using a uniform active region temperature, however, I was unable to determine internal parameters which produced simultaneous agreement with both measurements. The difference between the two measurements is that the active region temperature is uniform under pulsed conditions, but is radially varying under CW conditions due to the more effective heat sinking at the perimeter of the active region. The effective thermal conductivity is determined from measurements of the optical mode which provides the average junction temperature rise  $\Delta T_{jct}$ . To determine the local active region temperature, a thermal calculation for the temperature profile of a  $10 \mu\text{m}$  diameter vertical-cavity laser was made using a modified version of the current injection simulation described in Chapter 3. The thermal impedances of the various AlGaAs layers are calculated using the analytical formula of Eqn. (E.1) of

Appendix E. The model allows anisotropic resistivities, so that the mirror layers are modeled using the effective series resistivity for axial flow and the effective parallel resistivity for radial flow. The calculated radial mirror conductivity is  $0.068 \text{ mW/}^\circ\text{C}\mu\text{m}$  while the axial mirror conductivity is  $0.032 \text{ mW/}^\circ\text{C}\mu\text{m}$ . From the calculation an analytic form for the temperature profile across the active region is determined to be

$$T_{act}(r) = T_{sub} + \Delta T_{jct} \left( 1.2 - 0.3 \left( \frac{r}{r_{act}} \right)^3 \right) \quad (2.28)$$

where  $T_{act}$  is the temperature used in the gain model,  $T_{sub}$  is the substrate temperature,  $r_{act}$  is the active region radius and  $\Delta T_{jct}$  is given in Eqn. (2.23).

The model parameters for the two vertical-cavity laser structures analyzed here are given in Table 2.1. The round trip cavity parameters are calculated using the transmission matrix approach given in Appendix D. Structure A is described in detail in ref. [6] while structure B is described in ref. [8]. Structure A was designed, grown and fabricated by Geels. Based on my modeling, several changes appeared to be worthwhile. First, the carrier leakage appeared to be significant at the elevated temperatures and carrier densities present at peak power, so that the Al mole fraction of the layers cladding the active region was increased from 0.2 to 0.5. Second, the bottom mirror transmission was increased by using 17.5 periods instead of 18.5. Third, optical losses were reduced by using lower doping at the first four graded mirror interfaces on either side of the active region. Lastly, a higher gain offset was used in the design to improve the high temperature operation. The resulting structure B, designed and fabricated by myself [9] and grown and extensively characterized by Young, showed improved performance in nearly every parameter except drive voltage which was comparable.



Table 2.1. Device parameters used in the *L-I* simulations

parameter	symbol and units	Laser A [6]	Laser B [8]
Gain offset @ 300K	$\Delta\lambda$ (nm)	8	19
Radius	$r_{act}$ ( $\mu\text{m}$ )	5.7	5.0
Transmission	$T_r$ (%)	0.63	0.94
Internal loss	$L_i$ (%)	0.34	0.24
Scattering loss	$L_s$ (%)	0.13	0.06
Cavity shift	$d\lambda_c/dT_{jct}$ ( $\text{\AA}/^\circ\text{C}$ )	0.83	0.63
Eff. thermal cond.	$\sigma_{eff}$ ( $\text{mW}/^\circ\text{C}\mu\text{m}$ )	0.045	0.039
Injection eff.	$\eta_{inj}$	0.8	0.9
Diffusion const.	$D_a$ ( $\text{cm}^2/\text{s}$ )	40	40
Surface rec. velocity	$S_r$ ( $10^5\text{cm}/\text{s}$ )	2	2
Auger coeff.	$C_A$ ( $10^{-29}\text{cm}^6/\text{s}$ )	5.25	5.25
Leakage coeff.	$J_o$ ( $10^6\text{A}/\text{cm}^2$ )	2.5	2.5
Cladding Al fraction	$x$	0.2	0.5
Number of wells	$m$	3	3
Drive Voltage $V(J, T_{jct})$	$0.52J^{a_1/(T_{jct})} + a_2J$ $J$ ( $\text{A}/\text{cm}^2$ ), $T_{jct}$ (K)	$a_1 = 61$ $a_2 = 0.0023$	$a_1 = 81$ $a_2 = 0.0023$

One additional parameter introduced in the table is the surface loss  $L_s$ . While the transmission and loss parameters calculated from the one dimensional transmission matrix analysis agree with the measured threshold current density and external quantum efficiency measured for large diameter "broad area" vertical-cavity lasers, agreement for the calculated efficiency of smaller diameter "A" lasers required additional losses which increase with decreasing size[10]. We attribute these losses to scattering from the edges of the waveguide, corrugated by unintentional etching of the AlAs mirror layers during processing[10]. The round trip losses can be fit using:

$$L = L_i + L_s; \quad L_s = L_i(r_o / r_{mode}) \quad (2.29)$$

where  $L$  is the round trip cavity loss,  $L_i$  is the round trip loss due to internal losses and  $L_s$  is the round trip losses due to scattering. Since the perimeter to area ratio scales inversely with the modal radius,  $r_{mode}$ , this phenomenological model uses this form. The characteristic radius,  $r_o$ , is the radius at which surface scattering losses are equal to internal losses. For laser structure A this occurs at a radius of  $\approx 2.2 \mu\text{m}$ . Diffraction losses will also become important for these smaller radii and will increase much more rapidly with decreasing diameter, limiting the reduction in threshold current possible by simply scaling size. Having identified the importance of these losses, I attempted to minimize the scattering losses by encapsulating the waveguide pillar of structure B in silicon dioxide immediately after removal from the etching chamber. The resulting lasers showed much smaller surface scattering losses, with the smaller lasers yielding differential quantum efficiencies of 60%.

The final model parameters that need to be determined are the Auger coefficient  $C_A$  and the leakage current prefactor  $J_o$ . The values can be extracted by fitting the model's calculations with the measured characteristics for two different vertical-cavity lasers. The comparison of the calculations with the experimental data is shown in Figs 2.6 and 2.7. Figure 2.6 shows the  $I_{th}$  vs.  $T_{sub}$  characteristics under pulsed excitation. The dots show the experimental data while the dashed lines show the calculated values. With the higher carrier confinement barriers in laser B, carrier leakage has been suppressed so that the Auger coefficient can be determined. A value of  $C_A = 5.25 \times 10^{-30} \text{ cm}^6/\text{s}$ , 1.5 times higher than the value for GaAs, shows good agreement with the data.

The leakage current coefficient can then be determined for laser A. These two rapidly increasing recombination effects are responsible for the rollover in the  $L-I$  characteristics as shown in Fig. 2.7. In this figure the solid lines are the experimental data while the dots are the calculated  $L-I$  points. It should be kept in mind that the calculations assume single mode operation while the actual

devices had two to three transverse modes present at the peak output level. Nevertheless, the agreement is quite good, making the model a useful tool for exploring the device physics and alternate designs.

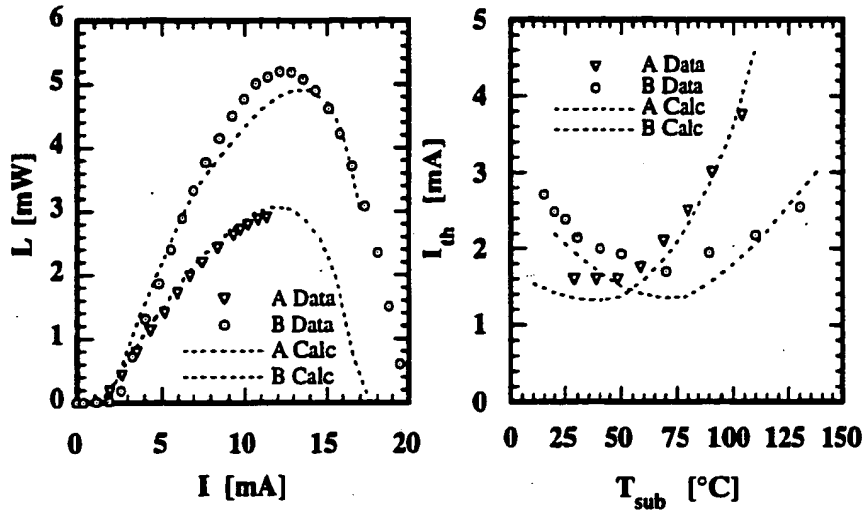
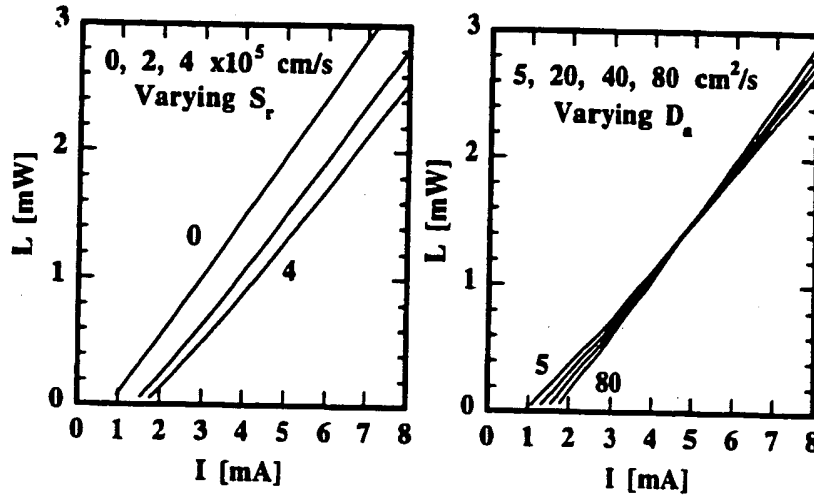


Fig. 2.6 and 2.7. Comparison of the calculated and experimental characteristics for the two laser structures using the model parameters given in Table 2.1. Laser A is an earlier  $10 \times 10 \mu\text{m}$  square device while Laser B is an improved  $10 \mu\text{m}$  diameter round device.

Before using the model, it is instructive to show the sensitivity of the calculation to the various device parameters used. The pulsed  $L-I$  characteristics calculated using the parameters for Laser A are shown in Fig. 2.8 and 2.9 where the ambipolar diffusion constant,  $D_a$ , and the surface recombination velocity,  $S_r$ , have been varied. Both parameters effect the threshold current because of the relative importance of the surface recombination. Increasing the surface recombination velocity primarily increases the threshold current. The increase begins to saturate as the recombination rate becomes diffusion limited. From the  $S_r = 0$  curve one can see that nearly half the threshold current is due to surface recombination. The diffusion constant acts as a method of carrier transfer, supplying carriers to the regions of highest recombination. At threshold, surface

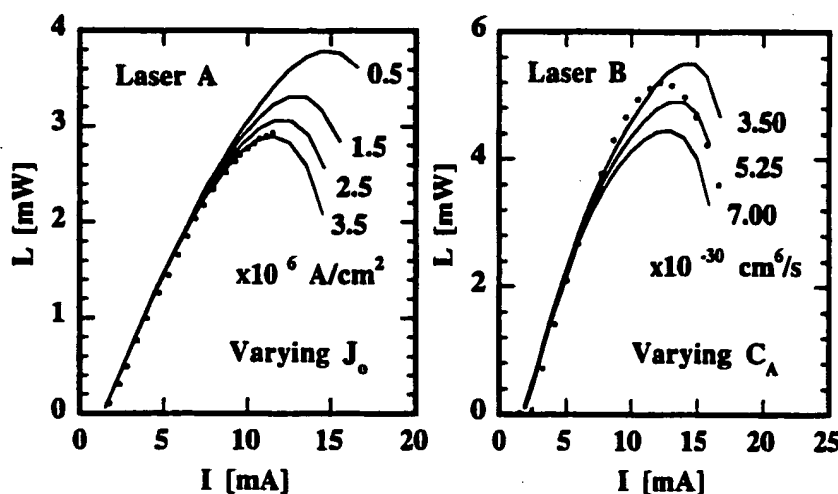
recombination is significant and hence a higher  $D_a$  results in a higher  $I_{th}$ . Above threshold, the spatial hole burning depletes carriers in the center and thus a higher  $D_a$  results in a higher external efficiency as carriers become transferred into the mode.



Figs. 2.8 and 2.9. Calculated  $L$ - $I$  characteristics for Laser A under pulsed operation. Fig. 2.8 shows varying values of surface recombination velocity with  $D_a = 40 \text{ cm}^2/\text{s}$ . Fig. 2.9 shows the effect of varying the ambipolar diffusion constant with  $S_r = 2 \times 10^5 \text{ cm/s}$ .

Another set of parameters to be explored are the Auger coefficient,  $C_A$ , and the leakage current coefficient,  $J_o$ . With its higher carrier confinement, the  $L$ - $I$  rollover of structure B is dominated by Auger recombination while the rollover in structure A is dominated by carrier leakage. This can be seen in Figs. 2.10 and 2.11, where the parameters are varied around the values used in Fig. 2.6. Clearly there is some uncertainty in the values to be used, but a much lower value for the leakage coefficient would produce too much output power for laser A. If instead a higher value for the Auger recombination were used, the output

power for laser *B* would be too low. In addition, the high temperature end of the  $I_{th}$  vs.  $T_{sub}$  characteristics, Fig. 2.7, are also sensitive to the values used.

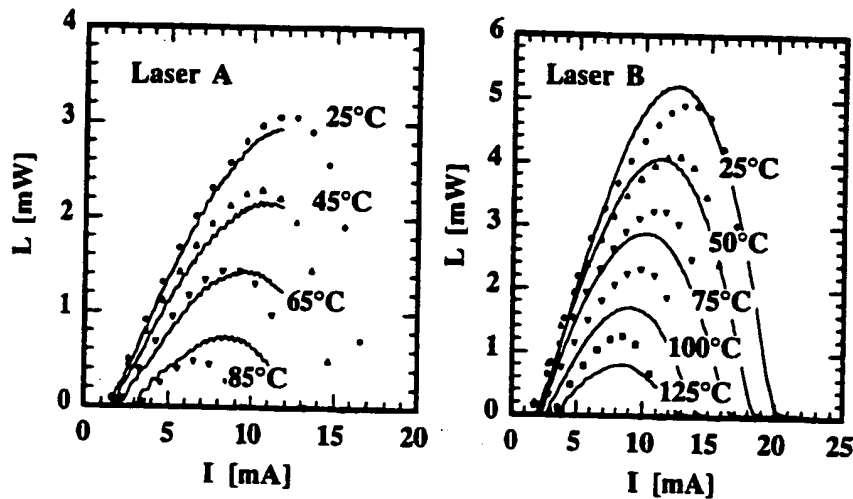


Figs. 2.10 and 2.11. Variation in calculated continuous wave (CW) operation of the two laser structures as different values are used for the Auger coefficient and leakage current. Dots show the experimental data.

The values given in Table 2.1 provide the best fit to the experimental data. No temperature dependence has been assumed in the values for  $S_r$ ,  $D_a$ ,  $C_A$  or  $J_0$ . Considering the large temperature variations, over  $100^\circ\text{C}$ , it is a naive assumption at best. Too many temperature dependent parameters, however, would make the model a giant curve fit, so I have chosen simplicity over accuracy. Future work by others may refine the model to include these effects. The temperature dependence of the Auger coefficient may be particularly important for long wavelength vertical-cavity lasers where the value is 3 to 10 times higher.

The best indication of a model's accuracy is the prediction of experimental data. Continuous wave  $L$ - $I$  characteristics have been taken for both laser

structures at varying stage temperatures. The comparison of the measured and calculated  $L-I$  curves is shown in Figs. 2.12 and 2.13. The predicted output power drops too quickly with increasing temperature for laser A and too slowly for laser B. Given that the leakage current model, Eqn. (2.8), is exponential with temperature while the Auger coefficient is temperature independent, this discrepancy is not surprising. Indeed, more involved numerical p-i-n junction models [11] show that the leakage current does not increase exponentially with applied voltage. Considering the saturated power variations shown above, the discrepancies between the measured and calculated output powers provide a sense of tolerance to the coefficients used in the model.



Figs. 2.12 and 2.13. Comparison of the measured and predicted  $L-I$  characteristics for the two vertical-cavity lasers for varying stage temperatures. Lines are experimental data, dots are predicted values. The room temperature curves are the same as Fig. 2.6

In summary, this section has applied the  $L-I$  model to experimental devices to determine the internal parameters to be used. Two different laser structures, one with  $\text{Al}_{0.2}\text{Ga}_{0.8}\text{As}$  cladding layers and a  $\approx 6$  nm gain offset and another with  $\text{Al}_{0.5}\text{Ga}_{0.5}\text{As}$  cladding layers and a  $\approx 19$  nm gain offset were analyzed, allowing a

separate determination of the Auger and leakage current coefficients. The model was then used to predict the  $L-I$  characteristics for various temperatures and compared with experiment to provide a sense of limitation to the model's predictive capability. The internal parameters determined here will now be used in the next section to examine various designs.

## 2.5 Predicted Current-to-Light Characteristics

This section looks at improvements in the laser performance for different designs. First, the temperature dependence of the threshold current is examined for varying gain offsets and threshold gain levels. Second, the improvements in output power and power conversion efficiency possible with reduced drive voltages are considered. Finally, reduced threshold currents are examined by using fewer quantum wells, higher reflectivity mirrors and alternate methods of carrier confinement.

### 2.5.1 Temperature sensitivity

The gain offset, defined as the difference between the cavity mode and the peak gain at a carrier density of  $4 \times 10^{18}/\text{cm}^3$  for an ambient temperature of 300K, can be controlled using *in-situ* monitored growth to within  $\sim 5$  nm of design. The threshold gain can be controlled by varying the mirror transmission and internal optical losses of the cavity design as discussed in Appendix D. The choice of these parameters has a strong effect on the temperature performance of the laser. To clarify the design choices,  $I_{th}$  vs.  $T_{sub}$  are presented here for varying parameters, using the  $10\text{ }\mu\text{m}$  diameter laser structure *B* as the basic model parameter set to be used.

Figure 2.14 show the threshold current variation with stage temperature for varying gain offsets. The minimum shifts to higher temperatures and higher values as the threshold is increased. The minimum value for the set of curves shows a monotonic increase with temperature, following the usual temperature dependence seen for conventional in-plane lasers with many longitudinal modes. Depending on the desired temperature range of operation, a different gain offset should be used.

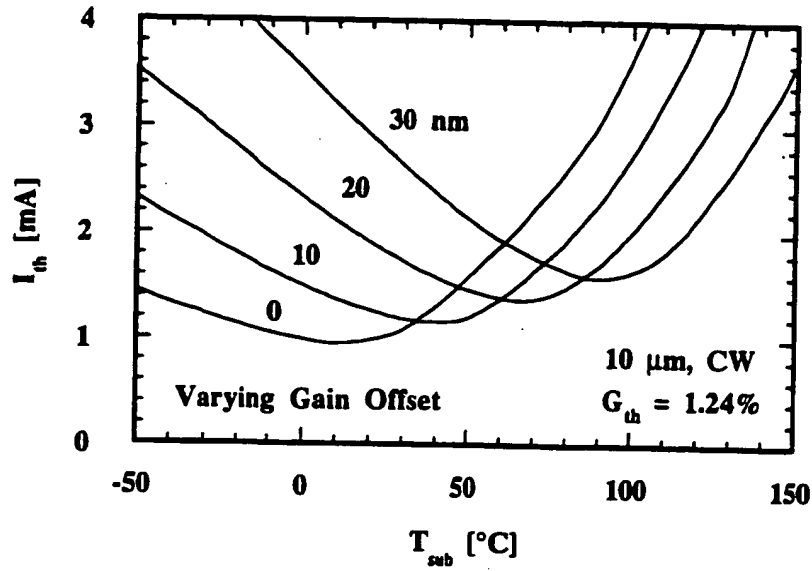


Fig. 2.14. Threshold current vs. stage temperature for varying gain offsets.

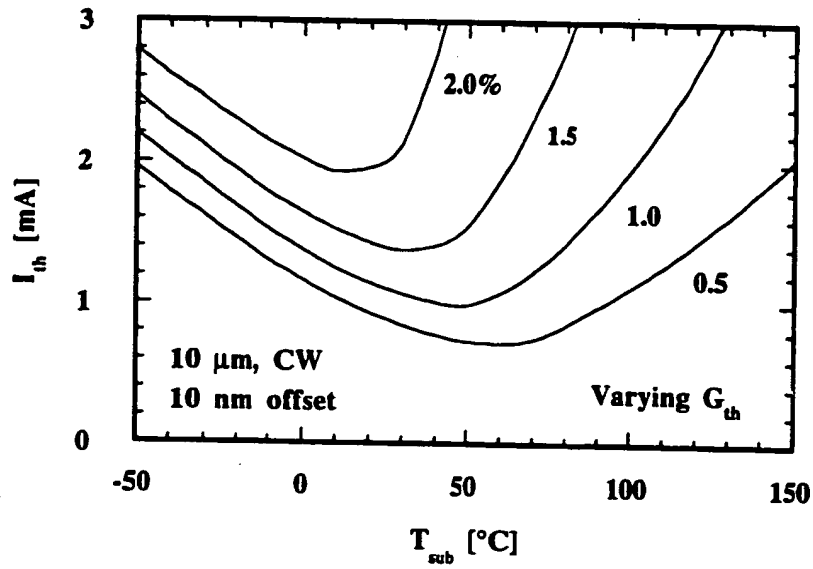


Fig. 2.15. Threshold current vs. stage temperature for varying threshold gain.



Laser *B* used an offset of 19 nm and a round trip threshold gain of 1.28%. If a wider range of temperature stabilized operation is desired, the threshold gain of the structure should be reduced. The  $I_{th}$  vs.  $T_{sub}$  curves are shown in Fig. 2.15 for a range of round trip threshold gains. Very low threshold currents and wide temperature range of stabilized operation is achieved for the low threshold gain designs. The tradeoff is that the lower threshold gain must be achieved by reducing the mirror transmission resulting in a lower optical efficiency. Designing the optical cavity requires a knowledge of the desired performance, both in terms of efficiency and temperature since tradeoffs are involved.

### 2.5.2 Power conversion efficiency

The power conversion efficiency is defined as the ratio of output light power to input electrical power and is an important device characteristic. While the laser is operating in the linear regime it can be expressed as:

$$\frac{P_{out}}{IV} = \eta_{opt} \eta_i \left( \frac{h\nu/q}{V} \right) \left( 1 - \frac{I_{th}}{I} \right) \quad (2.30)$$

Most improvements in the power efficiency of vertical-cavity lasers has been the result of reducing the drive voltage [12, 13]. Given that the photon energy is near 1.3 eV and the drive voltage has been in the range of 4 to 8 Volts, this has been a logical place to start. Reducing the drive voltage is important not only for improved efficiency, but also for reduced device heating. Reduced heating allows higher maximum output powers and increases the device density possible in array applications.

This improvement in performance with reduced drive voltage is shown in Fig. 2.16. Three  $I$ - $V$  characteristics representative of the advancement in mirror technology are shown on the left for a 10  $\mu\text{m}$  diameter device. The drive voltage drops from 8V to 4V while the differential resistance drops from 160 $\Omega$  to 92 $\Omega$ . The highest curve is representative of laser B [8] while the lowest curve is similar to the results reported by Peters [12]. Using the model parameters for structure

$B$ , the associated output power,  $P_{opt}$ , as function of input power,  $P_{elec}$ , are shown on the right. As can be seen, the rollover occurs at roughly the same input power, indicating that it is the junction temperature rise that drives the saturation of output power.

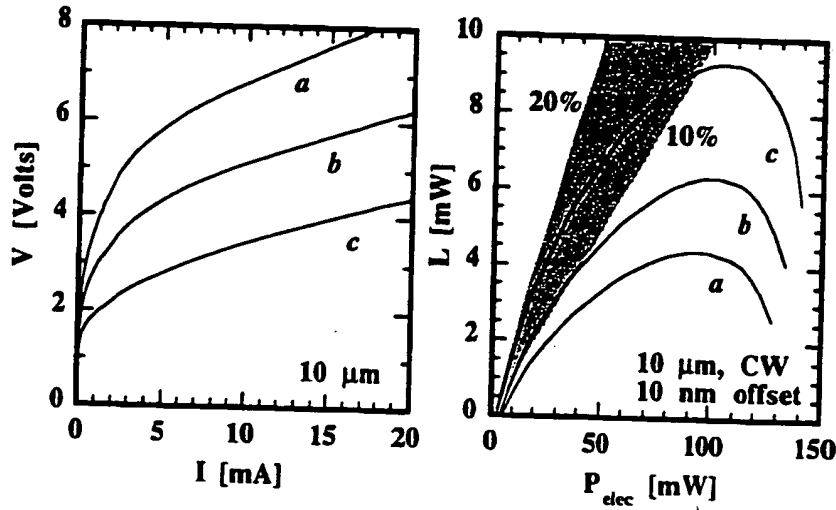


Fig. 2.16 Three  $I$ - $V$  characteristics and the resulting output power vs. input power characteristics. Curve  $a$  is for device structure B while curve  $b$  represents the current state of mirror technology. The shaded region show power conversion efficiencies from 10 to 20%.

A practical upper limit possible with improved voltage can be made using  $\eta_{opt} = 0.75$ ,  $V = 1.4V$ ,  $h\nu/q = 1.3V$ ,  $I_{th}/I = 0.1$ , and  $\eta_i = 0.7$  including spatial hole burning. Substituted into Eqn. (2.30), the power conversion efficiency is expressed as

$$\frac{P_{out}}{IV} \approx 0.75 \cdot 0.7 \cdot \left( \frac{1.3}{1.4} \right) (1 - 0.1) = 0.44. \quad (2.31)$$

As the voltage is improved, other factors in Eqn. (2.30) become more important. The optical efficiency of these devices here, 75%, is quite high. Most structures fabricated for low voltage have higher optical losses due to the doping and deeper optical penetration into the graded interface mirrors. It is also difficult to increase the efficiency above 70-80% because of the required transmission increases rapidly, resulting in a high threshold current. The internal efficiency, however, can be improved by improving the modal overlap with the carriers, reducing the spatial hole burning effect. The internal efficiency could then be increased to 0.9, increasing the power conversion efficiency to 46%. These current apertured designs are discussed in Chapter 6.

### 2.5.3 Reduced threshold current

One of the most attractive features of vertical-cavity lasers is their low threshold current. For array applications, it can become important to keep the power dissipated to a minimum as the number of elements can be quite large. In this case, output powers below 1 mW are required, making the threshold current an important issue. The question arises that, given the state of current technology, what threshold currents are possible to achieve? Of course, one can say that by simply scaling down to smaller sizes the threshold current is reduced. Several points limit the usefulness of this approach. First, diffraction losses in the unguided bottom mirror become significant, increasing rapidly as the diameter approaches  $4\text{ }\mu\text{m}$  [14]. Second, the thermal impedance current density and resistance increase rapidly as the area is reduced, again limiting the device. Finally, the output beam diffraction becomes larger, reducing some of the optical advantages of the device. In the analysis that follows, then, I will restrict the simulations to a  $6\text{ }\mu\text{m}$  diameter device using the model parameters for structure *B* except for lower drive voltage and mirror transmission.

From the variation in threshold current with gain shown in Fig. 2.15, it appears that the threshold can be lowered significantly by using a lower threshold gain cavity. For these calculations, I have reduced the transmission from 0.94% to 0.3% maintaining an optical efficiency of 50% while reducing the threshold

gain from 1.24% to 0.6%. Such a 99.7% reflectivity mirror is well within practical design limits. The  $J$ - $V$  characteristic used are the same as for curve c in Fig. 2.16, also quite realistic values. With the threshold gain reduced, the possibility of a design using fewer quantum wells should be considered. The  $I_{th}$  vs.  $T_{sub}$  characteristics for 1, 2 and 3 quantum well active region are shown in Fig. 2.17. A minimum threshold current of 0.27 mA is predicted for the laser using a 10 nm gain offset and one quantum well. The corresponding  $L$ - $I$  characteristics for the three designs are shown in Fig. 2.18. Clearly all three designs are capable of more than 1 mW of output power.

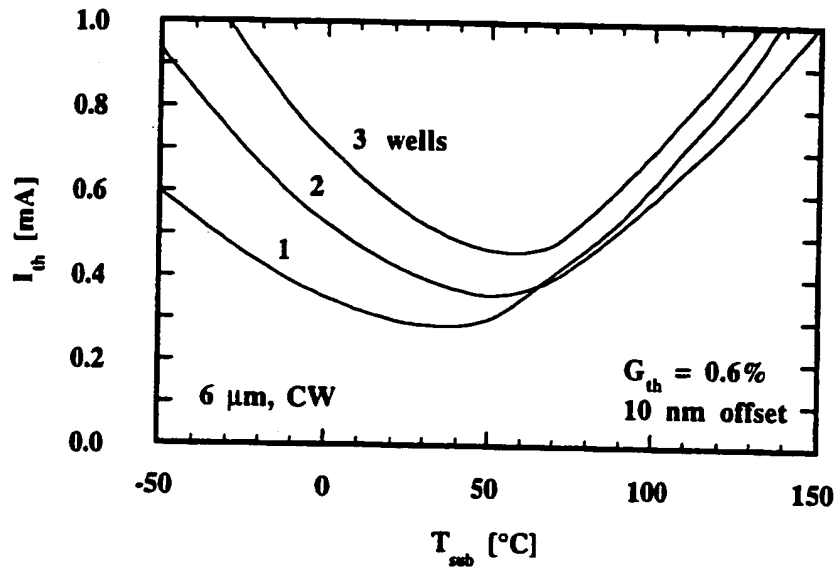


Fig. 2.17. Calculated threshold current for a 6  $\mu$ m diameter device using 1, 2 or three quantum wells, surface recombination included.

The inset shows the characteristics near threshold. The efficiency of the one quantum well design is slightly lower because the lower maximum gain of the well cannot convert as many carriers at the periphery of the device where the mode is weak. Additionally, the thermal limit on the output power occurs

sooner. If low threshold and sub-milliwatt powers are the goal, one quantum well is sufficient and desirable.

Reducing the threshold further requires removing the surface recombination. This can be done by stopping the etching just above the active region, letting the carriers diffuse away from the region of current injection instead of recombining at an etched surface. A better design is to restrict the current injection to a diameter less than the waveguide, allowing the outwardly diffusing carriers to contribute to the mode. An even more challenging solution is to use some kind of disordering or regrowth process to confine the active region without introducing surface recombination. Yet calculating the  $L$ - $I$  characteristics is simpler, allowing us to see the potential advantage of these approaches. These four cases are shown in Fig. 2.19. The etched boundary is the one quantum well curve of Figs. 2.17 and 2.18. The carrier diffusion curve replaces the surface recombination with an extended active region, letting the carriers diffuse outward beyond the edge of the optical waveguide.

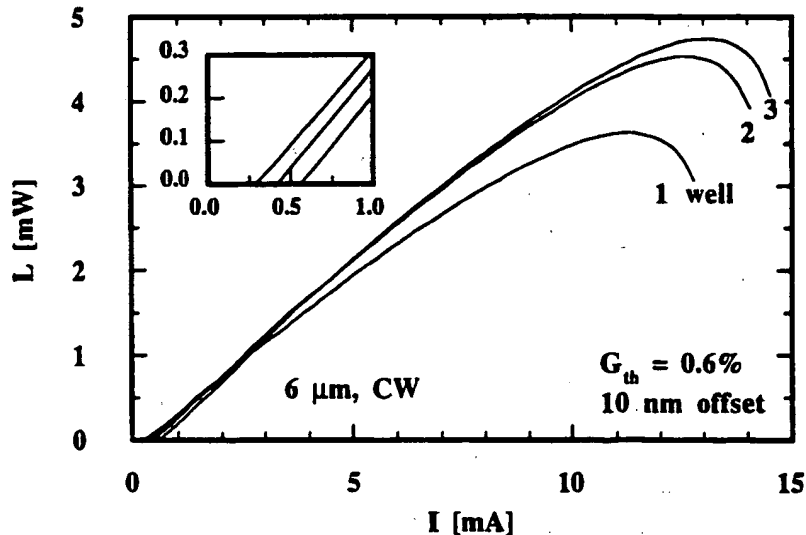


Fig. 2.18. Calculated current to light characteristics for the same three devices shown in Fig. 2.17. Inset shows the detail near threshold.

The current apertured curve injects the current in a three micron diameter aperture in the center of the waveguide. The last curve sets the surface recombination velocity to zero at the waveguide boundary. From the figure it is apparent that it is preferable not to etch through the active region, although the difference is not dramatic. This simple design should be capable of threshold currents near  $200\mu\text{A}$ . These values are not unrealistic, although they do require state of the art materials and processing. For example, Huffaker [15] recently reported a  $0.25\text{ mA}$  threshold for an  $8\mu\text{m}$  diffusion boundary device. Restricting the region of current injection is more effective, reducing the threshold current to  $140\mu\text{A}$ . An additional benefit is the increased efficiency resulting from a better modal overlap. These current apertured designs are discussed further in the next section on spatial hole burning. Finally, using a disordered or regrown active region is even more effective, reducing the threshold current to  $60\mu\text{A}$ !

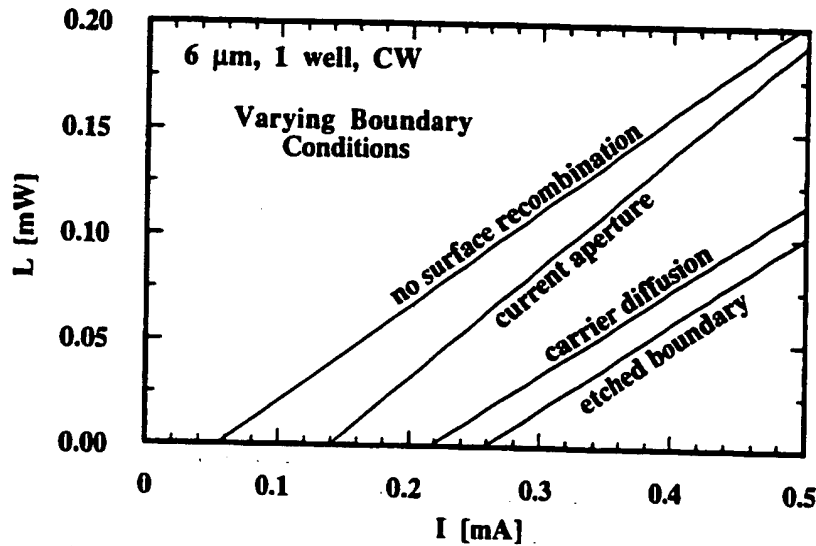


Fig. 2.19. Calculated  $L$ - $I$  characteristics for a  $6\mu\text{m}$  diameter vertical-cavity laser with a single quantum well active region for various boundary conditions. Etched boundary case is the same curve as in Fig. 2.18.

Depending on the application, such low threshold designs may or may not be desirable. If the application calls for only a  $100\mu\text{W}$  of power with minimal power dissipation, these low threshold designs are ideal. If instead output powers of several milliwatts are desired, hundreds of  $\mu\text{A}$  are meaningless and the design is better focused on high-efficiency multi-quantum-well cavities. I hope that the design tradeoffs have been clarified by the above examples. The last section of the chapter discusses spatial hole burning, multimode operation and current apertured designs.

## 2.6 Spatial Hole Burning

An index-guided pillar structure has many advantages, the foremost being simple fabrication. Additional advantage is the ability to make very low threshold lasers since the device can be scaled down in size. There are, however, two disadvantages related to the strong index guide resulting from the semiconductor-air index discontinuity at the edge of the vertical waveguide. First, the strong index discontinuity makes the waveguide a highly multimode structure, supporting many transverse modes. Second, the strong index step forces the optical intensity to be nearly zero at the boundary. The result is a poor overlap of the optical mode with the injected carriers which adversely affects the internal efficiency. Effectively, the outer annulus of carriers are not coupled to the mode as the optical intensity - gain product is insufficient to stimulate the carriers at the supplied rate. These carriers are lost to other recombination mechanisms, reducing the internal efficiency.

The radial carrier density profile is calculated to satisfy the steady state carrier and photon rate equations at each point on the  $L$ - $I$  curve. These carrier density profiles are shown in Fig. 2.20 for a  $10\mu\text{m}$  diameter laser. At threshold the carrier density is peaked in the center, decaying towards the perimeter due to surface recombination. As the current is increased, the rising non uniform stimulated transition rate results in a depletion of carriers in the center and a buildup at the edge. Finally, as the junction heats up the carriers density rises to maintain the required threshold gain. This rising carrier density dramatically

increases the effective threshold current due to Auger recombination, and the output power reduces to zero eliminating the reduced carrier density in the center.

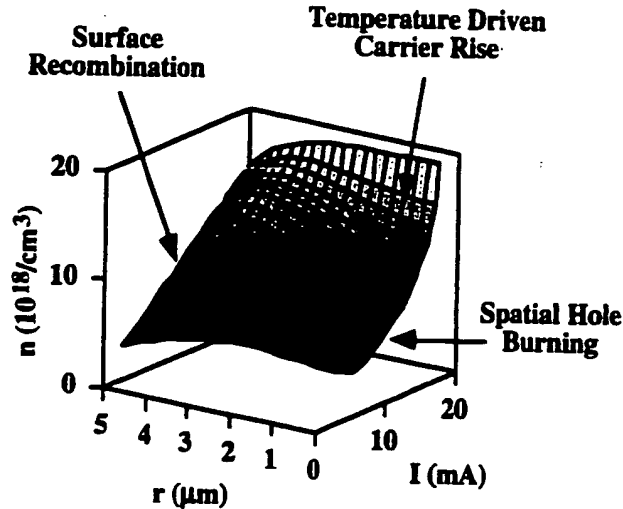


Fig. 2.20. Plot of the radial carrier density profile during the course of the  $L$ - $I$  curve. Carrier density and parameters are for the  $10 \mu\text{m}$  diameter laser structure  $B$  using the parameters in Table 2.1.

To satisfy the photon rate equation, the modal gain as defined in Eqn. (2.11) must be equal to the mode's losses as determined by the optical cavity properties. Thus integrating the gain profile, weighted by the normalized mode intensity, across the active region should be a constant for all the carrier density profiles shown. This is because the mode is above threshold. The higher order modes have a different radial intensity profile as shown in Fig. 2.21 and their modal gain will rise as the carrier profile peak shifts towards the perimeter. While the diffraction and surface scattering losses of these modes is higher than for the fundamental, the modal loss difference must be sufficient to prevent the lasing of these higher order modes. The calculated round trip modal gain for the three modes during the course of the  $L$ - $I$  curve is plotted in Fig. 2.22, calculated from the carrier density profiles shown in Fig. 2.20.



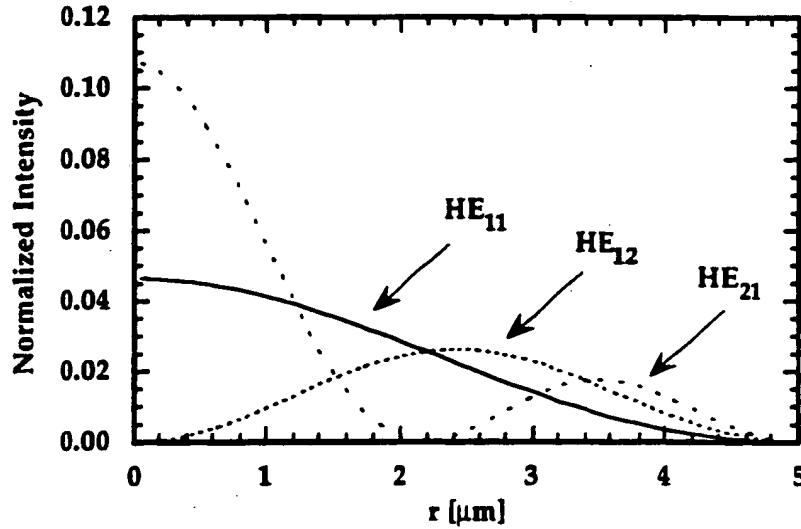


Fig. 2.21. The radial intensity distribution for the fundamental ( $HE_{11}$ ) and two higher order modes for a  $5\mu\text{m}$  diameter cylindrical dielectric waveguide. The intensity is normalized as in Eqn. (2.9).

As required, the modal gain for the lasing fundamental mode is a constant 1.24%. The gain of the higher order modes increases to a maximum of 1.58%. Thus the modal losses of the higher order modes would have to be more than double the 0.3% round trip loss of the fundamental to maintain single mode operation. Returning to the surface scattering loss described in Eqn. (2.29), the scattering losses of the higher order modes can be expected to be greater as the field strength at the boundary is higher. The smaller the diameter, the higher the scattering losses and the better the mode discrimination. Thus smaller diameter devices should have more stable single mode operation and this has been our experimental observation, with diameters  $\leq 8\mu\text{m}$  providing single mode operation.

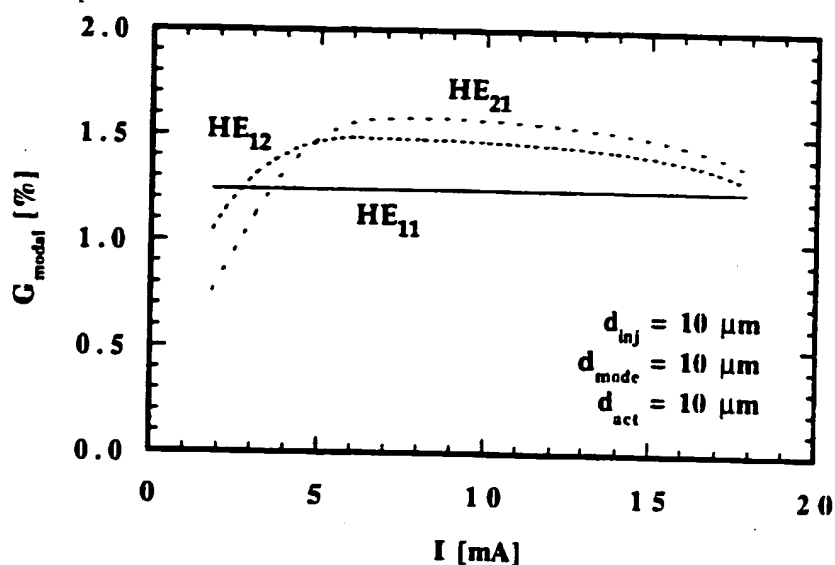


Fig. 2.22. Modal gain for the first three modes during the course of the  $L$ - $I$  curve. A modal loss discrimination of 0.34% is required to maintain single mode operation.

This technique of introducing mode selective loss can be used to promote fundamental mode operation can be used at the cost of additional losses. Introducing higher doping at the perimeter to increase free carrier losses, using low reflectivity ring contacts on the top reflector [16] or introducing an antiguide for increased diffraction [17] will provide such mode selective losses and have been used to make larger diameter single mode vertical-cavity lasers. The penalty is higher losses for the fundamental mode as well. A preferable approach is to avoid the spatial hole burning by adjusting the current injection to better match the fundamental mode profile.

In principle, such a current apertured design is straightforward. The current should be injected into a diameter less than the optical mode diameter, letting carrier diffusion spread the injected current so that the carrier profile matches the mode profile.

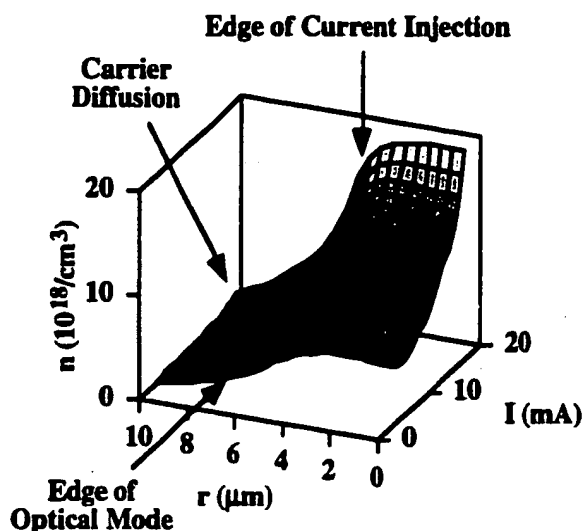


Fig. 2.23. Plot of the radial carrier density profile for a current apertured design. Current is injected up to a radius of  $5\ \mu\text{m}$  while the waveguide radius is  $7.5\ \mu\text{m}$  and the active region radius is  $10\ \mu\text{m}$ . The improved overlap with the mode nearly eliminates spatial hole burning.

To illustrate the benefits of this approach, calculations are made for an identical laser design as above except that the mode diameter is increased from 10 to  $15\ \mu\text{m}$  and the active region boundary is increased from 10 to  $20\ \mu\text{m}$ , keeping the current uniformly injected over a  $10\ \mu\text{m}$  diameter as before. The resulting carrier density profile plot is shown in Fig. 2.23. With the mode intensity strong across the region of current injection, the spatial hole burning is nearly eliminated. This has the benefit of improving the internal efficiency. The calculated  $L$ - $I$  characteristics for the two cases is shown in Fig. 2.24. While both structures have the same thermal impedance and rollover at roughly the same dissipated power, the current apertured design has a higher internal efficiency and thus produces more output power.

Not only has the efficiency been improved, but the modal gain discrimination has been dramatically improved. The modal gain curves for the current apertured design are shown in Fig. 2.25. The fundamental mode has a

higher gain throughout the  $L$ - $I$  curve. The mode discrimination is significant throughout the linear portion of the curve, ensuring single mode operation without compromising efficiency. As the output power saturates, the gain of the higher order modes rise because of the gain medium is cooler at the edge as described in Eqn. (2.28). This calculation used drive voltages approaching 8 V at peak power.

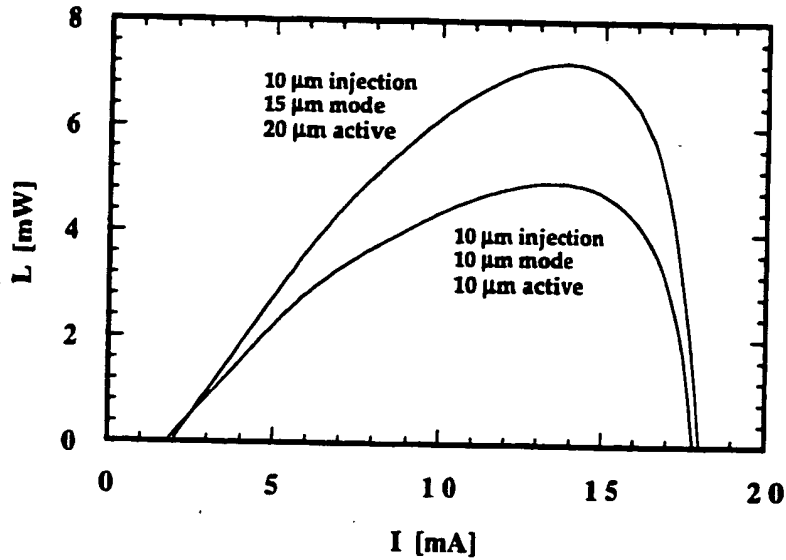


Fig. 2.24. Comparison of the etched pillar and current apertured  $L$ - $I$  characteristics, showing the improved efficiency resulting from improving the modal overlap with the injected current.

Lower voltage designs will the extend the range of high modal discrimination. While simple in concept, realizing such a design is more difficult. The intra cavity designs presented in this dissertation represent a first step towards these improved structures. Potential current apertured structures using intra-cavity contacts will be discussed in greater detail in Chapter 6.

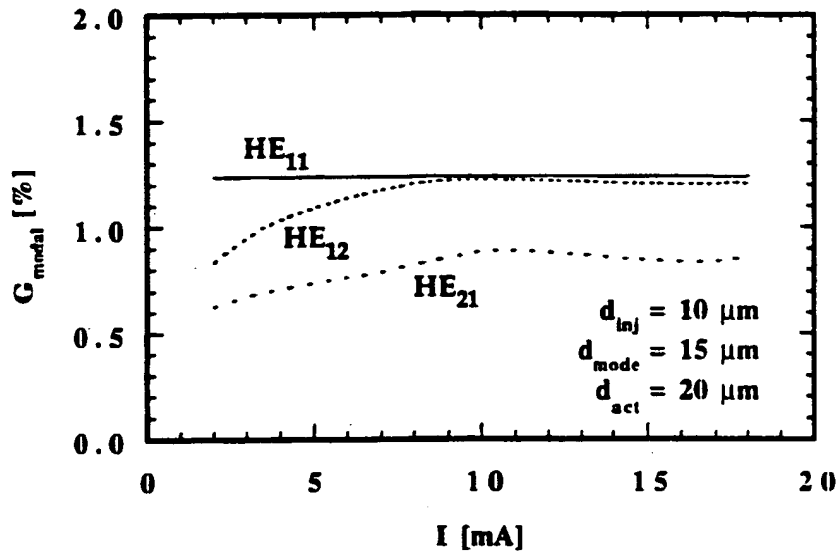


Fig. 2.25. Modal gain for the first three modes during the course of the  $I$ - $I$  curve for the current apertured design. The modal gain of the fundamental mode is higher for all biases, ensuring single mode operation.

In summary, a current-to-light model has been presented which includes the lateral effects of varying current injection, spatial hole burning, surface recombination and ambipolar carrier diffusion as well as thermal effects on the cavity mode and spectral gain curve. Bandgap renormalization was shown to be necessary to describe the gain offset operation of the devices while the rollover in output power has been attributed to Auger recombination for a well designed active region. The model has been used to explore the optimization of vertical-cavity laser performance in terms of temperature stabilized operation, power conversion efficiency, ultra-low threshold currents and single transverse mode operation. The current-to-light model has proven to be an effective tool for designing improved devices, and will be used in the following chapter to investigate the design of intra-cavity contacted vertical-cavity lasers.

## References

1. A. Yariv, *Optical Electronics*. 3 ed. 1985, New York: CBS Collage Publishing.
2. S.W. Corzine, R.H. Yan, and L.A. Coldren, "Theoretical gain in strained InGaAs/AlGaAs quantum wells including valence-band mixing effects." *Applied Physics Letters*. **57** (26) p. 2835-7. (1990)
3. S.M. Sze, *Physics of Semiconductor Devices*. 2cd Edition ed. 1981, New York: John Wiley & Sons.
4. W. Nakwaski and M. Osinski, "Thermal resistance of top-surface-emitting vertical-cavity semiconductor lasers and monolithic two-dimensional arrays." *Electronics Letters*. **28** (6) p. 572-4. (1992)
5. S.S. Kutateladze and V.M. Borishanski, *A Concise Encyclopedia of Heat Transfer*. 1966, Oxford: Permagon.
6. R.S. Geels, B.J. Thibeault, *et al.*, "Design and characterization of In/sub 0.2/Ga/sub 0.8/As MQW vertical-cavity surface-emitting lasers." *IEEE Journal of Quantum Electronics*. **29** (12) p. 2977-87. (1993)
7. S.Y. Hu, S.W. Corzine, *et al.*, "Lateral carrier diffusion and surface recombination in InGaAs/AlGaAs quantum well ridge-waveguide lasers." *Journal of Appliled Physics*. **76** (8). (1994)
8. D.B. Young, J.W. Scott, *et al.*, "Enhanced performance of offset-gain high-barrier vertical-cavity surface-emitting lasers." *IEEE Journal of Quantum Electronics*. **29** (6) p. 2013-22. (1993)

9. J.W. Scott, S.W. Corzine, D.B. Young, and L.A. Coldren, "Modeling the current to light characteristics of index-guided vertical-cavity surface-emitting lasers." *Applied Physics Letters*. **62** (10) p. 1050-2. (1993)
10. J.W. Scott, R.S. Geels, S.W. Corzine, and L.A. Coldren, "Modeling temperature effects and spatial hole burning to optimize vertical-cavity surface-emitting laser performance." *IEEE Journal of Quantum Electronics*. **29** (5) p. 1295-308. (1993)
11. J. Lee, M.O. Vassell, and G.J. Jan, "Energy-Band Diagrams of P-i-N Heterostructures for Single Quantum Well Lasers." *IEEE J. Quant. Elec.* **29** (6) p. 1469-1476. (1993)
12. M.G. Peters, B.J. Thibeault, *et al.*, "Band-gap engineered digital alloy interfaces for lower resistance vertical-cavity surface-emitting lasers." *Applied Physics Letters*. **63** (25) p. 3411-13. (1993)
13. K.L. Lear, S.A. Chalmers, and K.P. Killeen, "Low threshold voltage vertical-cavity surface-emitting laser." *Electronics Letters*. **29** (7) p. 584-6. (1993)
14. D.I. Babic, Y. Chung, N. Dagli, and J.E. Bowers, "Modal reflection of quarter-wave mirrors in vertical-cavity lasers." *IEEE Journal of Quantum Electronics*. **29** (6) p. 1950-62. (1993)
15. D.L. Huffaker, D.G. Deppe, and K. Kumar, "Native-oxide defined ring contact for low threshold vertical-cavity lasers." *Appl. Phys. Lett.* **65** (1) p. 97-99. (1994)

16. R.A. Morgan, G.D. Guth, *et al.*, "Transverse mode control of vertical-cavity top-surface-emitting lasers." *IEEE Photonics Technology Letters*. 5 (4) p. 374-7. (1993)
17. Y.A. Wu, C.J. Chang-Hasnain, *et al.*, "Single-transverse mode, low threshold current vertical-cavity surface-emitting laser." *IEEE Transactions on Electron Devices*. 40 (11) p. 2116-17. (1993)



## Chapter 3: Intra-Cavity Design

### 3.0 Chapter Overview

This chapter covers the design of the intra-cavity layers used to make contact to the active region within the optical cavity. The intra-cavity layers provide a lateral path from the contacts which distributes the current injected into the active region. The desire to maintain a short vertical cavity and low optical losses pushes the design towards thin, low-doped intra-cavity layers. Yet the relatively high resistance, particularly of the p-type material, will result in current crowding at the periphery as the diode resistance becomes comparable with the sheet resistance of the intra-cavity layers. As was shown in Chapter 2, spatial hole burning significantly reduces the laser efficiency. If the current crowds at the periphery where the mode is weak, the effect will be even more severe. This chapter introduces the use of a current-leveling layer in between the active region and a conductive layer. The resistive current-leveling layer serves to diffuse the injected current, limiting the current crowding.

At the same time, the increased resistance will result in heating, also limiting the device performance. In between two extremes lies a balanced design. This chapter presents the tools needed to analyze such structures and provides guidelines for the design of intra-cavity contacted vertical-cavity lasers. The chapter starts with an introduction to the current crowding problem by an analytical treatment of a simplified one-dimensional geometry. Formulas for the current crowding are derived for the two limiting cases. Typical numbers are used to show the scale of the problem, motivating the need for a current-leveled design. To allow a more accurate analysis, the numerical algorithm used to simulate a ring contacted laser structure is developed and applied to various designs. Finally, the current injection simulations are coupled with the model of Chapter 2 to generate  $L-I$  characteristics for intra-cavity-contacted vertical-cavity lasers, showing the tradeoffs in device performance associated with the intra-cavity design.

### 3.1 Analytical Analysis

Current crowding is a well known phenomenon in bipolar transistors. It occurs whenever contacts supply current laterally to a vertical junction. The voltage gradient required to supply the lateral flow of current results in an exponential variation in the vertical diode current, with the result that current is injected near the periphery of the device. Of course, if the lateral voltage variation is sufficiently low, the diode current variation will be negligible. Such is the case for a conductive metal contact on top of a diode, where it is assumed that the potential is essentially constant. In the case of a bipolar transistor, the current gain requires that the base be very thin, resulting in significant base resistance. In the case of a vertical-cavity laser, the requirement of a short cavity design, needed for single longitudinal mode operation and high speed response, limit the intra cavity layers to a thickness on the order of one micrometer while the requirement of a low round-trip loss limit the doping levels to the lower  $10^{18}/\text{cm}^3$  range. The result is that current crowding is also a concern for these intra-cavity contacted designs. To introduce the reader to the current crowding effect and the design tradeoffs, the current crowding effect in a simple geometry is first analyzed analytically.

#### 3.1.1 Current crowding

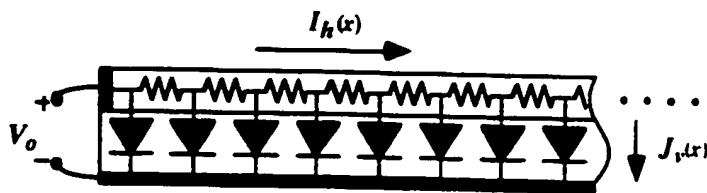


Fig. 3.1. Lateral injection into a conductive layer contacting a diode layer. As the diode becomes forward biased, the low dynamic resistance shunts the lateral resistance, resulting in current crowding.

A sketch of the geometry is shown in Fig. 3.1. A voltage  $V_0$  is applied

to the contact at  $x = 0$ . The conductive material has a thickness  $l_h$ , a conductivity  $\sigma_h$  and a width  $w$ . (If the lower contact also has resistance, the effective value is given by the parallel equivalent of the two layers, i.e.,  $(1/\sigma_h l_h) = (1/\sigma_1 l_1) + (1/\sigma_2 l_2)$ .) The horizontal current,  $I_h$ , is given by Ohm's law

$$I_h = -w l_h \sigma_h \frac{dV}{dx}, \quad (3.1)$$

while the forward biased diode current,  $J$ - $V$ , can be expressed as

$$J_v = J_d \exp\left(\frac{V - V_d}{V_T}\right), \quad (3.2)$$

where the diode material is characterized as having an current density  $J_d$  at a forward bias of  $V_d$ . The thermal voltage  $V_T$  may be  $k_B T_{jc}/q$  in the case of an ideal diode or something higher for a non ideal diode. The diode current acts as a sink for the horizontal current, so that the continuity equation is expressed as:

$$dI_h = -J_v w dx \quad \text{or} \quad -\frac{1}{w} \frac{dI_h}{dx} = J_v. \quad (3.3)$$

Substituting Eqns. (3.1) and (3.2) into (3.3) yields a second-order non-linear equation for the voltage in the conductive layer as a function of  $x$ .

$$\sigma_h l_h \frac{d^2 V}{dx^2} = J_d \exp\left(\frac{V - V_d}{V_T}\right). \quad (3.4)$$

Equation (3.4) can be made dimensionless by making the following change of variables:

$$y = (x + a) / \zeta_{cd} \quad \text{and} \quad H = \frac{V - V_d}{V_T}$$

where  $a$  is a constant, and the characteristic decay length,  $\zeta_{cd}$ , is defined as

$$\zeta_{cd} \equiv \sqrt{\frac{2 V_T \sigma_h l_h}{J_d}} = \sqrt{\frac{2 V_T}{R_{sh} J_d}} \quad (3.5)$$

with the sheet resistance defined as  $R_{sh} = 1/\sigma_h l_h$ . Equation (3.4) can then be rewritten as

$$\frac{d^2 H}{dy^2} = 2e^H, \quad (3.6)$$

which has the solution of

$$H(y) = \ln(1/y)^2 = -2 \ln y.$$

Returning to the real variables and enforcing the boundary condition that

$$V(0) = V_0$$

solves for the constant  $a$ , yielding

$$V(x) = V_d - 2V_{th} \ln \left( (x/l_{cd}) + e^{-(V_0 - V_d)/2V_T} \right). \quad (3.7)$$

This solution is valid until the voltage has decayed to nearly zero, which occurs at

$$x_{final} = \zeta_{cd} e^{V_d/2V_T}. \quad (3.8)$$

As we approach  $x_{final}$  the diode current  $J$ - $V$  has dropped to such low values that Eqn. (3.2) must be modified to give zero current at zero voltage, i.e., using the exact diode law. The currents are so low, however, that it takes a tremendous distance for this to occur, so that the solution Eqn. (3.7) is an excellent approximation. For a sense of scale, with a characteristic length  $\zeta_{cd} = 3 \mu\text{m}$ , a diode voltage  $V_d = 1.3\text{V}$  and a thermal voltage  $V_T = 0.026\text{V}$  the value for  $x_{final}$  is 216 kilometers! For all practical purposes, the voltage function  $V(x)$  given in Eqn. (3.7) satisfies the boundary conditions that  $V = V_0$  at the contact and that the diode current decay to zero at infinity.

With the voltage distribution known, the currents can be calculated from Eqns. (3.1) and (3.2):

$$J_v(x, V_0) = \frac{J_d}{\left( (x/l_{cd}) + e^{-(V_0 - V_d)/2V_T} \right)^2} \quad (3.9)$$

$$I_h(x, V_0) = \frac{wl_{cd} J_d}{\left( (x/l_{cd}) + e^{-(V_0 - V_d)/2V_T} \right)} \quad (3.10)$$

The above formulas can be further simplified by considering the profile when the applied voltage  $V_0$  is equal to the characteristic diode voltage  $V_d$ . This is really not a restriction. Any bias point can be used to characterize the diode in Eqn. (3.2). The new bias is reflected in the diode current prefactor  $J_d$  which changes the characteristic decay length  $\zeta_{cd}$  in Eqn. (3.5). Thus letting  $V_0 = V_d$  yields

$$J_v(x) = \frac{J_d}{\left( (x/\zeta_{cd}) + 1 \right)^2} \quad (3.11)$$

$$I_h(x) = \frac{w\zeta_{cd} J_d}{\left( (x/\zeta_{cd}) + 1 \right)} \quad (3.12)$$

Equation (3.11) shows that the diode current density has decayed to one quarter of its original value at a distance  $\zeta_{cd}$  from the contact. The value of horizontal current at  $x = 0$  provides the total current injected into the diode

$$I_d = I_h(0) = w \zeta_{cd} J_d . \quad (3.13)$$

From Eqn. (3.13) we see that the total diode current is simply the diode current density expected for the applied voltage times an area given by the width of the structure and the decay length  $\zeta_{cd}$ . Thus the decay length given in Eqn. (3.5) completely characterizes the current crowding behavior.

Consider a junction cladded by  $1\mu\text{m}$  thick p and n layers, each doped to a carrier concentration of  $1 \times 10^{18} \text{cm}^{-3}$ . The mobility is assumed to be  $2000 \text{cm}^2/\text{Vs}$  for the electrons and  $150 \text{cm}^2/\text{Vs}$  for the holes. This gives a sheet resistance of  $417\Omega/\square$  for the p-type material and  $32\Omega/\square$  for the n-type material, showing that the low mobility of holes is the limiting factor. The effective sheet resistance  $R_{sh} = (417+32)\Omega = 449\Omega/\square$ . For the diode, we'll use representative numbers of  $J_d = 1\text{kA}/\text{cm}^2$  with a thermal voltage  $V_T = 0.052\text{V}$  as might be expected for a laser junction at threshold with recombination occurring within the depletion region. Using the above values in Eqn. (3.5) gives a characteristic decay length of

$$\zeta_{cd} = \sqrt{\frac{2V_T}{R_{sh} J_d}} = \sqrt{\frac{2 \cdot 0.052\text{V}}{449\Omega \cdot 1000\text{A}/\text{cm}^2}} \cong 5\mu\text{m} . \quad (3.14)$$

Thus the diode current density would decay to one quarter of its original value  $5\mu\text{m}$  in from the edge at threshold. The example structure is starting to show current crowding at threshold. Due to their small size, average current densities much higher than  $10\text{kA}/\text{cm}^2$  are common in surface emitting lasers. Once the current is no longer uniformly injected, the current densities at the perimeter begin to increase dramatically. Equation (3.13) relates the current density at the

perimeter to the total diode current. Equation (3.13) can be combined with Eqn. (3.5) for the decay length and then inverted to give

$$J_d = \frac{1}{2V_T \sigma_h l_h} \left( \frac{I_d}{w} \right)^2 = \frac{R_{sh}}{2V_T} \left( \frac{I_d}{w} \right)^2, \quad (3.15)$$

$$\zeta_{cd} = \frac{2V_T \sigma_h l_h}{(I_d/w)} = \frac{2V_T}{R_{sh}(I_d/w)}. \quad (3.16)$$

These formulas have been derived assuming a single end contact to an unbounded diode in rectangular coordinates. For inward flow from a ring contact, the decreasing area will help reduce the decay rate as analyzed numerically below. Nevertheless, current crowding effects can be expected by the time that the decay length,  $\zeta_{cd}$ , is less than the device radius. Once current crowding effects begin, Eqn. (3.15) states that the current density at the edge increases proportional to the square of the bias current while Eqn. (3.16) states that the decay length decreases inversely proportional to the bias current. Using a width of  $2\pi r$  for  $w$  in Eqn. (3.16) yields an approximate formula for the ring contacted structure in terms of the radius:

$$\zeta_{cd} = \left( \frac{4\pi V_T}{R_{sh} I_d} \right) r. \quad (3.17)$$

Inserting the same numbers as in Eqn. (3.14) along with a current of 1 mA yields a decay length of  $1.4 r$ , decreasing linearly with increasing bias. Thus a  $10 \mu\text{m}$  diameter device using our example intra-cavity contacts at 10 mA bias would have most of the current injected within the first half  $\mu\text{m}$  of the edge! Such behavior will adversely affect the laser's efficiency and promote multiple transverse mode operation, exacerbating spatial hole-burning effects. What can be done to overcome this limitation of an intra-cavity design?

## 3.1.2 Current leveling

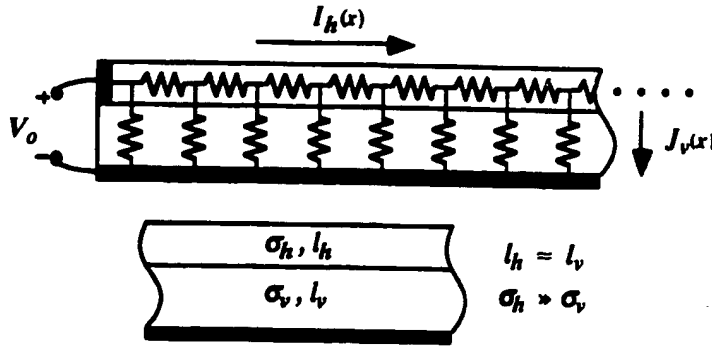


Fig. 3.2. Lateral injection through a two layer resistive network. The layer for horizontal flow is much more conductive than the resistive layer which limits vertical flow.

Current crowding occurs as the diode resistance becomes low, shunting the lateral flow in the contacting material. Since the diode resistance decreases with increasing bias, these effects are inevitable at some point. An alternate structure is shown in Fig. 3.2 where the diode has been replaced with a constant-resistivity material. With all linear elements the current distribution is independent of bias. If such a resistive current leveling layer is placed between the junction and the conductive layer, the current crowding can be limited. The injection distribution calculated for the resistive network alone represents the limiting case.

A sketch of the geometry is shown in Fig. 3.2. The subscript  $h$  stands for horizontal flow and the subscript  $v$  stands for vertical flow. A voltage  $V_0$  is applied to the contact at  $x = 0$ . The conductive material has a thickness  $l_h$ , a conductivity  $\sigma_h$  and a width  $w$ . The horizontal current,  $I_h$ , is given by Ohm's law

$$I_h = -w l_h \sigma_h \frac{dV}{dx}, \quad (3.18)$$

while the current density in the resistive layer,  $J$ - $V$ , can be expressed as



$$J_v = \sigma_v \frac{V}{l_v} . \quad (3.19)$$

The vertical current acts as a sink for the horizontal current, so that the continuity equation is again expressed as

$$dI_h = -J_v w dx \quad \text{or} \quad -\frac{1}{w} \frac{dI_h}{dx} = J_v . \quad (3.20)$$

Substituting Eqns. (3.18) and (3.19) into (3.20) yields a second-order linear equation for the voltage in the conductive layer as a function of  $x$ :

$$\sigma_h l_h \frac{d^2 V}{dx^2} = \frac{\sigma_v}{l_v} V . \quad (3.21)$$

The solution is a simple exponential decay:

$$V(x) = V_0 \exp(-x/\zeta_{cr}) \quad (3.22)$$

with a characteristic decay length  $\zeta_{cr}$  of

$$\zeta_{cr} = \sqrt{l_h l_v (\sigma_h / \sigma_v)} . \quad (3.23)$$

Some information about the design of the current leveling structure can be immediately determined from Eqn. (3.23). The decay length is proportional to the geometric mean of the two layer thicknesses. For a given total thickness, the decay length is maximized by designing the conductive and resistive layers with equal thicknesses. If each layer is  $0.5 \mu\text{m}$  thick, then a conductivity ratio of 50 will produce a decay length of  $3.5 \mu\text{m}$ . This is sufficient for a  $7 \mu\text{m}$  diameter intra-cavity contacted laser, where the cylindrical geometry can be expected to reduce the effective decay rate. The advantage of this design is that only  $0.5 \mu\text{m}$

of optically lossy, doped material need be used to conduct the current into the optical mode where it can efficiently contribute to the light output. In the case of a cylindrical geometry, the solution becomes the modified Bessel function. The solution for the horizontal current is the zero<sup>th</sup> order modified (or hyperbolic) Bessel function of the first kind,  $I_0(r/\zeta_{cr})$ , with the same characteristic decay length. More will be said on these solutions in section 3.2.3.

Using the solution for the voltage distribution, Eqn. (3.22), the horizontal and vertical current distributions can be calculated:

$$J_v(x, V_o) = \frac{\sigma_v}{l_v} V_o e^{-x/\zeta_{cr}} \quad (3.24)$$

$$I_h(x, V_o) = \frac{w}{\zeta_{cr}} \frac{V_o}{R_{sh}} e^{-x/\zeta_{cr}} \quad (3.25)$$

where the conductive layer sheet resistance,  $R_{sh}$ , is defined as  $1/\sigma_h/l_h$ . From Eqn. (3.25) the current-leveling resistance,  $R_{lev}$ , can be calculated:

$$R_{lev} = \frac{V_o}{I_h|_{x=0}} = \frac{\zeta_{cr}}{w} R_{sh} = \frac{1}{w} \sqrt{\frac{l_v/l_h}{\sigma_h \sigma_v}} \quad (3.26)$$

It is instructive to insert some typical numbers at this point. Using a 0.5  $\mu\text{m}$  thick conductive layer doped  $5 \times 10^{18} \text{ cm}^{-3}$  p-type, with a mobility of  $150 \text{ cm}^2/\text{Vs}$  gives a conductivity  $\sigma_h = 120/\Omega\text{cm}$ . For the resistive layer, a 0.5  $\mu\text{m}$  thick layer doped  $1 \times 10^{17} \text{ cm}^{-3}$  p-type with a mobility of  $400 \text{ cm}^2/\text{Vs}$  gives a conductivity  $\sigma_v = 6.4/\Omega\text{cm}$ . The associated decay length is  $2.17 \mu\text{m}$ . Returning to the  $7 \mu\text{m}$  diameter laser, using  $w = 2\pi r = 22 \mu\text{m}$  gives an estimated  $R_{lev} = 16.4 \Omega$ . With vertical cavity resistances on the order of hundreds of Ohms, these values show that a current leveling structure presents an acceptable solution to the current crowding problem.

### 3.1.3 Analytic design curves

An important design consideration is the comparison of the decay lengths for the same conductive layer with or without current leveling. From the analysis, design curves can be generated that give the current density profiles in dimensionless parameters, applicable to any set of intra-cavity structural parameters and bias. From the design curves, the tradeoffs of current crowding, resistance and optical loss become clear. While the formulas are only approximate, the insight into the design parameters are invaluable. The exact geometry is solved numerically in section 3.2. We begin by finding the bias current at which the diode current decay length without leveling is equal to the resistive network decay. Equating Eqn. (3.23) for  $\zeta_{cr}$  with Eqn. (3.5) for  $\zeta_{cd}$  gives the bias current  $I_\zeta$  when the two lengths are equal:

$$I_\zeta = I_d|_{\zeta_{cd}=\zeta_{cr}} = 2V_T w \sqrt{\sigma_h \sigma_v (l_h/l_v)} . \quad (3.27)$$

Combining Eqn. (3.11) with (3.15) and Eqn. (3.23) with (3.25) give the current density profiles scaled with diode current per unit width:

$$\frac{j_v^{res}}{I_d/w} = \frac{1}{\zeta_{cr}} e^{-x/\zeta_{cr}} \quad \text{and} \quad \frac{j_v^{diode}}{I_d/w} = \frac{1}{\zeta_{cd}} \frac{1}{\left((x/\zeta_{cd}) + 1\right)^2} .$$

$$\text{where} \quad \zeta_{cr} = \sqrt{l_h l_v (\sigma_h / \sigma_v)} \quad \text{and} \quad \zeta_{cd} = \frac{2 \sigma_h l_h V_T}{I_d/w} .$$

If we define the dimensionless parameters:

$$t = x / \zeta_{cr} , \quad i = I_d / I_\zeta , \quad \mathcal{F} = j_v / (I_d/w \zeta_{cr}) .$$

then the two current density profiles can be rewritten as:

$$\mathcal{G}_{res} = e^{-\ell}, \quad (3.28)$$

$$\mathcal{G}_{diode} = \frac{i}{(i\ell + 1)^2}. \quad (3.29)$$

Equations (3.28) and (3.29) are plotted in log and linear formats in Figs. 3.3 and 3.4.

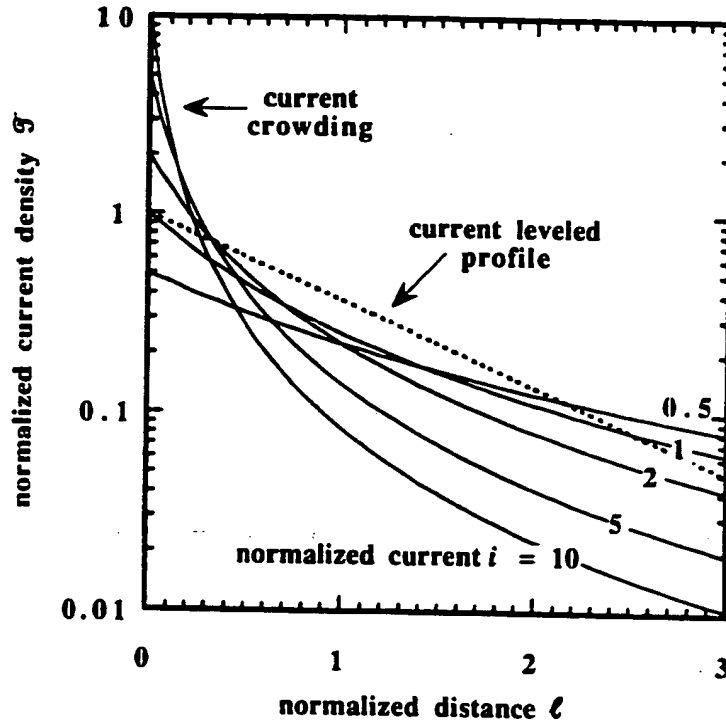


Fig. 3.3. Log plot of the normalized current density profiles for the diode limit (solid) and resistive limit (dashed).

The normalized current,  $i$ , gives the normalized unleveled current density,  $\mathcal{G}_{diode}$ , at the edge of the device. If the bias current exceeds  $I_T$  then  $i > 1$  and it is advantageous to use a current-leveled design. Consider again an intra-cavity contacted design where  $\sigma_h = 120/\Omega\text{cm}$ ,  $\sigma_v = 6.4/\Omega\text{cm}$ ,  $l_h = l_v = 0.5\mu\text{m}$  and  $V_T =$

0.052V. Equation (3.23) calculates a resistive decay length  $\zeta_{cr} = 2.16 \mu\text{m}$ . Using a width  $w = 2\pi r = 22 \mu\text{m}$  appropriate for a  $7 \mu\text{m}$  diameter laser, Eqn. (3.27), states two decay lengths become equal at a bias of  $I_\zeta = 6.3 \text{ mA}$ . Thus if one intends to drive a  $7 \mu\text{m}$  diameter laser with the above intra-cavity contact parameters above 6 mA it would be advantageous to introduce the current leveling layer. More detail for bias currents around  $i = 1$  are shown in Fig. 3.4. At the lower bias currents the diode current density falls below the resistive limit as the diode decay length begins to increase, reducing the current density for a given bias current.

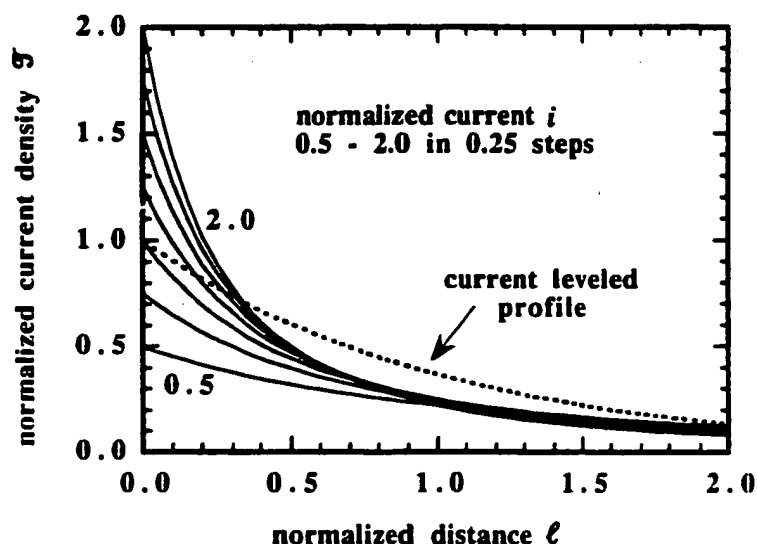


Fig. 3.4. Linear plot of the normalized current density profiles for the diode limit (solid) and resistive limit (dashed).

Using the above example, at a bias of  $i = 0.5$  or  $3.2 \text{ mA}$ , the decay length  $\zeta_{cd} = 2\zeta_{cr} = 4.3 \mu\text{m}$ . Here the decay length has exceeded the  $3.5 \mu\text{m}$  radius of the laser, and hence one can assume that the current injection in a ring contacted device will be fairly uniform for bias currents less than  $3 \text{ mA}$ . In practicality, the proposed current leveled intra-cavity contacted structure is a combination of both limits, as shown in Fig. 3.5. The current injection profile into the active region at

a given bias can be expected to decay at the lowest rate given in Figs. 3.3 and 3.4. Thus the decay of a current-leveled design is dominated by the solid curves for  $i < 1$  and the dashed curve for  $i > 1$ .

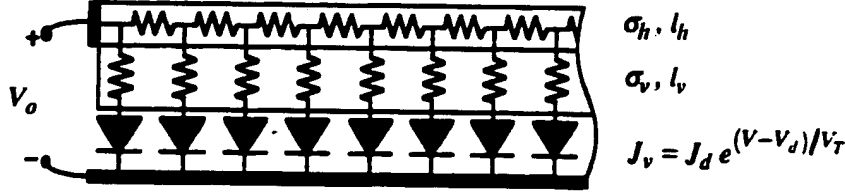


Fig. 3.5. Current leveled intra-cavity contacted design, showing material parameters and the equivalent circuit.

It should now be clear that the current crowding behavior is characterized by the parameters  $\zeta_{cr}$  and  $I_\zeta$  given in Eqns. (3.23) and (3.27) and that the penalty for limiting the current crowding is the leveling resistance,  $R_{lev}$ , given in Eqn. (3.26). The current crowding parameters can be expressed in terms of the leveling resistance:

$$I_\zeta = \frac{2V_T}{R_{lev}} \quad (3.30)$$

$$\zeta_{cr} = \frac{wR_{lev}}{R_{sh}} \quad (3.31)$$

$$\frac{\zeta_{cr}}{r} = 2\pi \frac{R_{lev}}{R_{sh}} \quad (3.32)$$

where  $R_{sh} = 1/(\sigma_h l_h)$  is the sheet resistance of the conductive layer,  $r = w / 2\pi$  is the radius and  $V_T$  is the thermal voltage. In our example calculation,  $V_T = 0.052V$ ,  $R_{lev} = 16.4\Omega$ ,  $w = 22 \mu m$  and the sheet resistance  $R_{sq} = 167\Omega/\square$ , yielding a current limiting onset at  $I_\zeta = 6.3 \text{ mA}$  with a resistive limited current density decay length  $\zeta_{cr} = 2.16 \mu m$ . The sheet resistance is inversely proportional to the

doping-thickness product, which is the primary contributor to the internal optical losses. Thus lower sheet resistance represents higher optical losses. The additional round trip optical losses,  $\Delta L_i$ , can be expressed as

$$\Delta L_i = 2\xi_{enh} \frac{d\alpha/dN}{q\mu R_{sh}}, \quad (3.33)$$

where  $d\alpha/dN$  is the ratio of optical absorption to carrier density.  $\xi_{enh}$  is the longitudinal enhancement factor and  $\mu$  is the carrier mobility. The round-trip optical losses for p-type material is estimated to be  $11.5\text{cm}^{-1}$  per  $1 \times 10^{18}\text{cm}^{-3}$  carriers. Using a sheet resistance  $R_{sh} = 167 \Omega/\square$ ,  $\mu = 150 \text{ cm}^2/\text{Vs}$  and  $d\alpha/dN = 11.5\text{cm}^{-1} / 1 \times 10^{18}\text{cm}^{-3}$  gives a loss of 0.56% for the above example. Equations (3.30), (3.31) and (3.33) express all three design tradeoffs: current crowding, additional resistance and optical losses associated with an intra-cavity contacted design. They provide approximate guidelines for device design.

Equations (3.30) and (3.32) are plotted in Fig. 3.6. The resistive decay length scaled by the radius is plotted in solid lines while the onset of current leveling is plotted in dashed lines. The dashed curves have been calculated for diode ideality factors varying from 1 to 4. The more ideal the diode characteristics, the sooner current crowding begins. A value of 2 is expected for heterojunction recombination because all the recombination occurs within the depletion region. Assuming  $\xi_{enh} = 1$ ,  $d\alpha/dN = 11.5\text{cm}^{-1} / 1 \times 10^{18}\text{cm}^{-3}$  and an average hole mobility of  $150 \text{ cm}^2/\text{Vs}$ , sheet resistances of 50, 100, 200 and  $500 \Omega/\square$ , correspond to round trip optical losses of 2, 1, 0.5 and 0.2% using Eqn. (3.33). The first question is, do we need current leveling? As a criterion, let's consider a decay rate equal to the device radius at 10 mA bias as acceptable. From the plot for a diode ideality factor of 2, the leveling resistance required is  $10 \Omega$ . The associated conductive layer is  $62 \Omega/\square$ , or an optical loss of 1.5% ! This is unacceptably high for a surface-emitting device. Consider instead a design with an optical loss of 0.5%. For the criteria of a decay rate equal to the radius, a leveling resistance of  $30 \Omega$  is required. In this case the current leveling will

determine the decay rate for bias currents above 3 mA. Without a current leveling structure, either current crowding or high optical losses are unavoidable.

The numbers used in the above calculations are for p-type materials in GaAs. If n-type materials were used instead, the average mobility of  $2000 \text{ cm}^2/\text{Vs}$  and lower loss coefficient  $da/dN = 5 \text{ cm}^{-1} / 1 \times 10^{18} \text{ cm}^{-3}$  reduce the optical losses for a given sheet resistance by a factor of 27.

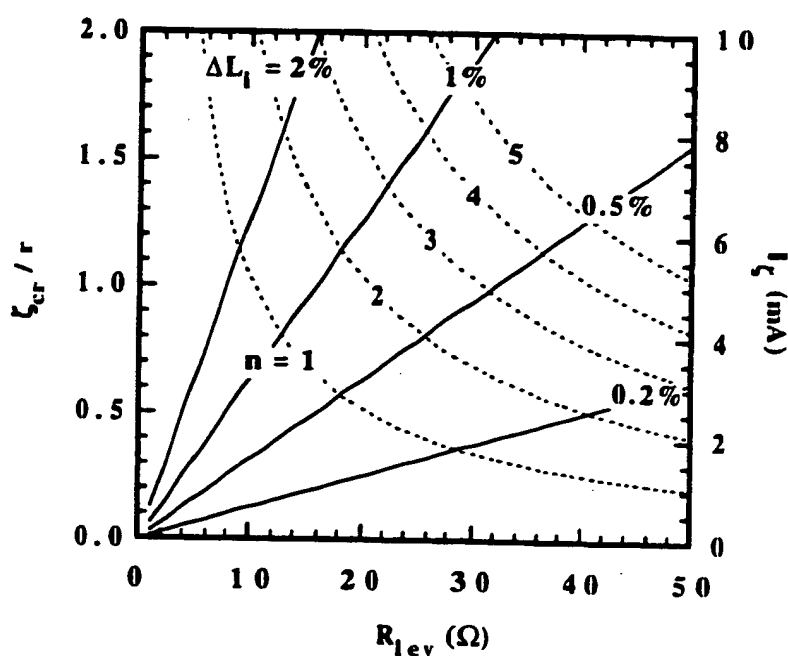


Fig. 3.6. Design curve for intra-cavity layers. The resistive decay length scaled by radius vs. the leveling resistance is plotted in solid lines for varying round trip optical losses. The bias at which current leveling begins vs. the leveling resistance is plotted in dashed lines for varying diode ideality factors.

While this looks encouraging, one must remember that a diode requires both p and n-type materials. If both contacts are intra-cavity, then it will be the p-type material which dominates the sheet resistance and current crowding. If only one contact is made intra-cavity, it is highly preferable that be the n-type material.



We have fabricated such a bottom-emitting structure [1] on a semi-insulating substrate using an n-type intra-cavity layer and a top p mirror. The optical losses of the p-doped mirror, however, are on the order of or even greater than an intra-cavity design.

The design that I fabricated was conservative, chosen to minimize the optical losses and yet avoid severe current crowding. The structure is shown in Fig. 3.7. The  $0.37\text{ }\mu\text{m}$  thick p+ layer is doped  $4 \times 10^{18}\text{ cm}^{-3}$  for a conductivity  $\sigma_{||} = 96/\Omega\text{cm}$  and a sheet resistance  $R_{sq} = 280\Omega/\square$ .

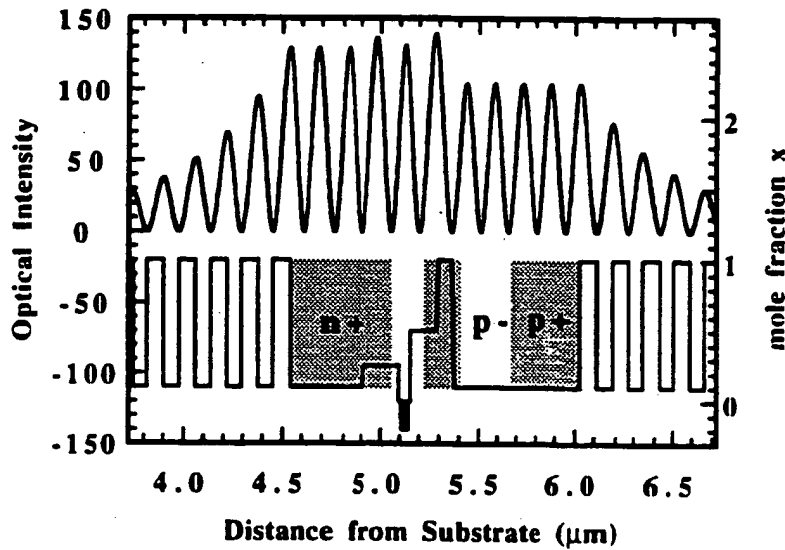


Fig. 3.7. Plot showing the detail of the intra-cavity design in wafer 931006h [2].

The  $0.28\text{ }\mu\text{m}$  thick p- layer is doped  $2 \times 10^{17}\text{ cm}^{-3}$  for a conductivity  $\sigma_{||} = 4.8/\Omega\text{cm}$ , yielding a resistive decay length  $\zeta_{cr} = 1.4\text{ }\mu\text{m}$ . For a  $7\text{ }\mu\text{m}$  device, the leveling structure introduces a resistance of  $R_{lev} = 18.4\Omega$  which limits current crowding at a bias  $I_{\zeta} = 5.6\text{ mA}$ , assuming a diode ideality factor of 2. Using  $\xi_{enh} = 1$  gives an associated round trip optical losses  $L_i = 0.34\%$ . To reduce the losses further in the actual device, I have positioned the conductive layer a mirror

period away from the active region as shown in Fig. 3.7. As can be determined by the standing wave ratio, the longitudinal enhancement factor  $\xi_{enh} = 100/130 = 0.77$  for this design which reduces the optical losses due to the conductive layer to 0.26%.

In summary, the effects of current crowding for an intra-cavity design have been analyzed in a simplified one-dimensional geometry, showing the need for a current-leveling layer to limit the current crowding. Formulas for the decay lengths characterizing the non uniform current density profiles were calculated. Finally, equations for the non uniform decay length, additional device resistance and optical losses associated with the intra-cavity layers were derived and plotted as design curves. These formulas were then used to analyze the intra-cavity design used in the lasers whose characteristics are presented in Chapter 5.

### 3.2 Numerical Analysis

The analytical analysis described above is very useful for understanding the tradeoffs of current crowding, additional resistance and optical loss associated with the current-leveled intra-cavity design. Simple formulas were derived by using a one-dimensional analysis. Yet actual devices are built in a ring contact configuration, making the above diode current density decay rates a worst case limit. The resistive limit, for example, is actually given by the hyperbolic Bessel function. Furthermore, a current-leveled design is a combination of the two extremes analyzed, crossing from a diode limited regime into a resistive network limited regime with increasing bias. And it is difficult to quantify the effect of current crowding on the overall laser performance. These issues can be resolved by using numerical techniques to solve for the current injection profiles in cylindrical coordinates. The resulting non-uniform current density profiles can then be used by the current-to-light model of Chapter 2 to simulate the overall laser performance.

### 3.2.1 Model formulation

The fundamental relation is the law of current continuity. All materials are treated as being linear, so that

$$J = -\frac{1}{\rho} \nabla V, \quad (3.34)$$

where  $J$  is the current density and  $\rho$  is the resistivity. Bias-dependent values of resistivity will be used for non-linear materials to enable the use of iterative matrix methods for the solution of the system of equations. The continuity equation can thus be written as

$$\nabla \cdot J = 0, \quad (3.35)$$

which yields the Poisson equation for the voltage distribution.

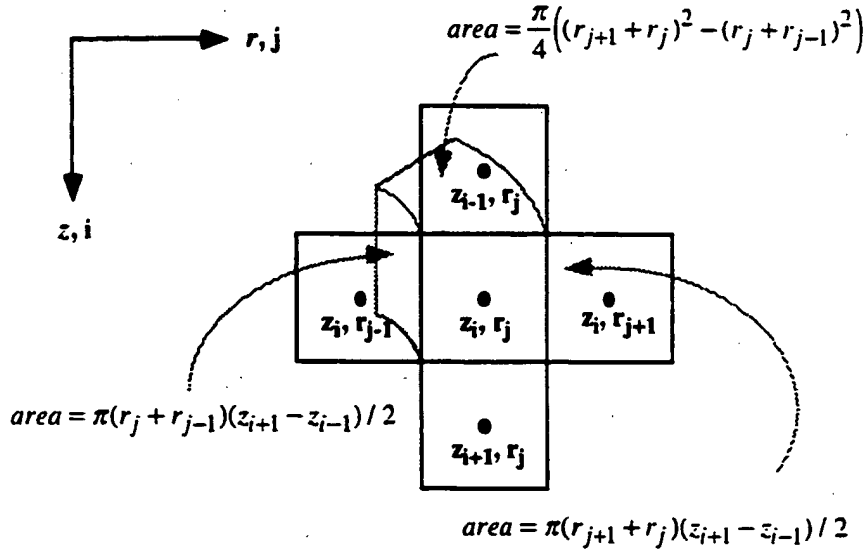


Fig. 3.8. Coordinate system and grid used for the current injection simulations. The areas used to calculate the currents between cells are shown.

To solve the equation, a centered grid is introduced for annular cells as shown in Fig. 3.8. Boundaries between cells are chosen to be centered between grid points, allowing variable grids if desired. Associated with each cell is an axial resistivity,  $\rho^z$ , and a radial resistivity,  $\rho^r$ , which allows the modeling of anisotropic materials. The current flowing between two cells is given by the current density  $J$  times the appropriate area. The formulas for the various areas are given in the figure. The voltage gradient is approximated as the voltage difference at the two grid points divided by the separation. Thus the difference equations for current flow can be written. The radial current flow from cell<sub>*i,j*</sub> to cell<sub>*i,j+1*</sub> is:

$$I_{i,j \rightarrow i,j+1} = \text{area} \cdot -\Delta V / \Delta r \cdot 1 / \rho, \quad \text{where}$$

$$\text{area} = \pi(r_{j+1} + r_j)(z_{i+1} - z_{i-1}) / 2.$$

$$-\Delta V / \Delta r = (V_{i,j} - V_{i,j+1}) / (r_{j+1} - r_j), \quad (3.36)$$

$$1 / \rho = 2 / (\rho_{i,j}^r + \rho_{i,j+1}^r).$$

Similarly, the axial current flow from cell<sub>*i,j*</sub> to cell<sub>*i+1,j*</sub> is:

$$I_{i,j \rightarrow i+1,j} = \text{area} \cdot -\Delta V / \Delta z \cdot 1 / \rho, \quad \text{where}$$

$$\text{area} = \frac{\pi}{4} \left( (r_{j+1} + r_j)^2 - (r_j + r_{j-1})^2 \right).$$

$$-\Delta V / \Delta z = (V_{i,j} - V_{i+1,j}) / (z_{i+1} - z_i), \quad (3.37)$$

$$1 / \rho = 2 / (\rho_{i,j}^z + \rho_{i+1,j}^z).$$

Equations (3.36) and (3.37) thus relate the currents between cells with the voltage matrix elements:

$$\begin{aligned}
I_{i,j \rightarrow i+1,j} &= \pi u z_{i,j} (V_{i,j} - V_{i+1,j}) , \\
I_{i,j \rightarrow i-1,j} &= \pi l z_{i,j} (V_{i,j} - V_{i-1,j}) , \\
I_{i,j \rightarrow i,j+1} &= \pi u r_{i,j} (V_{i,j} - V_{i,j+1}) , \\
I_{i,j \rightarrow i,j-1} &= \pi l r_{i,j} (V_{i,j} - V_{i,j-1}) .
\end{aligned} \tag{3.38}$$

where the matrix elements between upper and lower cells in either the  $z$  or  $r$  directions are defined as:

$$\begin{aligned}
u z_{i,j} &\equiv \frac{(r_{j+1} + r_{j-1})(r_{j+1} - r_{j-1}) + 2r_j(r_{j+1} - r_{j-1})}{2(\rho_{i,j}^z + \rho_{i+1,j}^z)(z_{i+1} - z_i)} , \\
l z_{i,j} &\equiv \frac{(r_{j+1} + r_{j-1})(r_{j+1} - r_{j-1}) + 2r_j(r_{j+1} - r_{j-1})}{2(\rho_{i-1,j}^z + \rho_{i,j}^z)(z_i - z_{i-1})} , \\
u r_{i,j} &\equiv \frac{(r_j + r_{j+1})(z_{i+1} - z_{i-1})}{2(\rho_{i,j}^r + \rho_{i,j+1}^r)(r_{j+1} - r_j)} , \\
l r_{i,j} &\equiv \frac{(r_{j-1} + r_j)(z_{i+1} - z_{i-1})}{2(\rho_{i,j-1}^r + \rho_{i,j}^r)(r_j - r_{j-1})} .
\end{aligned} \tag{3.39}$$

The total current is conserved and therefore  $\sum I = 0$ , or

$$I_{i,j \rightarrow i+1,j} + I_{i,j \rightarrow i-1,j} + I_{i,j \rightarrow i,j+1} + I_{i,j \rightarrow i,j-1} = 0 . \tag{3.40}$$

which can be combined with Eqn. (3.38) to define the voltage in cell  $i,j$  in terms of the voltages in the neighboring cells:

$$\begin{aligned}
&V_{i,j}(u z_{i,j} + l z_{i,j} + u r_{i,j} + l r_{i,j}) \\
&= u z_{i,j} V_{i+1,j} + l z_{i,j} V_{i-1,j} + u r_{i,j} V_{i,j+1} + l r_{i,j} V_{i,j-1} .
\end{aligned} \tag{3.41}$$

Equation (3.41) expresses the continuity equation in terms of the voltage distribution. Boundary conditions of either a fixed voltage or no current are included in Eqn. (3.41) by using the appropriate voltage or eliminating the

appropriate matrix element from both sides of the equation. For example, the boundary condition at the center is no current flow. Thus Eqn. (3.41) is modified at the  $r = 0$  ( $j = 1$ ) boundary by setting  $lr_{i,1} = 0$ , eliminating the current flow to the non-existent lower  $r$  cell in the center. If an annular ring contact with inner radius  $r_{cnt}$  were applied to the  $z = 0$  ( $i = 1$ ) surface, the boundary condition is enforced by setting  $lz_{1,j} = 0$  for  $r_j < r_{cnt}$  and by setting  $V_{0,j} = V_0$  for  $r_j > r_{cnt}$ . Equations (3.39) - (3.41) completely specify the system of equations to be solved.

The solution is complicated by the non-linearity of the diode elements, which have bias dependent resistivities

$$\begin{aligned}\rho_d^z &= \frac{1}{l_d} \frac{V_d}{J_d(V_d)}, \\ \rho_d^r &= 0.\end{aligned}\quad (3.42)$$

where  $l_d$  is the diode cell's thickness, and it has been assumed that all radial flow in the junction is due to ambipolar diffusion. An iterative technique known as alternating implicit technique (ADI) [3] can be used to solve for the voltage matrix  $V$  and the corresponding currents. The advantage of ADI is that it turns a large sparse matrix problem into simple banded matrix problems, reducing memory requirements. It has convergence advantages over other techniques in the case of non-linear matrix elements [4]. The technique is based on rewriting Eqn. (3.41), separating axial ( $i$ ) and radial ( $j$ ) solutions:

$$\begin{aligned}-uz_{i,j}V_{i+1,j} + V_{i,j}(uz_{i,j} + lz_{i,j} + ur_{i,j} + lr_{i,j}) - lz_{i,j}V_{i-1,j} \\ = ur_{i,j}V_{i,j+1} + lr_{i,j}V_{i,j-1}\end{aligned}\quad (3.43a)$$

$$\begin{aligned}-ur_{i,j}V_{i,j+1} + V_{i,j}(uz_{i,j} + lz_{i,j} + ur_{i,j} + lr_{i,j}) - lr_{i,j}V_{i,j-1} \\ = uz_{i,j}V_{i+1,j} + lz_{i,j}V_{i-1,j}\end{aligned}\quad (3.43b)$$

The left hand side of Eqns. (3.43a/b) couple together each element of a column/row of the voltage matrix in the form  $Ax = b$ . The matrix  $A$  is a tri-diagonal matrix so that only the elements one above, on or below the diagonal are non-zero. Using a simple algorithm, one can subtract rows to eliminate the lower off diagonal elements of  $A$  and then use back-substitution to solve for the vector  $x$  [5]. This process is very efficient, involving only a 3-by- $n$  matrix instead of  $n$ -by- $n$  matrix. Starting with an initial guess, the columns of  $V$  are solved for using Eqn. (3.43a), assuming that the bordering matrix elements on the right hand side of the equation are correct. The new values for the column are updated with some weighting factor, and then one proceeds to the next column, solving for axial voltage columns sweeping radially. Then one uses Eqn. (3.43b), solving for voltage rows sweeping axially. Each solution includes the boundary conditions at both ends, and thus the voltage matrix rapidly approaches the true solution of the continuity equation, Eqn. (3.41).

After a set of complete sweeps in both the axial and radial directions, the resistivity values for the nonlinear elements are recalculated. Eventually, the iterative process converges on a stable solution for the voltage and corresponding current distributions. Relaxation factors, introduced in the voltage and resistivity updates, can be used to insure convergence. Using a relaxation factor means that the new value is given by a weighted average of the old value and the calculated value. Relaxation factors less than one can be used to dampen numerical instabilities, as shown in the next section.

### 3.2.2 Grids and convergence

Before using a numerical model one must determine how coarse a grid can be used for reasonable accuracy. Coarse grids are desirable for reduced computation time. Comparing several simulations with increasingly finer grids allows a determination of an acceptable step size. The second issue is to determine what convergence criteria will be used and to what tolerance. This section shows sample calculations to resolve these numerical issues.

The example structure for analysis with a representative grid is shown in Fig. 3.9. A ring contact is made on top while a uniform ground plane makes

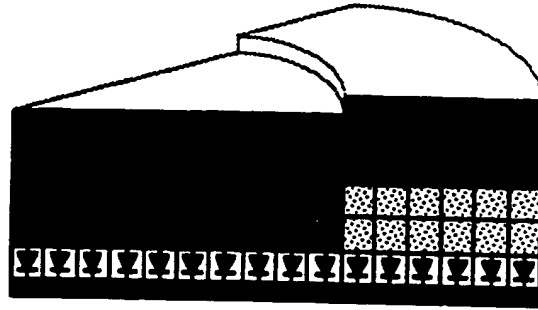


Fig. 3.9. Sample structure for calculations. The conductive material has a gray fill pattern while the current blocking material has a speckled fill pattern. Shown is a 10x4 grid.

contact across the bottom. Three materials are present in the structure: a conductive material shown in gray, a high resistivity blocking layer with a speckled fill pattern and a non-linear diode junction. In the drawing the resistive layer above the junction is divided into ten radial by four axial divisions. I'll call this a 10x4 grid. The conductive layer is  $1\mu\text{m}$  thick and doped  $2 \times 10^{18}\text{cm}^{-3}$  p-type with a mobility of  $150\text{cm}^2/\text{Vs}$  resulting in a resistivity of  $208\Omega\mu\text{m}$ . The diode will have the  $J$ - $V$  dependence of Eqn. (3.2) with an ideality factor of 2 and a characteristic current of  $1\text{kA}/\text{cm}^2$  at a bias voltage of 2V. The inner contact radius is  $5\mu\text{m}$  with an outer radius of  $8\mu\text{m}$ . Thus the structure is representative of a  $10\mu\text{m}$  diameter, intra-cavity contacted vertical-cavity laser.

At a bias of 2.25V there is significant current crowding. The current densities injected into the diode are calculated using several different grids are shown in Fig. 3.10. Grids of 5x4, 10x4, 20x4 and 20x16 calculated total currents of 6.70, 8.00, 8.59 and 8.76 mA respectively. From the current density profiles in Fig. 3.10, it is clear that the 10x4 case provides a reasonably accurate result even though the grid is coarse. The 10x4 grid will be used for the convergence calculations that follow.



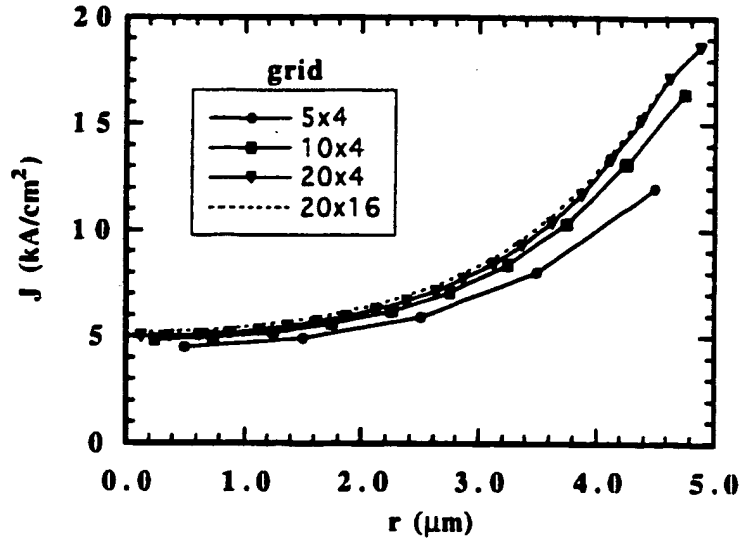


Fig. 3.10. Calculated current density injected into the diode region. The profiles are calculated for the same structure and bias voltage but varying grids. The 10x4 grid is shown in Fig. 3.9.

Convergence of an iterative numerical technique is usually determined by two parameters. One is the change in the values with each iteration. The other is some kind of absolute convergence. A slowly converging algorithm can have very small changes without actual convergence. For the current injection algorithm, two absolute convergence criteria can be established. One is that the current imbalance in each cell, normalized to the total current flow, fall below a certain value. A more stringent requirement is related to the total current flow in the structure. With contacts at the top and bottom, the total current flow from one plane (or disk) to the next should be the same. As a convergence criterion, we can consider the maximum deviation of the current flow from one radial plane to the next normalized to the total current flow. Thus the convergence is defined as:

$$conv = \max \left( \left| \frac{I_{i \rightarrow i+1}}{I_{ave}} \right| \right) \quad (3.44)$$

where

$$I_{i \rightarrow i+1} = \int_{axial\ grid\ i} J_{i \rightarrow i+1} dA = \sum_j \pi u z_{i,j} (V_{i,j} - V_{i+1,j}) \quad (3.45)$$

$$I_{ave} = \frac{1}{n} \sum_{i=1}^n I_{i \rightarrow i+1} \quad (3.46)$$

The iteration is repeated until the convergence falls within some tolerance. As previously described, the rate of convergence is dependent on the relaxation factors used for the voltage and non-linear resistive updates.

To determine what values to use it is very instructive to plot the convergence given in Eqn. (3.44) as a function of the number of iterations. In each case the voltage of all the interior points in Fig. 3.9 were initialized at 2V with a voltage of 2.25V applied to the ring contact. The ADI algorithm expressed in Eqn (3.43) is used to sweep through the structure. A complete set of radial and axial solutions represents an iteration. The convergence after each iteration is shown in Fig. 3.11. Curve **a** is for a voltage relaxation weighting  $w_v = 0.5$  and a resistance weighting  $w_r = 0.5$ . It shows a very stable, steady but slow convergence rate. Curve **b** is for relaxation weightings of 0.75 while curve **c** has no damping at all with  $w_v = w_r = 1$ . While the convergence rate is improved, numerical oscillations appear, resulting in a convergence limit of 0.0027%. Curve **d** uses a weighting of  $w_v = 1$  and  $w_r = 0.5$ , showing stable convergence properties and a good convergence rate. For the remaining calculations, the relaxation parameters of  $w_v = 1$  and  $w_r = 0.5$  are used. Also shown in the figure are the corresponding currents.

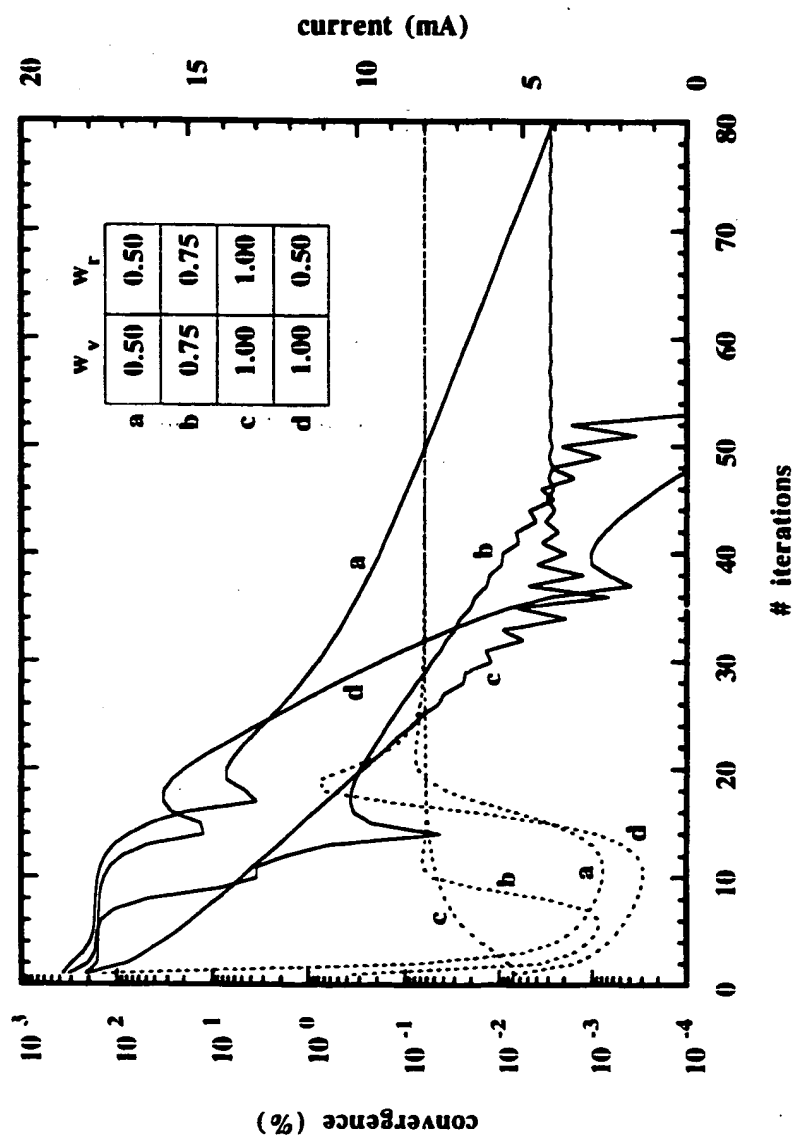


Fig. 3.11 Convergence of the total current flow vs. number of iterations for various relaxation weighting factors. The convergence becomes limited by numerical instabilities as the resistance weighting  $w_r$  approaches 1. Also shown are the corresponding currents as dashed lines.

A convergence tolerance of 0.1% to 0.01% is sufficient to ensure that the current has converged. All the above calculations were started from the same initial conditions. When calculating multiple  $I$ - $V$  points, the first  $I$ - $V$  point is calculated and then the old voltage distribution, scaled by the ratio of new to old bias voltages, is used as initial conditions for the next point. This reduces the number of iterations to less than 20 per  $I$ - $V$  point.

The numerical procedure, grid and convergence criteria have been discussed. We now turn to the calculation of some current injection profiles and compare them with the analytical formulas of the previous section.

### 3.2.3 Comparison of analytic and numerical solutions

We will continue to use the example 10  $\mu\text{m}$  diameter structure of Fig. 3.9 with a  $10 \times 4$  grid and the same sheet resistance of  $208 \Omega/\square$ . The calculated current injection profiles at a bias of 8 mA are shown in Fig. 3.12. The diode ideality factor,  $n$ , is varied from 1 to 10 so that the thermal voltage,  $V_T$ , in Eqn. (3.2) varies from 0.026 to 0.26V. As the thermal voltage is increased, the current crowding is reduced. Equations (3.11), (3.15) and (3.16) give analytic formulas for the injection current profiles. The numerical current density profiles are shown normalized to the analytic profiles in Fig. 3.13. The first observation is that the normalized profiles are fairly flat, indicating that the analytic profiles given by Eqns. (3.11) and (3.16) are good approximations. The next observation is that the value of the current density at the edge,  $J_d$ , given by Eqn. (3.15) is accurate in the current-crowded regime but underestimates the current density for more uniform injection profiles. This can be understood by considering that the analytic solution assumes that the structure is infinite. Hence, biases with decay lengths on the order of or longer than the radius will result in an underestimation of the current densities. At the center, the rapidly decreasing area results in higher current densities than predicted analytically by a one dimensional formula. Nevertheless, the analytic equations do provide a good measure of the current profiles, particularly in the case of current crowding with decay lengths much less than the device radius.

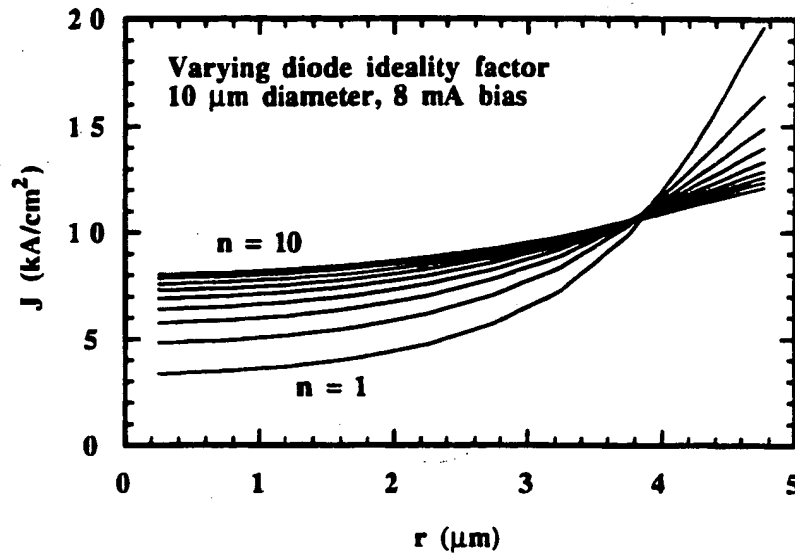


Fig. 3.12. Current density profile injected into the 10  $\mu\text{m}$  diameter diode at a bias of 8 mA. The diode ideality factor is varied from 1 to 10 in steps of 1.

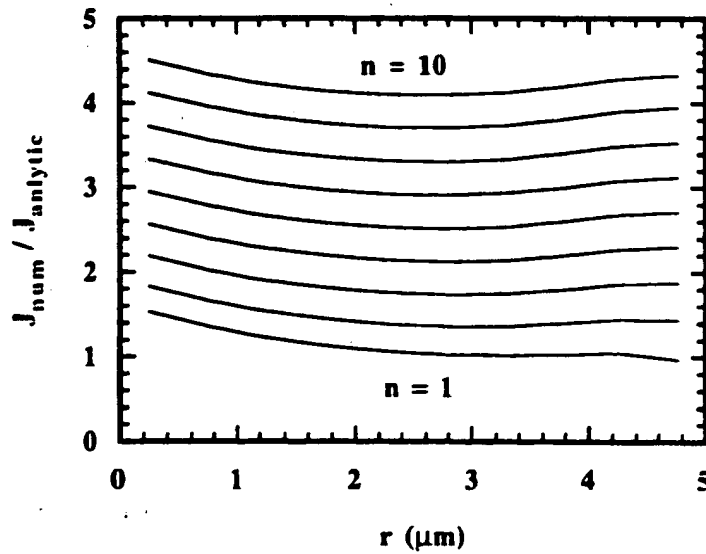


Fig. 3.13. The numerical curves of Fig. 3.12 normalized by the analytic curves calculated using Eqns (3.11), (3.15) and (3.16).

As mentioned previously, the resistive network does have an analytical solution in cylindrical coordinates. The solution is the zero<sup>th</sup> order modified (or hyperbolic) Bessel function of the first kind,  $I_0(r/\zeta_{cr})$ , where the characteristic decay length  $\zeta_{cr}$  is defined in Eqn. (3.23). The current injection profiles are independent of bias because all elements are linear. Using again the 10x4 grid and a sheet resistance of  $208 \Omega/\square$  the current injection profiles are calculated numerically and compared with the Bessel function solution. Simulations are made for leveling layer resistivities 10, 25, 50 and 100 times higher than the conductive layer. The current density profiles in Fig. 3.14 have been normalized to the average current density that would be present if the current were uniformly injected. Hence, the total current is the same for each curve.

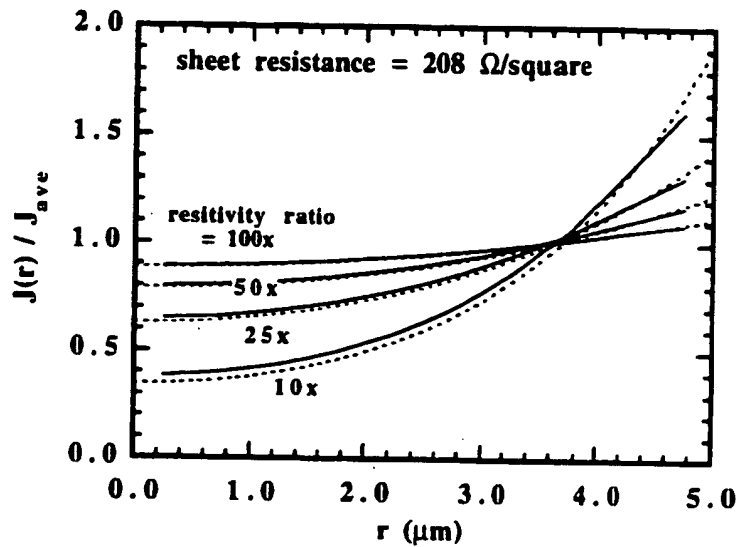


Fig. 3.14. Current density profiles for the resistive network in cylindrical coordinates. Solid lines show calculation, dashed lines show modified Bessel function solution.

The Bessel function solutions are shown as a dashed lines. The excellent agreement shows both the accuracy of the numerical model and the utility of the Bessel function solution for determine the resistive limited injection profile. The leveling resistance is also determined from the calculation. The numerically

calculated leveling resistances are 8.83, 19.8, 36.8 and  $70.2\Omega$  for the 10x, 25x, 50x and 100x leveling structures. The resistance should be higher than that of the disk if uniformly injected. Using a resistivity of  $104\Omega\mu\text{m}$ , a thickness of  $0.5\mu\text{m}$  and a radius of  $5\mu\text{m}$  gives a lower limit on the leveling resistance of 6.6, 17, 33 and  $66\Omega$ . The one dimensional formula, Eqn. (3.26), predicts leveling resistances of 10.5, 16.5, 23 and  $33\Omega$ . Thus the current leveling resistance is best estimated as the higher of the two calculations, with Eqn. (3.26) applicable for  $\zeta_{cr} < r_{act}/2$ . As decay lengths become one the order of the radius, it is better to calculate the one-dimensional resistance of the leveling layer.

Next we turn to calculating the current density profiles with and without current leveling. I will continue to use a  $10\mu\text{m}$  diameter device with the contacting configuration shown in Fig. 3.9. The diode junction is characterized as having a current density of  $1\text{kA}/\text{cm}^2$  at a bias of 2V with an ideality factor of 2. For the case of no leveling, a  $1\mu\text{m}$  thick intra-cavity layer doped p-type for a sheet resistance of  $208\Omega/\square$  is used. For the current-leveled designs, the  $0.5\mu\text{m}$  thick conductive layer is doped twice as high to maintain the same sheet resistance and optical losses of the unleveled design. The resistive leveling layer is also  $0.5\mu\text{m}$  thick, so that the total cavity thickness is constant. Simulations are made for leveling layer resistivities 10, 50 and 100 times higher than the  $104\Omega\mu\text{m}$  of the conductive layer.

The calculated current density profiles for the unleveled design are shown in Fig. 3.15. One can clearly observe the transition from uniform injection to current crowding. Up to currents of 5 mA the current injection is fairly uniform. Above that bias, however, current crowding begins. Visually, one can subtract one curve from the next to see the differential increase in the current distribution. Most of the additional current is injected in the outermost  $\mu\text{m}$  for bias currents above 13 mA. This is most clear when one remembers that the area of each annulus is proportional to the radius. For example, the area between 0 and  $3.5\mu\text{m}$  is equal to the area between  $3.5$  and  $5\mu\text{m}$ . As shown in the  $L-I$  simulations below, such current crowding will reduce the laser efficiency and promote lasing

of higher-order transverse modes. The current crowding can be reduced by introducing a current leveling layer.

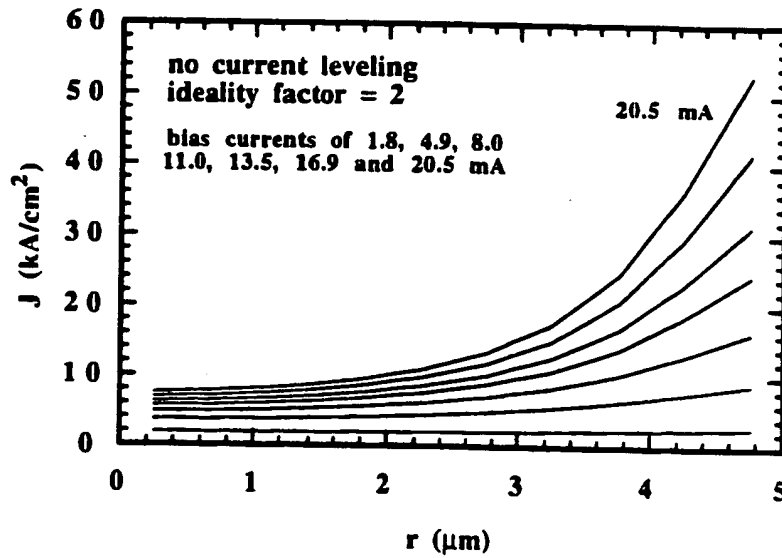


Fig. 3.15. Calculated current injection profiles for a 10  $\mu\text{m}$  diameter laser with a diode ideality factor of 2 and no current leveling.

The formula for the resistive decay length is given in Eqn. (3.23). It is equal to the product of the geometric mean of the two layers and the square root of their conductivity ratios. Thus for our example with both layer thicknesses equal to 0.5  $\mu\text{m}$ , ratios of 10x, 50x and 100x correspond to resistive-limited decay lengths of 1.6, 3.5 and 5  $\mu\text{m}$  respectively. The bias current at which the diode decay rate equals the resistive limit is given by Eqn. (3.27) and are calculated to be 9.9, 4.4 and 3.1 mA respectively. The current injection profiles in the case of no leveling, 10x and 50x ratios are plotted in Fig. 3.16 at three biases. Both current-leveled designs show significantly less current crowding than the unleveled design.



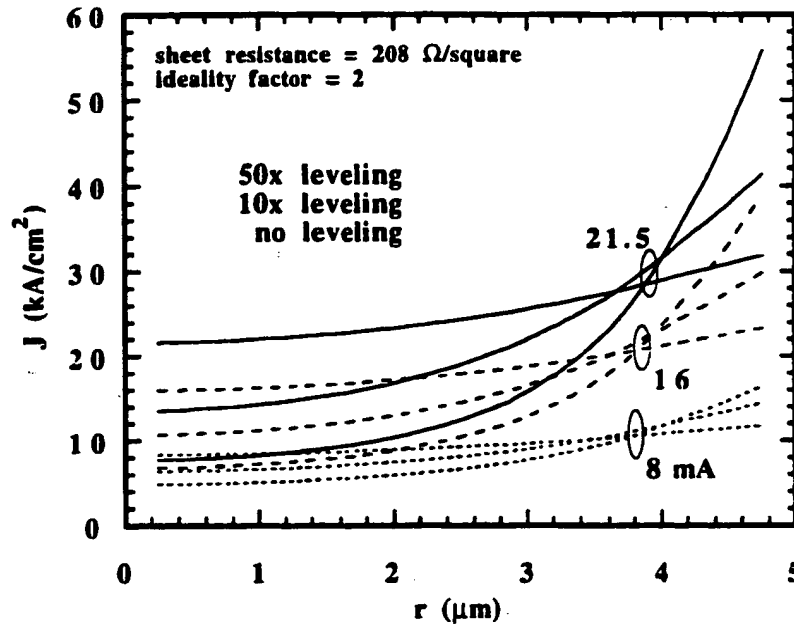


Fig. 3.16. Current injection profiles at three bias currents for three different intra-cavity designs. In all three designs the conductive layer has a sheet resistance of 208  $\Omega/\text{square}$ .

### 3.2.4 Effect of current leveling on laser performance

To determine the effect of the current crowding / current leveling on device performance, the current injection profiles are used as input to the  $L$ - $I$  model developed in Chapter 2. The same parameter set used for device structure *B* in Table 3.1 will be used except for different cavity parameters and voltages. Equation (3.33) predicts an optical loss of 0.46% for the p-type conductive layer. The optical losses for the n-type conductive layer are negligible. I will again assume that the surface scattering losses are 0.06%. Thus the total optical losses will be estimated as 0.52%. A mirror transmission of 0.80% is used to maintain the threshold gain at comparable levels. A gain offset of 10 nm is used for the room temperature cavity mode. As shown in Fig. 3.9, the injected current is allowed to diffuse out from the current constriction radius at 5  $\mu\text{m}$  to an active

region boundary, taken to be  $7.5\text{ }\mu\text{m}$ . The voltage due to an additional series resistance of  $50\Omega$ , accounting for current spreading and ohmic contacts, is added to the calculated voltage of the current injection simulation to determine the total power dissipated in the laser.

The resulting single-mode  $L$ - $I$  curves are shown in Fig. 3.17. Shown are the  $L$ - $I$  curves for no leveling (1x) and the use of current leveling layers with resistivities that are 10x, 25x, 50x and 100x more resistive, assuming that only the fundamental  $\text{HE}_{11}$  mode is above threshold.

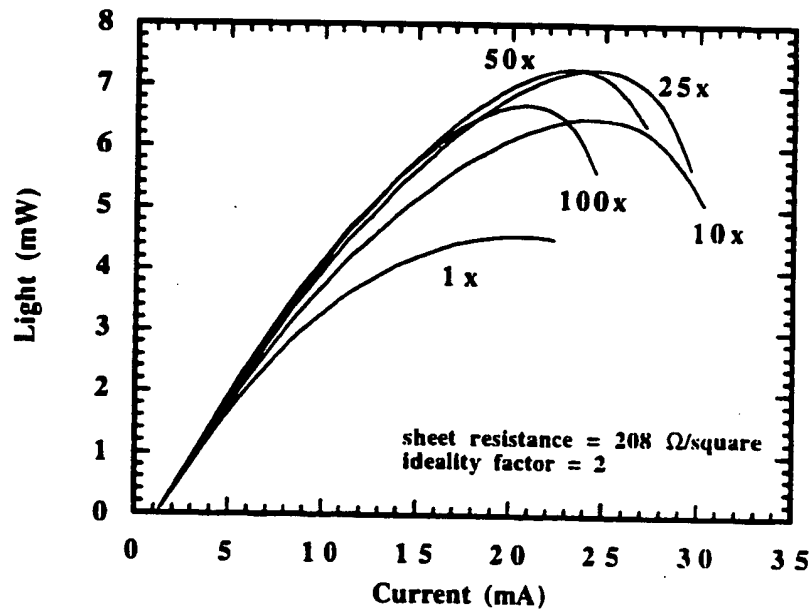


Fig. 3.17. Calculated current-to-light characteristics for intra-cavity contacted vertical cavity lasers with varying current-leveling layers.

Without current leveling, the current-to-light characteristics becomes sub-linear at powers of  $\sim 1.5\text{ mW}$  and the output power saturates at  $4.5\text{ mW}$  due to excessive current crowding. With the introduction of 10x leveling, the linearity greatly improves and output power increases to a thermally limited  $6.5\text{ mW}$ . Increasing

to 25x leveling improves the internal efficiency slightly, increasing the output power to 7.3 mW. Higher values of leveling resistance result in greater drive voltage and heating without improving the output power. Output power is not the only important feature to be considered, however.

Another important parameter is the transverse mode pattern. For many applications, single-transverse-mode operation is desirable. The diffraction angle and far-field patterns of higher-order modes are different from the fundamental's. If the transverse mode structure is varying with drive current and the coupling of the light is not perfect, random errors can be introduced which limit the bit error rate performance of the lasers.

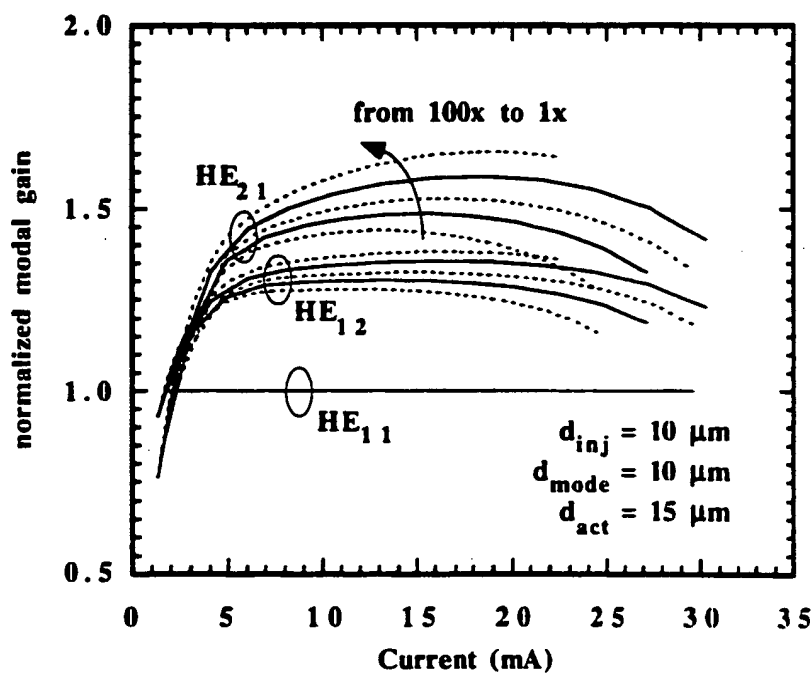


Fig. 3.18. Modal gains of the first three transverse modes during the course of the  $L-I$  curves shown in Fig. 3.17. Calculation assumes that only the fundamental  $HE_{11}$  mode is lasing.

It is desirable, then, to maintain single mode operation for communications applications. In the previous chapter, it was shown that spatial hole burning resulted in higher gains for the higher-order modes. The current crowding behavior results in a similar detrimental effect. The effect of current crowding together with spatial hole burning is shown in Fig. 3.18. The calculations correspond to the same device structures whose  $L$ - $I$  characteristics are shown in Fig. 3.17. Again, the modal gain of the lasing fundamental mode is constant for all five device structures. As before, the modal gain of the higher-order modes starts below that of the fundamental, but quickly rises above at bias currents greater than 2 mA. The modal gains are normalized to the  $(0.80) + (0.52) = 1.32\%$  round-trip threshold gain of the fundamental mode. The greater the current crowding, the greater the modal gain of the higher-order modes. The  $10\times$  curves (short dashed lines) are very similar to the uniform injection case shown in Fig. 3.22. The unleveled  $1\times$  case results in modal gains 65% higher than the fundamentals. Thus it will be very difficult to introduce sufficient mode selective loss to suppress multiple transverse mode operation in an intra-cavity contacted structure without current leveling.

The intra-cavity contacted lasers fabricated in this work used a  $10\times$  leveling layer. Their characteristics are described in Chapter 5. In order to observe the current crowding effect, laser diameters of 5, 7, 10 and 15  $\mu\text{m}$  were fabricated. Only the smallest laser has single-mode operation. The 7  $\mu\text{m}$  laser has a side mode suppression ratio (MSR) of 16 dB, while typical 8  $\mu\text{m}$  etched pillar structures have exhibited MSRs of 30 dB or more. This is an indication of the current crowding effect. The 15  $\mu\text{m}$  laser shows multiple transverse mode operation throughout its  $L$ - $I$  curve, indicating that the current crowding effects are strong as expected for such a large diameter. The active-region  $J$ - $V$  characteristics were measured on test structures as shown in Fig. E.4 of Appendix E. The drive voltage was greatly improved, and yet the characteristics are far from ideal. Even after subtracting the series resistance, the diodes are characterized by an ideality factor of 10! This results in drive voltages and series resistance much higher than one would expect theoretically. At the same time,

the onset of current crowding occurs at much higher biases. Pulsed  $L-I$  characteristics will be shown in chapter 6 which show these effects. As the active-region properties are improved, reducing the drive voltage and associated heating, the current-leveled designs will become more important to the laser performance. Simulations of the experimental lasers using the models presented in Chapters 2 and 3 will be presented in Chapter 6 along with the predicted performance of improved designs.

In summary, analytical and numerical models have been presented which assist in the design and analysis of intra-cavity contacted structures. An analytical analysis of the current crowded and current-leveled designs was presented for a one dimensional geometry. This allowed the tradeoff of optical loss, device resistance and non-uniform injection to be quantified in terms of the device design. A more accurate numerical model was then developed and applied to various designs, showing the effect of current leveling on laser performance and transverse mode operation. Together with the current-to-light model of Chapter 2, the current injection model presented here allows a comprehensive analysis of intra-cavity contacted vertical-cavity laser designs.

### References

1. B.J. Thibeault, J.W. Scott, *et al.*, "Integrable InGaAs/GaAs vertical-cavity surface-emitting lasers." *Electronics Letters*. **29** (25) p. 2197-9. (1993)
2. J.W. Scott, B.J. Thibeault, D.B. Young, and L.A. Coldren. "High Efficiency Sub-Milliamp Vertical-cavity lasers With Intra-Cavity Contacts." *IEEE Photonics Technology Letters*. **6** (6) p. 678-680. (1994)
3. D.W. Peaceman and H.H. Rachford, *J. Soc. Indus. Appl. Math.* **3** (28). (1955)

4. D.W. Hewett, D.J. Larson, and S. Doss, "Solution of Simultaneous Partial Differential Equations Using Dynamic ADI: Solution of the Streamlined Darwin Field Equations." *Journal of Computational Physics*. **101** (1) p. 11-24. (1992)
5. J.J. Dongarra, C.B. Moler, J.R. Bunch, and G.W. Stewart. *Linpack User's Guide*. 1979, Philadelphia: SIAM.

## Chapter 4: *In-Situ* Control and Laser Fabrication

### 4.0 Chapter Overview

This chapter presents the technology developed to realize the intra-cavity contacted vertical-cavity laser. As discussed in Chapter 2, the *L-I* characteristics are sensitive to the gain offset used, requiring wavelength control to within 5 nm of design. At a wavelength of 1  $\mu\text{m}$ , the 5 nm tolerance translates to a 0.5 % accuracy in the material growth. Thus an *in-situ* white light monitor has been developed for the Molecular-Beam-Epitaxy (MBE) system to enable the required accuracy. The crystal is then fabricated into laser arrays. The multiple mesas require accurate etch depths while the lateral waveguide must be defined with smooth, vertical etching to minimize optical scattering losses. Thus an *in-situ* laser-monitored chlorine Reactive-Ion-Etch (RIE) system has been developed along with a sacrificial mask process to enable accurate reproduction of the device structure. Various processes are used to allow the formation of the two ring contacts to the intra-cavity layers and the coplanar-waveguide interconnect metal. This technology is outlined in this chapter, providing a description of the *in-situ* control and the fabrication sequences used to fabricate the lasers whose characteristics are described in detail in Chapter 5.

The chapter is divided into three sections. First, the growth control and wafer uniformity is presented, comparing the calculated and measured spectra and the final wafer characteristics. Second, the fabrication steps of device etching and current constriction formation are discussed. The result is a finished three mesa structure ready for contacts. The chapter concludes with the processes used for the p and n-type alloyed ohmic contacts, interconnect metal and passivating dielectric including the self-aligned processes used to provide a ring contact at the base of a 3  $\mu\text{m}$  tall mesa with a clear emission window.

#### 4.1 Growth Control

The laser cavity is determined by the path length between the two mirrors. Unlike all other semiconductor lasers, this short vertical cavity is defined by the epitaxial growth process. MBE growth of the cavity provides the device designer with the ability to control material properties on a scale much shorter than the optical wavelength of  $\approx 3000\text{\AA}$  in the semiconductor, impossible in the case of conventional in-plane lasers. Yet, as has been shown in Chapter 2, the lasing wavelength must be controlled to within  $\sim 0.5\%$  to provide temperature characteristics as designed. Most MBE systems specify repeatability on the order of 10%, more than order of magnitude poorer. Producing more accurate growths has been a major challenge for vertical-cavity laser crystal growers. With the techniques described below, accuracy on our systems have been improved to better than 0.3%. The initial improvements are attributed primarily to the work of Geels and Young. The white light *in-situ* control is from a collaboration of Thilbeault and myself [1], based on initial work by Chalmers [2] at Sandia.

The first improvement was to use very careful reflection high energy electron diffraction (RHEED) measurements. The RHEED spot patterns were focused on a camera, converted by a photodetector on the screen into a signal and plotted on a chart recorder. The RHEED signal oscillates with each monolayer of deposition showing a strong, well-defined diffraction pattern when the monolayer is complete. Monitoring the oscillations with time shows the growth rate. The signal dampens with growth as islands form on the surface. Closing the shutters to interrupt growth allows the surface to smooth, returning the RHEED signal to its original intensity. The measurement must be done on an unrotated wafer to keep the spot pattern constant. The effusion cells which emit the source materials have significant non-uniformity, on the order of a 15% variation across a 2 inch wafer depending on the chamber geometry. The RHEED pattern is taken from a small sample placed in the center of a wafer holder so that it can be placed consistently. Measurements of the growth rate are



performed, and then these growth rates are used to grow an AlAs/GaAs distributed Bragg reflector under rotation. Under rotation the center-to-edge thickness variation is about 3% with a parabolic dependency. The reflectivity spectrum of the mirror is measured, providing a calibration factor between the RHEED growth rates and the rotated mirror thicknesses.

Using this careful RHEED growth rate calibration, it was determined that the material flux rate from the effusion cells showed hysteresis as the cell temperature was cycled. Typically, the cell temperature is adjusted to vary the relative Ga and Al flux rates to provide different material compositions while maintaining an overall growth rate of  $\sim 1\mu\text{m/hr}$ . Instead, we use short period digital superlattices to provide varying effective compositions so that the cell temperatures are held constant. Combined with the above calibration procedure, this results in a  $\pm 1\%$  thickness variation from run to run. In the case of the Indium composition in the quantum wells, this control is sufficient. The electron and hole wavefunctions penetrate into the GaAs barriers surrounding the InGaAs wells, reducing the sensitivity of the gain peak on the Indium composition. A lower GaAs rate results in a thinner well but higher Indium composition, resulting in canceling effects of higher confinement energy and lower bandgap. The effects are additive for varying Indium content, yet still the variation is reduced. Using the QWGain program, the peak wavelength shift in the gain spectrum of a nominal  $80\text{\AA}$  thick  $\text{In}_{0.175}\text{Ga}_{0.825}\text{As}$  quantum well for varying material flux can be calculated. A 2% increase in Ga flux results in a -1.7 nm shift while a 2% increase in In flux results in a +2.0 nm shift in the peak wavelength. In either case, the spectral gain peak shifts are an order of magnitude lower than the absolute flux variation and are acceptable for vertical-cavity laser growth.

While much improved by the careful RHEED calibration and constant cell temperatures, the 61% control of flux rate results in a comparable deviation in cavity thickness and thus the 20 nm uncertainty in lasing wavelength is on the edge of usefulness, ensuring only that some part of the wafer will operate as designed. It was necessary, then, to introduce some *in-situ* control. A

modification of an *in-situ* technique introduced by Chalmers [2] was used. White light was launched into multimode fiber and passed through a fiber coupler. The light was then focused onto the wafer in the growth position using the pyrometer optical port. The reflected signal was captured by the same fiber, and the other end of the fiber coupler was connected to an optical spectrum analyzer to allow rapid determination of the reflected spectrum. The experimental setup is shown in Fig. 4.1. The pyrometer measurements use the black body infrared radiation to determine substrate temperature. The presence of infrared mirror stacks make the measurement inaccurate. Calibrations showed a wavelength shift of  $0.84\text{\AA}/^{\circ}\text{C}$ .

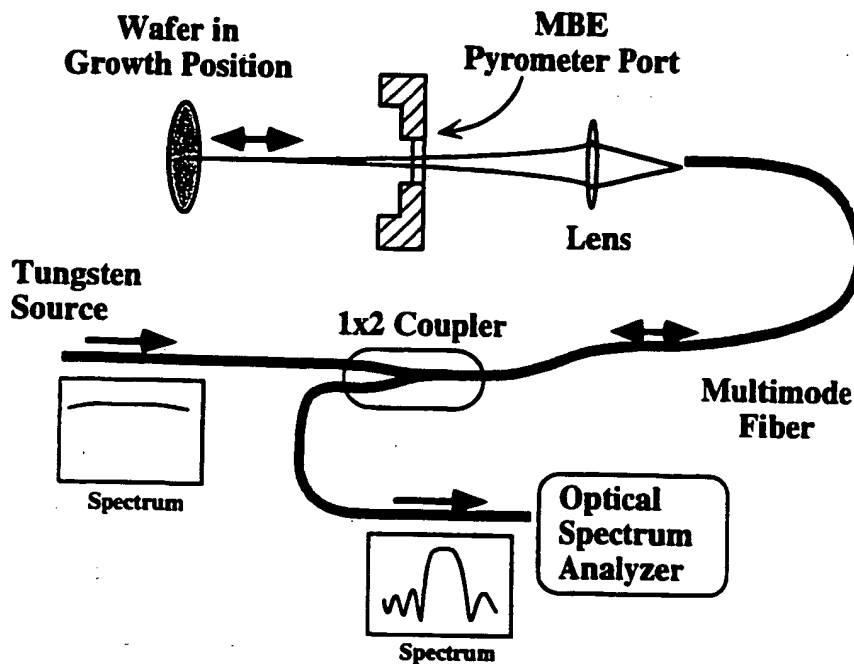


Fig. 4.1. Experimental setup used to measure the reflectivity spectrum of a wafer in the growth position. A broad-band light source is focused into a fiber, reflected off the wafer using lenses, recaptured into the fiber and measured by an optical spectrum analyzer.

Thus the sample could be cooled in the growth position to 200°C where the thermocouple was accurate, a spectrum taken and compared with calculations, and returned to growth temperatures in less than 30 minutes. This procedure was used twice during the growth of wafer 931006b, the intra-cavity wafer, to ensure accurate growth. First, the bottom 10 mirror periods were grown and then the spectrum was taken to check the growth rate. As shown in Fig. 4.2, the spectrums are shifted by 8 to 12.5 nm on the short and long wavelength sides, respectively. From the calibration, the 175°C difference would be expected to generate a 14.7 nm difference. Thus the thickness would appear to be approximately 0.5% thinner than design and certainly within tolerance. The substrate was returned to the 600°C growth temperature and the growth resumed.

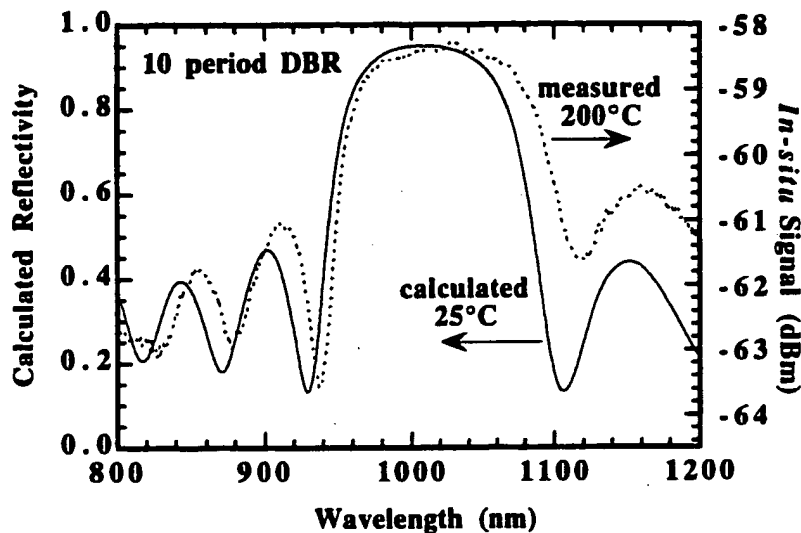


Fig. 4.2. Comparison of the *in-situ* measured and calculated reflectivity spectrum for a 10 period AlAs/Al<sub>0.1</sub>Ga<sub>0.9</sub>As distributed Bragg reflector.

Once the growth of the bottom mirror, the active region and the optical cavity were nearly finished, growth was again interrupted and the wafer cooled to 200°C. The measured shift in wavelength from design was used to check the

growth rates. By stopping the growth  $\approx 400\text{\AA}$  before the cavity was completed, adjustments could be made to increase or decrease the resonant wavelength as appropriate. In addition, the shifted resonance of the short cavity ensured that the resonance would be apparent as the quantum well absorption edge would be at much longer wavelengths. As shown in Fig. 4.3, the measured and calculated cavity modes differ by 11 nm. Including the expected shift, the wavelength was determined to be short by 3.7 nm and therefore within tolerance.

The growth was then completed, and the reflectivity spectrum was measured across the wafer. Due to rotation, the spectrum depends only on the wafer radius.

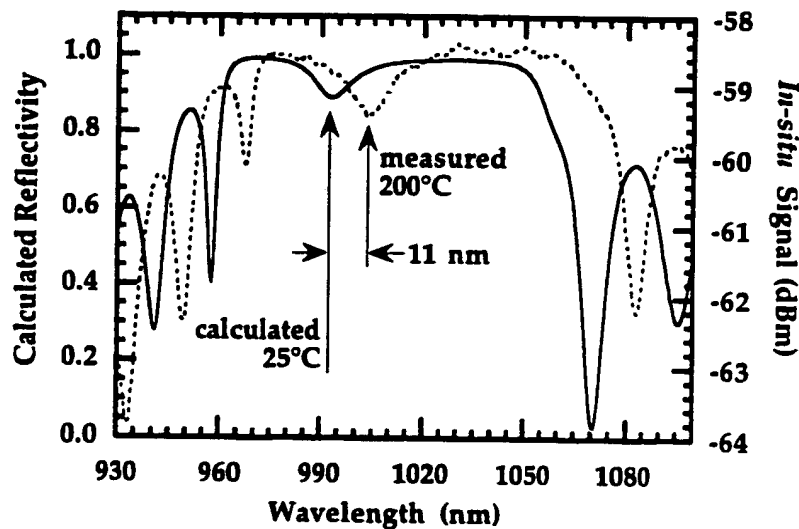


Fig. 4.3. Measured and calculated reflectivity spectrum for the bottom mirror and cavity stopped  $390\text{\AA}$  short of design thickness. Including the temperature difference, the measurement predicts that the mode will be 3.7 nm shorter than design.

In addition, a small piece was cleaved off and etched back to the cavity so that the room temperature photoluminescence spectrum could be measured without the filter of the cavity resonance. These spectra are shown in Fig. 4.4. Anticipating a room temperature photoluminescence near 975 nm, indicating a

gain peak near 980 nm, the design called for the cavity mode at 1010 nm in the center so that the gain offset would vary from 30 nm in the center to alignment at the wafer edge. This would put the majority of the wafer at ~15 nm offset and allow laser measurements for a range of gain offsets.

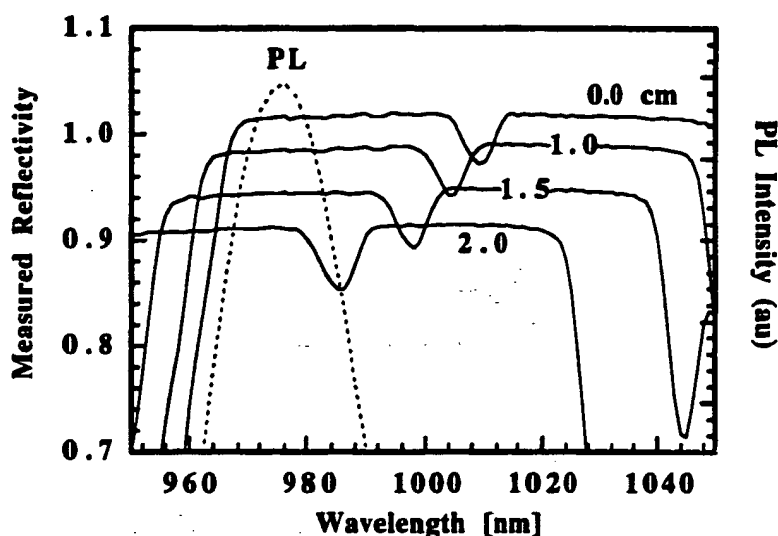


Fig. 4.4. Measured reflectivity spectra at several radii and the photoluminescence spectrum. The cavity resonances at a distance of 0, 1, 1.5 and 2 cm from center appear at 1009, 1004, 998 and 985 nm respectively while the PL peak is at 975 nm.

The measured cavity mode in the center was 1009 nm, a deviation of only 0.1% from design! As can be seen in Fig. 4.4, gain offsets have been achieved across the wafer. The cavity resonance width is broadened by the measurement resolution. The experimental characteristics of the lasers fabricated from this wafer are shown in Chapter 5. Using careful RHEED calibrations and in-situ white light monitoring, the vertical cavity can now be grown with sufficient accuracy. Subsequent growths of other vertical-cavity lasers using this technique have shown a cavity resonance reproducibility better than 3 nm, making the growth a time consuming but accurate and dependable procedure.

## 4.2 Structure Formation

Realizing an intra-cavity contacted vertical-cavity laser is a demanding fabrication challenge. Etch depths to multiple levels must be controlled to within  $0.1\text{ }\mu\text{m}$  while the total etch depths are greater than  $3\text{ }\mu\text{m}$ ! At the same time, the optical waveguide must have smooth and vertical sidewalls to avoid optical scattering even though the mirror materials alternate between GaAs and chemically reactive AlAs. The structure to be fabricated is shown in Fig. 4.5. The layers are constructed from an SEM of the epitaxial cross section. Both intra-cavity layers are contacted using alloyed contacts with  $\sim 0.5\text{ }\mu\text{m}$  thick electroplated Au interconnect metal used to minimize microwave losses in the transmission lines. Silicon nitride is used to passivate the surface and the exposed active region boundary below the p-mesa and provide structural support by filling the undercut as shown. This section focuses on the realization of the structure using a combination of dry etching and selective wet etching.

The waveguide and p-mesa are formed first using a combination of a removable Ni mask and sacrificial Si mask. I developed a solid-Si source for the E-Beam evaporator using float-zone polycrystalline Si as a source material. The silicon can be evaporated at a rate of  $2\text{--}4\text{ }\text{\AA}/\text{s}$  in a stable fashion and the thickness is monitored using a crystal oscillator. Calibrations showed that the silicon etch rate in our Cl reactive ion etcher was about 3.5 times slower than the AlGaAs materials used in the laser. Thus a deposition of a  $2850\text{ }\text{\AA}$  thick Si dot by liftoff will generate a  $1\text{ }\mu\text{m}$  thick p-mesa when etched. This two step-mesa process has been adopted by others in our lab to make other laterally contacted optoelectronic devices [3-5].

To form the center waveguide, a  $1000\text{ }\text{\AA}$  thick Ni dot is deposited by liftoff in the center of Si dot. The Ni forms an involatile NiCl surface in the etcher which is sputtered at a rate of  $\sim 20\text{ }\text{\AA}/\text{min}$ . and thus provides a very stable mask. Photoresist masks have also been used, but they become toughened by the Cl plasma making it very difficult to completely remove all traces of the organic material. After the etch, however, this Ni must be removed.

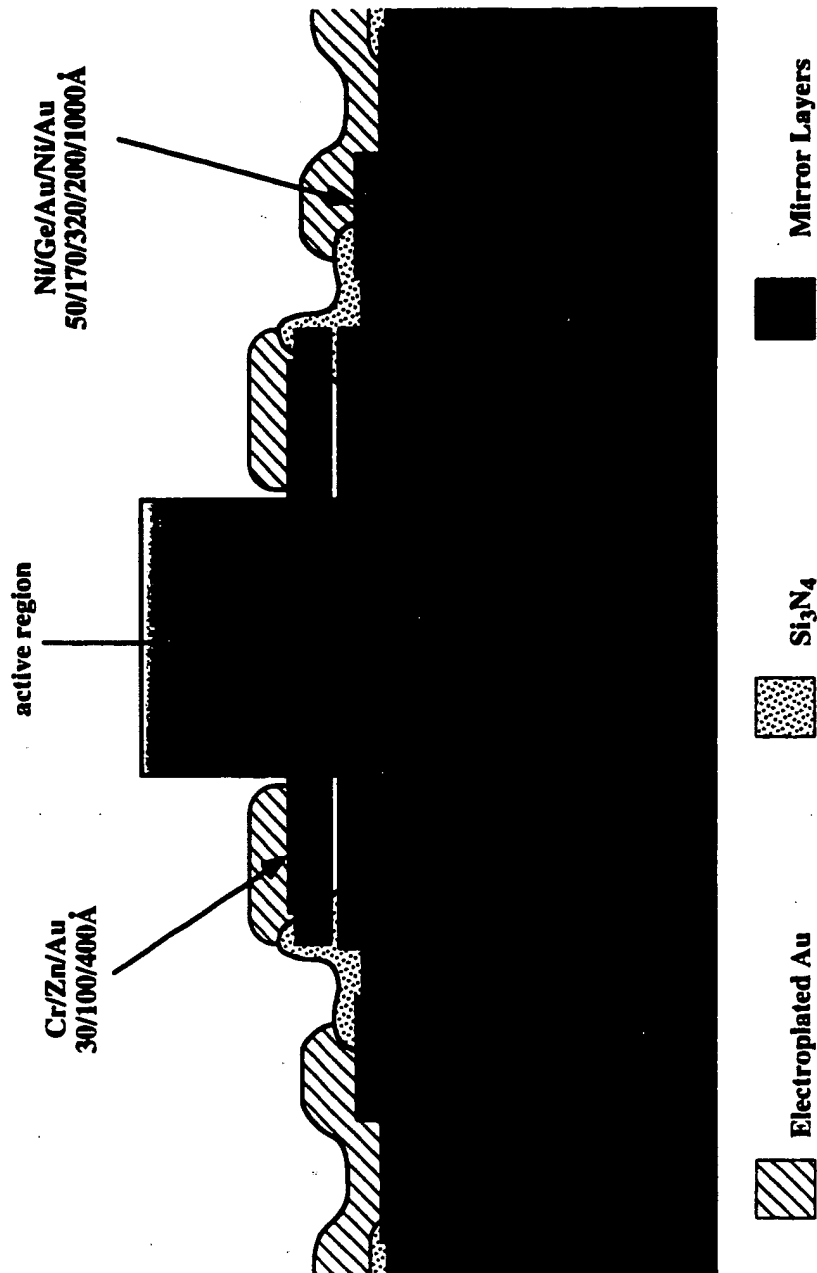


Fig. 4.5. Structure of the intra-cavity contacted vertical-cavity laser showing the epitaxial layers, the lateral waveguide, current constriction and the contact metalization.

As shown in Fig. 4.6, a layer of organic material called polydimethylglutarimide (PMGI) is placed between the Ni and the Si so that the Ni can be removed using Shipley's 1165 photoresist stripper which does not etch the AlAs layers. Like the other deep UV sensitive e-beam resists, PMGI is etched in the Cl plasma and does not leave a rough surface after RIE etch nor an impermeable scum. Its chemistry does not interact with standard positive photoresists and their developers so that a photoresist liftoff mask can be used on top of the PMGI to define the Ni dots. Thus the procedure is to deposit a Si dot by liftoff, spin on and bake PMGI, deposit a Ni dot on top of the PMGI in the center of the Si dot by liftoff and then load the sample into the Cl RIE.

The RIE system has an load lock chamber so that a base pressure below  $1 \times 10^{-6}$  torr can be achieved in less than two hours. The cathode is approximately 4 inches in diameter and is spaced 4 cm from the anode [6]. First an oxygen plasma (10mtorr, -350V bias, 50W RF power) is used to etch the PMGI leaving the Cl etch mask shown in Fig. 4.6.

Next the chamber is left to pump for ~30 min. to ensure removal of oxygen. The presence of oxygen in the Cl etch affects the etch quality differently depending on its concentration. Significant partial pressures result in oxidized Al containing materials so that the etch rate of the GaAs is higher and the etched surfaces become stratified and rough. The load lock is essential to avoid exposing the Cl coated surfaces of the chamber to water vapor which desorbs at a very low rate, requiring overnight to several days to pump down. Once a plasma is struck, however, the kinetic energy of the excited gas can release these semi-bonded gases resulting in changed etch characteristics and memory effects. Trace amounts of oxygen have a very different effect, aiding the Cl in removing GaCl and AlCl compounds on the sidewalls which normally are stable without the kinetic energy of the Cl ions. The result is a curved surface instead of vertical etching. Such a situation developed in our system where the etches were sometimes straight, sometimes curved in a sporadic fashion. Eventually we traced it down to a ZnSe sample which had been etched (actually sputtered) so that Zn was deposited on the sidewalls. Its high binding energy with oxygen



meant that each time oxygen was introduced, it would absorb onto the chamber walls and could only be removed by exciting a plasma. Thus the Cl etching of AlGaAs samples resulted in curved etch surfaces which became more vertical with successive Cl etches, only to revert to the curved etch characteristic once an O<sub>2</sub> etch was used to etch photoresist before a Cl etch. With careful monitoring of the etch rate and etch properties (etch rate was ~50% higher for the curved surfaces), we determined this memory effect and I was able to trace it back to the ZnSe sample. Wiping down the chamber with a 1:10 HCl:H<sub>2</sub>O solution removed the Zn and the six-month problem.

• Ni / PMGI / Si + O<sub>2</sub> RIE



• Cl<sub>2</sub> RIE + Ni liftoff

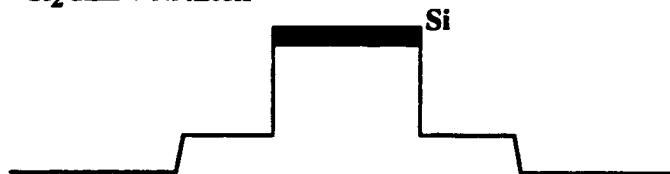


Fig. 4.6. Two mesas produced in a single reactive ion etching run using a sacrificial silicon mask and a removable nickel mask.

With sample ready as shown in the upper part of Fig. 4.6, a Cl etch (1 mtorr, -350Vbias, 50W RF power) is used to generate the two mesa structure shown in the lower part of the figure. Early in my graduate career, I introduced an *in-situ* HeNe laser monitor for the Cl reactive ion etcher. The setup is shown in Fig. 4.7. A HeNe laser is positioned to reflect its beam off of the sample and back onto a photodetector.

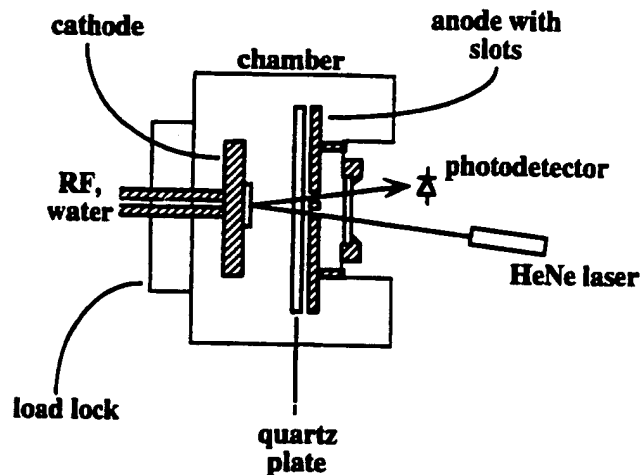


Fig. 4.7. In-situ laser monitor developed to monitor etch depths in the Cl reactive ion etcher.

A viewport in the back of the chamber and slots in the anode make it possible to place all the monitoring apparatus outside the vacuum system so that alignment is quick. Using this system, the etch depth can be controlled to less than  $1000\text{\AA}$  regardless of etch depth by simply shutting off the plasma at the desired point. The optical signal represents the interference of the reflected signal at the surface and the multiple layers below. The *in-situ* monitored signal for the intra-cavity laser etch is shown in Fig. 4.8. The lower-index AlAs is transparent to the HeNe wavelength while the higher-index GaAs is absorbing. The result is a very strong and repeatable signature which allows precise control of the etch depth. The technique has been so useful that laser monitors have subsequently been installed on most dry etching systems in our lab and have been used to make numerous devices [7-9]. To generate the plot, the photocurrent has been terminated on a  $10\text{k}\Omega$  load and the resulting voltage captured by an analog to digital card. No additional processing is required, although a very-low-pass filter makes the signal less noisy. Each mirror period is a total of  $1500\text{\AA}$  thick, so the etch rate can be determined to be  $35.6\text{ \AA/s}$ . In fact, *in-situ* monitoring is an

excellent way of determining etch rate as a function of bias, pressure, etc. A single sample can provide a wealth of data.

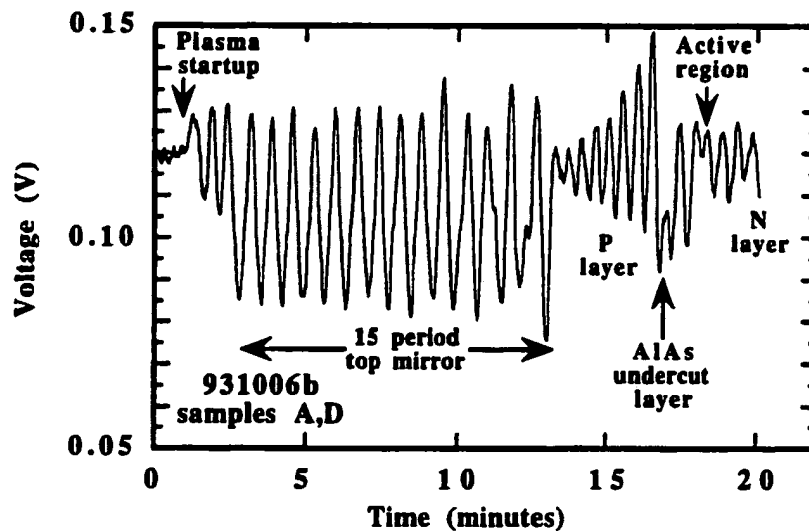


Fig. 4.8. Reflected light from the etched surface as a function of time. The various layers are indicated in the plot. Low reflectivity corresponds to AlAs, high reflectivity to GaAs.

With the waveguide formed and the p and n intra cavity surfaces exposed, the next step is to undercut the p-mesa to the edge of the waveguide as shown in Fig. 4.9. First the waveguide mesa is encapsulated with photoresist so that the

#### • Photomask and Selective Etch

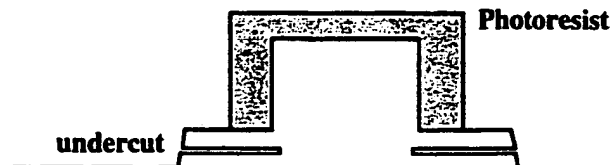


Fig. 4.9. Vertical waveguide is masked so that only the undercut layer is selectively etched.

only exposed AlAs layer is at the edge of the p-mesa. I have tried a number of selective etches and have found HCl to give repeatable results. It turns out to be very important to remove all the oxidized AlAs before using the selective etch. A strong base selectively removes the oxide without etching the unoxidized material. In addition, a short etch in a dilute, non-selective etch immediately followed by the selective etch improved the uniformity of the etch.

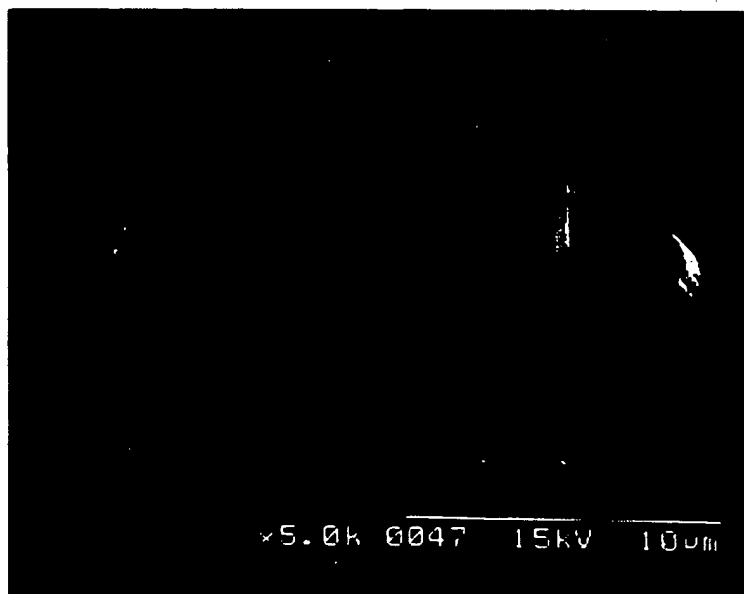


Fig. 4.10. Undercut test structures with the p-mesa but no waveguide above. The smaller mesas are 4, 6, 8 and 10  $\mu\text{m}$  in diameter while the larger mesas are 12, 14 and 16  $\mu\text{m}$ . The undercut rings on the larger structures indicate an undercut depth of 5.5  $\mu\text{m}$ .

The final procedure used was a 2 min. dip in 1:4 photoresist developer:DI followed by a 30s DI water rinse, a 10s etch in 1:1:100  $\text{H}_2\text{SO}_4\text{:H}_2\text{O}_2\text{:DI}$  directly followed by a 50s etch in 1:10  $\text{HCl:DI}$  terminated in a DI water rinse. This consistently produced a 5.0 to 5.5  $\mu\text{m}$  undercut. Test structures on the wafer allowed the determination of the amount and uniformity of the undercut as shown in Fig. 4.10. Some crystallographic dependence of the etch is apparent, resulting a more square than round undercut profile.

The photoresist mask is removed in photoresist stripper. I installed a high-frequency 13.56 MHz power supply and matching network on our parallel-plate plasma etcher to enable low-damage isotropic etching. Using this system a  $\text{CF}_4$  plasma (300mtorr, 100W, 2 min.) is used to remove the Si on top of the waveguide. An SEM of the structure is shown in Fig. 4.11. As well as the vertical waveguide walls and p-mesa, the edge of the undercut appears as a dark

ring around the periphery of the p-mesa. Also apparent are the photoresist ring on top of the p-mesa due to the slight non-selective etch and some degradation of the top edge of the waveguide. This has been minimized by using a 3/4 wave thick low-index layer on top instead of the usual 1/4-wave layer.



**Fig. 4.11** Central waveguide and p-mesa with n intra-cavity layer in field after current constricting undercut etch. Undercut appears as dark ring around p-mesa.

To complete the structure the last step is to etch the n-mesa, leaving only the undoped bottom mirror and the semi-insulating GaAs substrate in the field. This isolation is important to provide low-capacitance interconnect lines for the high speed testing. The waveguide and p-mesa are protected by photoresist using a "D" shaped mask to allow for a n-type semi-ring contact, broken by the interconnect line to the inner p-type ring contact. The n-mesa's "D" is oriented to minimize the parasitic capacitance due to the overlap of the p interconnect line and the underlying n intra-cavity layer. Microwave measurements discussed in the next chapter show the shunt capacitance to be 0.03 pF for the 7  $\mu\text{m}$  diameter

laser. The exposed n intra-cavity material is  $\text{Al}_{0.1}\text{Ga}_{0.9}\text{As}$  while the first mirror layer is AlAs. The situation is ideal for application of a selective etch. A solution of 10:1 saturated citric acid: $\text{H}_2\text{O}_2$  is used to etch the n-material and selectively stop on the AlAs [10]. The saturated citric acid is formed by combining equal parts by weight of anhydrous citric acid crystals and DI water. The etch takes about 3 minutes to complete, leaving an oxidized AlAs surface that looks green. The oxide is removed in a 30s dip in 1:10  $\text{NH}_4\text{OH}$ :DI solution. Leaving the sample in air for more than 1 hr, the remaining AlAs oxidizes so that it can also be removed. Thus the final surface is the chemically-stable low-index  $\text{Al}_{0.1}\text{Ga}_{0.9}\text{As}$  mirror layer. The photoresist is stripped off and the structure is completely formed; top reflector and vertical waveguide, undercut p intra-cavity mesa around the base and outer n intra-cavity mesa.



**Fig. 4.12.** Breakdown of the selective etch stop on AlAs in proximity to the p-n junction. The mirror layers are undoped.

Closer inspection of the flat edge of the n-mesa shows that the selective etch broke through one or two mirror layers there as shown in Fig. 4.12. These trenches only occurred at that location which is within 3 microns of the p-n junction. Even though the junction was masked with photoresist, the photo-generated voltage may have been sufficient to break down the selectivity of the citric etch. I suspect that if the etch were done in darkness the pits would not have formed, but I did not verify this hypothesis.

### 4.3 Contacts and Interconnects

With all three mesas formed, the final task is to provide ohmic contacts to the intra-cavity layers and interconnect metallization while still leaving the top surface of the central waveguide clear for light emission. First, n-ohmic contacts are deposited. Next, the surface is passivated with  $\text{Si}_3\text{N}_4$  and a window is opened around the base of the waveguide. P-ohmic metal is deposited and then the contacts are alloyed.

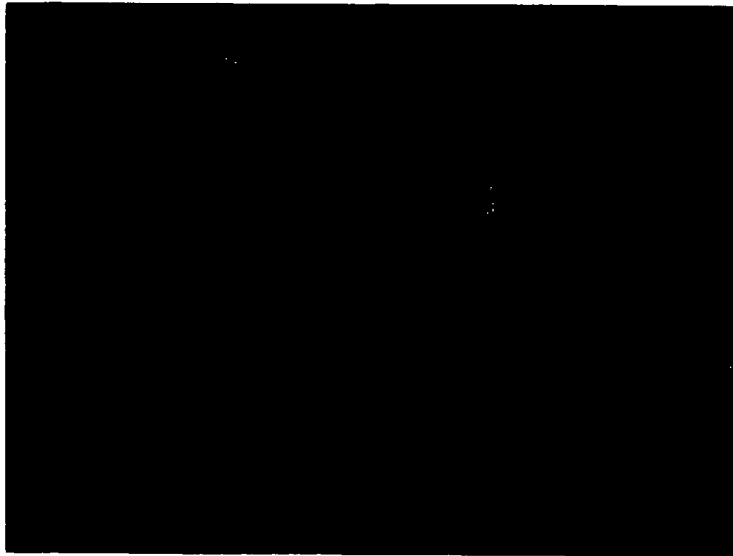


Fig. 4.13. 5  $\mu\text{m}$  diameter intra-cavity laser after n-ohmic deposition.

Interconnect metal is deposited over the entire surface and then an etch-back process is used to separate the p and n lines. This procedure is outlined below with emphasis on the more unusual self-aligned techniques.

First, n-ohmics are deposited using a two-level photoresist liftoff mask. The two level mask is formed using a lower level of Shipley 820-27 photoresist which is flood exposed with a minimal exposure. Then an upper level of AZ P4330 photoresist is spun on top. Both resists are baked on a hot plate. The two level mask is exposed and developed conventionally, the flood exposure resulting in a  $\sim 1\text{-}2\text{ }\mu\text{m}$  undercut of the upper resist. This masking scheme, introduced by G.R. Robinson, is very quick and effective. The AuGe n-ohmics are deposited by e-beam evaporation. The excess metal is lifted off in photoresist stripper, leaving the structure shown in Fig. 4.13. The n-ohmic is the horseshoe ring which steps over the edge of the "D" shaped n-mesa. Also visible on the right is the slight trench due to the breakdown of the selective n-mesa etch stop.

The next step is to coat the surface with plasma-enhanced chemical-vapor deposited silicon nitride ( $\text{Si}_3\text{N}_4$ ). Using a photoresist mask, a  $\text{CF}_4$  plasma is used to etch vias in the dielectric around the base of waveguide on the p-mesa and down to the n-ohmic as shown schematically in Fig. 4.14. The photoresist mask is then stripped. A SEM of a  $5\text{ }\mu\text{m}$  diameter laser at this stage is shown in Fig. 4.15. The lasers are now ready for p-ohmic metal, but first the top of the waveguide must be protected. This is done with e-beam evaporated silicon dioxide.

• Photomask and  $\text{CF}_4$  nitride etch

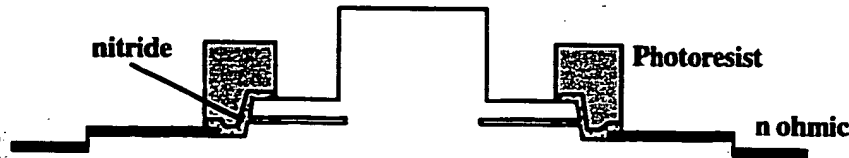


Fig. 4.14. N ohmic is deposited by e-beam, silicon nitride is deposited and vias to the n ohmic and p-mesa are dry etched by a  $\text{CF}_4$  plasma.



I use a piece of quartz rod and a fairly fast sweep of the beam (6-8 Hz) to keep the deposition fairly constant. Image-reversal photoresist is spun on, baked and patterned to open scribe streets. The reversal process is not perfect, conveniently resulting in a slight etching of the "remaining" resist so that the thin residual layer on top of the pillars is also removed. The layer is thin on top because the resist is a nominal  $1.5\text{ }\mu\text{m}$  thick while the pillars are over  $3\text{ }\mu\text{m}$  thick.  $1500\text{\AA}$  of silicon dioxide is then evaporated and lifted off in photoresist stripper. The breaks in the oxide film due to the scribe streets greatly improves the liftoff. The result is a self-aligned oxide mask protecting the tops of the pillar. Using the two-level photoresist mask, a Cr/Zn/Au p ohmic-metal is deposited on top of the p-mesa and central waveguide. The p and n-ohmics are now deposited. The dielectric via process is shown schematically in Fig. 4.15. The self-aligned p-ohmic ring contact is shown in Fig. 4.16.



**Fig. 4.15.** SEM of a  $5\text{ }\mu\text{m}$  diameter laser after vias are etched in the dielectric to the n ohmic and p-mesa surface and oxide has been deposited on top of the waveguide. The dielectric appears dark due to charging.

Given that the p intra-cavity layer has a sheet resistance of  $\sim 600\Omega/\text{square}$ , it is important to minimize the distance from the edge of the contact to the waveguide. Using this self-aligned process, the ring contact is always positioned perfectly around the base of the waveguide. Such close tolerances would be difficult to achieve using standard alignment processes

• Evaporate silicon dioxide and p ohmic

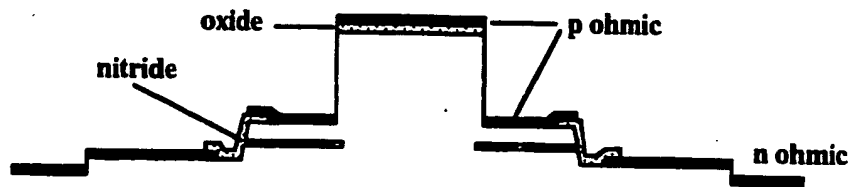


Fig. 4.16. Silicon dioxide is deposited using a self aligned process on top of the waveguide, and p-ohmic is then deposited by thermal evaporation

because of the  $4\text{ }\mu\text{m}$  tall waveguide structure. To complete the contacts the lasers are alloyed in an rapid thermal anneal at  $420^\circ\text{C}$  for 30s with a 5% hydrogen forming gas. All that remains is to form the interconnect metal and clear off the top of the waveguide.

The interconnect metal must provide a low-resistance path, both DC and RF, for the signal to reach the lasers. It must provide step coverage over the various mesas. It must provide a good surface for wire bonding as well as having good adhesion to the nitride layer in the field. These qualities were achieved using a combination of e-beam deposited Ti/Au and electroplated Au. The laser wafer was loaded into the evaporator on a  $45^\circ$  angle rotating substrate holder I built for the lab. Taking into account the geometry,  $170\text{\AA}$  of Ti for adhesion and  $3400\text{\AA}$  of Au was evaporated. The angled, rotated deposition ensures good step coverage and has become an important tool for vertical-cavity laser fabrication. Next, the wafer was unloaded and electroplated in a cyanide based gold electroplating bath using pulsed plating ( $1\mu\text{s}$  pulses, 50% duty cycle) to increase the gold thickness to  $\approx 1\mu\text{m}$ , ensuring low resistance, eliminating potential voids

at the steps and providing a softer, more porous surface for better wirebond adhesion.

The sample is now masked and etched in a cyanide-based gold etch (Transene technostrip D gold etch) which does not attack AlAs as the iodine based etchants do. Using the image reversal resist process, the tops of the waveguide are also exposed as well as the separation between lines as shown in the upper part of Fig. 4.17. The gold is wet etched down to the Ti adhesion layer. The sample is then loaded into the Cl RIE and etched for 8 min. (1 mtorr, -350V bias, 50 W RF power) which reactively removes the Ti in the field and sputters off the p-ohmic from the top of the waveguide. The Cl etch rate of the oxide ( $\approx 20\text{\AA}/\text{min.}$ ) and nitride ( $\approx 80\text{\AA}/\text{min.}$ ) are sufficiently slow to act as effective etch stops. The lasers are removed from the chamber, the photoresist stripped and the interconnects are complete.

- Evaporate and electroplate interconnect metal and mask for wet etching

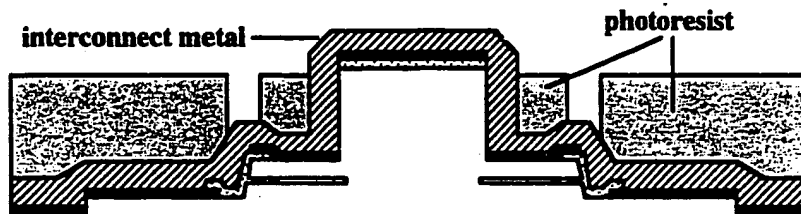
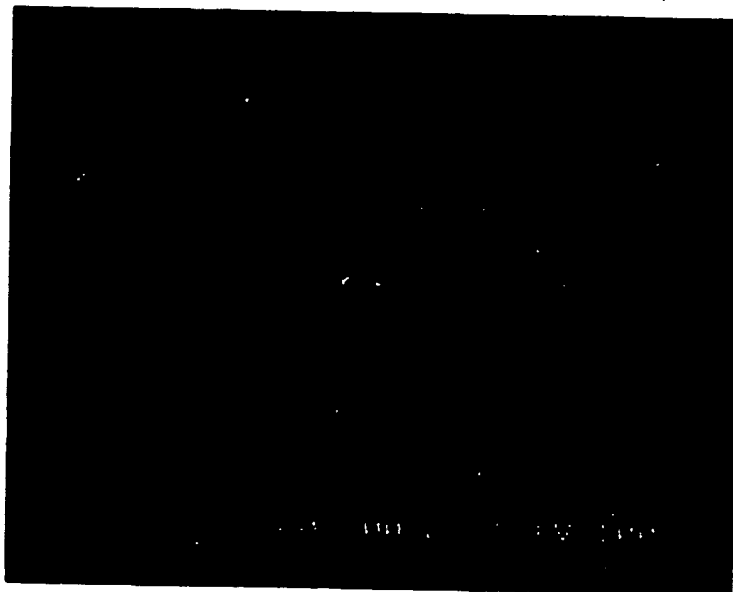


Fig. 4.17. Interconnect metal is deposited over the entire surface and then masked as shown. After etching, the p and n lines are now isolated.

The final step is to mask one last time with the image reversal resist to expose the tops of the upper mirror / vertical waveguides and then remove the oxide in a  $\text{CF}_4$  plasma. The result is the structure originally shown in Fig. 4.5. Figures 4.18, 4.19 and 4.20 show SEM images of the final devices. Shown are the high density arrays for comparison of different device diameters, a close view of a  $10\text{ }\mu\text{m}$  diameter laser and part of the  $2\times 18$  high frequency arrays. The high

density arrays allow comparison of different size devices without concern for varying material parameters such as gain offset.



**Fig. 4.18.** High density arrays of intra-cavity contacted vertical-cavity lasers. Waveguide diameters of 5, 7, 10 and 15 $\mu\text{m}$  were fabricated and are shown in the photo.

The high frequency arrays use a tapered coplanar transmission line configuration to provide a constant 50 $\Omega$  impedance transition from the probe pad spacing compatible with a microwave probe down to the devices. As well as providing a well controlled impedance, the 600  $\mu\text{m}$  long lines move the probes back so that a fiber probe can easily access the lasers. The lasers are spaced on 250  $\mu\text{m}$  centers for coupling into standard multimode fiber ribbon. Gold is left over most of the surface to provide a good ground plane for the microwave measurements discussed in the next chapter.

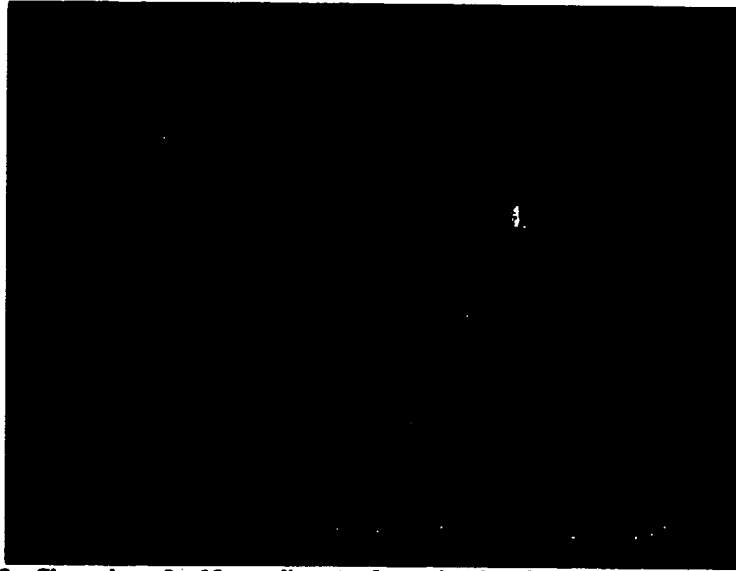


**Fig. 4.19.** Close view of a 10  $\mu\text{m}$  diameter laser showing the central p ring contact and mesa, outer n ring contact and mesa and the interconnect metal.

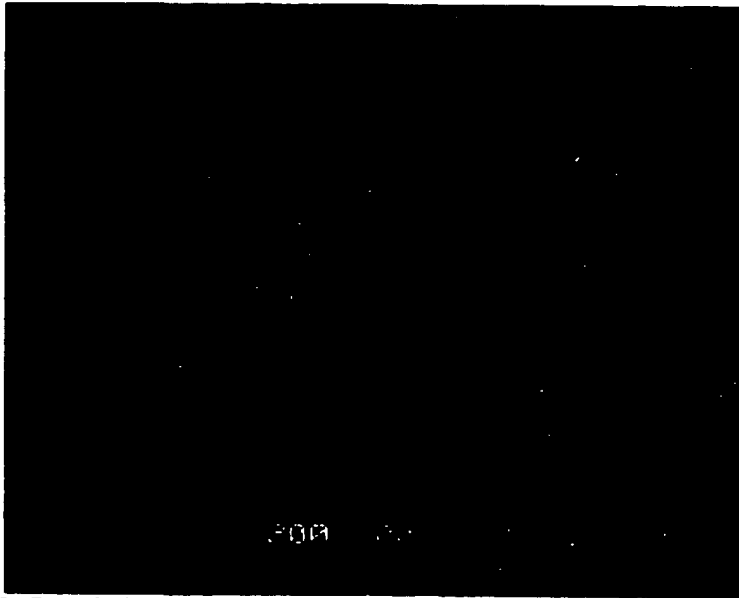


**Fig. 4.20.** Part of a high frequency laser array showing the tapered coplanar transmission lines. The coplanar lines allow rapid microwave characterization of the lasers.

### References

1. J.W. Scott, B.J. Thibeault, D.B. Young, and L.A. Coldren, "High Efficiency Sub-Milliwatt Vertical Cavity Lasers With Intra-Cavity Contacts" *IEEE Photonics Technology Letters*, **6** (6) pp. 678-680. 1994
2. S.A. Chalmers and K.P. Killeen, "Method for accurate growth of vertical-cavity surface-emitting lasers." *Applied Physics Letters*, **62** (11) pp. 1182-4. 1993
3. C.C. Barron, M. Whitehead, K.-K. Law, J.W. Scott, M.E. Heimbuch, and L.A. Coldren, "K-band operation of asymmetric Fabry-Perot modulators." *IEEE Photonics Technology Letters*, **4** (5) pp. 459-61. 1992
4. Z.M. Chuang, J.W. Scott, D.B. Young, and L.A. Coldren, "Strained InGaAs/GaAs quantum well constricted-mesa lasers and application in a vertical-twin-guide tunable laser." *IEEE Photonics Technology Letters*, **4** (4) pp. 315-18. 1992
5. B.J. Thibeault, J.W. Scott, M.G. Peters, F.H. Peters, D.B. Young, and L.A. Coldren, "Integrable InGaAs/GaAs vertical-cavity surface-emitting lasers" *Electronics Letters*, **29** (25) pp. 2197-9. 1993
6. G.A. Vawter, L.A. Coldren, J.L. Merz, and E.L. Hu, "Nonselective etching of GaAs/AlGaAs double heterostructure laser facets by  $\text{Cl}_2$  reactive ion etching in a load-locked system" *Applied Physics Lett.*, **51** (10) pp. 719-721. 1987
7. C.P. Chao, S.Y. Hu, P. Floyd, K.-K. Law, S.W. Corzine, J.L. Merz, A.C. Gossard, and L.A. Coldren, "Fabrication of low-threshold InGaAs/GaAs ridge waveguide lasers by using in situ monitored reactive ion etching." *IEEE Photonics Technology Letters*, **3** (7) pp. 585-7. 1991

8. C.P. Chao, S.Y. Hu, K.-K. Law, B. Young, J.L. Merz, and A.C. Gossard, "Low-threshold InGaAs/GaAs strained layer single quantum well lasers with simple ridge waveguide structure." *Journal of Applied Physics*, **69** (11) pp. 7892-4. 1991
9. S.Y. Hu, S.W. Corzine, K.K. Law, D.B. Young, A.C. Gossard, L.A. Coldren, and J.L. Merz, "Lateral carrier diffusion and surface recombination in InGaAs/AlGaAs quantum well ridge-waveguide lasers" *Journal of Applied Physics*, **76** (8). 1994
10. C. Juang, K.J. Kuhn, and R.B. Darling, "Selective etching of GaAs and  $\text{Al}_{0.3}\text{Ga}_{0.7}\text{As}$  with citric acid/hydrogen peroxide solutions" *J. Vac. Sci. Tech., B*, **8** (5) pp. 1122. 1990

## Chapter 5: Intra-Cavity Laser Characteristics

### 5.0 Chapter Overview

This chapter presents the measured characteristics of the intra-cavity contacted vertical-cavity lasers. First the laser structure is discussed. Next the DC characteristics such as current-to-light ( $L-I$ ), current-voltage ( $I-V$ ) and spectral measurements are shown. After a brief discussion of the lasing characteristics under pulsed operation, the focus turns to high-speed measurements. While the DC properties of vertical-cavity lasers are fairly well known, there is much less data on their high-speed properties. Using the unique configuration of these intra-cavity contacted lasers, high-speed measurements can be made on wafer. By avoiding the issues of packaging and the associated parasitics, very clean measurements are made.

The high-speed characterization begins with small-signal scattering-parameter measurements using a vector network analyzer. From the  $S_{11}$  measurements an equivalent circuit for the  $7\mu\text{m}$  laser is constructed. From the  $S_{21}$  measurements the modulation response and carrier-transport effects are determined. The  $7\mu\text{m}$  diameter laser has a 3dB bandwidth in excess of 8GHz at a bias of only 4 mA. The 3dB electrical bandwidth vs. the square-root of current above threshold is plotted for the various diameter devices. The slope of the plot yields the Modulation Current Efficiency Factor (MCEF) and is shown to agree with theory. The  $7\mu\text{m}$  diameter laser has a very high value of  $5.7\text{ GHz}/\sqrt{\text{mA}}$ , higher than any in-plane laser reported to date. Achieving a high MCEF is particularly important for high-speed low-power applications such as parallel optical interconnects, a very promising area for vertical-cavity lasers.

Large-signal modulation of the lasers is then used for Gigabit/s digital-data transmission, verifying their suitability for such applications. Taking advantage of the unique configuration of these lasers, on-wafer high-speed Bit Error Rate (BER) measurements are made for the first time. The BER measurements of varying-diameter laser arrays show that all the lasers are capable of data



transmission at 3Gbit/s, the maximum rate of the test equipment, with no error floor. Perhaps one of the most interesting applications for vertical-cavity lasers is for low cost, high-speed parallel data links. One promising application is to extend computer buses off the board using multimode graded-index fiber arrays. Sixty four electrical channels operating at 100MHz could be multiplexed up to 8 channels at 1.6 Gbit/s with commercial GaAs circuits and then transmitted in parallel using the laser arrays, making maximum use of the optical links while avoiding complicated microwave circuits. Such a link has an aggregate data rate in excess of 13 Gigabit/s! For such applications it would be desirable to use simple on/off modulation of the lasers to minimize the complexity of the driver and receiver circuits. Thus further measurements are made at 1.6 Gbit/s on the submilliamp 7  $\mu\text{m}$  lasers under full on/off current-modulation conditions. The sensitivity of the BER performance is determined due to variations between devices and variation of substrate temperature. The laser arrays show remarkable uniformity, indicating no unusual or detrimental response under large-signal modulation.

### 5.1 Device Structure

To generate an intra-cavity structure, one starts with the conventional vertical-cavity laser design as discussed in Appendix D and inserts additional layers that are multiples of half wavelengths. P-type and n-type layers on either side of the active region provide an electrical path for the current to reach the active region from the ring contacts as shown in Fig. 5.1. A current constriction must be formed to force the current into the optical mode. This current-blocking layer can be formed by ion implantation, diffusion, selective oxidation or a simple selective wet etch as was used here. Even with a current constriction, there is concern that the current will crowd near the periphery of the device where the optical mode is weak, resulting in spatial hole burning effects and poor device efficiency. These current crowding effects have been minimized by the introduction of a resistive layer as discussed in Chapter 3. The resistive layer limits the current crowding, effectively acting to diffuse the injected current.

The layer structure and doping are shown in Fig. 5.2. The active region is formed from three  $80\text{\AA}$   $\text{In}_{0.2}\text{Ga}_{0.8}\text{As}$  quantum wells with  $80\text{\AA}$  GaAs barriers. On either side are  $100\text{\AA}$  GaAs smoothing layers before the carrier confinement layers. Below the active region is a  $\text{Al}_{0.25}\text{Ga}_{0.75}\text{As}$  n-type confinement layer followed by a  $1.25\lambda$   $\text{Al}_{0.1}\text{Ga}_{0.9}\text{As}$  n-type intra-cavity contact layer. Above the active region is an  $\text{Al}_{0.5}\text{Ga}_{0.5}\text{As}$  p-type confinement layer, a  $0.25\lambda$  AlAs current constriction layer and a  $2.25\lambda$   $\text{Al}_{0.1}\text{Ga}_{0.9}\text{As}$  p-type intra-cavity contact layer.

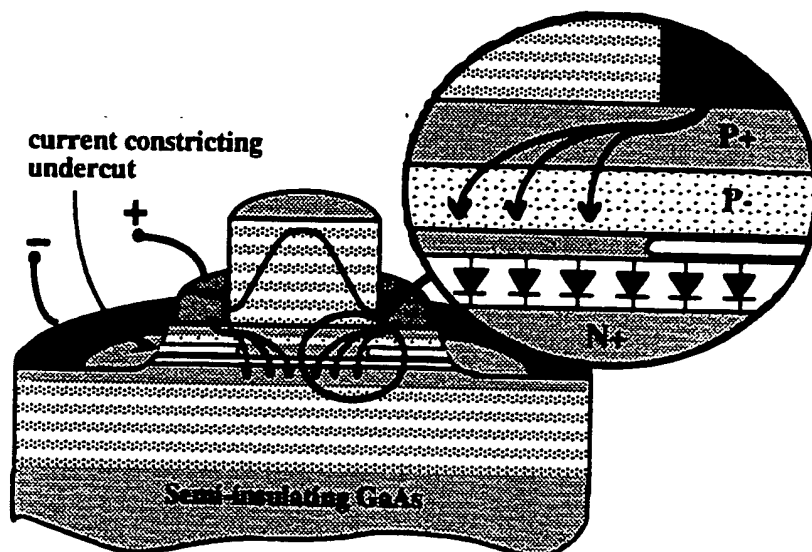


Fig. 5.1. Schematic of the intra-cavity contacted vertical-cavity laser. Both contacts and emission are from the top surface. The substrate is semi-insulating GaAs and both epitaxial mirrors are undoped. A current constriction etch is used to avoid shunt current paths. A resistive layer has been introduced in the cavity to limit current crowding.

A selective wet etch is used to etch the current constriction layer to force the current into the optical waveguide. The p-type intra-cavity contact layer consists of a  $1\lambda$  thick p- layer below a  $1.25\lambda$  thick p+ layer. The DBR mirror layers are formed from AlAs/ $\text{Al}_{0.1}\text{Ga}_{0.9}\text{As}$  pairs, each layer  $1/4$  optical wave thick. The lower mirror consists of 28.5 periods while the upper mirror consists of 15 periods. The center wavelength of the reflectors and cavity mode are designed

for 1010 nm to provide a 20 nm offset from the gain peak on the majority of the wafer.  $\text{Al}_{0.1}\text{Ga}_{0.9}\text{As}$  is used instead of GaAs to allow efficient optical pumping of the laser in other experiments.

Along with the layer structure, Fig. 5.2 shows the doping profile as shaded regions. The dopants are set back 500 Å from either side of the active region. The n+ Si doping density is  $2 \times 10^{18} \text{ cm}^{-3}$ . The Al content on the n side is kept below 30% to avoid DX center compensation [1]. Earlier devices with 50% Al content had exhibited drive voltages 2V higher than these devices due to space-charge buildup in unintended intrinsic regions.

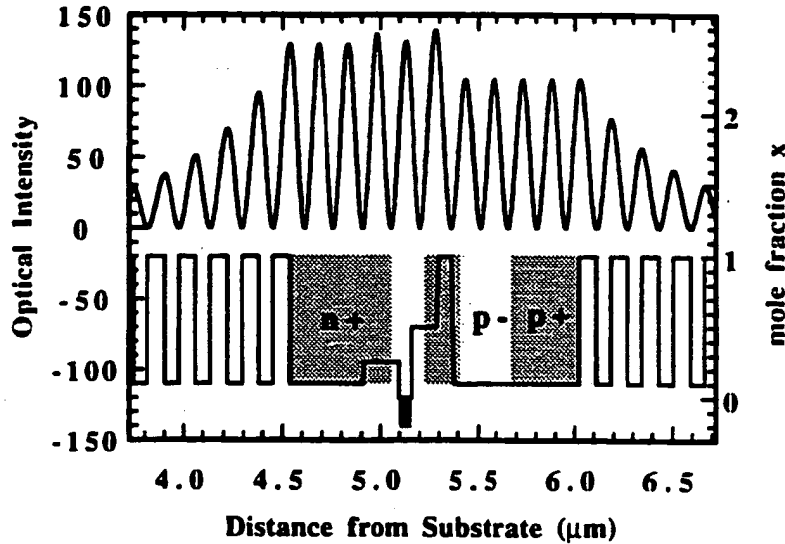


Fig. 5.2. Detail of the cavity design. Shown are the axial standing wave pattern, the material composition and doping as a function of position. Positive mole fractions are for  $\text{Al}_x\text{Ga}_{1-x}\text{As}$  while the absolute value of negative mole fractions indicate  $\text{In}_x\text{Ga}_{1-x}\text{As}$ .

The p dopant used is Be. The heavily shaded p+ doping density is  $4 \times 10^{18} \text{ cm}^{-3}$  while the lightly doped p- was  $2 \times 10^{17} \text{ cm}^{-3}$ . The p+ layer is used to distribute the current while the p- layer acts to diffuse the injected current to reduce current crowding. The design and analysis of this current-leveling structure has been

discussed in Chapter 3. All doped heterointerfaces used a parabolic grading to minimize the barrier to majority carrier flow [2]. The DBR mirrors and substrate are undoped. The entire vertical-cavity laser structure, grown by B. J. Tibault, is on a semi-insulating substrate.

The calculated longitudinal standing wave pattern, normalized to the field emitting from the top surface, is also shown in Fig. 5.2. The optical losses are presumed to be dominated by free-carrier losses, taken to be  $5 \text{ cm}^{-1}$  per  $10^{18} \text{ cm}^{-3}$  for electrons and  $11.5 \text{ cm}^{-1}$  per  $10^{18} \text{ cm}^{-3}$  for holes. The threshold gain, determined using a transmission matrix approach, is predicted to be  $1500 \text{ cm}^{-1}$  or equivalently a round trip gain of 1.32%. The relative standing wave amplitude at the quantum wells of 131 yields an effective transmission coefficient of 0.87% for the upper surface. The amplitude in the substrate is 0.016, yielding an effective bottom transmission coefficient of 0.014%. The optical efficiency, defined as the fraction of photons generated that escape the device, is thus calculated to be 0.66. Assuming an internal efficiency of 0.8, a typical value in our experience, the expected external quantum efficiency is 52%. The modeling in Chapter 2 shows, however, that limited optical overlap with carriers injected near the periphery of the device leads to additional losses. The measured external differential efficiency of 46% indicates that the optical modeling is effective in predicting the device performance.

Lasers with four waveguide diameters were fabricated: 5, 7, 10 and 15  $\mu\text{m}$ . As shown at the end of Chapter 4, the lasers are fabricated into two kinds of arrays. In the high-density arrays, all four sizes are repeated in close proximity to allow direct comparison between devices. Although the lasers are high-speed devices, the probe pad configuration is not suited to high-speed testing. The high-speed configuration uses  $2 \times 18$  arrays of a single diameter laser on  $250 \mu\text{m}$  centers. This makes them suitable for coupling into standard multimode ribbon-fiber arrays. In addition, each laser is accessed using a  $600 \mu\text{m}$  long tapered coplanar transmission line to make the transition from the two ring contacts to  $75 \mu\text{m}$  pitch, ground-signal-ground probe pads compatible with a high-frequency electrical probe. The transmission lines provide both controlled electrical

connections and remove the probe from the lasers, making the fiber access more convenient. Replicas of the transmission lines in the diagnostic die are terminated in open, short and resistive loads so that the electrical properties of the lines can be accurately measured. They are very well characterized as  $55\Omega$  transmission lines, the slightly higher impedance than design a result of the reduced line thickness during the interconnect metal etch back process. In the following sections, the DC and pulsed measurements are made on the high-density arrays. The microwave and digital measurements are made on the high-frequency arrays. The measurements show the advantages of the laser structure and indicate the directions for future improvement.

## 5.2 CW Characteristics

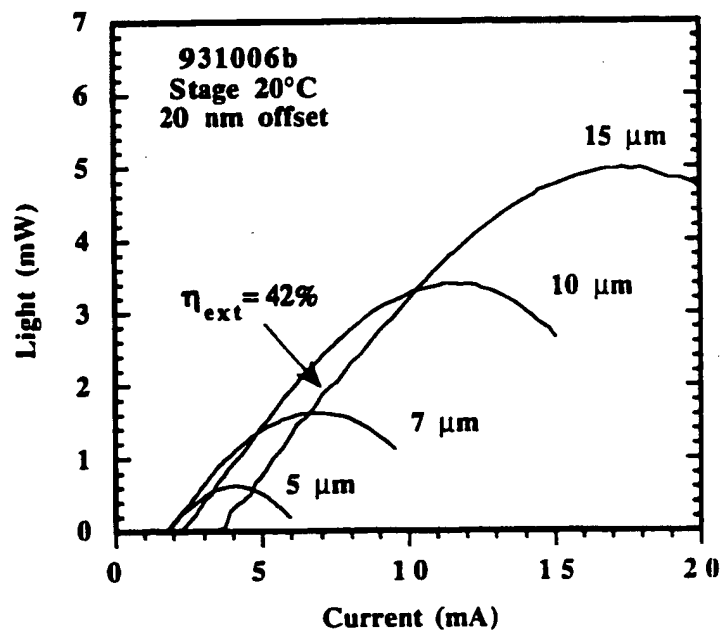


Fig. 5.3. Comparison of the four laser diameters for a cavity mode 20 nm longer than the photoluminescence peak.

Two high-density arrays were characterized. One had a 25 nm offset from the room temperature photoluminescence (PL) peak while the other had a 15 nm offset. The threshold current is notably higher for the larger gain-offset devices. Both lasers have very linear  $L-I$  characteristics, showing little non-linearity due to current crowding. The 10 nm offset lasers have excellent characteristics. The 5 and 7  $\mu\text{m}$  diameter lasers have sub-milliamp threshold currents. The measured threshold currents were 0.76, 0.72, 0.99 and 1.8 mA for the 5, 7, 10 and 15  $\mu\text{m}$  diameter devices respectively. The maximum output powers are 1, 2, 1, 3.7 and 6 mW while the differential efficiencies are 31, 38, 43 and 46% respectively.

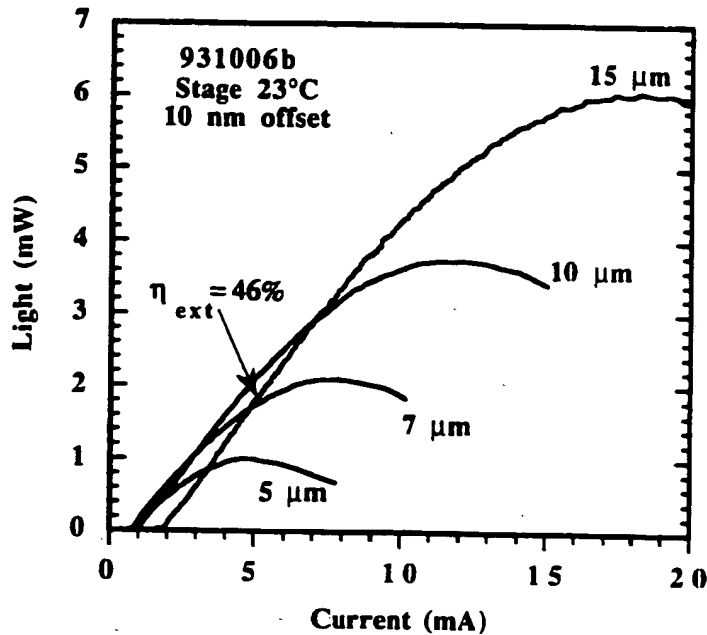


Fig. 5.4. Comparison of the four laser diameters for a cavity mode 10 nm longer than the photoluminescence peak.

The variation in external efficiency indicates that the size dependent losses are significant. This is not surprising given the large number of processing steps during which the waveguide sidewalls were exposed. One would expect that the

higher-order transverse modes would be suppressed in the smaller devices and this is indeed the case. The  $I$ - $V$  characteristics of the four device sizes are shown in Fig. 5.5. The lasers had operating voltages between three and four volts for most of the  $L$ - $I$  curve. Given that the photon energy is 1.24 eV, this indicates that there is significant room for improvement. As discussed at the end of Appendix E, the active region's resistance properties are shown to be far from optimized. In better optimized devices, the drive voltage should be nearly half of the present value. This alone should result in a doubling of the thermally limited output power. Also indicated are the voltages and differential resistance at peak power.

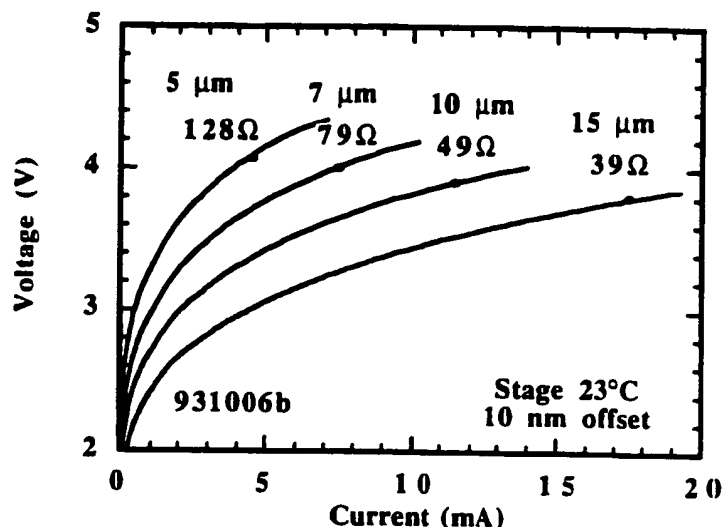


Fig. 5.5. Comparison of the  $I$ - $V$  characteristics for the four laser diameters.

The differential resistance numbers are somewhat misleading due to the thermally reduced drive voltages across the active region. It would be better to consider pulsed measurements to determine the true series resistance. This will be done later in this chapter.

The power conversion efficiencies of the 10 nm offset lasers are shown in Fig. 5.6 with maximum values of 6.5, 10, 12 and 12.8% respectively. Most importantly, the maximum efficiencies are achieved at very low power levels.

For example, at a 3 mA bias the 7  $\mu\text{m}$  laser produces 1 mW of optical power at an input power of only 10 mW. These high efficiencies at low power levels are essential for high-density interconnect applications. While the performance is quite good, they could be much better. If the drive voltages were halved the efficiency would double.

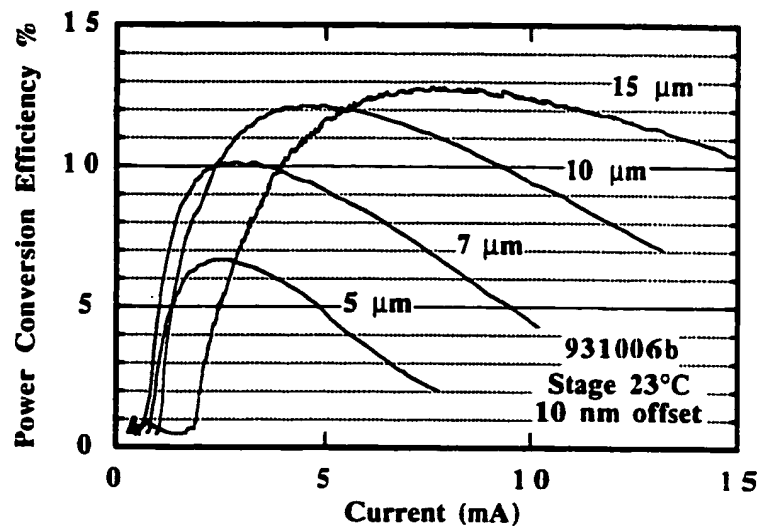


Fig. 5.6. Power conversion efficiency of the four devices. The 7  $\mu\text{m}$  diameter device reaches a 10% conversion efficiency at a drive current of only 2.5 mA.

The device physics is shown in greater detail when the  $L-I$  curves are scaled by the device area as shown in Fig. 5.7. One striking feature is the high current densities, particularly in the smaller diameters. Another interesting feature is that the smaller devices achieve higher maximum optical intensities. This is due to the better heat dissipation *per unit area* of the smaller devices as they approach a more ideal point source with a three-dimensional heat flow. The inset shows the detail near threshold. The threshold current densities are 4.7, 2.1, 1.4 and 1.1  $\text{kA}/\text{cm}^2$  for the 5, 7, 10 and 15  $\mu\text{m}$  diameter lasers respectively. The threshold current density for the 5  $\mu\text{m}$  device is notably higher, another indication



that the optical losses are significantly higher for this very-small -diameter device and that the quantum wells are being driven to very high gain levels.

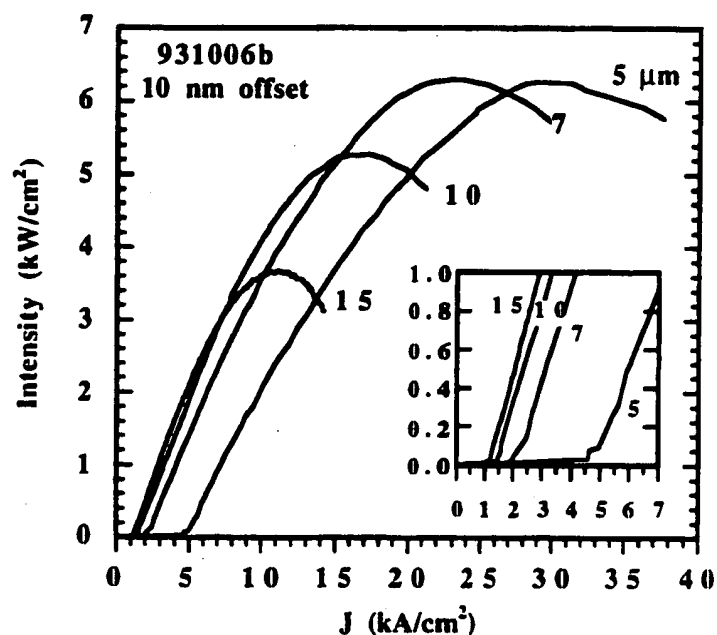


Fig. 5.7.  $L$ - $I$  curves of Fig. 5.4 scaled with area assuming the diameter is  $0.5 \mu\text{m}$  less than the waveguide dimension due to the undercut etch. Inset shows the detail near threshold.

The optical spectrum of the lasers at various bias currents was measured using an Anritsu Optical Spectrum Analyzer with a  $0.1 \text{ nm}$  resolution. The measured spectra for the four device sizes are shown in Fig. 5.8. Each plot has a  $60\text{dB}$  vertical scale and a  $12 \text{ nm}$  horizontal scale. Due to heating, the spectrum shifts to longer wavelengths with increasing bias. While the short cavity forces a single axial-mode pattern, there are many possible transverse modes. The higher-order transverse modes occur on the short wavelength side of the fundamental mode.

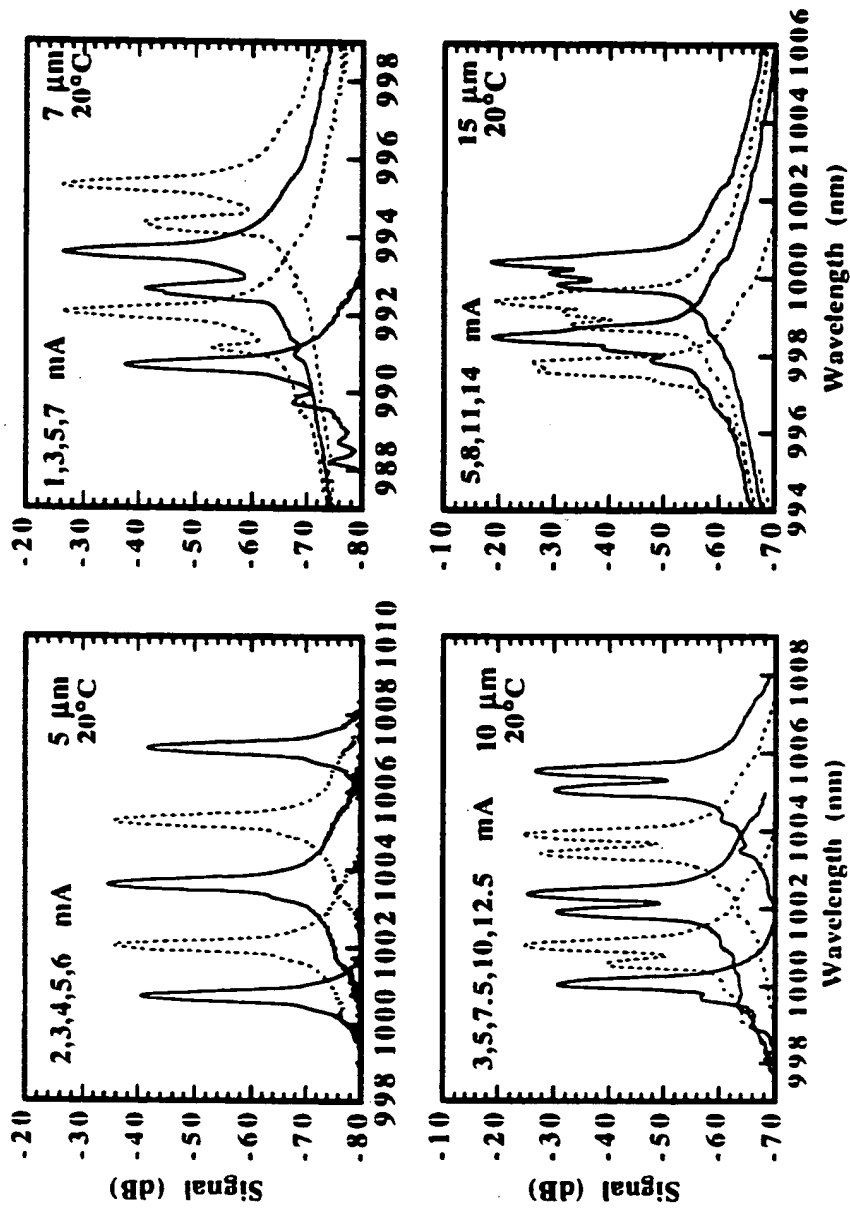


Fig. 5.8. Measured CW spectra of the four lasers during the course of the I-I curve

As can be seen in the figure, the lasers' transverse-mode properties vary from single-mode to multimode. As the cavity diameter gets wider, the mode spacing becomes less, varying from a 2.0 nm spacing for the 5  $\mu\text{m}$  diameter lasers to 0.19 nm for the 15  $\mu\text{m}$  laser. As discussed in Chapter 2, the higher scattering and diffraction losses of the smaller devices provide a mode discrimination so that they lase in a single transverse mode. The Mode Suppression Ratio (MSR) of the 5  $\mu\text{m}$  laser is 41dB while the 7  $\mu\text{m}$  has an MSR of 15 dB. The 10  $\mu\text{m}$  laser starts with a single transverse mode but, due to spatial hole burning, a second-order mode lases at power levels above 1.5 mW. The two competing modes result in a far-field pattern which shifts between two lobes and a single lobe. The 15  $\mu\text{m}$  laser begins lasing in a two lobe far field pattern, and evolves into a four lobe "clover" pattern at higher power levels. A current apertured design, as analyzed in Chapter 6, could be used to allow higher single mode powers if desirable.

The spectrum in Fig. 5.8 can also be used to estimate the lasers' thermal impedance. To determine the shift in wavelength with temperature, a 7  $\mu\text{m}$  laser was held at a constant bias while the stage temperature was varied. As shown in Fig. 5.9, the slope  $d\lambda/dT$  is a constant  $0.73 \text{ \AA}/^\circ\text{C}$ . The lasing wavelength shift of the four devices as a function of dissipated power is shown on the left in Fig. 5.10. The data points are from the spectra shown in Fig. 5.8 while the solid lines are the curve fits. The slopes are 3.32, 1.94, 1.44 and  $0.83 \text{ \AA}/\text{mW}$ . Dividing by the measured  $d\lambda/dT$  gives thermal impedances of 4.53, 2.65, 1.96 and  $1.13 \text{ }^\circ\text{C}/\text{mW}$  for the 5, 7, 10 and 15  $\mu\text{m}$  diameter lasers respectively. The mode separation can be used to accurately determine the waveguide diameter. From the wavelength spacing between the fundamental and the next higher transverse mode of 2.0, 0.92, 0.49 and 0.19 nm, the waveguide diameters are calculated to be 4.4, 6.6, 9.2 and 14.8  $\mu\text{m}$  respectively. Using these calculated diameters, the thermal impedances are plotted vs. the inverse radius to compare with the simple formula for thermal impedance, Eqn. (3.23). As shown on the right in Fig. 5.10, the agreement is quite good using an effective thermal conductivity of  $0.038 \text{ mW}/^\circ\text{C}\mu\text{m}$ .

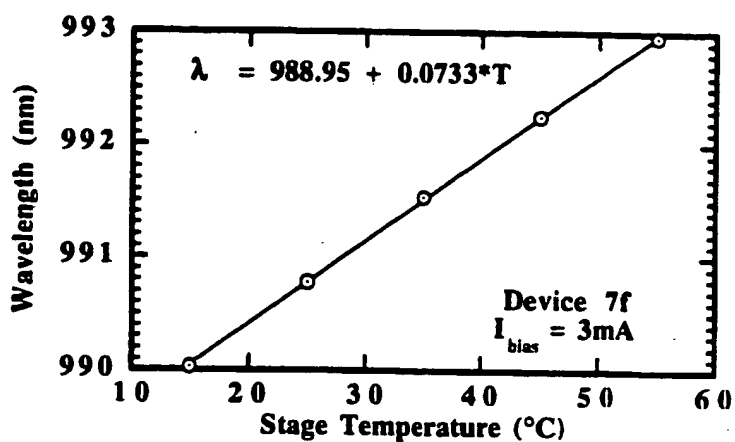


Fig. 5.9. Lasing wavelength of the 7 μm laser as a function of stage temperature.

The effective thermal conductivity of the mirror layers can be approximated by the geometric mean of the high and low index materials.

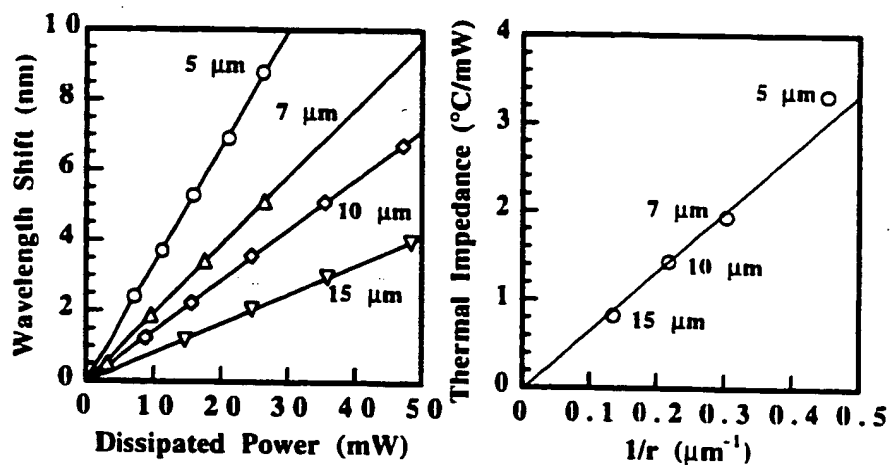


Fig. 5.10. Graphical calculation of the effective thermal conductivity based on the spectral measurements shown in Fig. 5.8. On the left are the thermally driven wavelength shifts, on the right is the corresponding thermal impedances.

As shown in Fig. 5.2, the mirror layers were made from  $\text{Al}_{0.1}\text{Ga}_{0.9}\text{As}$  and  $\text{AlAs}$  so that the only GaAs in the laser was the barriers cladding the quantum wells. This design makes it fairly easy to achieve efficient optical pumping of the structure. Unfortunately, the use of the ternary  $\text{Al}_{0.1}\text{Ga}_{0.9}\text{As}$  significantly increases the thermal impedance. Using Eqn. (E.1) of Appendix E, the thermal conductivities are calculated to be 0.091 for  $\text{AlAs}$  and 0.014 for  $\text{Al}_{0.1}\text{Ga}_{0.9}\text{As}$  resulting in a geometric mean of 0.036  $\text{mW}/^\circ\text{C}\mu\text{m}$ , in good agreement with the measured value. In future designs GaAs would be used for the high-index material. Its thermal conductivity of 0.044  $\text{mW}/^\circ\text{C}\mu\text{m}$  would give an effective thermal conductivity of 0.063  $\text{mW}/^\circ\text{C}\mu\text{m}$ , two times higher than the experimental value. The output powers of the lasers would be expected to double with this change alone!

### 5.3 Pulsed Characteristics

Pulsed measurements of the  $L$ - $I$ - $V$  characteristics are made to remove the heating effects. From the  $I$ - $V$  curves the true series resistance can be determined. Usually, the pulsed  $L$ - $I$  curve is linear until junction heating becomes significant. In the case of an intra-cavity contacted design, current crowding should result in sub-linear characteristics as the current crowding begins to adversely affect the internal efficiency. The following pulsed data shows this behavior, confirming our understanding of the device physics.

The pulsed measurements are made using a coaxial probe with a 1 GHz bandwidth and an inductive-current probe with a 100 MHz bandwidth. The light is focused into an integrating sphere with a high-speed InGaAs detector. CW  $L$ - $I$  curves made with a calibrated broad-area Ge detector are first taken and then compared with CW  $L$ - $I$  curves made with the InGaAs detector. Then pulsed measurements are made, calibrating the current scales to give equal quantum efficiencies at low bias levels. The optical spectra of the pulses are checked to ensure that the junction heating is less than  $10^\circ\text{C}$  during the course of the pulse. In addition, the shape of the optical pulse was monitored to be sure that the light signal was constant during the pulse, another indication that heating was not

significant. For the measurement, the pulses were 200 ns long with the data taken from the average of a 100 ns window at the end of the pulse.

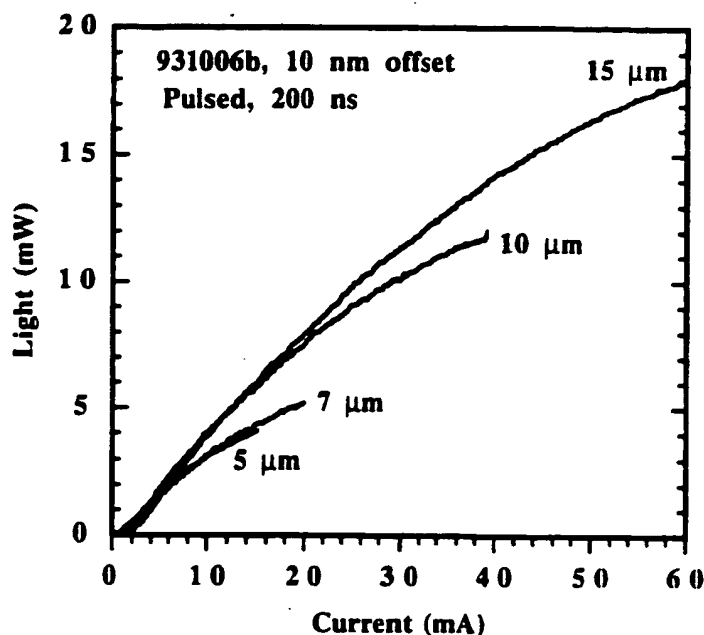


Fig. 5.11. Measured  $L-I$  characteristics for the four device diameters under pulsed operation. The non linearity indicates the onset of current crowding.

The measured  $L-I$  curves for the four devices are shown in Fig. 5.11. The 5 μm laser produced more than 4 mW of single mode power while the 15 μm laser produced more than 18 mW of infrared light. One can clearly see the non-linearity in the curves, showing the effect of current crowding. One would expect the effect to be less for the smaller devices, and this is indeed the case when the curves are replotted in terms of current density as shown in Fig. 5.12. It is clear from the figure that the 5 μm laser operates with less saturation at far higher current densities than the 15 μm laser, even without heating effects. The comparison between the 7 and 10 μm lasers is not so clear. Keep in mind that the non-linearity is due to current crowding at the edges where the transverse mode intensity is approaching zero. In the case of the 10 μm device, there is a strong

presence of a higher order mode which reduces the saturation effect. The above plots clearly show that current crowding can be an important design consideration for intra-cavity contacted vertical-cavity lasers.

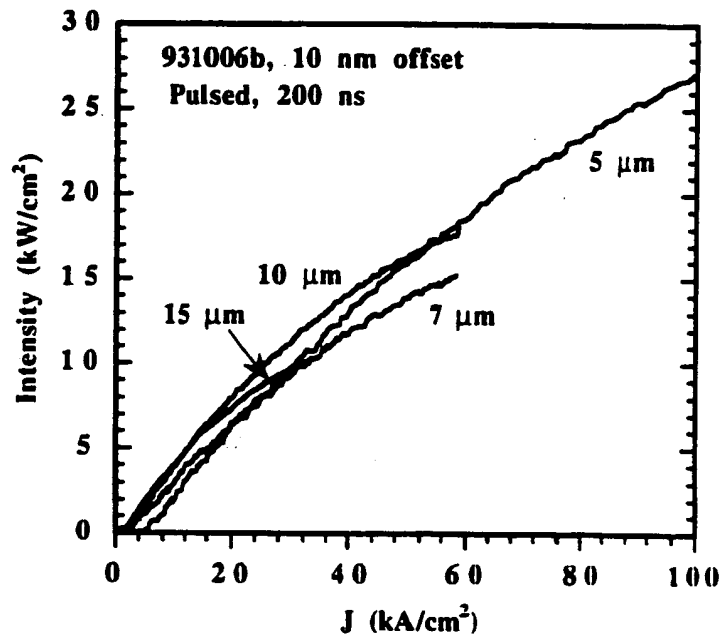


Fig. 5.12. Measured pulsed  $L-I$  characteristics scaled by device area.

The final information to extract from the pulsed measurements is the series resistance. At the high current densities present under pulsed operation, the junction resistance will be low so that the differential resistance is dominated by the series resistance. The measured  $I-V$  characteristics are shown in Fig. 5.13. The measured differential resistances are 132, 81, 57 and  $37\Omega$  for the 5, 7, 10 and 15  $\mu\text{m}$  lasers respectively. While these are fairly close to the CW values, they are measured at much higher biases. For example, under pulsed operation the differential resistances at the peak power points indicated in Fig. 5.5 are 192.

119, 87 and  $54 \Omega$  respectively. Under high frequency modulation it is the pulsed differential resistance which will determine the reflection coefficient.

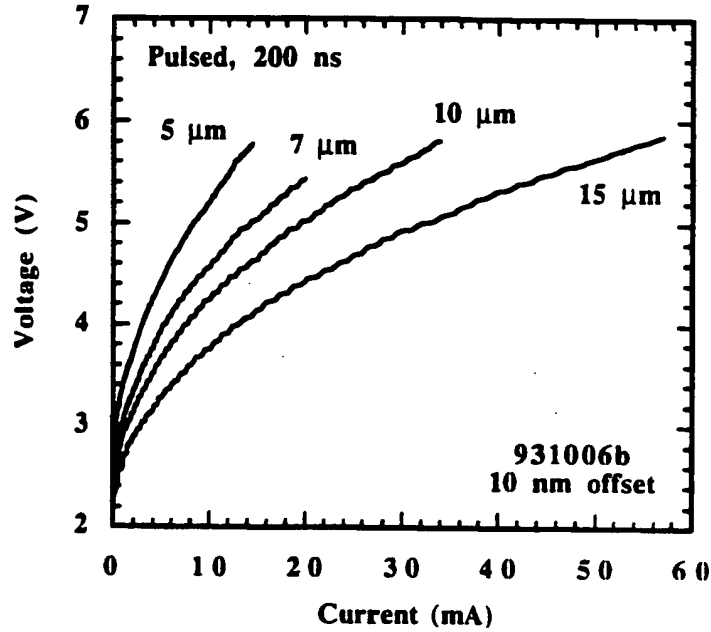


Fig. 5.13. Measured voltage as function of current under pulsed operation. The slopes yield differential resistances of 132, 81, 57 and  $37 \Omega$  for the 5, 7, 10 and  $15 \mu\text{m}$  lasers respectively.

While the voltages are higher for the smaller devices, the resistance does not simply scale with area. Instead, the series resistances are well fit by

$$R = \frac{1518 \Omega \mu\text{m}}{2\pi r} + \frac{325 \Omega \mu\text{m}^2}{\pi r^2}. \quad (5.1)$$

In Eqn. (5.1) the resistance is dominated by the ohmic "end resistance,"  $1518 \Omega \mu\text{m}$ . This is presumed to be due to the p-ohmic contact. The indication is that the resistance could be significantly improved if the p-ohmic resistances were optimized. In my structure, the p-ohmic metal was chosen to be removable off



the top of the waveguide using a Cl RIE etch. If the ring contact were deposited by liftoff, a more optimal metallization could be used.

#### 5.4 Microwave Response

One of the most attractive features of intra-cavity contacted vertical-cavity lasers is that emission is from and both contacts are on the surface of a semi-insulating GaAs substrate. This makes it possible to make high-speed measurements on wafer using the techniques developed for monolithic microwave integrated circuits. The experimental setup is shown schematically in Fig. 5.14. The sample is held by vacuum onto a temperature-controlled stage.

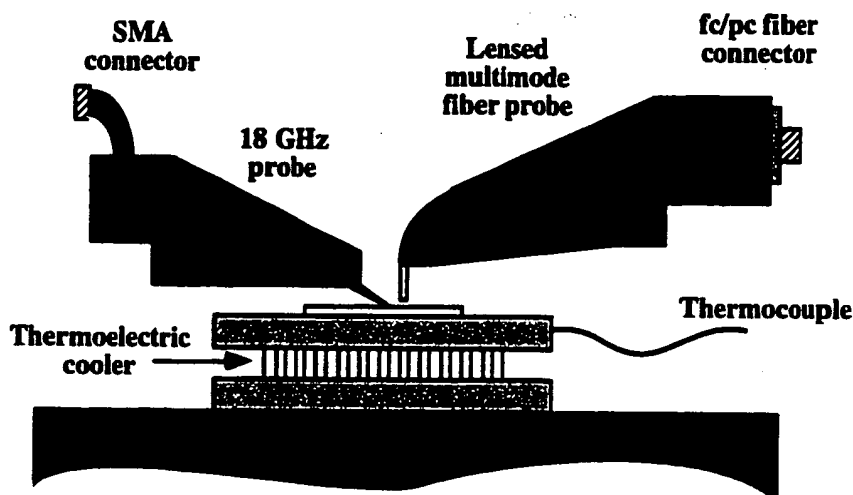


Fig. 5.14. Experimental setup used for high-speed characterization.

An 18GHz Cascade probe is used for electrical connection. The light is captured by a lensed multimode fiber 50 - 100  $\mu\text{m}$  above the surface. Both probes are mounted on x-y-z stages for positioning. The entire setup was mounted on an optical-isolation table for stability. Two kinds of S parameter measurements are made. The  $S_{11}$  measurements provide information on the input impedance. The  $S_{21}$  measurements reflect the modulation response of the laser. Careful calibration is required for both measurements.

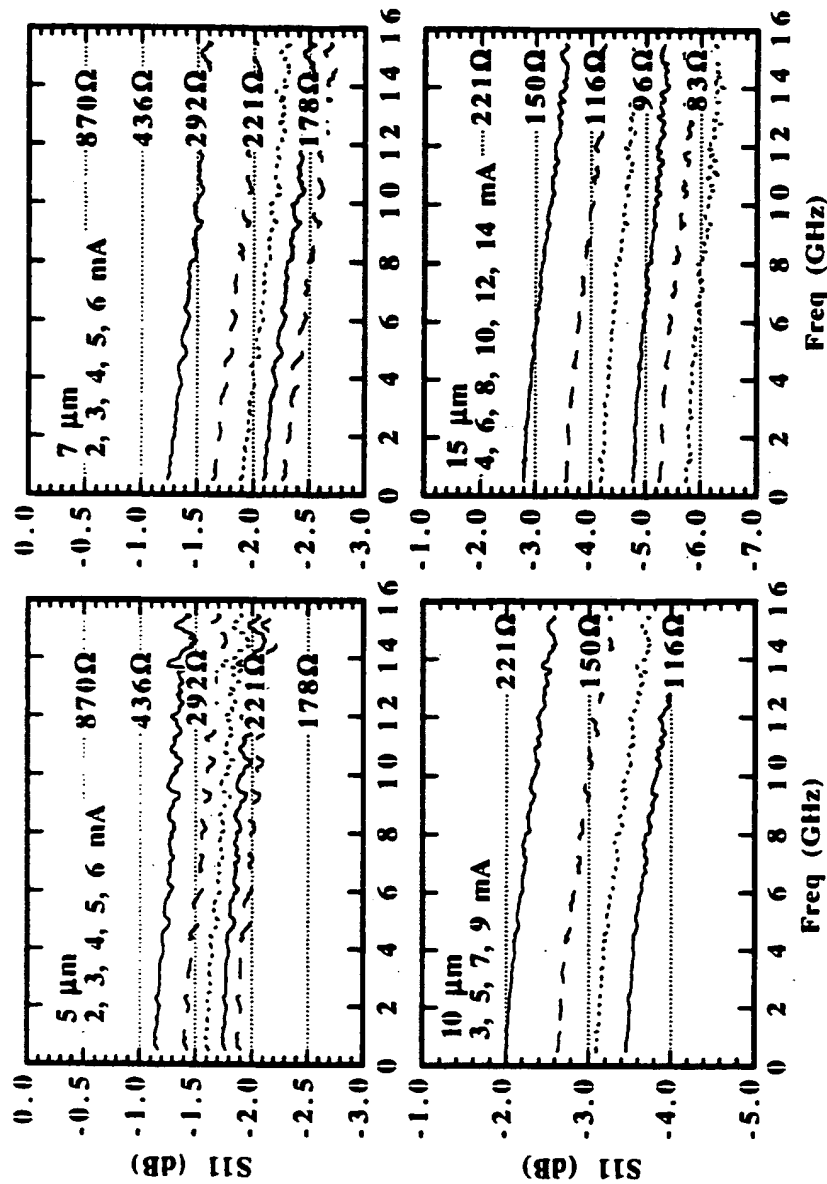


Fig. 5.15. Measured reflection coefficient,  $10\log(S_{11})$ , for the four laser sizes at varying bias

For the  $S_{11}$  measurements, a calibration substrate is used to set the reference plane at the probe tips. The calibration substrate has open, short and  $50\Omega$  loads which match the coplanar-transmission-line probe tips. For the  $S_{21}$  measurements, a through calibration is used, connecting all the microwave cables together in series with the two network ports. In addition, the amplifier and photodetector responses must be measured and subtracted from the data. The detector is a 25GHz New Focus detector which uses a top-surface-illuminated InGaAs detector and has a multimode-fiber input. A cascaded pair of 18dB, 20GHz New Focus amplifiers are used to compensate for the low responsivity of the detector ( $\sim 0.1\text{A/W}$ ) and the power loss in the laser. With the above test system and Hewlett Packard 8510 network analyzer, the laser properties can be measured quite rapidly.

The magnitude of the reflection coefficient,  $S_{11}$ , for the four sizes at various biases is shown in Fig. 5.15. Also shown is the equivalent load resistance corresponding with the reflection coefficient. The reflection coefficient varies by less than 0.5 dB from 1 to 15 GHz, with input impedances near  $250\Omega$  for the  $7\text{ }\mu\text{m}$  diameter device at 3 mA bias. To characterize the coplanar transmission lines, open, short and  $\approx 100\Omega$  loaded test lines fabricated along with the lasers are measured. The data matches the theoretical characteristics of a transmission line with a  $55\Omega$  characteristic impedance. From the shorted line, the series resistance is determined to be  $1.2\Omega$ . From the open line, the line is determined to have a phase of 22 degrees at 15 GHz. Using this model for the coplanar transmission lines, an equivalent circuit for the laser can be constructed to match the measured data. Given the particularly good performance of the  $7\text{ }\mu\text{m}$  laser, I chose to model its input impedance at a representative bias of 3 mA. An admittance Smith chart plot of the S parameters for the laser and the open, shorted and loaded transmission lines is shown in Fig. 5.16 as scanned from 0.5 to 15.5 GHz. As can be seen in the figure, the reflection coefficient does not follow a constant resistance curve. The simplest device model which agrees with the data is shown in Fig. 5.17. The series resistance is  $150\Omega$  while the parasitic shunt capacitance is 30 fF.

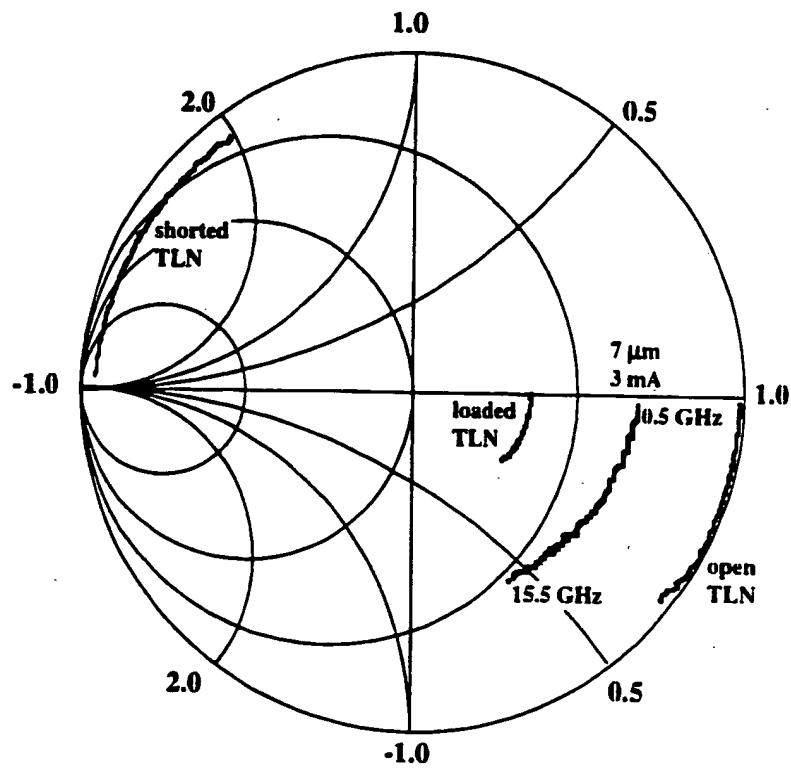


Fig. 5.16.  $S_{11}$  plotted on a Smith chart. Shown are the data for the 7  $\mu\text{m}$  laser at a 3 mA bias and the data for open, shorted and load terminated coplanar transmission lines

The junction resistance is  $110\Omega$  in parallel with a diode capacitance of  $80\text{ fF}$ . Even with the relatively high resistances, the capacitance values are so low that the laser is not capacitance (RC) limited. The two relevant time constants are determined by the effective resistance seen looking out of the two capacitors. In a  $Z_0 = 50\Omega$  test system, the time constant associated with the parasitic capacitor is given by  $\tau_p = C_p(Z_0/(R_s + R_d)) = 1.3\text{ ps}$  while the time constant associated with the diode capacitor is given by  $\tau_d = C_d(R_d/(R_s + Z_0)) = 5.7\text{ ps}$ . Thus the RC limited bandwidth is  $28\text{ GHz}$ , well above the maximum modulation bandwidth measured.

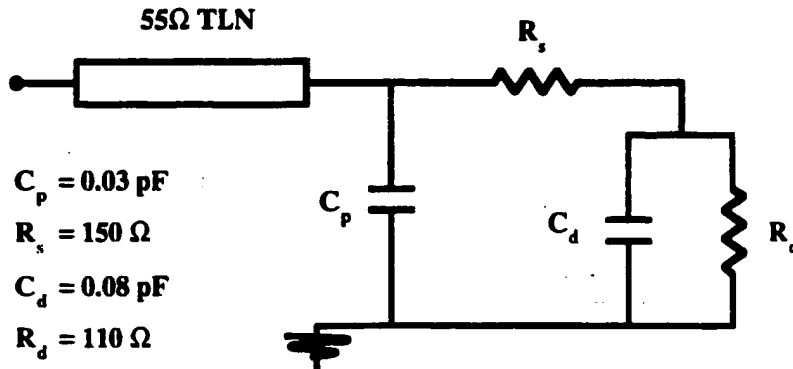


Fig. 5.17. Equivalent circuit for the  $7\ \mu\text{m}$  diameter laser at a bias of  $3\text{ mA}$ .

While the RC bandwidth is sufficiently high, the diode resistance is higher than is usually expected. Using a  $2kT$  diode law, the differential resistance at  $3\text{ mA}$  should be closer to  $17\ \Omega$ . If we assume an  $nkT$  diode law, then the ideality factor,  $n$ , would have to be  $13$  to agree with the small signal model in Fig. 5.17. The highly non-ideal diode characteristic is in good agreement with the measured  $I$ - $V$  characteristics of the diode shown in Fig. 5.13. The indication is that significant improvements in the laser performance will be observed with improved active regions. This will be confirmed by the presence of a transport limited bandwidths in the  $S_{21}$  measurements.

The  $S_{21}$  data for the 7  $\mu\text{m}$  laser is shown in Fig. 5.18. Shown are the experimental data as a dashed lines and the theoretical fit as solid lines. The laser had a threshold of 0.85 mA. The normalized modulation response can be written as [3]:

$$\frac{L}{I}(f) = C_o + \frac{1}{1 + (jf/f_p)} \frac{1}{1 + (jf/f_r)^2 + (jf/f_d)} \quad (5.2)$$

where  $L$  and  $I$  are the small signal light output and modulation current respectively,  $f$  is the modulation frequency,  $f_r$  is the relaxation oscillation frequency,  $f_d$  is the damping frequency,  $f_p$  is a single-order parasitic-rolloff frequency and  $C_o$  is an offset to account for normalization error. The damping frequency is defined here as  $f_d = 2\pi(f_r)^2/\gamma$ , where  $\gamma$  is the damping rate.

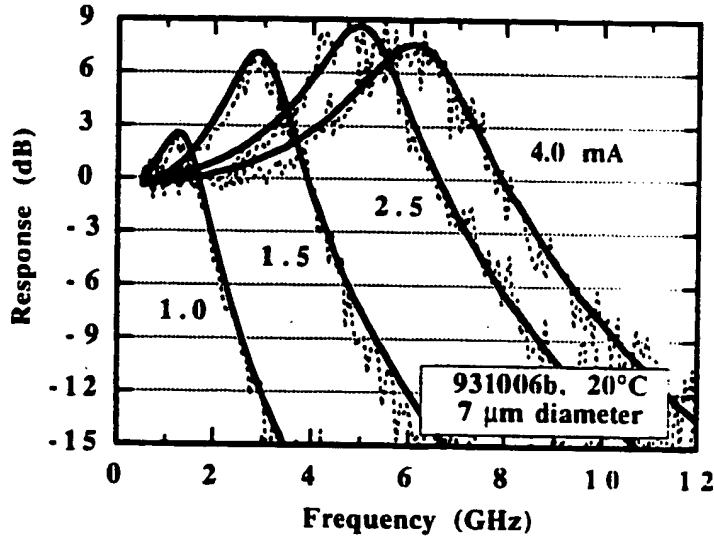


Fig. 5.18. Measured small signal response of the 7  $\mu\text{m}$  laser adjusted for the detector and amplifier responses. Dashed lines show data, solid lines show theoretical fit.

A maximum 3dB electrical bandwidth of 8.5 GHz is observed at an injection current of only 4 mA. At higher drive currents the modulation response showed little change, indicating that the effective threshold current was increasing and the differential gain was decreasing as the junction temperature rose. Note that the relaxation oscillation peak showed little dampening, indicating that higher speeds should be possible by improving the thermal and electrical designs. The parameters used in the curve fits are shown in Table 5.1. The fit of Eqn (5.2) at 4 mA has a relaxation peak at 6.3 GHz and a damping frequency of 19 GHz indicating an intrinsic bandwidth in excess of 27 GHz. For a good fit it was necessary to include a parasitic roll off at 9 GHz. The parasitic rolloff may be due to transport effects [3] associated with the 500Å doping setbacks and low mobility in the AlGaAs cladding the active region. The modulation response of the 7  $\mu$ m laser at 4.5 mA of drive current has been taken at stage temperatures varying from 15°C to 60°C. The 3dB bandwidth varied from 9.3 to 6.0 GHz respectively with little change in the threshold current.

Table 5.1. Parameters used in the curve fits shown in Fig. 5.18.

	$f_r$ (GHz)	$f_d$ (GHz)	$f_p$ (GHz)	$C_o$ (dB)
1.0 mA	1.46	2.01	9.00	-0.78
1.5 mA	3.00	7.59	9.00	-0.65
2.5 mA	5.10	16.0	9.00	-0.23
4.0 mA	6.30	18.9	9.00	-0.38

In the absence of damping and parasitics, the 3 dB bandwidth of a semiconductor laser under small signal direct current modulation is proportional to the square-root of injected current above threshold. To characterize low-threshold high-speed lasers, Chen *et. al.* [4] have suggested the modulation-current-efficiency-factor (MCEF) as the figure of merit, defined as

$$MCEF = f_{3dB} / \sqrt{(I - I_{th})} , \quad (5.3)$$

where  $f_{3dB}$  is the 3 dB bandwidth of the laser under direct current modulation,  $I$  is the bias current at which the modulation bandwidth is measured and  $I_{th}$  is the threshold current of the laser. For applications such as high-bandwidth computer interconnects the laser should provide the highest bandwidth at the lowest current, and thus the optimal laser will have a low threshold current and a high MCEF. In the absence of damping and parasitics, the 3 dB bandwidth of a semiconductor laser under direct current modulation can be written as [4]

$$f_{3dB} \cong 1.55 f_r = \frac{1.55}{2\pi} \sqrt{\frac{v_g G' P}{\tau_p}} \quad (5.4)$$

$$= \frac{1.55}{2\pi} \sqrt{\frac{v_g G' \eta_i}{q V_{opt}} (I - I_{th})} \quad (5.5)$$

where  $f_r$  is the resonance frequency,  $v_g$  is the group velocity,  $G'$  is the differential gain,  $\tau_p$  is the photon lifetime described in chapter 2,  $\eta_i$  is the internal efficiency,  $q$  is the electronic charge and  $V_{opt}$  is the modal volume. The modulation current efficiency factor, Eqn. (5.3), can thus be expressed in terms of the internal parameters

$$MCEF = \frac{1.55}{2\pi} \sqrt{\xi_{enh} \frac{v_g G' \eta_i}{q V_{opt}}} \quad (5.6)$$

where I have introduced the enhancement factor,  $\xi_{enh}$ , into the equation. In the case of a vertical-cavity laser the electric field at the quantum wells is nearly doubled due to their location at the peak of the strong standing wave in the cavity, resulting in an enhancement of the stimulated emission rate as discussed in Appendix D. In Eqn. (5.6) this periodic gain-enhancement factor must be included, a value of 1.83 for our device structure. Historically, comparisons of



laser modulation efficiency have been based on output power. However, modern high-speed in-plane lasers use facet coatings to optimize performance while vertical-cavity laser mirror reflectivities vary with the number of mirror periods. With varying output coupling the relationship between output power and internal field strength vary from device to device. Figures of merit based on output power can be misleading by showing higher values for lower external efficiency lasers. More meaningful comparisons can be made from benchmarks based on injected current rather than output power.

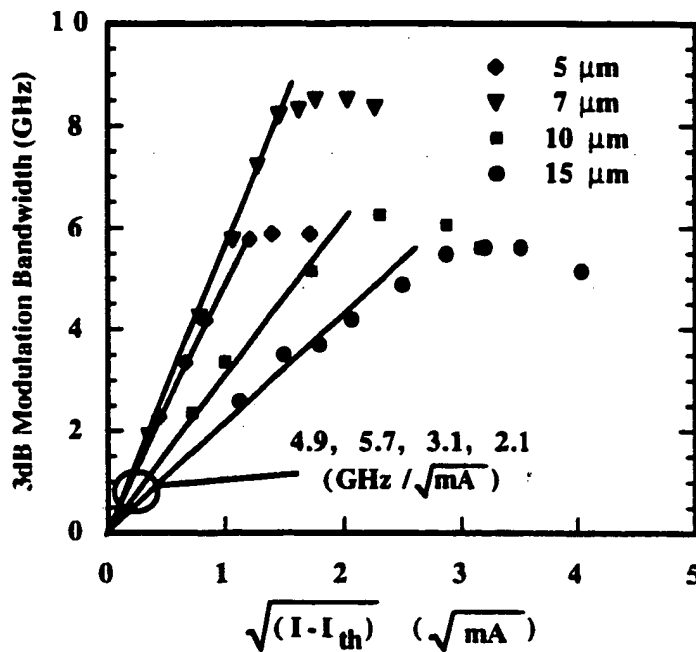


Fig. 5.19. Bandwidth vs. the square root of current above threshold for the four laser diameters. The slope is the modulation current efficiency factor MCEF. The 7  $\mu\text{m}$  device has a very high MCEF of 5.7 GHz/ $\sqrt{\text{mA}}$ .

The 3dB bandwidth as a function of the square-root of the current above threshold for the various laser diameters are plotted in Fig. 5.19. The slope yields the modulation-current-efficiency-factor. Equation (5.6) would suggest

that the modulation efficiency would be inversely proportional to device diameter. The trend towards higher modulation efficiency was observed down to the 7  $\mu\text{m}$  device which displayed the highest MCEF of 5.7 GHz/ $\sqrt{\text{mA}}$ , higher than any in-plane semiconductor laser. For comparison, Chen *et al.* recently reported [4] record levels of 5 GHz/ $\sqrt{\text{mA}}$ , with previous values of 2-3 GHz/ $\sqrt{\text{mA}}$  in high-speed bulk lasers and 2-4 GHz/ $\sqrt{\text{mA}}$  in high-speed quantum well lasers. The surface emitting lasers reported here have not been optimized for high speed other than to minimize the device parasitics. In fact, they were optimized for high quantum efficiency. Lasers with higher mirror reflectivities would operate at a lower threshold gain, resulting in a higher differential gain. For example, Shtengel *et al.* recently reported [5] on bandwidths as high as 14 GHz for a high reflectivity-low external efficiency gain-guided vertical-cavity laser operating at a wavelength of 0.78  $\mu\text{m}$ .

It is interesting to explore the reason for such high performance and to determine what are the potential performance limits. The modal volume of a vertical-cavity laser is quite small, although the cavity length of these lasers have an additional micrometer compared to many vertical-cavity structures to allow for the intra-cavity contacts. From the calculated standing wave pattern in Fig. 5.2, the effective length is determined to be 2.2  $\mu\text{m}$ . The transverse mode is mostly contained in a mode diameter of 6  $\mu\text{m}$ . By multiplying the modal area by the effective length, the modal volume  $V_{\text{opt}}$  is calculated to be  $6.22 \times 10^{-11} \text{ cm}^3$ . An estimate of the internal efficiency which includes both the injection efficiency and spatial hole burning effects can be made by dividing the measured external efficiency of the 15  $\mu\text{m}$  laser, 46%, by the calculated optical efficiency of 66% yielding an internal efficiency  $\eta_i$  of 0.7. The plane wave threshold gain of the cavity has been calculated to be  $1500 \text{ cm}^{-1}$ . Using the QWGain program, we predict a differential gain  $G'$  of  $5.4 \times 10^{-16} \text{ cm}^2$  at that point on the quantum well gain curve. Using the above values along with a group index of 4 in Eqn. (5.6) yields a predicted MCEF for the 7  $\mu\text{m}$  laser of 5.6 GHz/ $\sqrt{\text{mA}}$ , in good agreement with the measured value of 5.7 GHz/ $\sqrt{\text{mA}}$ . We can go one step further by dividing out the diameter so that the MCEF is expressed as

$$MCEF = \frac{33.6 \text{ GHz} / \sqrt{\text{mA}}}{D(\mu\text{m})}, \quad (5.7)$$

where  $D$  is the device diameter. This theoretical line is plotted in Fig. 5.20, showing good agreement except for the 5  $\mu\text{m}$  laser. As discussed in the previous sections, the quantum wells of the smallest lasers are driven very hard due to the higher optical losses of the very small waveguide and the relatively high mirror transmission.

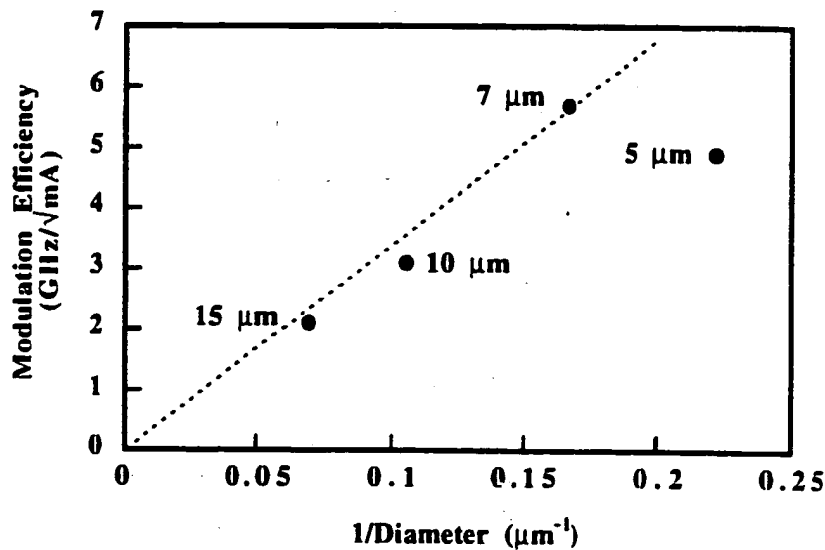


Fig. 5.20. Modulation efficiency vs. inverse diameter. Theoretical line based on device parameters.

The result is that the wells are biased to saturation levels so that the differential gain is much lower, reducing the MCEF for this device. Cavity designs optimized for high speed would use a higher reflectivity output coupler to keep the differential gain higher at the expense of reduced external efficiency. In such a design, an MCEF in excess of 7  $\text{GHz}/\sqrt{\text{mA}}$  appear quite possible to achieve.

Returning to Fig. 5.19, it is clear that all the lasers are capable of GHz modulation at low bias currents. In the next section, their high modulation efficiency will enable high-speed digital data transmission at low current levels.

### 5.5 Digital Data Transmission

One application area where vertical-cavity lasers are expected to have a significant impact in the near future is data communication, either board-to-board or computer-to-computer. Existing, low-speed 32 or 64 bit wide electrical data bus interfaces operating at 100 Mbit/s can be replaced by partially-multiplexed high-speed (Gigabit/s) optical data-bus interfaces, either free-space or via optical-ribbon fiber. In this fashion, the tradeoffs of fiber cost and high-speed electronics can be optimized for a given application.

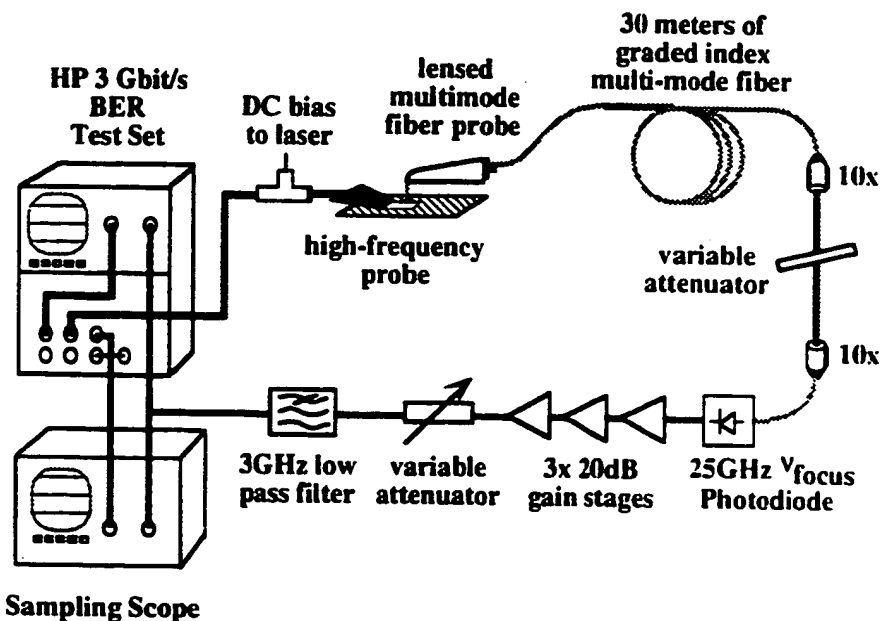


Fig. 5.21. Test setup used to make Bit Error Rate measurements.

This section presents results of an investigation of the system performance of the linear arrays of intra-cavity contacted, top-emitting vertical-cavity lasers. The

system performance experiments were chosen from the perspective of demonstrating compatibility with digital logic circuits under varying environmental conditions.

A block diagram schematic of the set-up employed to perform the optical data transmission experiment is shown in Fig. 5.21. Light from the laser is coupled into the multimode fiber (50  $\mu\text{m}$  core diameter/125  $\mu\text{m}$  cladding diameter) via a Cascade optical probe mounted on an  $x$ - $y$ - $z$  stage.

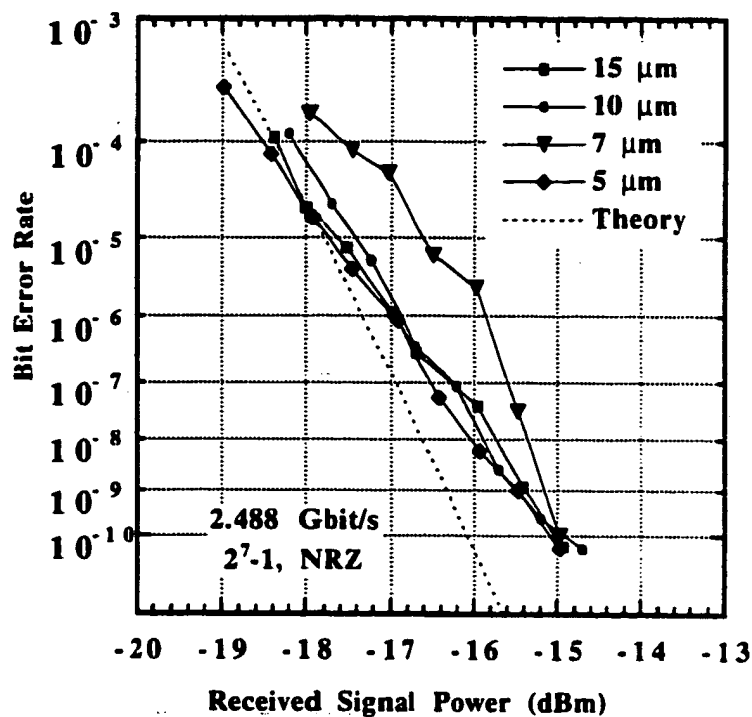


Fig. 5.22. Measured bit error rate vs. received signal power at 2.488 Gbit/s. No error floor was observed for any of the lasers.

As the Cascade microwave probe (which supplies the laser bias and modulation signals) is also mounted on an  $x$ - $y$ - $z$  stage, the data transmission performance of different devices on the wafer could be quickly and conveniently evaluated. The wafer itself is mounted on a temperature-controllable vacuum

chuck as previously shown in Fig. 5.14. This flexible measurement setup exhibited excellent stability in spite of the use of wafer probes for the electrical and optical coupling, indicating the potential for automated testing in a manufacturing environment.

Bit error rate (BER) measurements were performed at 2.488 Gbit/s for all device sizes. The corresponding BER curves are shown in Fig. 5.22. Thermal noise in the  $25\Omega$  (two  $50\Omega$  terminations in parallel) front end limits the receiver sensitivity to  $\approx -18$  dBm at a BER of  $10^{-9}$ . For the 2.488 Gbit/s measurements, the lasers were biased so that the zero logic level was slightly above threshold, introducing an extinction ratio penalty of 1.4 dB. For comparison, a theoretical curve taking into account thermal noise, amplifier noise and finite extinction ratio is shown as well [6]. The agreement with theory shows that the lasers are replicating the large signal modulation pattern, so that the BER curve can be predicted by considering the receiver alone. All devices could be operated at 3 Gbit/s, the limiting bit rate of the test equipment used, with no additional penalty.

Optical-coupling efficiency into the lensed multimode fiber, held 50 to 100  $\mu\text{m}$  above the surface, was greater than 80%. There were several fc/pc connectors in the link while the coupling efficiency of the free-space optical attenuator was  $\approx 50\%$ . It is interesting that all the lasers, from the single mode 5  $\mu\text{m}$  device to the multimode 15  $\mu\text{m}$  device, showed no error floor. An eye diagram of the 5  $\mu\text{m}$  laser at a received optical power of -14 dBm (50  $\mu\text{W}$ ) is shown in Fig. 5.23. High light levels are on the lower part of the plot. The zero is one division from the top. From the above experiments, it is clear that the lasers are capable of multi-Gigabit data rates at very low current levels.

In order to evaluate the performance of the vertical-cavity lasers for board-to-board interconnects, BER curves were measured at stage temperatures of 20°C, 40°C and 60°C under full on/off current modulation. On/off modulation is an attractive feature for the simplified implementation of data links. The bias and drive conditions were identical in each case. A bit rate of 1.6 Gbit/s was chosen as representative of the bit rates employed in these applications. As can be seen from the BER curves shown in Fig. 5.24, no appreciable degradation in

BER performance can be observed, indicating the robustness of vertical-cavity laser modulation in environments with large temperature gradients or variations.

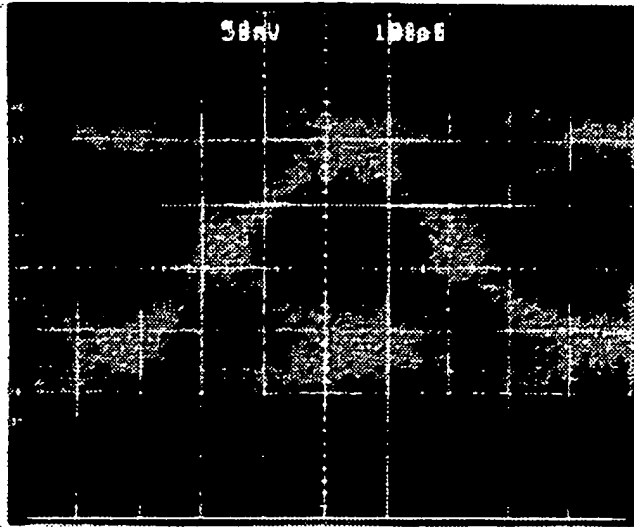


**Fig. 5.23. Eye diagram at 2.488 Gbit/s for the 5  $\mu$ m laser at a received power of -14 dBm**

For these and the following experiments, the lasers were biased at an average current of 3mA with a modulation signal amplitude of 1V peak to peak into 50 $\Omega$ . This was sufficient to ensure that the lasers were driven well below the threshold voltage in the zero current state. No additional penalty due to turn-on delay was observed with this on/off modulation condition due to the low threshold current.

Finally, a block of 10 devices in an array of 7  $\mu$ m devices were each used as transmitters in the optical data link to evaluate the uniformity of the device performance under the same identical operating conditions. The received optical power required to obtain a BER of  $10^{-9}$  was first recorded for device #1 in the array. The optical and microwave probes were displaced laterally to the next device in the array and, under identical operating conditions, the received optical power required to achieve a BER of  $10^{-9}$  was recorded. This procedure was repeated for all 10 devices. Figure 5.25 plots the received optical power for a

BER of  $10^{-9}$  for each device. The total spread in received optical power is less than 0.6 dB, clearly illustrating the uniformity of the devices' modulation response. Combined with a well-controlled gain-offset growth for temperature-stabilized output power, these BER characteristics indicate that it should be possible to develop vertical-cavity laser based parallel-data links using simplified electronics and without temperature control. Such a data link holds promise of providing very low cost, high bandwidth networks.

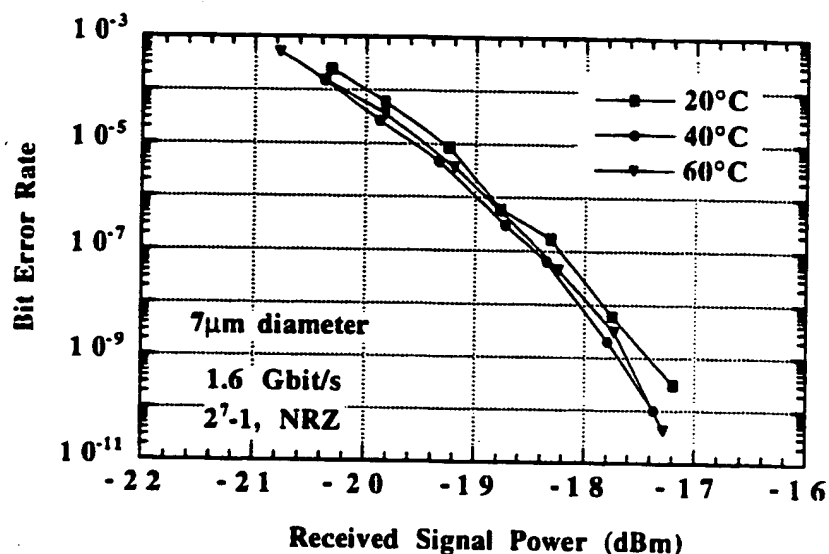


Fig. 5.24. Digital data transmission under on/off modulation using the 7  $\mu$ m diameter lasers from 20 - 60°C.

In summary, measurements of intra-cavity contacted, top-surface emitting vertical-cavity lasers have shown output powers greater than 1mW, 3dB bandwidths in excess of 8GHz and the capability for gigabit data rates at bias currents of only a few milliamps and power consumption below 10 mW. The advantages of intra-cavity contacts on semi-insulating substrates has enabled the realization of the high-speed potential of vertical-cavity lasers. Measurements of



the thermal and electrical properties indicate that significantly higher speeds and efficiencies will be achieved as the laser designs are improved.

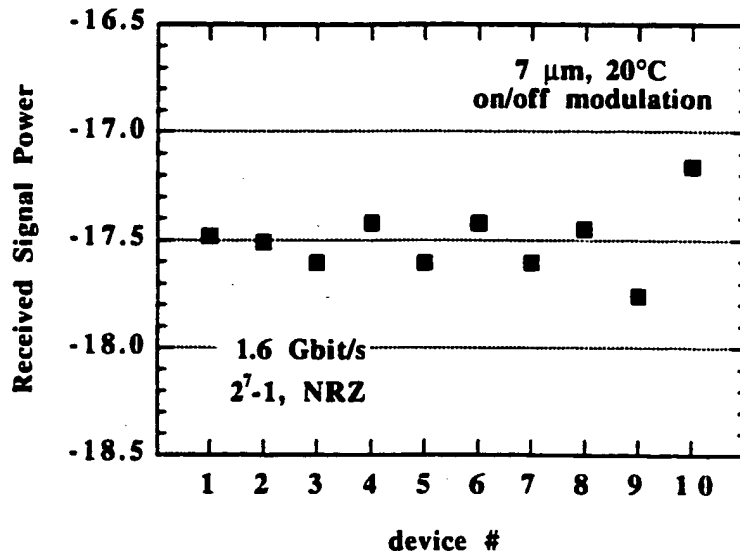


Fig. 5.25. Variation in received signal power to achieve a BER of  $10^{-9}$  for ten adjacent devices in a linear array biased under identical, full on/off modulation with a peak current of 6 mA.

### References

1. N. Chand, R. Fischer, J. Klem, T. Henderson, P. Pearah, W.T. Masselink, Y.C. Chang, and H. Morkoc, "Beryllium and silicon doping studies in  $\text{Al}_x\text{Ga}_{1-x}\text{As}$  and new results on persistent photoconductivity." *Journal of Vacuum Science & Technology B*, 3 (2) pp. 644-8. 1985
2. M.G. Peters, B.J. Thibeault, D.B. Young, J.W. Scott, F.H. Peters, A.C. Gossard, and L.A. Coldren, "Band-gap engineered digital alloy interfaces for lower resistance vertical-cavity surface-emitting lasers." *Applied Physics Letters*, 63 (25) pp. 3411-13. 1993

3. R. Nagarajan, T. Fukushima, M. Ishikawa, J.E. Bowers, R.S. Geels, and L.A. Coldren, "Transport Limits in High-Speed Quantum-Well Lasers: Theory and Experiment" *IEEE Photonics Tech. Lett.*, **4** (2) pp. 121-123. 1992
4. T.R. Chen, B. Zhao, L. Eng, Y.H. Zhuang, J. O'Brien, and A. Yariv, "Very high modulation efficiency of ultralow threshold current single quantum well lasers" *Electron. Lett.*, **29** (17) pp. 1525-1526. 1993
5. G. Shtengel, H. Temkin, P. Brusenbach, T. Uchida, M. Kim, C. Parsons, W.E. Quinn, and S.E. Swirhun, "High-speed vertical-cavity surface emitting laser." *IEEE Photonics Technology Letters*, **5** (12) pp. 1359-62. 1993
6. G.P. Agrawal, Fiber-Optic Communication Systems, ed. K. Chang. New York: John Wiley & Sons, Inc. pp 162-176. 1992. Section 4.5 covers BER theory.

## **Chapter 6: Laser Analysis and Improved Designs**

### **6.0 Chapter Overview**

In this chapter the numerical models developed in Chapters 2 and 3 are applied to the intra-cavity lasers presented in Chapter 5. The models are first used to simulate the lasers and then they are used to predict the performance of improved designs, indicating directions for future device work. The most important advancement is the current-apertured intra-cavity design which promises higher efficiency and single-mode operation while maintaining low parasitics. At the same time, the limitations of the models are highlighted throughout the chapter, indicating directions for future modeling work.

### **6.1 Analyzing the Intra-Cavity Lasers**

#### **6.1.1 Summary of the Analysis**

The analysis presented below begins with current-injection simulations using the model of Chapter 3 to simulate the intra-cavity lasers' electrical properties. Excellent agreement with experiment is obtained once the p-ohmic contact resistance and the reduced drive voltage due to heating have been accounted for. The non-uniform current-injection profiles, resulting from the ring-contacted geometry, are then used to calculate the  $L-I$  characteristics for the four diameters of 5, 7, 10 and 15  $\mu\text{m}$  using the model of Chapter 2. While the round-trip cavity parameters calculated in the beginning of Chapter 5, are sufficient for the 15  $\mu\text{m}$  laser, it is necessary to include additional optical losses attributed to sidewall scattering in order to match the experimental external efficiency of the smaller lasers. Once additional optical scattering losses have been added, good agreement is found for the threshold currents in all cases using the active-region parameters determined in Chapter 2. The 10 and 15  $\mu\text{m}$  lasers operate with multiple transverse modes due to lower scattering losses, current crowding effects and spatial hole burning. The output power of the larger

devices is accurately predicted only when running a multimode  $L-I$  simulation including the next higher-order transverse mode.

### 6.1.2 Current-injection Simulation

The laser structure must be modeled as a combination of diode and resistive materials to simulate the intra-cavity contact performance. The ring-contacted structure as modeled is shown in Fig. 6.1 along with the numerical mesh. As discussed in Chapter 3, the  $0.4\text{ }\mu\text{m}$  thick p+ layer has a resistivity of  $104\Omega\mu\text{m}$  and the  $0.3\text{ }\mu\text{m}$  thick p- layer has a resistivity of  $1040\Omega\mu\text{m}$ . The  $0.3\text{ }\mu\text{m}$  thick n+ layer has a resistivity of  $16\Omega\mu\text{m}$ . The structure has two non-ohmic regions; the undercut layer's GaAs/AlAs heterobarrier and the p-i-n active region.

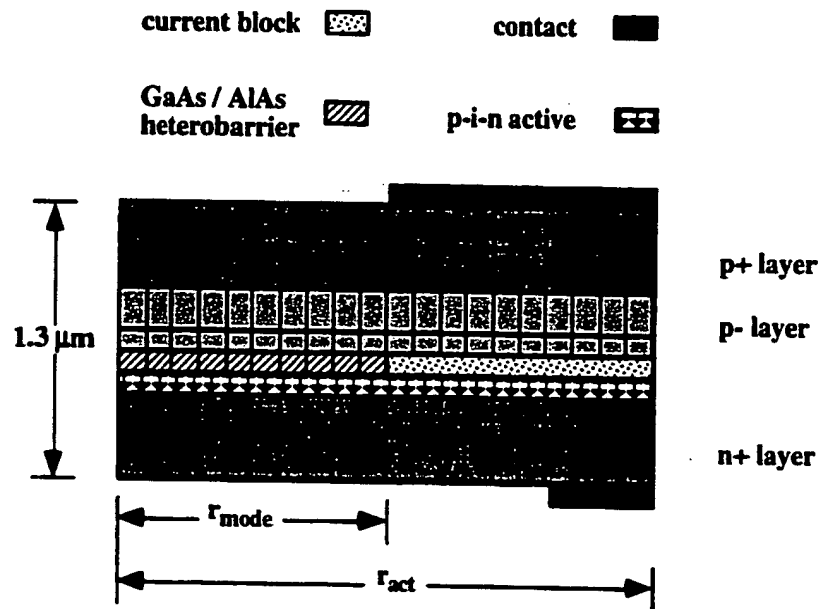


Fig. 6.1. Structure modeled for the current-injection simulations

The measured  $J-V$  characteristics of these layers are shown in the end of Appendix E. The heterojunction is characterized as having a current density of  $1\text{ kA/cm}^2$  at a bias of  $0.46\text{ V}$  with a non-ideality factor of  $3.6$ . The p-i-n diode is

characterized as having a current density of  $1 \text{ kA/cm}^2$  at a bias of  $1.89 \text{ V}$  with a non-ideality factor of 17! With such a high non-ideality factor one would expect fairly uniform injection even without the current leveling layer. The penalty is higher drive voltages, greater heat generation and higher dynamic resistance. These structural parameters are used as inputs for the current-injection simulations

The  $I$ - $V$  characteristics are calculated for all four device diameters. In order to achieve agreement with the measured characteristics it is necessary to include an additional series resistance. This additional resistance can be attributed to the p-ohmic contact and thus it should scale with the perimeter. By adding a contact resistance of 47, 32, 19 and  $15 \Omega$  to the calculated  $I$ - $V$  characteristics for the 5, 7, 10 and  $15 \mu\text{m}$  lasers, excellent agreement with the pulsed  $I$ - $V$  characteristics is achieved as shown in Fig. 6.2. These series resistances all deviate less than 15% from an end resistance of  $686 \Omega\mu\text{m}$ , indicating that the additional resistance can be attributed to the ohmic contact.

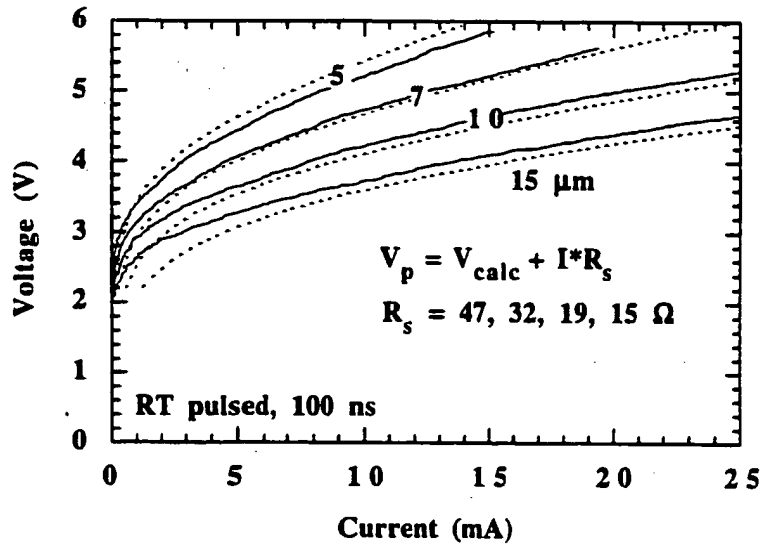


Fig. 6.2. Calculated (dash) and measured (solid)  $I$ - $V$  characteristics for the four laser diameters. The calculated curves include the series resistance shown. Measured data taken under pulsed operation to avoid heating.

For proper simulation of the CW current-to-light characteristics, it is essential that the calculated  $I$ - $V$  match with experiment or else the junction heating will not be predicted accurately. When continuous wave (CW) measurements are made, the junction heating can be significant, showing temperature rises as high as 100°C. Experimentally, the voltage drop in the diode materials reduces with increasing temperature in a linear fashion and thus cannot be attributed to the thermal voltage  $V_T$ . The behavior is better modeled as a change in the diode voltage,  $V_d$ , in Eqn. (3.2). The CW  $I$ - $V$  characteristics can therefore be approximated by subtracting an amount proportional to the temperature rise from the drive voltage calculated assuming a constant temperature. The advantage is that the current-injection and current-to-light simulations remain decoupled while still maintaining self-consistency.

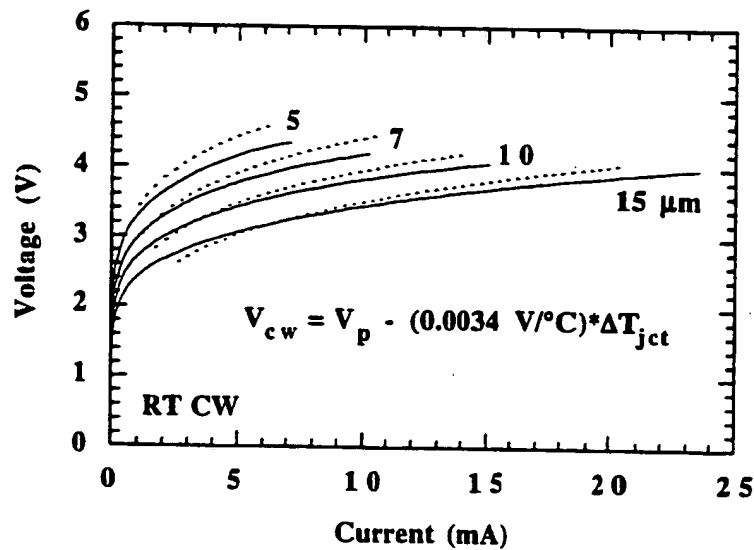


Fig. 6.3. Calculated (dash) and measured (solid)  $I$ - $V$  characteristics for the four laser diameters. The calculated curves include a reduction in drive voltage with increasing junction temperature.

The thermal impedance for the four lasers was calculated in Chapter 5 and determined to agree well with the analytic formula. Using this formula, and the dissipated power in the laser, allows a CW  $I$ - $V$  characteristic to be approximated as shown in Fig. 6.3. A voltage reduction of 0.34V per 100°C temperature rise fits well to the experimental data. It is important that the calculated and experimental voltages agree. The  $L$ - $I$  simulations use the calculated voltage to determine the input power in the device and the corresponding current-density profiles for the injected current. For the following calculations, the  $L$ - $I$  program adds the series resistance to the calculated voltage as in Fig. 6.2 and then the resulting voltage is reduced depending on the junction temperature as in Fig. 6.3. These two adjustments are all that is needed to model the lasers electrical properties with high accuracy.

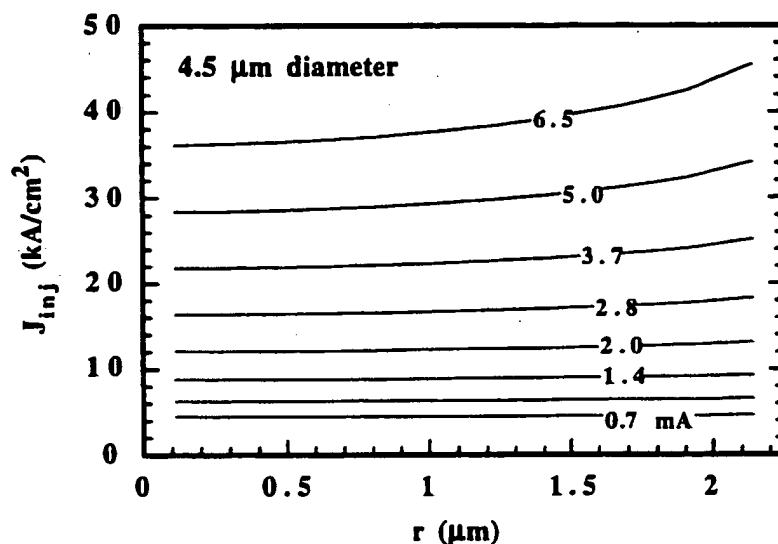


Fig. 6.4. Calculated current-density profiles for the 5  $\mu\text{m}$  diameter laser. Bias values range from threshold to just above maximum optical output power levels.

The calculated current-density profiles for the two extreme cases of the 5 and 15  $\mu\text{m}$  lasers are shown in Figs 6.4 and 6.5 respectively. In each case the

profiles are plotted for a range of bias currents representative from threshold to just past peak power. The 5  $\mu\text{m}$  laser (actual diameter 4.5  $\mu\text{m}$ ) has fairly uniform current injection. In contrast, the 15  $\mu\text{m}$  laser has current densities twice as high at the edge than the center, even though the average current densities are less than half that of the 5  $\mu\text{m}$  laser. Neither case is in the fully resistive-limited regime. From the current distributions one can expect that the 15  $\mu\text{m}$  laser will strongly prefer multimode operation, as is observed experimentally. The current-density profiles can now be used to calculate the  $L$ - $I$  characteristics.

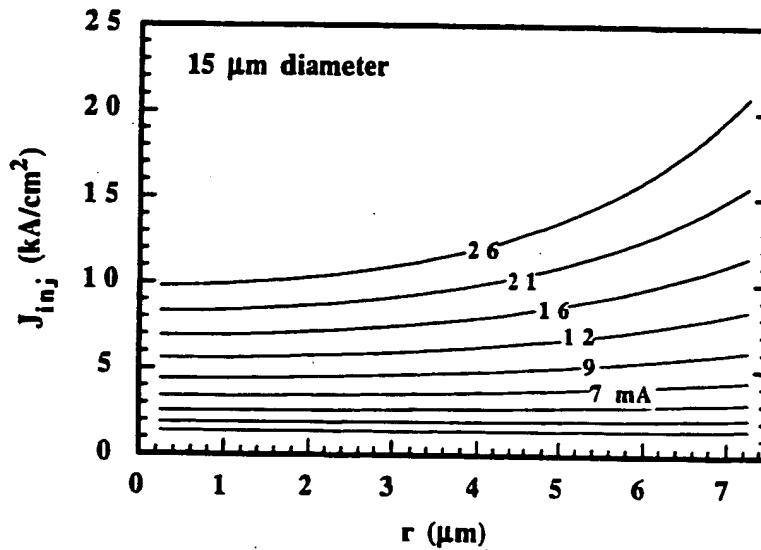


Fig. 6.5. Calculated current-density profiles for the 15  $\mu\text{m}$  diameter laser. Bias values range from threshold to just above maximum optical output power levels.

Before continuing to the  $L$ - $I$  calculations, several points can be made regarding future work. The high non-ideality factor of the active-region diode has made the current injection fairly uniform, with current crowding well below the resistive limit. The penalty is that the drive voltage is between 3 and 4 volts while the photon energy is only 1.24 eV, resulting in lower power-conversion efficiency and greater temperature rise for a given output power. Improved active region designs would optimize doping and bandgap profiles to reduce the



non-ideality factor to somewhere in the range of 2 - 4 while maintaining carrier confinement. The predicted performance of lasers with such improved active regions and current leveling have been shown in Chapter 3.

### 6.1.3 Current-to-Light Simulation

The parameters used on the  $L$ - $I$  simulation for the four laser sizes are shown in Table 6.1. The structural parameters are calculated in Chapter 5. The active-region parameters such as diffusion constant, etc. are the same as in the simulations in Chapter 2. In addition to the non-uniform current-injection profiles, there are two important differences from the simulations in Chapter 2.

Table 6.1. Parameters used in the  $L$ - $I$  simulations of the intra-cavity lasers.

parameter	symbol	5 $\mu\text{m}$	7 $\mu\text{m}$	10 $\mu\text{m}$	15 $\mu\text{m}$
Gain offset	$\Delta\lambda$ ( $\mu\text{m}$ )	4	4	4	4
Active Radius	$r_{act}$ ( $\mu\text{m}$ )	7.5	8.5	10	12.5
Mode Radius	$r_{mode}$ ( $\mu\text{m}$ )	2.25	3.5	5.0	7.5
Transmission	$T_r$ (%)	0.87	0.87	0.87	0.87
Internal loss	$L_i$ (%)	0.45	0.45	0.45	0.45
Scatt. loss mode1	$L_s^1$ (%)	0.48	0.15	0	0
Scatt. loss mode2	$L_s^2$ (%)	N/A	N/A	0.15	0
Series Resistance	$R_s$ ( $\Omega$ )	47	32	19	15
Eff. thermal cond.	$\sigma_{eff}$ ( $\text{mW}/^\circ\text{C}\mu\text{m}$ )	0.038	0.038	0.038	0.038
Injection eff.	$\eta_{inj}$	0.9	0.9	0.9	0.9
Diffusion const.	$D_a$ ( $\text{cm}^2/\text{s}$ )	40	40	40	40
Surface rec. velocity	$S_r$ ( $10^5 \text{cm/s}$ )	2	2	2	2
Auger coeff.	$C_A$ ( $10^{-29} \text{cm}^6/\text{s}$ )	5.25	5.25	5.25	5.25
Leakage coeff.	$J_o$ ( $10^6 \text{A}/\text{cm}^2$ )	2.5	2.5	2.5	2.5
Cladding Al fraction	$x$	0.2	0.2	0.2	0.2

First, carriers are allowed to diffuse out from the region of current injection (coincident with the mode diameter) to the active region radius some 5  $\mu\text{m}$

further. Second, the calculations include a higher order transverse mode for the 10 and 15  $\mu\text{m}$  diameter lasers. I have added optical scattering losses  $L_s^1$  and  $L_s^2$  for the fundamental and next higher-order mode.

The values used for the scattering losses are chosen to match the measured external efficiency and output power. The trend of higher scattering losses for the smaller lasers and higher-order modes is consistent with the hypothesis that they are due to sidewall scattering and diffraction.

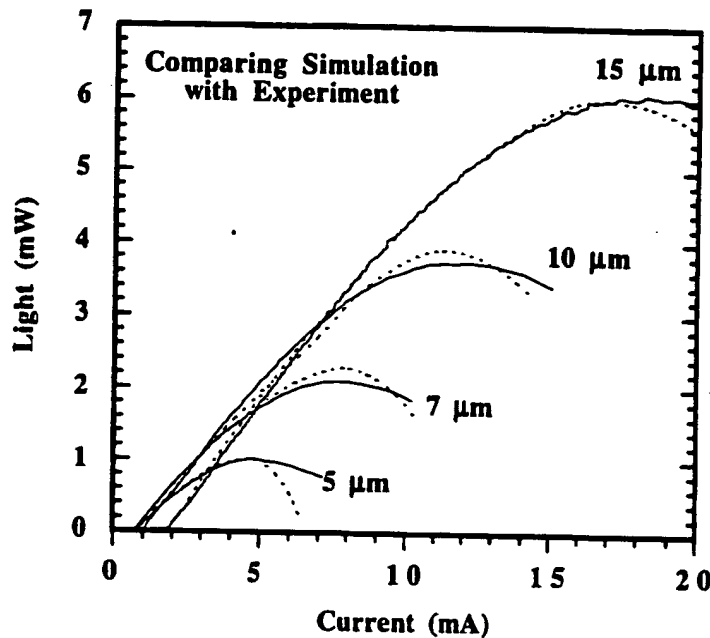


Fig. 6.6. Comparison of the measured and calculated CW  $L$ - $I$  characteristics of the intra-cavity contacted lasers using the parameters in Table 6.1.

Including higher-order modes, however, reduces the convergence rate of the calculation as the partitioning of current between modes is a subtle process, sensitive to the threshold gain of each mode and the current-injection profile. The result is that the calculation time increases from 10 minutes to 90 minutes for an  $L$ - $I$  curve. Thus I have not made an extensive investigation of the

multimode modeling and this remains an interesting area for future modeling work.

The calculated  $L$ - $I$  characteristics are shown in Fig. 6.6. The close agreement of measured and calculated threshold currents is very encouraging. In order to match the saturated output power levels, it was necessary to model the current leakage with a cladding layer Al content of 20%. The actual device structure had a cladding of  $\text{Al}_{0.5}\text{Ga}_{0.5}\text{As}$  on the p side and  $\text{Al}_{0.25}\text{Ga}_{0.75}\text{As}$  on the n side. The simple leakage current model with  $\text{Al}_{0.2}\text{Ga}_{0.8}\text{As}$  cladding effectively limits the carrier density to  $\sim 1.2 \times 10^{19} \text{cm}^{-3}$  instead of the  $\sim 2 \times 10^{19} \text{cm}^{-3}$  limit due to Auger recombination in the  $\text{Al}_{0.5}\text{Ga}_{0.5}\text{As}$  cladded active regions. Better models for the carrier confinement in the active region at these elevated carrier densities and temperatures are required to improve the simulation's ability to predict the maximum output power of new designs.

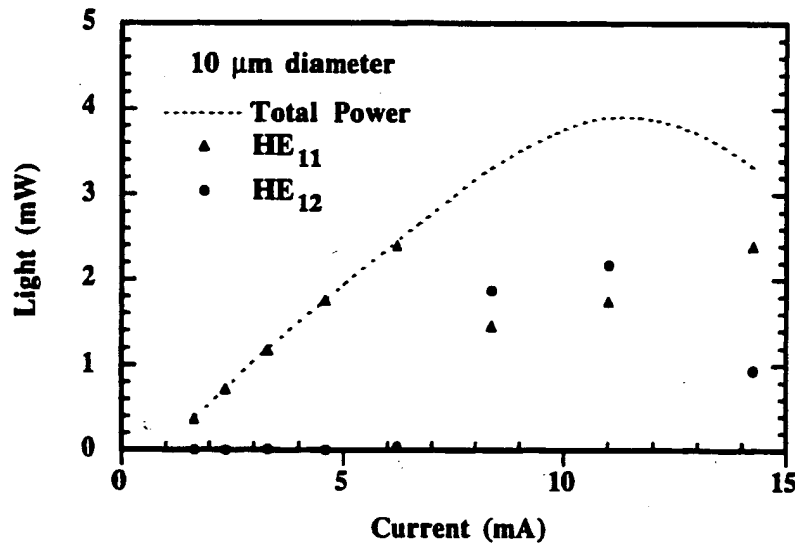


Fig. 6.7. Calculated multimode  $L$ - $I$  characteristics of the  $10 \mu\text{m}$  laser showing the partitioning of power between the modes.

It is interesting to observe the partitioning of the output power in the multimode calculations. As expected, the 15  $\mu\text{m}$  laser operates with a single mode only at threshold and then rapidly becomes multimode. Due to the current crowding, the higher-order mode dominates, with almost no power in the fundamental mode. The 10  $\mu\text{m}$  laser is more interesting. Experimentally, the laser operates with a single mode up to 5 mA and then lases with two modes competing for power, resulting in an unstable far field pattern. The calculated power in each mode and the total output power is plotted in Fig. 6.7. One observes the initially single mode behavior transforming into multimode operation as the spatial hole burning and current crowding effects increase the gain of the higher-order transverse mode. The point is that the calculations are capable of producing multimode results, although further research is required to determine the proper scattering loss to be used for each mode and to develop improved algorithms for solving the multimode equations.

## 6.2 Major Improvements for Minor Changes

With the analysis of the experimental devices complete, the question arises as to the potential performance of this device structure. This section focuses on the improvements arising from further optimization of the thermal design and the active region's electrical properties. Improvements are made one by one, showing the *predicted* changes in device performance.

The simplest change is to replace the  $\text{Al}_{0.1}\text{Ga}_{0.1}\text{As}$  high index material with GaAs. As discussed in the end of Section 5.2, the effective thermal conductivity of the structure could be expected to improve from 0.038  $\text{mW}/^\circ\text{C}\mu\text{m}$  to 0.063  $\text{mW}/^\circ\text{C}\mu\text{m}$ . The resulting  $L-I$  is plotted as curve *b* in Fig. 6.8 along with the calculation for the experimental device, curve *a*. With this change alone, the output power of this sub-milliamp threshold laser increases to nearly 4 mW. Another straightforward change is to improve the carrier confinement by using  $\text{Al}_{0.5}\text{Ga}_{0.5}\text{As}$  cladding layers on both sides of the active region as in device structure *B* in Chapter 2. Shown as the dashed curve *c*, the maximum output power rises to 6 mW, saturating at a junction temperature of

140°C. These high output powers would allow the laser's intrinsic modulation bandwidths to more than double. Overall, major improvements in the laser performance can be expected for the simple design changes analyzed above. Yet for many applications more power is not required. Instead, improvements in device efficiency at low-power levels are required to minimize the power consumption of arrays. Additionally, single-transverse-mode operation is important in many applications. Both these improvements in laser performance can be achieved using a current-apertured design.

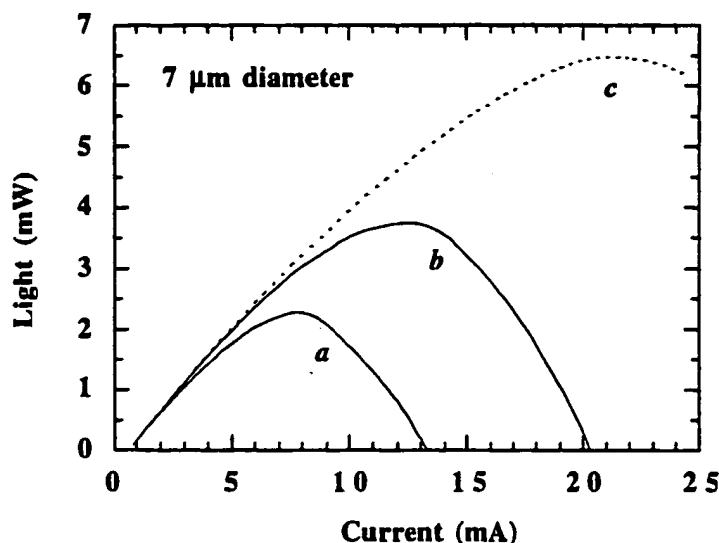


Fig. 6.8. Calculated  $L$ - $I$  curves for the  $7\text{ }\mu\text{m}$  laser. Curve  $a$  is for the unmodified device, curve  $b$  is for an improved thermal design and curve  $c$  has the same design as curve  $b$  but improved carrier confinement as well.

### 6.3 Current-Apertured Design

The intra-cavity contacted lasers presented in Chapter 5 were fabricated using semiconductor distributed Bragg reflectors on both sides of the cavity. In an alternate realization, the top mirror could be a dielectric stack deposited by e-beam evaporation. Very-high-reflectivity mirrors using  $\text{SiO}_2/\text{TiO}_2$  distributed

Bragg reflectors are routinely used in the optics industry. If silver or gold is deposited on top for a bottom-emission design, only a few periods are required for reflectivities above 99.8% as discussed in Appendix D. The dielectric-metal mirror reflectivity is high over a very-broad spectral band, relaxing the requirements on thickness control compared with a GaAs/AlAs mirror. In addition, the fabrication sequence becomes greatly simplified without the  $3\text{ }\mu\text{m}$  thick top mirror. Most importantly, post-growth deposition of the top mirror allows the development of current-apertured designs.

A current-apertured vertical-cavity laser design is shown in Fig. 6.9. The idealized schematic shows the n-contact on the underside as modeled in the current-injection simulations. The current block is grown into the material using, for example, an n-type  $\text{Al}_{0.25}\text{Ga}_{0.75}\text{As}$  layer. Ion implantation or zinc diffusion is used to convert the blocking layer to p-type in the center, forming a current aperture without introducing a large index discontinuity that would constrict the mode.

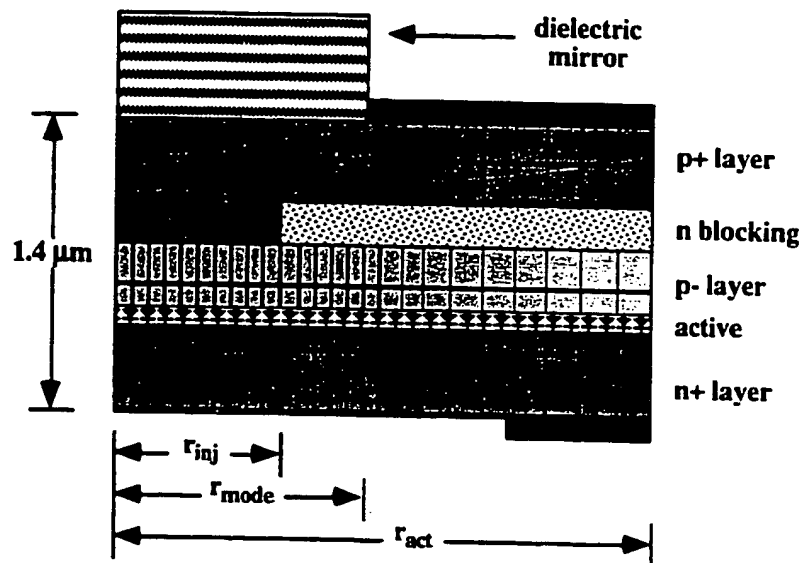


Fig. 6.9. Schematic of the current-aperture design modeled in this section.

This design [1] allows current aperturing without introducing the reliability issues of proton damage or regrowth techniques which have been unable to maintain the highly planar surfaces required by high-quality-factor vertical cavities.

The advantages of a current-apertured design arise from an optimized overlap of the current injection with the fundamental transverse-mode profile. Laser efficiency is improved while suppressing multimode operation. This was shown in Chapter 2 for vertically-contacted structures. The intra-cavity structures, however, make it possible to realize such designs. One important design consideration is the resistivity used for the p- layer between the current block and the active region. This leveling layer serves two functions. At high biases, when the diode's dynamic resistance is low, the leveling layer limits the current crowding. At low biases, when the diode's dynamic resistance is high, the leveling layer keeps the current from spreading out between the blocking layer and the junction.

The laser structure will be modeled as follows. The p-i-n diode is characterized as having a current density of  $1 \text{ kA/cm}^2$  at a bias of 1.6V with a non-ideality factor of 3.6. Still non-ideal, this diode has realistic values for a well engineered p-i-n double-heterodiode [2]. The conductive p+ layer again has a resistivity of  $104 \Omega\mu\text{m}$ . The p-type converted current-aperture layer is modeled with a resistivity of  $208 \Omega\mu\text{m}$ . The n+ layer again has a relatively low resistivity of  $16 \Omega\mu\text{m}$ , making the results insensitive to the exact placement of the n-contact. Thus the n-contact can be placed below the n layer for numerical convenience as in Fig. 6.9 without compromising accuracy. The current constriction radius,  $r_{inj}$ , is set at  $2.5 \mu\text{m}$  while the p contact and optical mode radius,  $r_{mode}$ , is set at  $4.5 \mu\text{m}$ . The active region radius,  $r_{act}$ , is set at  $8.5 \mu\text{m}$ .

The spreading of current underneath the blocking layer has a significant affect on the laser's threshold. The relation between the leveling-layer resistance and the current distribution near threshold bias levels is quantified in Figs. 6.10 and 6.11. Fig. 6.10 shows the current density injected into junction at a bias of 1 mA. The calculation was made for a  $0.3 \mu\text{m}$  p- layer with resistivities of 416,

1041 and 2080  $\Omega\mu\text{m}$  corresponding to doping densities of  $1 \times 10^{18}$ ,  $5 \times 10^{17}$  and  $1 \times 10^{17} \text{cm}^{-3}$  respectively. The current is progressively better confined, resulting in higher current densities in the center for the same bias.

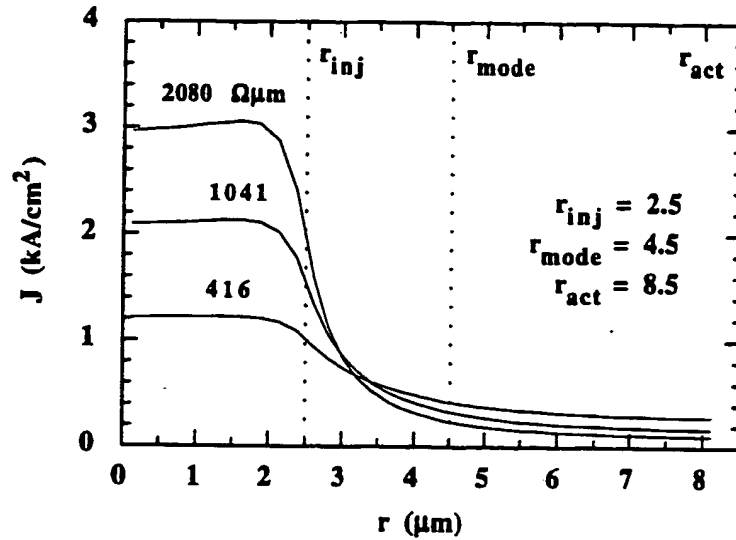


Fig. 6.10. Current-density profile at a bias of 1 mA for progressively more resistive leveling layers. Structure is shown in Fig. 6.9.

While the confinement seems good for all three cases, the cylindrical geometry makes the leakage significant. It is instructive to plot the product of the current density with the radius, so that the area under the curve is proportional to the current. This is shown in Fig. 6.11 for the same three cases. Also shown is the optical mode intensity. From the area under the curve, one can see that the threshold current would be more than doubled with the lower resistance leveling layer. This analysis is for a diode with a non-ideality factor of 3.6. The higher the non-ideality factor, the greater the confinement problem. For low threshold currents it is essential that the structure provide good carrier confinement. For the remaining calculations I will use a leveling layer resistivity of 2080  $\Omega\mu\text{m}$ .



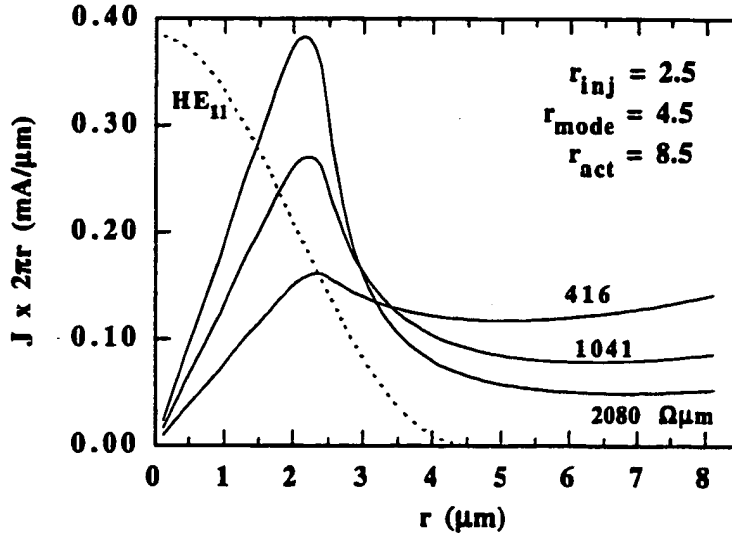


Fig. 6.11. Current-density profiles of Fig. 6.9 multiplied by  $2\pi r$ . Area under each curve equal to the injected current of 1 mA. The fundamental mode is shown as a dashed line. Threshold currents would be doubled for the lower resistance case.

With the structure defined, current-injection simulations were performed to generate the  $I$ - $V$  and current-density profiles. As an example, the voltage distribution in the structure at a bias of 2.5V/ 8mA is shown in Fig. 6.12. The current blocking region and junction mesh points are labeled for clarity. One can identify the various voltage drops from the figure. Surprisingly, the blocking region supports a maximum voltage drop of only 1.1V due to a voltage divider effect with the high resistance of an unbiased junction. The voltage drop from the p contact to the center of the p+ layer is 0.34V. The voltage drop across the junction is 1.9V in the center while the voltage drop from the center to contact in the n+ layer is less than 0.1V. The current-density profiles calculated for the structure are shown in Fig. 6.13. The inset shows the calculated  $I$ - $V$  curve. The structure has a calculated resistance of 87 $\Omega$ . From the curves it is clear that the overlap with a 9  $\mu m$  diameter mode should be excellent, with minimal spatial hole burning.

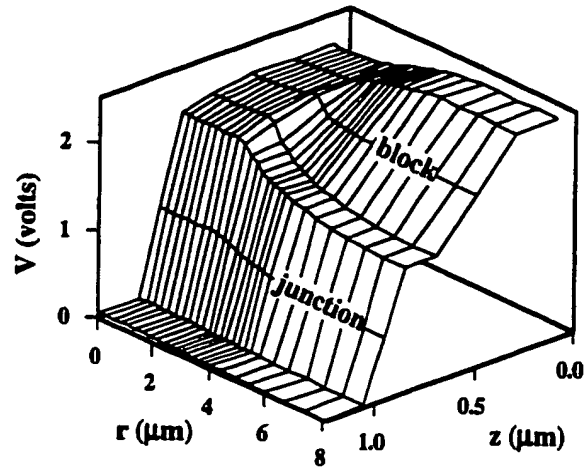


Fig. 6.12. Voltage distribution in the current-apertured structure at a bias of 2.5V / 8 mA. The junction and current blocking grid points are identified for clarity.

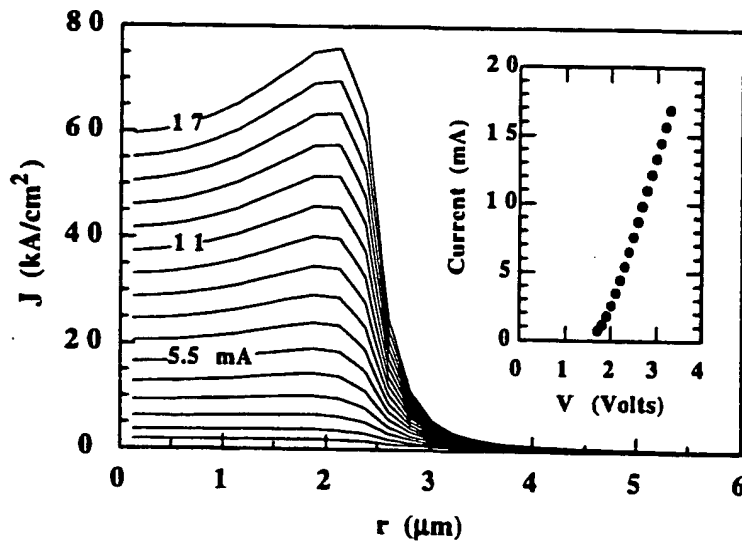


Fig. 6.13. Calculated  $I$ - $V$  and associated current-density profiles for the current-apertured structure shown in Fig. 6.9.

The calculated  $L$ - $I$  characteristics are shown in Fig. 6.14 along with the calculated curve for the 7  $\mu\text{m}$  laser. The  $L$ - $I$  calculations used the current-injection profiles in shown in Fig. 6.13 and an optical mode diameter of 9  $\mu\text{m}$ . All other parameters including optical loss and thermal impedance are identical to the 7  $\mu\text{m}$  laser given in Table 6.1. With a larger mode and ohmic contact, the optical scattering losses and contact resistances should be lower for the current-apertured design, but I have kept them identical to make the calculation conservative. The output power and linearity of the laser characteristics have been dramatically improved. Although not shown, if the improved thermal design with an effective thermal conductivity of 0.063 mW/ $^{\circ}\text{C}$  is used the output power continues to increase to 10 mW. The power conversion efficiency has

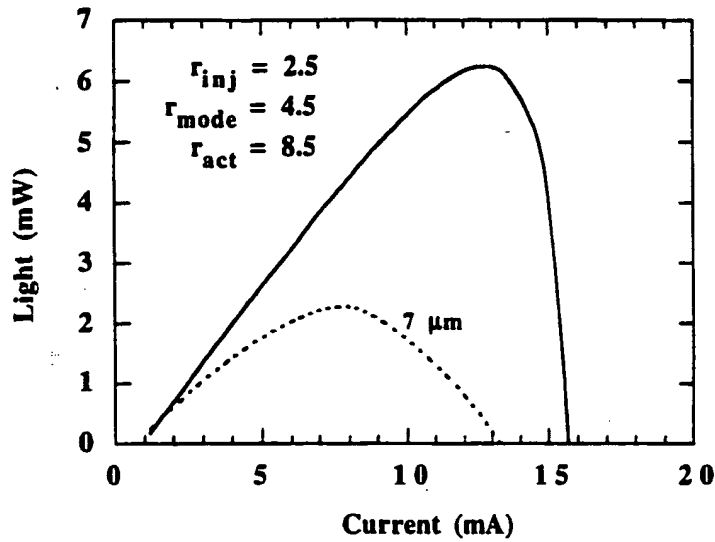


Fig. 6.14. Calculated  $L$ - $I$  characteristics for the current-apertured laser using the current-injection calculations in Fig. 6.13 and the model parameters for the 7  $\mu\text{m}$  laser in Table 6.1. Also shown for reference is the calculated  $L$ - $I$  curve for the 7  $\mu\text{m}$  laser as in Fig. 6.6.

also been doubled from 10% to 20%, requiring only 5.1 mW of input power to produce 1 mW of optical power. The differential efficiency is 51%, nearly equal to the product of the optical efficiency,  $\eta_{opt}$ , and the injection efficiency,  $\eta_{inj}$ .

The current-apertured design enables a return to the idealized one dimensional performance discussed in Appendix D.

In addition to the improved efficiency, single-transverse-mode operation has been ensured. As a reference, the modal-gain curves for the  $7\text{ }\mu\text{m}$  laser calculations of Fig. 6.2 are shown in Fig. 6.15. While the laser operated with a single mode under CW operation, multimode operation was observed during large-signal modulation. The modal-gain curves show that a mode discrimination of at least 0.2% for the first order mode and 0.3% for the second-order mode is required to maintain single-mode operation.

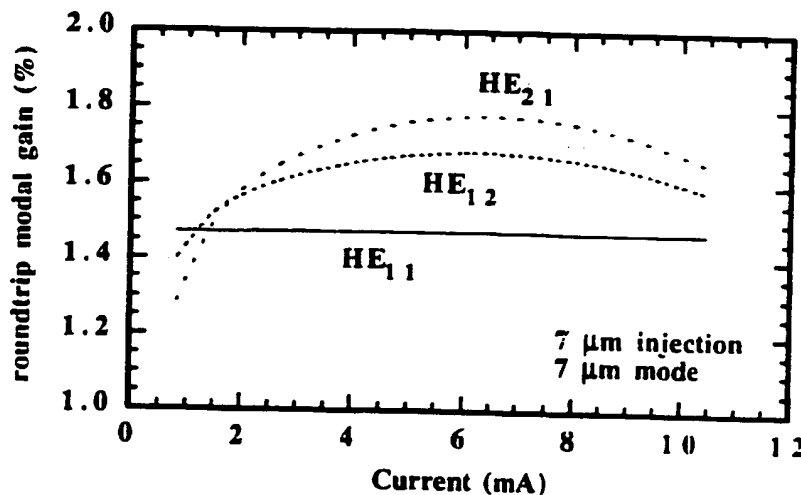


Fig. 6.15. Roundtrip modal gain of the first three transverse modes during the course of the  $L-I$  curve of the  $7\text{ }\mu\text{m}$  laser shown in Fig. 6.14. Calculations assume that only the fundamental mode is lasing.

In contrast, the modal-gain curves for the current-apertured laser, shown in Fig. 6.16, show that the higher-order modes never even reach the threshold-gain level of the fundamental mode. With the single-longitudinal-mode properties of the short vertical cavity, the current-apertured intra-cavity design ensures single-mode operation.

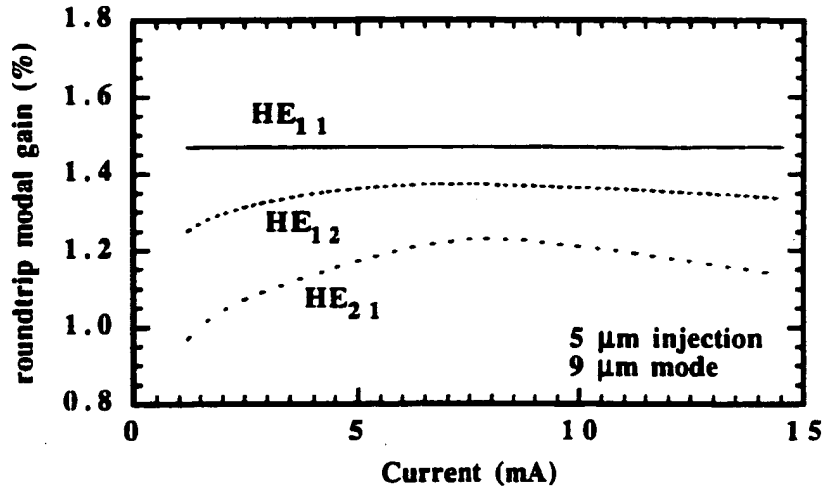


Fig. 6.16. Roundtrip modal gain of the first three transverse modes during the course of the  $L$ - $I$  curve shown in Fig. 6.14 for the current-apertured laser design. Single mode operation is ensured at all biases.

The intra-cavity contacted lasers presented in Chapter 5 represent the state of the art in vertical-cavity laser performance, yet they are merely a stepping stone to a much higher performance class of vertical-cavity lasers. This section has introduced a realizable current-apertured structure based on the intra-cavity contacted lasers developed in my doctoral work. In addition to the improved electrical and optical properties analyzed in detail in this section, current-apertured lasers fabricated on semi-insulating substrates would have all the high-speed advantages of an intra-cavity contacted design. While much work remains in the areas of diode ideality, selective doping and dielectric mirror technology, the future looks very bright for these advanced laser designs.

#### 6.4 Conclusion

During the course of my doctoral work, I have had the opportunity to participate in the evolution of a new class of semiconductor laser. Starting with a proposal for a periodic-gain vertical-cavity laser with semiconductor distributed

Bragg reflectors [3], I have been intimately involved in the development of three generations of index-guided vertical-cavity laser designs. The futile attempts to realize a sidewall-contacted periodic-gain structure evolved into the high-speed intra-cavity contacted designs. During this period, I have developed device models to simulate the devices and show the directions for improved device performance. The coupling between theory and experiment has been a focus of my work. In many ways the process is similar to the iterations used by the numerical models of Chapters 2 and 3. Using the design tools available, a device structure is designed and then fabricated. The experimental characteristics are then used to refine the model, and a new design created. This cycle iterates towards producing an optimized device with comprehensive device models. The refined device models reflect our understanding of the internal physics. With each iteration, our understanding approaches the reality that was always there. The clearer our perception, the better our choices will be. Careful modeling ensures that the maximum amount of information is gained from each cycle.

This search for reality is particularly important in the cleanroom. One mistake, one processing flaw, and the devices can become useless. For a fabrication cycle taking three weeks or more, each step must be completely understood. Yet there was no existing process for the fabrication of vertical-cavity lasers, let alone the intra-cavity contacted design. Many times I came up with a fabrication sequence only to find my understanding did not match reality. Fabrication is a humbling experience, for there are far too many variables to control. Only by careful observation, watching for correlations that may appear days apart, was I able to make sense of the many processing steps and machines involved and create a well controlled, repeatable process. More of my time was spent in the cleanroom than anywhere else. Yet the common struggle provides a kind of community, and I have been fortunate to benefit from an excellent group of students fabricating devices at UC Santa Barbara.

My primary interest has been to understand the device physics and the development of predictive models, without becoming a professional programmer. The separation of the thermal, electrical, optical and current-to-light simulations

greatly reduces the computation time. The strongly index-guided structures with their simple geometry have allowed such a separation. Models for the more common proton-implanted "gain-guided" structures, in contrast, require the coupling of the equations into a single self-consistent solution. In parallel with my progress in device modeling there has been a dramatic improvement in the power and availability of computers. The calculations in Chapter 6 were made over the course of a few days on a personal computer using the HiQ platform. At the outset of my research such easy access to powerful numerical tools was unheard of. Perhaps the most challenging modeling problem is a general solution for the optical modes in the more complex vertical-cavity laser designs which are a hybrid of the gain-guided and index-guided structures. The high quality-factors of the vertical cavities require highly-accurate solutions, yet the strong index discontinuities at both the distributed-Bragg-reflector interfaces and the current constriction make it difficult to employ beam propagation methods. The development of comprehensive optical models remain a challenging research topic.

When I began this work, vertical-cavity lasers were an optoelectronic curiosity. I have now demonstrated sub-milliamp thresholds, temperature-insensitive operation, multi-gigabit data transmission, single-mode operation and record modulation efficiency with arrays of these low-beam-divergence lasers. In the course of our research, our group has claimed that vertical-cavity lasers are superior to in-plane lasers in almost every respect except power. Their performance in the commercial marketplace, however, will show if our understanding is in agreement with reality.

#### References

1. US Patent # 5,343,487
2. A. Yuen, *Private Communication*. Hewlett Packard, Palo Alto, CA, 1994
3. US Patent # 4,873,696

## Appendix A: Refractive Index of $\text{Al}_x\text{Ga}_{1-x}\text{As}$

A refractive index model used for calculating the optical properties of AlGaAs has been published by Afromowitz[1]. The model builds upon a single oscillator model in which the index,  $n$ , at a photon energy,  $E_{hv}$ , is given by:

$$n^2 - 1 = \frac{E_o E_d}{E_o^2 - E_{hv}^2} \quad (\text{A.1})$$

which results from a delta function oscillator of strength  $\pi E_d/2$  at an energy  $E_o$ . Instead of assuming a delta function, the absorption in the Afromowitz model is treated as having a quadratic dependence on photon energy over a limited band, and zero elsewhere. The Kramers-Kronig relations are used to express the real part of the dielectric constant in term of the absorption. The relation is then expanded in terms of energy moments. The values for the absorption strength and bandwidth of the quadratic model are chosen to agree with the known single oscillator values for GaAs and AlAs. To interpolate between the binary materials, the single oscillator energy,  $E_o$ , is scaled with the direct band gap energy,  $E_\Gamma$ , while the oscillator strength,  $E_d$ , is taken to be a linear function of the aluminum composition  $x$ . The functional forms for the various energies are:

$$E_o = 3.65 + 0.871x + 0.179x^2 \quad (\text{A.2})$$

$$E_d = 36.1 - 2.45x \quad (\text{A.3})$$

$$E_\Gamma = 1.424 + 1.266x + 0.26x^2 \quad (\text{A.4})$$

where all energies are in units of eV. The resulting model is:

$$n^2 - 1 = M_{-1} + M_{-3}E_{hv}^2 + \frac{\eta}{\pi} E_{hv}^4 \ln \left( \frac{E_\Gamma^2 - E_{hv}^2}{E_o^2 - E_{hv}^2} \right) \quad (\text{A.5})$$



$$M_{-1} = \frac{\eta}{2\pi} (E_f^4 - E_\Gamma^4) \quad (\text{A.6})$$

$$M_{-3} = \frac{\eta}{\pi} (E_f^2 - E_\Gamma^2) \quad (\text{A.7})$$

where the absorption band cutoff energy,  $E_f$ , and the quadratic absorption coefficient,  $\eta$ , are defined as:

$$E_f = \sqrt{2E_o^2 - E_\Gamma^2} \quad (\text{A.8})$$

$$\eta = \frac{\pi E_d}{2E_o^3 (E_o^2 - E_\Gamma^2)} \quad (\text{A.9})$$

The reflectivity spectrum is often measured at photon energies above the bandgap. Equation (A.5) has a pole at  $E_{hv} = E_\Gamma$ , and therefore it must be modified to be applicable in the absorbing regime. Corzine [2] has suggested using a linear increase in the index above the band edge to agree with the data of Casey and Panish [3]. For photon energies  $E_{hv} > E_\Gamma$ , Eqn. (A.5) is replaced with:

$$n = n(E_\Gamma^-) + \frac{0.35}{eV} (E_{hv} - E_\Gamma^-) \quad (\text{A.10})$$

where  $E_\Gamma^- = E_\Gamma - 25 \text{ meV}$  and  $n(E_\Gamma^-)$  is calculated using Eqn. (A.5). The resulting index model is used in our group to design vertical cavity lasers. A plot showing the index of various alloys vs. wavelength is shown in Fig. A1 below.

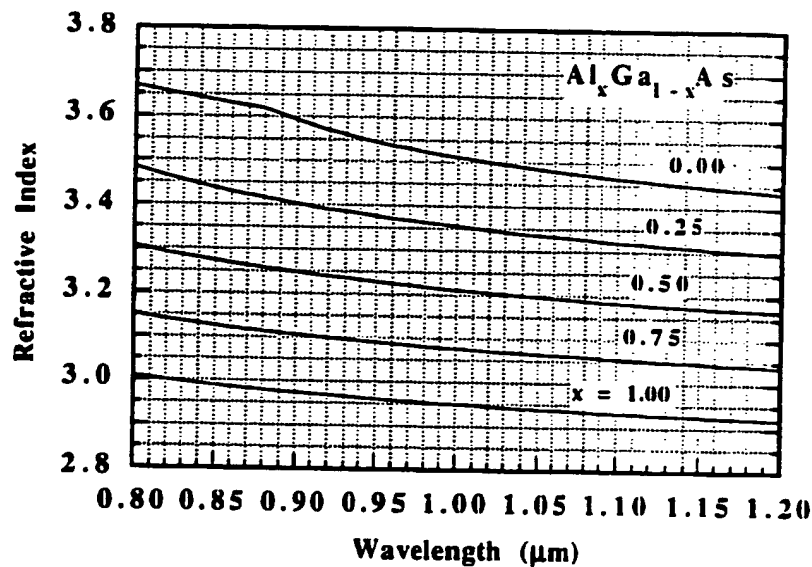


Fig. A1. Plot of the index of refraction given in Eqn. (A.5) as a function of wavelength for various aluminum mole fractions  $x$ .

Many vertical cavities in the AlGaAs system have been designed at UCSB using this model.

#### References

1. M.A. Afromowitz, "Refractive Index of  $\text{Ga}_{1-x}\text{Al}_x\text{As}$ " *Solid State Comm.* 15 (59) pp. 59-63. (1974)
2. S.W. Corzine, *Design of Vertical-Cavity Surface Emitting-Lasers with Strained and Unstrained Active Regions*, Ph.D. Dissertation. University of California at Santa Barbara (1993) ECE technical report #93-09
3. H.C. Casey and M.B. Panish, *Heterostructure Lasers, Part A*. Orlando: Academic Press, 1978, figure 2.5-6, p.46.



## Appendix B: Quantum Well Model

### B.1 Quantum Well Active Regions

The active region is the location where the current is converted into light. This is achieved through stimulated emission process where the electric field of an electromagnetic wave stimulates a transition of an electron in the conduction band into a vacancy in the valence band, generating a photon and increasing the intensity of the wave. The transition rate is proportional to the product of the gain and the optical intensity, and thus once the threshold gain has been achieved the relation between the additional injected current and output light intensity is linear. The current required to maintain the threshold gain is called the threshold current. It is desirable to minimize and stabilize the threshold current to simplify laser drive electronics, improve power conversion efficiency, reduce temperature sensitivity and so on. Accurate gain models are essential to the design of temperature stabilized operation.

The gain is produced by creating a population inversion in the active region, where electrons populate the conduction band and empty states or holes exist in the valence band. The carrier population is described by Fermi-Dirac statistics, and thus only a range of photon energies near the bandgap experience gain. Those below the conduction to valence band transition energies (longer  $\lambda$ ) do not interact and hence the material is transparent with no gain or absorption. Those photon energies well above the band edge (shorter  $\lambda$ ) interact with states which are not inverted and hence the photons stimulate transitions from the valence band into the conduction band, resulting in absorption. In between the gain experiences a peak value.

The relationship between peak gain per unit length and current per unit volume  $J_{nom}$  is schematically shown in Fig. B.1, where the electron and hole densities are assumed to be equal due to charge neutrality. Note that there is a transparency current density above which the gain increases rapidly. If the curve

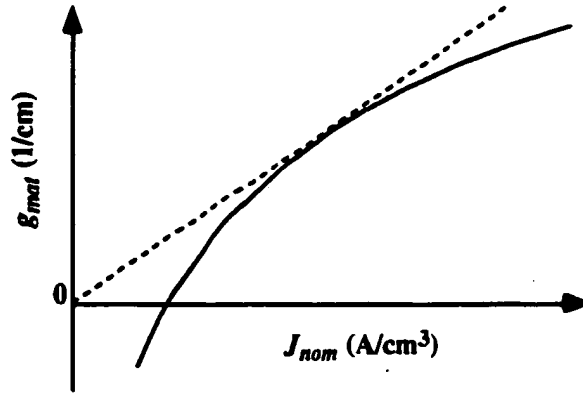
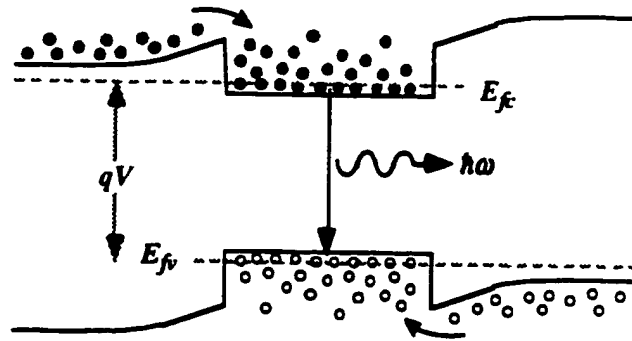


Fig. B.1. Gain per pass and current density normalized to the material thickness. A linear relationship as shown by the dashed line would have a constant threshold current density ( $\text{A/cm}^2$ ) for any active region thickness.

were linear through the origin, the total threshold current density,  $J_{nom}/l_{act}$ , required for a given  $g_{mat}l_{act}$  would be independent of thickness. The presence of the transparency offset makes it preferable to use thinner active regions. On the other hand, the saturation in gain with increasing current results in inefficient use of current to produce gain if the layer is too thin. Also shown in the figure is a dashed line from the origin, representing an idealized linear relation. The higher the slope, the lower the threshold current for a given per pass gain. The maximum slope is for the line drawn which is tangent to the curve. The tangent point therefore represents the optimal operating point of the gain material to minimize the threshold current. One would choose the thickness to operate the active region at the tangent point. In practice, other concerns make this a first order estimate of an appropriate design.

In order to generate the population inversion, the active region is placed in the center of a p-i-n junction of a III-V semiconductor under forward bias as shown in Fig. B.2. The wider bandgap materials on either side of the active layer



**Fig. B.2.** Schematic energy band diagram of a p-i-n junction with an active region cladded by higher bandgap materials. The active region acts as a trap for the electrons and holes, making it possible to achieve a population inversion in a limited volume.

are called the cladding layers. Due to their wider bandgap, the cladding layers are transparent to light generated in the active region. The cladding on the left has been doped n-type by introducing silicon (Group IV on the periodic chart) into the lattice during growth, replacing a small fraction of Group III atoms (Ga, Al). The extra electron is thermally excited into the conduction band. The cladding on the right has been doped p-type by introducing beryllium, again replacing a small fraction of Group III atoms in the crystal. The beryllium is a Group II element, leaving one electron missing relative to the Group III atoms. This electron vacancy creates a hole in the occupied valence band. Due to the interaction of the electronic states with the crystal potential, the electrons in states at the top of the valence band behave as if they had a negative mass, with their energy decreasing with increasing velocity. Thus a vacancy behaves like a positively charged, positive mass particle and is called a hole. In equilibrium, the electrons and holes on either side of the junction diffuse towards each other, leaving ionized dopants behind. The ionized dopants form a dipole whose electric field retards further diffusion. Under forward bias, the applied field reduces this built-in dipole field and both carriers diffuse into the center of the junction. The lower bandgap active region makes an efficient trap so that there are high densities of electrons in the

conduction band and vacancies in the valence band in the same space, creating a population inversion.

The electrons and holes recombine in the active region in various manners. In a good material, the primary mechanism is spontaneous emission. In addition, there can be recombination due to surface and interface states. At high carrier densities, recombination due to Auger processes and leakage out of the active region can become significant as well. To minimize the threshold current, the active region thickness is reduced. Eventually, the confinement of the carrier between the cladding layers affects the electronic states and the bulk electronic states no longer describe the structure's properties. When the confinement region width is on the order of 100Å, the electron and hole wavefunctions becomes quantized in the confined direction. The confined layer is then called a quantum well. The primary advantages are a step function density of states and the ability to modify the bandstructure by introducing strain in the active crystal material. These advantages are discussed in the next section.

### B.2 Temperature and carrier dependence of the gain spectrum

The relationship between carrier density, temperature and the density of states is the found using the Fermi-Dirac distribution or Fermi function:

$$f_{c,v} = \frac{1}{1 + \exp((E_{e,h} - E_{fc,fv})/k_B T_{jct})} \quad (B.1)$$

where  $E_{fc,fv}$  are the quasi Fermi levels in the conduction and valence bands,  $k_B$  is Boltzmann's constant and  $T_{jct}$  is the junction temperature. Under forward bias the system is not in equilibrium, however the high carrier densities in the two respective bands allows us to define quasi Fermi levels independently for each carrier pool as shown in Fig. B.2. The difference between the quasi Fermi levels

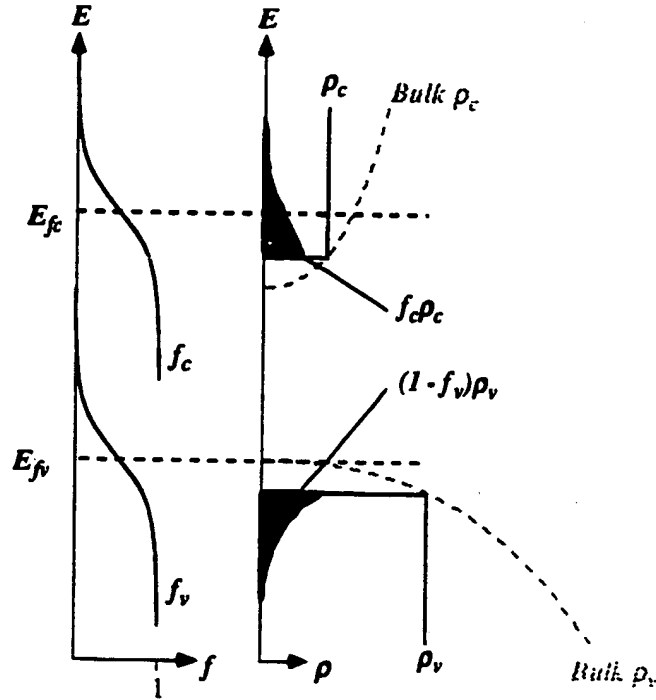


Fig. B.3. Schematic of the Fermi-Dirac distributions, the density of states and their product for the valence and conduction bands for a quantum well. The shaded areas represent the electron and hole densities in the well.

is equal to the product of the applied voltage and the electron charge. The Fermi function gives the probability of a state being occupied as a function of the energy of that state, the local quasi Fermi level and the local temperature. Note that the Fermi function has a value of  $1/2$  for states at the quasi Fermi level and approximates the exponentially decaying Boltzmann distribution function for energies more than several  $k_B T_{j\alpha}$  away from the quasi Fermi level. The density of states,  $\rho_{c,v}(E)$ , gives the density of electronic states at an energy  $E$  in an interval  $dE$ . The product of the Fermi function and the density of states gives the density of occupied states. The integral over the conduction band energies gives the total electron density. Likewise, the product of the valence band density of



states with one minus the Fermi function gives the density of unoccupied or vacant states, which gives the hole density when integrated over the valence band. This is shown schematically as the areas in Fig. B.3. Also shown are dashed lines representing the bulk density of states that would exist without the quantization.

At the high carrier densities typical in a laser junction, charge neutrality is a good assumption. The quasi Fermi level positions will adjust relative to the bandgap so that the shaded areas shown in the Fig. B.3 are equal. The gain for a photon of energy  $\hbar\omega$  is given by [1]:

$$g(\hbar\omega) = \left( \frac{1}{\hbar\omega} \right) \frac{\pi q^2 \hbar n_g}{\epsilon_0 c n^2} |M_T|^2 \rho_{red}(\hbar\omega) (f_c - f_v) \quad (\text{B.2})$$

$$\rho_{red}(\hbar\omega) \equiv \frac{\rho_c \rho_v}{\rho_c + \rho_v}, \quad E_e - E_h = \hbar\omega \quad (\text{B.3})$$

where  $q$  is the electron charge,  $\hbar$  is Plank's constant,  $n_g$  is the group index,  $n$  the real index,  $c$  is the speed of light,  $M_T$  is the transition matrix element and  $\rho_{red}$  is the reduced density of states. This simple definition of  $\rho_{red}$  is only applicable to quantum wells with parabolic bands, but is useful to provide a feel for the gain dependency on the density of states in the two bands. To determine the total gain, a lineshape function must be convoluted with the gain function to include the finite lifetime of the states. Equation (B.2) shows that the transition rate increases with a higher probability of an electron in the excited state  $f_c$  and a higher probability of a vacant ground state  $(1-f_v)$ . Consider the gain for a photon of energy just above the band edge. A lower total carrier density is required to produce a given gain for the quantum well than the bulk because of the step density of states. As can be seen from the area under the curve, many more carriers would be required to maintain the same quasi Fermi levels in the bulk case. The result is that quantum well produce more gain for a given carrier density.

The other important advantage of quantum wells is the ability to alter the band structure by introducing strain [2]. Strain is introduced by growing the quantum well material on a substrate with a different lattice constant. For thin layers, the crystal adjusts to match the lattice constant of the substrate while maintaining the unit cell volume by compensating in the growth direction. This has important effects on the density of states. In Fig. B.3 the density of states are shown to be different for the valence and conduction bands, with  $\rho_v$  larger as is typically the case. Since the density of states in k-space are identical and transitions must be made between electronic states with the same  $k$  (the photon wave vector is negligible) the reduced density of states of Eqn. (B.3) must be used. Thus for a given carrier density, the higher density of states results in a lower vacancy probability in Eqn. (B.2) without increasing the gain. The best situation is for equal density of states in the conduction and valence bands. It has been shown that the band structure and density of states can be modified by growing strained materials. In a GaAs/Al<sub>0.2</sub>Ga<sub>0.8</sub>As unstrained quantum well, the valence band density of states is 5-10 times higher than that of the conduction band. In an In<sub>0.2</sub>Ga<sub>0.8</sub>As/GaAs strained quantum well, the ratio is closer to 2. The result is more gain for a given carrier density.

The above two band picture of quantum well gain is highly simplified. In fact there are several degenerate valence bands whose states become mixed with the introduction of quantum wells. These band mixing effects must be included to accurately calculate the gain of quantum wells and to include the effects of strain. Corzine wrote a comprehensive program, QWGain, which calculates the quantum well gain properties. Details of the calculation are given in ref's. [1, 3]. As an example, plots of the gain per pass vs. wavelength and the peak gain per pass vs. sheet carrier density are shown in Fig. B.4. The calculation is for a compressively strained 80Å In<sub>0.175</sub>Ga<sub>0.825</sub>As quantum well with GaAs barriers where the gain per pass is the  $g_{mat}l_{well}$  product. With a higher gain per pass, less quantum well material is needed than in the case of bulk material, reducing the threshold current.

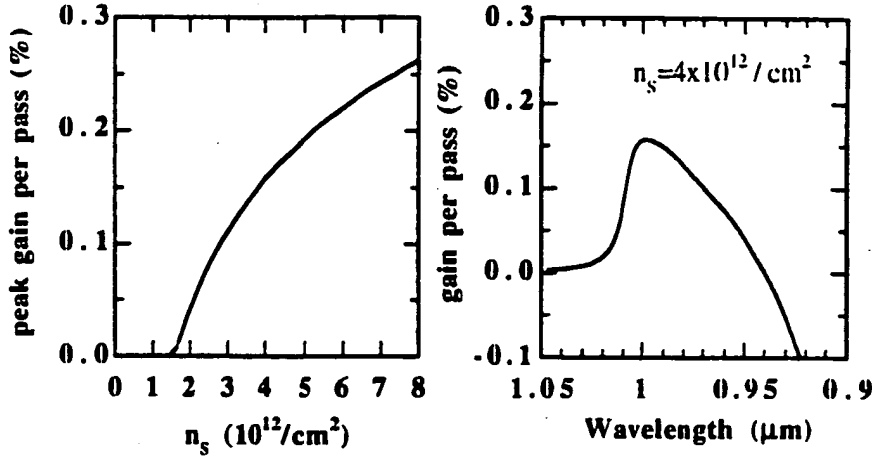


Fig. B.4. Calculated peak gain and gain spectrum for an  $\text{In}_{0.175}\text{Ga}_{0.825}\text{As}$  quantum well. Calculation made with Corzine's QWGain program.

for a given cavity design. In addition, the advantages of the longitudinal enhancement factor is significant only for  $l_{act} < 600\text{\AA}$ . Quantum wells have therefore become the active material used for most vertical cavity lasers. For the example cavity design in Section D.2.5, the round trip threshold gain  $G_{th}$  is 1.32%. Using the calculated  $\xi_{enh} = 1.82$  for the three wells yields a gain per pass per well of  $1.32\% / (2 \cdot 3 \cdot 1.82) = 0.12\%$  which is in the middle of the peak gain curve, well below the saturation value of  $\sim 0.25\%$ . Using fewer wells would thus be undesirable as the threshold current would actually increase.

The above calculations were made at a temperature of 300K. The QWGain program calculations of peak gain vs. current have been extensively verified by measurement of in-plane lasers of varying length. An important consideration for vertical-cavity lasers is the change in the gain curves with temperature. The QWGain program includes temperature variation in the Fermi-Dirac distribution. This results in an increasing tail for the distributions shown in Fig. B.3. For modeling vertical-cavity lasers it was necessary to include the band shrinkage with increasing temperature. Furthermore, my modeling of the threshold current

of vertical-cavity lasers with temperature indicated that the spectral gain curve was shifting towards longer wavelengths as the carrier density increased. This shift can be attributed to bandgap renormalization. Since it is the gain at the resonant wavelength that determines the threshold carrier density, shifting gain curves will have significant effects on the measured current-to-light characteristics. It has been necessary, then, to modify the spectral gain curves of the QWGain program to include the effect of temperature and renormalization on the bandgap.

To include the effect of temperature on the bandgap, it is assumed that the InGaAs-GaAs band offset remains constant so that the bandgap shrinkage with temperature for the  $\text{In}_x\text{Ga}_{1-x}\text{As}$  is the same as for GaAs [4]:

$$E_{g \text{ GaAs}} = 1.519 - \frac{\alpha T_{jct}^2}{T_{jct} + \beta} \quad (\text{B.4})$$

$$E_{g \text{ InGaAs}}(x) = E_{g \text{ GaAs}} - 1.506x + 0.422x^2 \quad (\text{B.5})$$

where  $x$  is the indium mole fraction and the bandgap  $E_g$  is for the unstrained material. Using the standard values of  $\alpha = 5.405 \times 10^{-4}$  and  $\beta = 204$ , Eqn. (B.4) predicts a shift in the gain peak with temperature at a rate of  $-0.45 \text{ meV}/^\circ\text{C}$  at 300K. For a lasing wavelength of one micron, that translates to a shift of  $+3.6 \text{ \AA}/^\circ\text{C}$ . The step function density of states results in a sharp edge for the gain spectrum as seen in Fig. B.4. As well as spreading out on the shorter wavelength side due to an increasing Fermi function tail, the spectrum also shifts towards longer wavelengths with increasing temperature.

To include the bandgap renormalization, a phenomenological model of this many body effect is used. The bandgap renormalization is a result of Coulomb interactions present in the spatially overlapping electron and hole densities in the active region. Since the Coulomb potential is dependent on the distance between particles, it is not surprising that the effect is roughly proportional to the cube root of the carrier density. The model used is

$$\Delta E_g = -C_r n^{1/3}, \quad (\text{B.6})$$

where  $n$  is the carrier density per unit volume. Recent bandstructure calculations including strain and many body effects confirm this functional form at the higher carrier densities of interest. The coefficient I have used is  $C_r = 3.2 \times 10^{-8} \text{ eVcm}$ , the experimental value for GaAs and in agreement with the more recent calculations for a strained  $\text{In}_{0.2}\text{Ga}_{0.8}\text{As}$  quantum well [5]. Combining the above two shifts in the spectral gain curve with the output of the QWGain program yields the gain curves used for modeling the active region. The calculated gain curves and the curve fits used in the numerical laser simulations are discussed in the next section.

### B.3 Numerical gain calculations and curve fits

The QWGain program written by Corzine[6] calculates the material gain of an InGaAs quantum well as a function of carrier density or current density. The current-to-light simulations of Chapter 2 use a curve fit to express the gain as a function of carrier density, wavelength and temperature. Using a curve fit reduces the computation time as the gain is calculated many times during the simulation. This appendix presents the calculated gain curves for an undoped  $80\text{\AA}$  thick  $\text{In}_{0.175}\text{Ga}_{0.825}\text{As}$  quantum well with  $120\text{\AA}$  of GaAs barrier material per well and then fits a simple model to the calculated spectrum. The appendix concludes with a discussion of the importance of a gain offset design for making temperature stabilized vertical cavity lasers.

The curve fit used is shown in Fig. B.5. A linear slope is used for the shorter wavelength side and a parabolic curve for the long wavelength side. The two functions are matched at  $\lambda_0$  which is chosen to ensure that the gain curve and

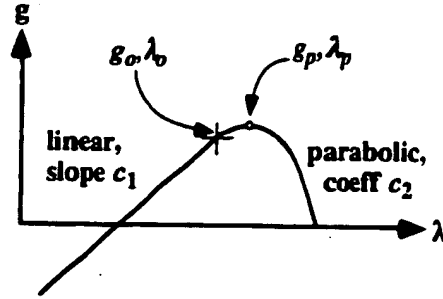


Fig. B.5. Two piece curve fit to the QWGain calculations. The two functions are matched to make the gain curve and its derivative continuous.

its derivative are continuous. The peak gain is a function of carrier density and is expressed as a log fit:

$$g_p(n, T_{jct}) = g_e(T_{jct}) \ln(n/n_t(T_{jct})) \quad (B.7)$$

where the transparency carrier density,  $n_t$ , and the gain at  $e$  times  $n_t$ ,  $g_e$ , are temperature dependent. In Eqn. (B.7) and all following equations the gain is units of  $\text{cm}^{-1}$ , the carrier density is in units of  $1 \times 10^{18} \text{cm}^{-3}$ , the temperature is in Kelvin and the wavelength is in units of  $\mu\text{m}$ . Linear fits are used for the peak gain coefficients:

$$g_e(T_{jct}) = 1869 + 0.3857 T_{jct} \quad (B.8)$$

$$n_t(T_{jct}) = 0.01326 T_{jct} - 2.125 \quad (B.9)$$

The peak wavelength can be expressed using Eqns. (B.4) and (B.6) to calculate the shifts in peak energy and then convert to wavelength:

$$E_p(n, T_{jct}) = E_o - \frac{\alpha T_{jct}^2}{T_{jct} + \beta} - C_r n^{1/3} \quad (\text{B.10})$$

$$\lambda_p(n, T_{jct}) = \frac{1.24 \mu\text{eV}}{E_p(n, T_{jct})} \quad (\text{B.11})$$

where the standard values for the thermal bandgap shrinkage of GaAs [4] of  $\alpha = 5.405 \times 10^{-4} \text{ eV K}^{-2}$  and  $\beta = 204 \text{ K}$  are used. The experimental value for GaAs of  $C_r = 3.2 \times 10^{-8} \text{ eV cm}$  is used to account for bandgap renormalization, in agreement with recent calculations for a strained  $\text{In}_{0.2}\text{Ga}_{0.8}\text{As}$  quantum well [5]. The value of  $E_o$  is chosen to agree with the experimental gain peak. The functional form of the spectral gain curve shown in Fig. B.5 is:

$$g(n, \lambda, T_{jct}) = \begin{cases} g_o + c_1(\lambda - \lambda_o) & \lambda \leq \lambda_o \\ g_p - c_2(\lambda - \lambda_p)^2 & \lambda > \lambda_o > \lambda_g \\ 0 & \lambda \geq \lambda_g \end{cases} \quad (\text{B.12})$$

where the crossover wavelengths and gain are defined as:

$$\lambda_o \equiv \lambda_p - (c_1/2c_2) \quad (\text{B.13})$$

$$g_o \equiv g_p - (c_1^2/4c_2) \quad (\text{B.14})$$

$$\lambda_g \equiv \lambda_p + \sqrt{g_p/c_2} \quad (\text{B.15})$$

With  $g_p$  and  $\lambda_p$  known, the curve fit problem has been reduced to determining the parabolic and linear constants as a function of carrier density and temperature. The procedure used is to first calculate best fits for  $c_1$  and  $c_2$  for spectral curves

calculated at carrier densities of 3, 5, 7 and  $9 \times 10^{18}/\text{cm}^3$ . The spectral gain curve "constants" are then fitted to linear function of  $n$ :

$$c_1(n, T_{j\alpha}) = a_1(T_{j\alpha}) + b_1(T_{j\alpha}) n \quad (\text{B.16})$$

$$c_2(n, T_{j\alpha}) = a_2(T_{j\alpha}) + b_2(T_{j\alpha}) n \quad (\text{B.17})$$

This is done for several temperatures spanning the temperature range of interest, in this case 300K, 350K, 400K and 450K. The  $a$  and  $b$  coefficients are then fitted to linear functions of temperature. The results are:

$$a_1(T_{j\alpha}) = 82285 - 133.5 T_{j\alpha} \quad (\text{B.18})$$

$$b_1(T_{j\alpha}) = -4885 + 10 T_{j\alpha} \quad (\text{B.19})$$

$$a_2(T_{j\alpha}) = (12.2 - 0.02 T_{j\alpha}) \times 10^6 \quad (\text{B.20})$$

$$b_2(T_{j\alpha}) = 0 \quad (\text{B.21})$$

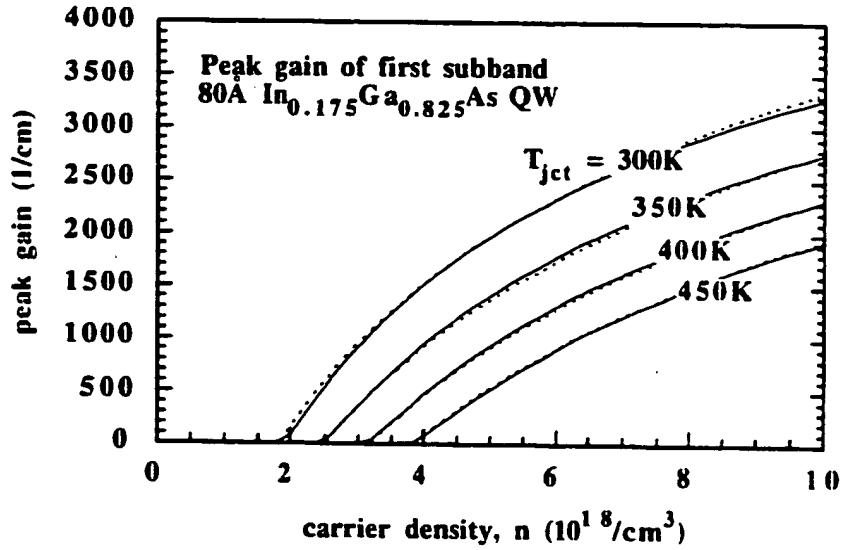


Fig. B.6. Peak gain of the first quantum well subband vs. carrier density for varying junction temperatures. The solid lines are the QWGain calculation, the dashed lines are the curve fit.



Equations (B.7 - B.21) provide the material gain,  $g_{mat}$ , as a function of wavelength, carrier density and temperature. The curve fit is easily implemented as a gain function for the current-to-light simulations.

The curve fit is compared with the QWGain calculations in Figs. B.6 and B.7. The log function, Fig. B.6, shows an excellent fit over this broad temperature range. The peak gain has been limited to the contribution of the first subband because the cavity mode is presumed to be tuned near the band edge. Using  $E_0 = 1.396$  eV the gain spectrum fit shown in Fig. B.7 has reasonably good agreement with the calculated spectra. The largest error is a shift of the peak wavelength at low carrier densities. At a carrier density of  $3 \times 10^{18} \text{ cm}^{-3}$  the peaks are shifted by 7nm, with better agreement at higher carrier densities. The plots for higher temperatures are similar. Overall, this simple curve fit is a good approximation to the actual gain calculations and is very useful for exploring vertical cavity laser designs.

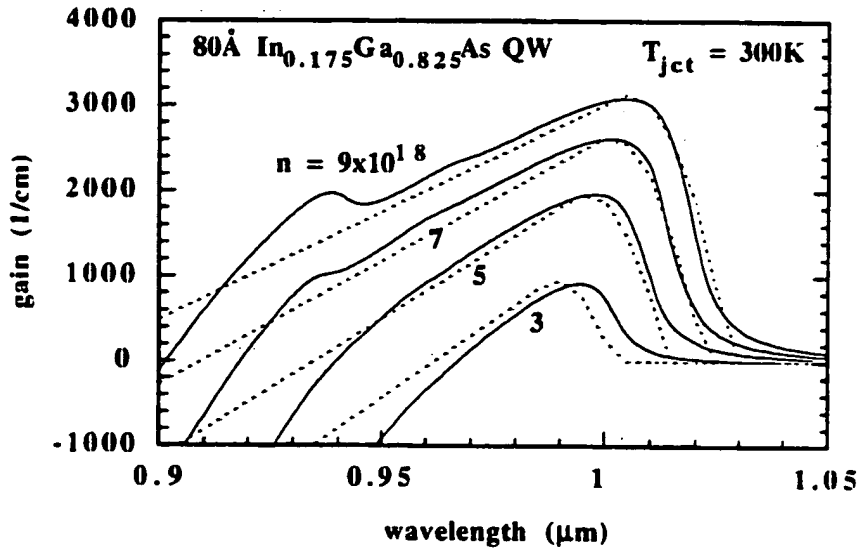


Fig. B.7. Gain spectrum for four carrier densities at a junction temperature of 300K. The solid lines are the QWGain calculation, the dashed lines are the curve fit.

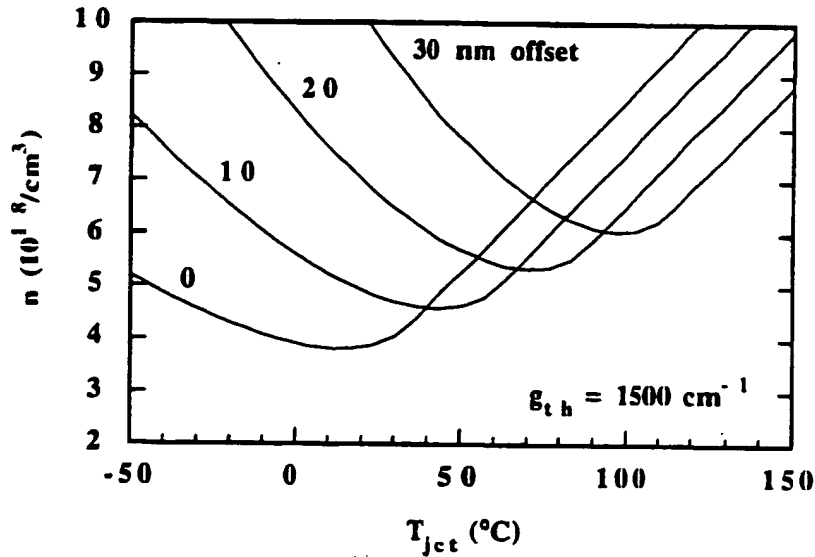


Fig. B.8. Calculated threshold carrier density vs. junction temperature for an 80Å  $\text{In}_{0.175}\text{Ga}_{0.825}\text{As}$  quantum well. The minimum shifts and becomes higher as the gain offset is increased.

Using this analytical gain function, the threshold carrier density can be calculated as a function of junction temperature. Figure B.8 shows the calculations for gain offsets varying in 10 nm steps with the threshold gain held constant at  $1500 \text{ cm}^{-1}$ . The minimum shifts to higher temperature with increasing offset while the minimum carrier density rises due to the elevated temperature. Figure B.9 shows the calculations for varying threshold gain with a constant gain offset of 10 nm. As the threshold gain is decreased, the minimum shifts to higher temperatures due to a reduced Coulomb effect while the minimum width becomes broader. Finally, the limitations of the quantum well gain on the cavity design become clear. Operating at a higher mirror transmission increases the optical efficiency, but also increases the threshold gain which reduces the span for temperature stabilized operation. Adding more quantum wells also reduces the threshold gain but increases the threshold current. Thus the required external

efficiency, threshold current and temperature range of operation force a tradeoff in cavity design.

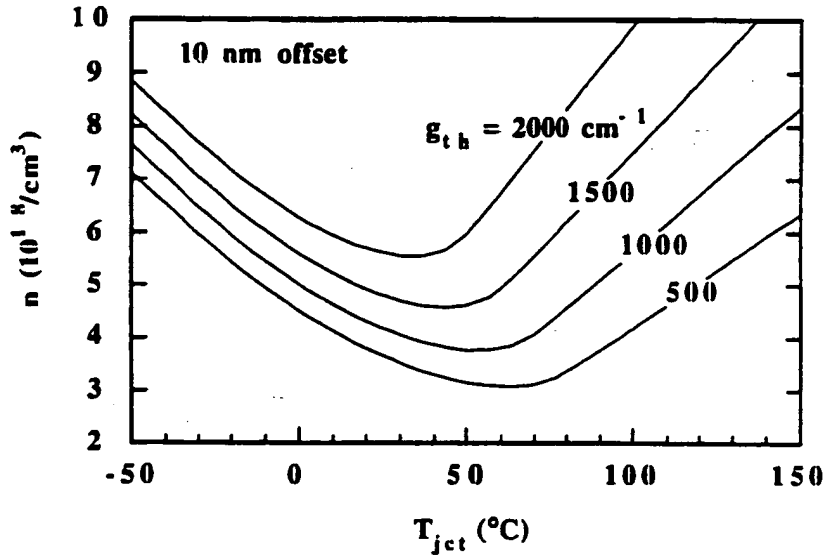


Fig. B.9. Calculated threshold carrier density vs. junction temperature for an 80Å  $\text{In}_{0.175}\text{Ga}_{0.825}\text{As}$  quantum well. The minimum shifts and becomes broader as the threshold gain is reduced.

The final characteristic needed is the relationship between carrier density and current density. There are several recombination currents to consider:

$$J_{th} = \frac{J_{spont}(n) + J_{barr}(n) + J_{Auger}(n)}{\eta_{inj}} + J_{leak}(n) \quad (\text{B.22})$$

where  $J_{spont}$  is the spontaneous emission in the quantum wells,  $J_{barr}$  is the spontaneous emission in the barriers,  $J_{Auger}$  is the Auger recombination and  $J_{leak}$  is the leakage current out of the active region. In Eqn. (B.22) it has been assumed that only the fraction  $\eta_{inj}$  of the injected current recombines in the quantum wells. The first three terms in Eqn. (B.22) scale with the number of quantum

wells and are plotted in Fig. B.10. At lower carrier densities and temperatures,  $J_{\text{spont}}$  is the dominant current. As the carrier density rises  $J_{\text{Auger}}$  becomes important. The Auger current is given as  $C_A n^3$ , and the GaAs Auger coefficient of  $3.5 \times 10^{-30} \text{ cm}^6/\text{s}$  has been used. The appropriate value for the InGaAs wells is unclear, although my modeling in Chapter 2 indicates a value roughly 1.5 times higher as might be expected due to the smaller bandgap. As can be seen in the figure, the spontaneous emission, calculated from the bandstructure, actually decreases with increasing temperature because the matrix elements are lower for the states further from the band edge. The spontaneous emission in the 120Å of barrier material is calculated using a  $Bpn$  dependence where the barrier carrier densities have been calculated by integrating the Fermi function assuming parabolic bulk bands.

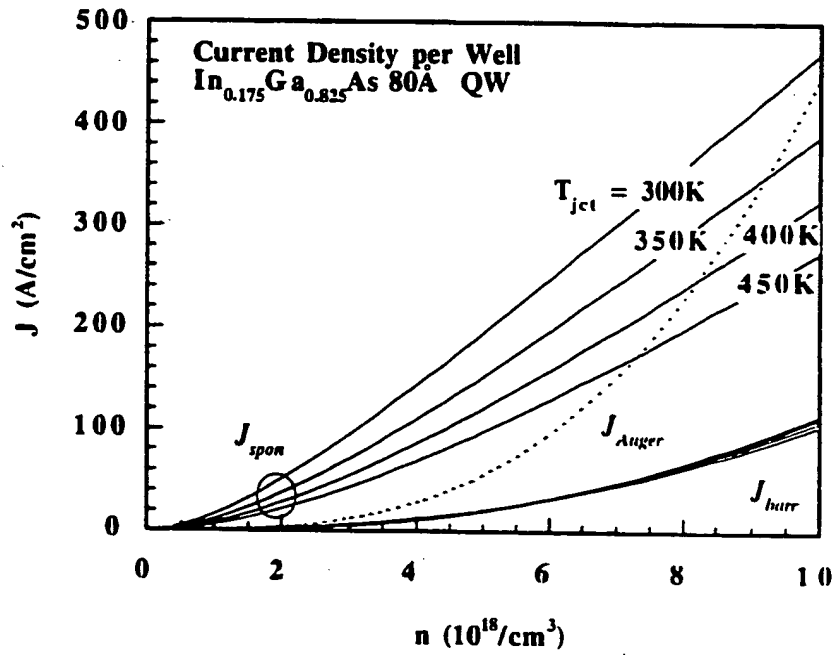


Fig. B.10. Plots of the various current densities necessary to maintain a given carrier density in the quantum well. The curves have been calculated for several temperatures to show the temperature dependence.

Depending on the cladding confinement, the leakage current,  $J_{\text{leak}}$ , can become important at elevated carrier densities and temperature. In a practical laser with limited lateral dimensions, the perimeter to area ratio is significant so that edge effects make an important contribution to the threshold current. In particular, surface recombination or carrier diffusion at the perimeter can double the threshold current of a 10  $\mu\text{m}$  diameter laser. Rather than presenting overly optimistic threshold currents here, those calculations and the models for the various currents are covered in Chapter 2 as the current-to-light characteristics including lateral effects are calculated.

Some final practical notes on active regions are in order. One other additional advantage of InGaAs strained active layers is that the strain lowers the bandgap below that of the GaAs substrate. This allows the development of through the substrate "bottom emission" designs. An additional benefit is that GaAs can be used for the contact layers. Since AlGaAs tends to oxidize over time, the GaAs contacts are more stable. As discussed in greater detail in Appendix E, the thermal impedance of the AlGaAs alloys can be as much as 10 times higher than GaAs, making it preferable to use GaAs as the high index material in the mirror layers. An additional limitation to the total number of quantum wells is the critical thickness limit on the total stress before the material relaxes [7]. The three quantum well design appears to be stable at molecular beam epitaxy growth temperatures of  $\sim 650^\circ\text{C}$  but this may not hold true at higher temperatures used for other growth or processing techniques. In future devices, alternate material systems may be used which allow the growth of tensile strained barriers to compensate the compressively strained wells. Such a strain compensated active region allows larger numbers of quantum wells which can be desirable for higher efficiencies, higher speed or broader ranges of temperature stabilized operation.

In summary, the gain properties of quantum wells have been introduced to highlight the dependence on wavelength and temperature. The advantages of strained quantum wells have been discussed and specific numerical calculations of the quantum well gain spectrum have been presented, including the bandgap

shrinkage and renormalization due to temperature and many body effects respectively. A curve fit has been introduced which allow numerically efficient simulation of the active region in the current-to-light calculations. Finally, some sample calculations were made to illustrate the effects of the gain offset and the threshold gain level on the temperature stabilized operation of vertical-cavity lasers. Depending on the required laser properties the threshold current, temperature operating range and external efficiency must be balanced for optimal operation.

### References

1. S.W. Corzine, R.H. Yan, and L.A. Coldren, *Optical Gain in III-V Bulk and Quantum Well Structures*, in *Quantum Well Lasers*, P.S. Zory, Editor, 1993, Academic Press: New York, p. chapter 1.
2. E. Yablonovich and E.O. Kane, "Reduction of Lasing Threshold Current Density by the Lowering of Valence Band Effective Mass" *IEEE J. Lightwave Technology*, **4** pp. 504, 1986
3. S.W. Corzine, *Design of Vertical-Cavity Surface Emitting-Lasers with Strained and Unstrained Active Regions*, Ph.D. Dissertation, University of California at Santa Barbara (1993) ECE technical report #93-09
4. S.M. Sze, Physics of Semiconductor Devices, 2nd Edition ed. New York: John Wiley & Sons, 1981, temperature  $E_g$  dependence in Chapter 1
5. D. Ahn and S.L. Chuang, "The Theory of Strained-Layer Quantum-Well Lasers with Bandgap Renormalization" *IEEE Journal of Quantum Electronics*, **30** (2) pp. 350-365, 1994

6. S.W. Corzine, R.H. Yan, and L.A. Coldren. "Theoretical gain in strained InGaAs/AlGaAs quantum wells including valence-band mixing effects." *Applied Physics Letters*, **57** (26) pp. 2835-7. 1990
7. J.W. Mathews and A.E. Blakeslee, "Defects in Epitaxial Multilayers" *J. Crystal Growth*, **27** pp. 118-125. 1974

## Appendix C: Laser Fabrication Process

The fabrication process for the intra-cavity contacted lasers presented in Chapter 5 is outlined in detail below. Italics are used to comment on various steps. Reference to the figures of Chapter 5 are made for clarity. The various chemicals have been carefully chosen to avoid unintended etching of the exposed AlAs layers in the structure. The process was developed using the equipment available in the cleanroom at UC Santa Barbara. The process begins assuming that the wafer surface is clean, as would be the case if the wafer had just been removed from the growth system.

### 1 Liftoff Si

*(two level photoresist mask for clean liftoff)*

Spin Shiply 820-27 3k RPM 30s

Hot Plate Bake 95°C 2min

Flood Expose 5s, 7.5 mW/cm<sup>2</sup>

Hot Plate Bake 95°C 2min

Spin AZ P4110 4k RPM 30s

Hot Plate Bake 95°C 2min

Expose 8s, 7.5 mW/cm<sup>2</sup>, pmesa mask

Develop ~60s 1:4 400k:DI

Inspect for undercut. (looks like a dark ring)

Dip 20s 1:10 NH<sub>4</sub>OH:DI, DI rinse

Load into EBeam Evaporator

Pump down to < 1x10<sup>-6</sup> torr

Evaporate

Si ~2850Å



Liftoff in Acetone  
Rinse in Methanol, DI  
Inspect for clean liftoff

## 2 Waveguide Mask

*(nickel liftoff layer)*

Prebake sample 170°C 10min  
Spin SAL110-PL 5K rpm 30s  
Bake hot plate 210°C 5min

*(two level photoresist mask for clean liftoff)*

Spin Shiply 820-27 3k RPM 30s  
Hot Plate Bake 95°C 2min  
Flood Expose 5s, 7.5 mW/cm<sup>2</sup>  
Hot Plate Bake 95°C 2min  
Spin AZ P4110 4k RPM 30s  
Hot Plate Bake 95°C 2min  
Expose 8s, 7.5 mW/cm<sup>2</sup>, mirr mask  
Develop ~60s 1:4 AZ400k:DI  
Inspect for undercut. *(looks like a dark ring)*

Load into EBeam Evaporator

Pump down to  $< 1 \times 10^{-6}$  torr

Evaporate

Ti 200Å *(improves adhesion)*

Ni 1000Å *(Chlorine etch mask)*

Liftoff in N Butyl Acetate

Blow Dry *(use two beakers, the second to keep samples clean)*

### 3 RIE Etch

*(Etch central waveguide and p mesa)*

Load sample into RIE #1 *(Laser Monitor on Sample)*

Pump down  $\leq 7 \times 10^{-6}$  torr *(5min to etch through, 13 to remove all grass)*

O<sub>2</sub> Etch 10 mtorr 350V 60W 18min

Pump down  $\leq 2 \times 10^{-6}$  torr *(wait at least 1 hr to avoid undercut profile)*

Cl<sub>2</sub> 1mt 350V 7.5sccm 60W

Use laser monitor to determine endpoint. ~23min

*(Etch through active cladding layer just into n contact)*

Unload sample, Inspect, Reload and Etch if needed

Liftoff in Microposit 1165 Remover @ 120°C ~20min

Use stirrer to provide agitation + ultrasonic 10s

Rinse DI, Blow dry.

Inspect, SEM

*(dispose 1165 in waste bottle)*

[Refer to Fig. 4.6]

### 5 Current Constriction Etch

*(Image reversal resist to protect central waveguide from etching)*

Dehydration Hot Plate Bake 115°C 1+ min.

Repeat 4 times:

Spin ELIR 5K RPM 30s

Hot Plate Bake 100°C 90s

Expose 20s, 7.5 mW/cm<sup>2</sup>, udie mask

Hot Plate Bake 115°C 1 min.

*(lower sample slowly to hot plate to avoid bubble formation)*

Flood Expose 2 min., 7.5 mW/cm<sup>2</sup>

Develop 1:4 AZ400k:DI 60s

Rinse DI, Blow dry

Bake 120°C 30 min.

*(promotes photoresist adhesion)*

*(this sequence is followed without breaks to provide a uniform undercur across the wafer)*

Etch 90s 1:4 AZ400k:DI

*(remove aluminum oxides)*

.....DI Dip.....

Etch 15s 1:1:100 H<sub>2</sub>SO<sub>4</sub>:H<sub>2</sub>O<sub>2</sub>:DI

*(remove dry etching damage)*

....then directly into....

Etch 40s 1:10 HCl:DI

*(selectively etch AlAs)*

Rinse 30s DI, Blow Dry.

[Refer to Figs. 4.9, 4.10]

O<sub>2</sub> etch PR skin in PEIIA 150W 300 mtorr 5 min. 30kHz

Strip mask Microposit 1165 Remover @ 120°C ~30min

DI rinse, Blow Dry

*(strip remaining Si on top of waveguide)*

CF<sub>4</sub> 300 mtorr 100W 1min 30s 13.56 MHz

O<sub>2</sub> 300 mtorr 100W 30s 30 kHz

Dip 1:10 NH<sub>4</sub>OH:DI ~10s

DI rinse, Blow Dry

[Refer to Fig. 4.11]

**6 N Mesa Etch**

*(protect laser, mask off for n mesa isolation etch)*

Prebake sample 170°C 10min

Spin AZ4330 3.5k rpm 30s

Hot Plate Bake 1min 30s 95°C

Expose 15s 7.5mW/cm<sup>2</sup>, nmesa mask

Develop 1min 10s 1:4 AZ400k:DI, DI rinse, blow dry

*(use fresh developer mix for each piece to avoid photoresist scum)*

If needed, Etch photoresist scum in PEIIA

O<sub>2</sub> 300 mtorr 150W 1min 30 kHz

Bake 120°C 20min *(promotes photoresist adhesion)*

Selective etch Ga<sub>0.9</sub>Al<sub>0.1</sub>As 1:10 H<sub>2</sub>O<sub>2</sub>:Citric Acid

*(citric acid is anhydrous powder mixed 50/50 by weight with water)*

~70s to go purple, + 60s to go green

continue etch till surface is green & clear

*(Perform in the dark to avoid accelerated etch pins?)*

DI rinse, blow dry

*(may need to let oxidize for ~1hr)*

Remove AlAs by dip 30s 1:10 NH<sub>4</sub>OH:DI

DI rinse, Blow Dry

Strip mask Microposit 1165 Remover @ 120°C ~30min

DI rinse, Blow Dry

Etch PR scum PEIIA O<sub>2</sub> 300 mtorr 150W 3min 30kHz if needed

Inspect, SEM

[Refer to Fig. 4.12]

**7 N Ohmic**

*(two level photoresist mask for clean liftoff)*

Spin Shiply 820-27 3k RPM 30s

Hot Plate Bake 95°C 2min

Flood Expose 5s, 7.5 mW/cm<sup>2</sup>

Hot Plate Bake 95°C 2min

Spin AZ P4330 5k RPM 30s

Hot Plate Bake 95°C 2min

Expose 17s, 7.5 mW/cm<sup>2</sup>, nohmic mask

Develop ~60s 1:4 AZ400k:DI

DI Rinse, Blow Dry

Inspect for undercut. *(looks like a dark ring)*

Dip ~ 10s 1:10 NH<sub>4</sub>OH:DI

Load into EBeam Evaporator

Pump down to < 2x10<sup>-6</sup> torr

Evaporate

Ni 50Å

Ge 170Å

Au 320Å

Ni 200Å

Au 1000Å

Liftoff in 1165 Remover @ 120°C ~20min

Squirt dropper clean, DI rinse, Blow Dry.

Dip 1:10 NH<sub>4</sub>OH:DI ~20s, DI rinse, Blow dry

then load immediately into....

PECVD deposit ~1500Å Si<sub>3</sub>N<sub>4</sub>

*(run a 15min condition and a test run ~15min first!)*

[Refer to Fig. 4.13]

## 8 Dielectric Via

*(open vias in nitride to n ohmic and p mesa)*

Dehydration Bake 170°C 10 min.

HMDS spin 30s 4K rpm

Spin AZ P4210 4k RPM 30s

Hot Plate Bake 95°C 1min 30s

Expose 15s 7.5mW/cm<sup>2</sup> udie mask *(this must not be over exposed)*

Develop 1min 30s 1:4 AZ400k:DI

DI rinse. Blow dry

CF<sub>4</sub> etch nitride 300 mtorr 100W 2min 30 kHz

Dip 15s DI, Blow dry

CF<sub>4</sub> etch nitride 300 mtorr 100W 1min 13.56 MHz

O<sub>2</sub> etch PR skin 300 mtorr 100W 5min 30 kHz

[Refer to Figs. 4.14, 4.15]

Strip in 1165 Remover 150°C 10 min. + squirt dropper

DI Rinse, Blow dry

## 9 Window Protect

*(mask to expose waveguide tops to deposit SiO<sub>2</sub> protection)*

Dehydration Hot Plate Bake 115°C 1+ min.

Spin HMDS 4k RPM 30s

Repeat 3 times:

Spin ELIR 5K RPM 30s

Hot Plate Bake 100°C 90s

220 Appendix C Laser Fabrication Process

Expose 20s, 7.5 mW/cm<sup>2</sup>, scribe mask  
Develop 1:4 AZ400k:DI 60s (*opens lines between arrays for SiO<sub>2</sub> liftoff*)  
Rinse DI, Blow dry  
Flood Expose 2 min., 7.5 mW/cm<sup>2</sup>  
Hot Plate Bake 115°C 1 min.  
Develop 1:4 AZ400k:DI 60s (*exposes tops of waveguides*)  
Rinse DI, Blow dry  
  
Dip 1:10 NH<sub>4</sub>OH:DI ~20s, DI rinse  
Load into EBeam Evaporator (*include test piece*)  
Pump down to < 2x10<sup>-6</sup> torr  
Evaporate  
SiO<sub>2</sub> 1400Å (sweep 8,7....4Å/sec)  
  
CF<sub>4</sub> 300 mtorr 100W 40s 13.56 MHz to etch sidewalls  
  
Liftoff in 150°C Microposit 1165 Remover ~10min + agitation  
Rinse DI, Blow dry.  
Inspect for clean liftoff  
O<sub>2</sub> 300 mtorr 100W 60s 30 kHz for photoresist scum

**10 P Metal and Alloy**

(*double resist masking to open window on pmesa for p ohmic metal*)  
Spin Shiply 820-27 3k RPM 30s  
Hot Plate Bake 95°C 2min  
Flood Expose 5s, 7.5 mW/cm<sup>2</sup>  
Hot Plate Bake 95°C 2min  
Spin AZ P4330 4k RPM 30s  
Hot Plate Bake 95°C 2min  
Expose 12s, 7.5 mW/cm<sup>2</sup>, pmesa mask

Develop ~60s 1:4 AZ400k:DI

Inspect for undercut. (looks like a dark ring)

Dip sample 1:10 NH<sub>4</sub>OH:DI ~30s, DI rinse, Blow dry

Load into Thermal Evaporator

*(align samples on holder to sources carefully)*

Pump down to  $< 1 \times 10^{-6}$  torr

Evaporate P contact

Cr	30Å	~80 Amp
----	-----	---------

Zn	100Å	~45 Amp
----	------	---------

Au	400Å	~120 Amp
----	------	----------

Liftoff in 150°C Microposit 1165 Remover ~10min

Use dropper to squirt clean the surface

Rinse DI, Blow dry.

[Refer to Fig. 4.16]

Alloy in RTA 420°C 30s with 5% H<sub>2</sub> forming gas

## 11 Interconnect Metal and Patterning

Load into EBeam System. (*Include metal etch test piece!*)

Ti	100Å
----	------

Au	2000Å
----	-------

Use rotation at 45° angle 11 inches above crucible

*(actual thickness 1.7x more due to geometry, include test piece)*

Electroplate Au 0.5µm, total ~5 min. using Cyanide Bath

*(include test piece)*



Dehydration Bake 170°C 10 min.

Spin HMDS 4k RPM 30s

Spin ELIR 3k RPM 30s

Bake 95°C 1 min.

Expose Metal Mask 8s

Bake 115°C 1 min.

Blank expose 30s

Dev 1:4 AZ400k:DI 50s

*(the tops of the waveguides should be clear at this point!)*

[Refer to Fig. 4.17]

Au Wet Etch

use Cyanide based etch (Technostrip D) to remove Au ~5min

*(watch for undercutting! Use test piece for exact time)*

Cl<sub>2</sub> Ion Mill

*(Do a practice etch on part of the metal etch test piece first)*

Load into RIE #1

Include metal etch test piece for laser monitor

Pump down  $\leq 2E^{-6}$  torr

Cl<sub>2</sub> Etch 1mtorr 350v

till dielectric etch of SiO<sub>2</sub> shows on laser monitor . ~8min

Liftoff in ~150°C Microposit 1165 Remover ~10min

Use dropper to squirt clean the surface

Rinse DI, Blow dry.

#### 14 Mirror Window Etch

*(Lasers are essentially finished. Now remove the  $\text{SiO}_2$  from the precious top mirror surface)*

Dehydration Bake 170°C 10 min.

Spin HMDS 4k RPM 30s

Spin ELIR 3k RPM 30s

Bake 95°C 1 min.

Blank expose 12s

Bake 115°C 1 min.

Dev 1:4 AZ400k:DI 50s

*(the tops of the waveguides should be exposed at this point!)*

Repeat as needed until tops are clear

CF<sub>4</sub> etch PEIIA 300 mtorr 200W 13.56Mhz

DI Rinse, Blow Dry

*(Always run a 5min chamber condition cycle before 1st etch)*

O<sub>2</sub> etch PR skin 300 mtorr 100W 5min 30 kHz

Strip in 1165 Remover 150°C 10 min. + agitation

DI Rinse, Blow dry

[Refer to Fig. 4.19]

## **Appendix D: Vertical-Cavity Design**

### **D.1 Appendix Overview**

This appendix covers the design of the vertical cavity for a surface emitting laser. To first order, the layer structure is chosen for the desired external quantum efficiency, threshold gain and operating wavelength. The spectral and temperature dependence of the material gain, typically from quantum wells, sets limitations to the design. Consideration of the electrical and thermal material properties results in modified layer structures. These varying design aspects must be balanced in the final layer structure specification. The resulting one dimensional structure can then be grown using a well controlled epitaxial technique as discussed in Chapter 4. Various two and three dimensional effects which determine the structure to be fabricated are addressed in Chapters 2&3. Analytical approaches for the mirror and cavity design have been discussed in detail elsewhere [1-4]. This appendix focuses on the more general numerical approach that I have used for the design of various vertical-cavity lasers.

The first section provides a general discussion of the cavity design, comparing a vertical-cavity laser with a more conventional in-plane laser and then introducing the parameters used to characterize the cavity's optical properties. With the parameters defined, some typical values are used to compare the two types of lasers. The second section develops the transmission matrix techniques used to analyze a cavity's optical properties. Using the transmission matrix, the important concept of the longitudinal enhancement factor is introduced and analyzed and then the properties of distributed Bragg reflectors are explored. The appendix ends by showing how the round trip cavity parameters are determined for a cavity design.

Using the cavity and material parameters covered in this appendix as input, the current-to-light model in Chapter 2 can then be used to calculate the current to light characteristics for practical index-guided vertical-cavity laser structures. This appendix provides the basic vertical-cavity layer structure which can be modified to accommodate intra-cavity contacted designs.

## D.2 Introduction to Vertical-Cavity Laser Design

All lasers require a gain medium inside a resonant cavity. In the case of semiconductor lasers, the gain is provided by a population inversion at a forward biased pn junction. It will be assumed that the reader has a basic understanding of the conventional in-plane semiconductor laser; a good introduction to the subject is given in chapter 15 of ref. [5]. Heterojunction bounded active regions are placed in the center of the pn junction to trap and spatially confine the injected electrons and holes, minimizing diffusion currents at the p-n junction boundaries and maximizing the population inversion for a given drive current. The materials cladding the active region are essentially transparent to the optical field as the bandgaps are chosen to be greater than the photon energy of the active material. In each round trip propagation between the two mirrors the power gained by the resonant field must compensate for the power lost in order to be lasing. As well as providing optical gain, the population inversion in the active region results in spontaneous emission and other carrier recombination effects. The current required to maintain the associated inversion is called the threshold current.

Below the threshold current, the power gained in one round trip inside the cavity is less than the optical power losses due to transmission, absorption and scattering. As the current is raised above a mode's threshold, the gain for that resonant mode becomes greater than its losses. As a result, a photon spontaneously emitted into that mode will be amplified with each round trip oscillation. The intensity of the above threshold mode increases rapidly, depleting the carrier density and reducing the population inversion until the gain equals the loss and a steady state is achieved. In steady state operation this process results in a linear relationship between the light output power and the increase of current above threshold, as long as the threshold current remains constant.

Having given a brief description of laser oscillation, the discussion now turns to the specifics of a vertical-cavity laser. As a starting point of reference, a typical all-epitaxial vertical-cavity laser is detailed in Fig. D.1. The cavity is formed by very high reflectivity distributed Bragg reflectors on either side of an

active region. In the figure, the active region is comprised of three quantum wells, each well only  $80\text{\AA}$  thick. The injected current is converted to light by a mere  $240\text{\AA}$  of material, with internal efficiencies, defined as the fraction of electrons converted

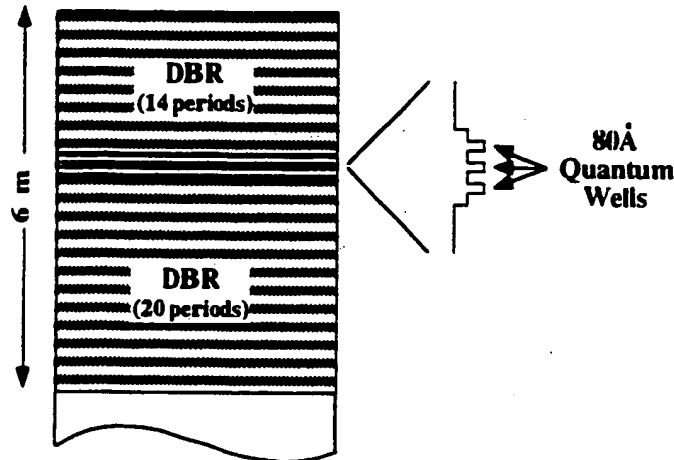


Fig. D.1 A typical vertical-cavity laser cavity.

to photons, on the order of 80%. Since the light is only amplified when passing through such a thin layer, it is crucial that the reflectors transmit only a very small fraction of the power out of the cavities. Otherwise, the gain cannot compensate for the losses and the structure will not be able to lase. Typical reflectivities are 99.2% for the output coupler and 99.9+ % for the other, with additional losses due to free carrier optical absorption on the order of 0.2% for each pass. To realize these high reflectivities, the distributed Bragg reflectors must be grown with precision.

To distinguish their unique characteristics further, it can be useful to compare the power flow in a vertical-cavity laser with the more conventional in-plane semiconductor laser. First consider the lasing diagram for the in-plane laser on the left in Fig. D.2. The schematic shows the intensity of the optical field increasing exponentially to the end, where approximately 70% is transmitted out the facet. The remaining 30% is reflected back into the cavity, amplified by the

gain medium to the other facet where 30% is again reflected back and the cycle repeats. The lasing condition is that the light intensity return to its original value after one round trip. This lasing condition is expressed as

$$R_1 R_2 e^{2g_{eff}^{th} l_{act} - 2\alpha_{eff} l_{cav}} = 1, \quad (D.1)$$

which is typically rewritten as

$$2g_{eff}^{th} l_{act} = 2\alpha_{eff} l_{cav} + \ln\left(\frac{1}{R_1 R_2}\right), \quad (D.2)$$

where  $R_1$  and  $R_2$  are the front and back facet power reflectivities,  $l_{act}$  is the length of the active region and  $l_{cav}$  is the effective length of the cavity. The effective cavity length includes the power penetration of the fields into the distributed reflectors. The effective power gain and loss coefficients,  $g_{eff}$  and  $\alpha_{eff}$ , include overlap integrals with the optical mode. The effective gain which satisfies the threshold condition is denoted as  $g_{eff}^{th}$ .

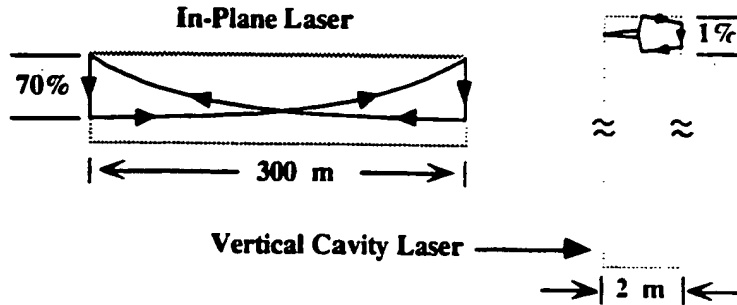


Fig. D.2. Schematic comparing the optical power flow in an in-plane laser and a vertical-cavity laser.

and are defined below. Equation (D.2) expresses the exponential gain coefficient required to compensate for the internal losses and the distributed mirror loss. It is a

useful equation because the gain and losses are generally uniform along the longitudinal axis of an in-plane laser.

The lasing diagram for a vertical-cavity laser, shown on the right in Fig.D.2, is quite different. The gain region is a very small fraction of the cavity, amplifying the wave power ~0.5% over a few hundred angstroms. The short gain length is schematically shown as a step in the optical power as the fields traverse the active region. The entire effective cavity length is only a couple of microns, while the reflectivities are very high and the losses are low. In addition the mirrors are not single boundaries as shown but distributed, with optical penetration depths on the order of a half micron. The mirror layers introduce free carrier absorption losses due to dopants. The growth in the vertical direction allows the designer freedom to vary the dopant distributions and the associated optical losses in less than a quarter of an optical wavelength. This rapid variation of optical parameters along the longitudinal axis calls for a different analysis than in Eqn. (D.2). Just as MOSFET analysis can be simplified by considering sheet charge instead of the detailed charge density profile, we can instead think of integrated or round trip cavity parameters, by using the following definitions:

$$R_1 R_2 = (1 - T_1)(1 - T_2) = 1 - (T_1 + T_2) \quad (D.3)$$

$$e^{2g_{eff}l_{act}} = 1 + 2g_{eff}l_{act} = 1 + G \quad (D.4)$$

$$e^{2\alpha_{eff}l_{cav}} = 1 + 2\alpha_{eff}l_{cav} = 1 + L \quad (D.5)$$

where  $T_1$  and  $T_2$  are the transmission coefficient of the two respective mirrors.  $G$  is the fractional round trip gain and  $L$  is the fractional round trip loss. All of these round trip parameters are on the order of 1% in most designs. Inserting Eqns. (D.3-D.5) into Eqn. (D.1) and keeping only first order terms yield

$$G_{th} = L + (T_1 + T_2) \quad (D.6)$$

which states that the round trip gain due to the active region must equal the power lost due to absorption and transmission. Rather than trying to analytically calculate these values for a complex structure, the  $L$ ,  $T$  and  $G$  parameters can easily be extracted from a transmission matrix analysis which is described in the next section.

Using these round-trip parameters we can express the optical efficiency  $\eta_{opt}$ , defined as the fraction of photons generated which escape out a facet. The optical efficiency is found by taking the ratio of mirror transmission to the total round trip losses,

$$\eta_{opt}^i = \frac{T_i}{T_1 + T_2 + L} = \frac{T_i}{G_{th}} \quad (D.7)$$

The external quantum efficiency out the  $i^{th}$  side, defined as the fraction of injected carriers that are emitted out as photons, is given by the product of the internal efficiency  $\eta_{int}$ , defined as the fraction of electrons converted into photons, with the optical efficiency,

$$\eta_{ext}^i = \eta_{int} \eta_{opt}^i \quad (D.8)$$

The current-to-light characteristic is then expressed as

$$P_{out}^i = \eta_{ext}^i \frac{h\nu}{q} (I - I_{th}) \quad (D.9)$$

where  $P_{out}$  is the light power,  $h\nu$  is the photon energy,  $q$  is the electronic charge and  $I_{th}$  is the threshold current. Equation (D.9) states that the output power is linear with increasing current above threshold. The derivative  $dP_{out}/dI$  is not necessarily constant. The threshold current, defined as the current necessary to maintain the required optical gain, can change with current due to heating related



effects and spatial hole burning. At this point, I want simply to point out that while increasing the mirror transmission  $T_i$  in Eqn. (D.7) results in a higher optical and thus external efficiency, it also increases  $G_{th}$  in Eqn.(D.6), increasing the threshold current. To optimize a laser design for a particular output power, a tradeoff must be made in Eqn.(D.9) between a higher external efficiency and a higher threshold current. More will be said on the relation between  $G_{th}$  and  $I_{th}$  in section D.3.

Returning to Fig. D.2, another striking difference is the length of the cavity. A typical in-plane laser cavity length is approximately  $300\text{ }\mu\text{m}$ . For a lasing wavelength of  $1\text{ }\mu\text{m}$  and an index of refraction for GaAs of  $\sim 3.5$ , there are approximately 2000 half wavelengths inside the cavity. The next resonant mode will have 2001 nodes, with an energy shift of  $\sim 1/2000$  between modes. There are, therefore, many longitudinal modes within the gain spectrum of the active region as shown on the left in Fig. D.3. The mode with the highest gain will achieve threshold and lase first. Due to the close spacing of modes, the gain difference between adjacent modes (i.e. mode discrimination) is small and there will typically be several lasing modes under dynamic modulation or in the presence of optical feedback.

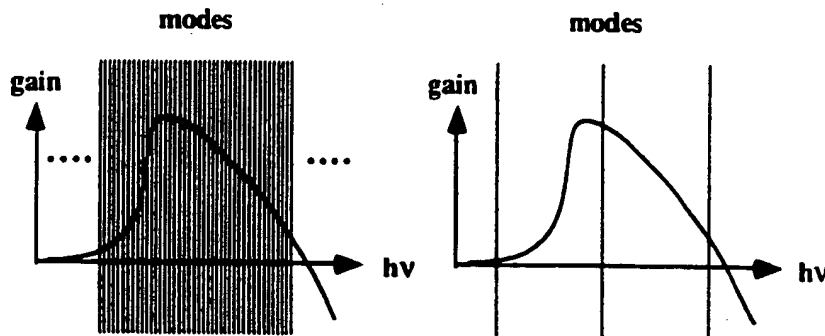


Fig. D.3. Schematic comparing the spacing of resonant cavity modes for an in-plane laser (left) with a vertical-cavity laser (right) relative to the gain curve of the active material.

In comparison, the effective cavity length of a vertical-cavity laser is roughly  $2 \mu\text{m}$ , leading to approximately 7 longitudinal standing wave nodes within the cavity. The next resonant mode will have  $\sim 1/7$  energy shift and thus the short cavity leads to a wide mode spacing. As shown on the right in Fig. D.3, the other modes are completely outside the gain spectrum. As a result, vertical-cavity lasers will lase with only a single longitudinal mode. There can be many transverse modes, however, and these two dimensional effects will be discussed in later chapters. The points to be made here are: 1) the length of the cavity, and not the peak gain, determines the lasing wavelength for vertical-cavity lasers and 2) the threshold current will be dependent on the carrier densities necessary to produce the required gain *at the resonant cavity wavelength*

As a final conclusion to this section, the effective power gain and loss coefficients are defined and analyzed. From this analysis, it will become clear how the design emphasis differs for the two different types of lasers. It is assumed that in each material, the plane wave propagation constant  $k$  can be written as

$$k = k_r + jk_i = k + j(g_{\text{mat}}(z) - \alpha_{\text{mat}}(z)) / 2 . \quad (\text{D.10})$$

and that the solution to the wave equation for the entire structure is separable into a product of traveling waves along the longitudinal ( $z$ ) axis and a standing wave for the transverse ( $x,y$ ) axis,

$$E(x, y, z) = E_0 \psi(x, y) e^{j(\omega t \mp (\beta + j(g_{\text{eff}} - \alpha_{\text{eff}}))z)} . \quad (\text{D.11})$$

In Eqn. (D.11)  $E_0$  is a constant electric field polarization for TE waves (or constant magnetic field polarization for TM waves), the "-" is for positive  $z$  traveling waves while the "+" is for negative  $z$  traveling waves,  $\omega$  is the angular frequency and  $j = \sqrt{-1}$ . The propagation constant  $\beta$  is determined by the condition that the transverse mode profile  $\psi$  decay to zero at infinity. For this wave, the gain and loss coefficients are defined as[2]:

$$g_{eff} \equiv \xi_{enh} \frac{1}{\beta} \frac{\int_{gain} k_r g_{mat} |\psi|^2 dx dy}{\int_{total} |\psi|^2 dx dy} \quad (D.12)$$

$$\alpha_{eff} \equiv \xi_{enh} \frac{1}{\beta} \frac{\int_{loss} k_r \alpha_{mat} |\psi|^2 dx dy}{\int_{total} |\psi|^2 dx dy} \quad (D.13)$$

with the enhancement factor  $\xi_{enh}$  taking into account longitudinal standing wave effects. For most lasers the gain and loss regions are averaged over many wavelengths and  $\xi_{enh}$  has a value of one. For vertical-cavity lasers, however, the longitudinal direction is the growth direction and material properties change in very short distances. In this case,  $\xi_{enh}$  can have a value approaching two. This will be discussed in detail in the next section.

Eqns. (D.12) can be simplified in the case of either laser structure. Consider first the in-plane laser. The material growth is in the transverse direction, and thus the gain is only over a limited cross sectional area. In the longitudinal direction, the layer structure is constant. Thus for the in-plane laser  $\xi_{enh}$  can be considered to be unity and  $l_{act} = l_{cav}$ . Furthermore, the material gain is a constant for the active region and can be moved out of the integral. If we define

$$\Gamma_{xy}^s \equiv \frac{n_{act}}{n_{eff}} \frac{\int_{gain} |\psi|^2 dx dy}{\int_{total} |\psi|^2 dx dy} \quad (D.14)$$

and

$$n_{eff} \equiv \frac{c\beta}{\omega}, \quad (D.15)$$

where  $n_{act}$  the real index in the active region,  $c$  is the speed of light and  $n_{eff}$  the effective index for the waveguide, then Eqn. (D.12) reduces to

$$g_{eff} = \Gamma_{xy}^g g_{mat} \quad (D.16)$$

which states that the effective gain is given by the material gain times the fraction of optical power contained within the active region. Eqn. (D.2) can then be rewritten as

$$g_{mat}^{th} = \frac{\alpha_{eff} + \frac{1}{l_{cav}} \ln\left(\frac{1}{R_1 R_2}\right)}{\Gamma_{xy}^g} \quad (D.17)$$

Eqn. (D.17) allows us to evaluate for the required material gain for an in-plane laser. Using typical values of  $15 \text{ cm}^{-1}$  for  $\alpha_{eff}$ ,  $300 \text{ } \mu\text{m}$  for  $l_{cav}$ , 0.32 for both  $R_1$  and  $R_2$ , and 0.06 for the confinement factor yields a threshold gain of:

$$g_{mat}^{th} = \frac{15 \text{ cm}^{-1} + 75 \text{ cm}^{-1}}{0.06} = 1500 \text{ cm}^{-1} \quad (D.18)$$

which is well within the operating limits of the quantum wells.

Next consider Eqn. (D.12) for a vertical-cavity laser structure. The growth is in the longitudinal direction and the gain is present for a region much shorter than the wavelength. The longitudinal enhancement factor,  $\xi_{enh}$ , therefore approaches its maximum value of two. In the transverse direction the layer structure and gain are constant. In the case of a strong index guide, such as a pillar structure, the gain region extends across the entire width of the mode so the transverse confinement factor is unity. Equation (D.12) reduces to,

$$g_{eff} = \xi_{enh} g_{mat} \quad (D.19)$$

which states that the effective gain is given by the material gain multiplied by the enhancement due to the strong standing wave pattern in the cavity. Inserting Eqn. (D.19) into Eqn. (D.4) yields Eqn. (D.6) rewritten in terms of the material gain.

$$g_{\text{mat}}^{\text{th}} = \frac{L + T_1 + T_2}{2\xi_{\text{enh}}l_{\text{act}}} \quad (\text{D.20})$$

Equation (D.20) allows us to evaluate for the required material gain for a vertical-cavity laser. Using typical values of  $L = 0.004$ ,  $T_1 = 0.008$ ,  $T_2 = 0.001$ ,  $l_{\text{act}} = 240 \text{ \AA}$  and  $\xi_{\text{enh}} = 1.83$  yields,

$$g_{\text{mat}}^{\text{th}} = \frac{0.004 + 0.008 + 0.001}{(2)(1.83)(240 \times 10^{-8} \text{ cm})} = 1480 \text{ cm}^{-1}, \quad (\text{D.21})$$

which is comparable to the requirements of an in-plane laser, if the cavity mode is located near the peak gain. Using the above values in Eqn. (D.7) yields a very practical optical efficiency of 60% from the output mirror. As can be seen from the above analysis, it is the transverse confinement factor and the cavity length which dominates the in-plane laser performance. For a vertical-cavity laser, it is the mirror transmission coefficients and the lasing wavelength as determined by the cavity dimensions which dominate the vertical-cavity laser performance. With good design tools the laser properties can be accurately predicted. One of the most important cavity design tools is described in the next section.

### D.3 Transmission Matrix Analysis

The transmission matrix analysis has proven to be a very effective tool for the design of multilayer dielectric structures. Simple 2x2 matrices represent the wave propagation and interface boundary conditions for each layer in the optical system. By multiplying these matrices together, the overall optical response of a complicated structure can be predicted. This section begins with a derivation of the formalism due to its importance for vertical-cavity laser design. The technique is then applied to a very simple structure to show how the longitudinal enhancement

factor is included. Next, index dispersion data is introduced and a distributed Bragg reflector is designed and analyzed. Finally, the technique is applied to a typical vertical-cavity structure, showing how the cavity's optical parameters are extracted from the analysis.

### D.3.1 Waves in conducting medium

While the optical materials used are mostly transparent, the inclusion of optical gain or loss is essential to model the cavity properties. The optical loss is a conductivity at optical frequencies, and this introduces complex propagation constants and permittivities. The derivation begins with Maxwell's equations:

$$\nabla \times \mathbf{E} = -\frac{\partial \mathbf{B}}{\partial t} \quad (\text{D.22.a}) \quad \nabla \cdot \mathbf{D} = \rho \quad (\text{D.22.c})$$

$$\nabla \times \mathbf{H} = \frac{\partial \mathbf{D}}{\partial t} + \mathbf{J} \quad (\text{D.22.b}) \quad \nabla \cdot \mathbf{B} = 0 \quad (\text{D.22.d})$$

where  $\mathbf{E}$  is the electric field,  $\mathbf{B}$  is the magnetic field,  $\mathbf{D}$  is the electric displacement,  $\mathbf{J}$  is the current density,  $\mathbf{H}$  is the magnetic intensity and  $\rho$  is the free charge. Bold symbols represent vectors. Furthermore the following linear relationships are assumed valid:

$$\mathbf{B} = \mu \mathbf{H} \quad (\text{D.23.a})$$

$$\mathbf{D} = \epsilon \mathbf{E} \quad (\text{D.23.b})$$

$$\mathbf{J} = \sigma \mathbf{E} \quad (\text{D.23.c})$$

where  $\mu$  is the permeability,  $\epsilon$  is the permittivity, and  $\sigma$  is the conductivity. Equations (D.23) are valid for most isotropic media.

For simplicity, and without losing utility, we seek plane wave solutions to Maxwell's equations which are traveling along the  $z$  axis at normal incidence to the interfaces on the  $xy$  plane as shown in Fig.2.4. The electric field is assumed polarized along the  $x$  axis. Further, assume that the materials are non magnetic so

that  $\mu = \mu_0$  and that there is no free charge so that  $\rho = 0$ . Searching for a monochromatic plane wave solution we assume the waves are traveling along the  $z$  axis,  $k = \pm \hat{u}_z k$ , with the fields having the form:

$$E = \hat{u}_x E e^{j(\omega t \mp kz)} \quad (\text{D.24.a}) \quad H = \pm \hat{u}_y H e^{j(\omega t \mp kz)} \quad (\text{D.24.b})$$

where  $\omega$  is the angular frequency and the  $\hat{u}_i$  are unit vectors for the corresponding axis. Positive  $z$  traveling waves use the upper sign, negative traveling waves use

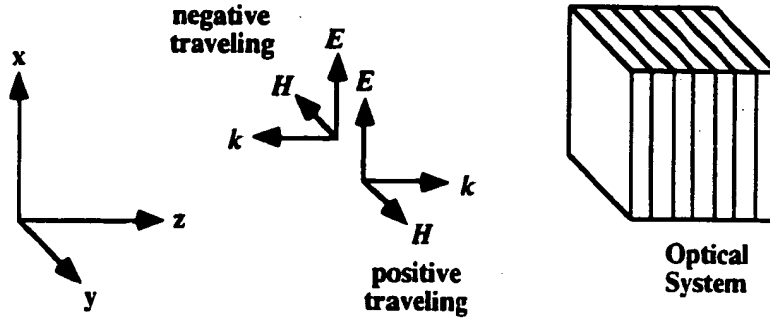


Fig. D.4. Coordinate system and field polarizations for the calculation.

the lower sign. For these waves the del and time derivative operators become:

$$\nabla \Rightarrow \mp jk \hat{u}_z \quad \text{and} \quad \frac{\partial}{\partial t} \Rightarrow j\omega$$

Since  $H$  and  $E$  are perpendicular to  $k$ , Eqns (D.24) automatically satisfy (D.22.c,d) Substituting Eqns (D.23) and (D.24) into Eqn. (D.22.a,b) yield:

$$\pm k E = \omega \mu_0 H \quad (\text{D.25.a})$$

$$\pm k H = \omega \epsilon E - j\sigma E \quad (\text{D.25.b})$$

which can be combined for the eigenvalue equation:

$$k^2 = \omega^2 \mu_0 \epsilon_0 \left( \epsilon_r - j \frac{\sigma}{\epsilon_0 \omega} \right) \quad (\text{D.26})$$

or equivalently

$$k^2 = k_0^2 (\epsilon_r + \epsilon_i) \quad (\text{D.27})$$

$$k_0^2 \equiv \omega^2 \epsilon_0 \mu_0 \quad (\text{D.28.a}); \quad \epsilon_r \equiv n^2 \quad (\text{D.28.b}); \quad \epsilon_i \equiv -\sigma / \epsilon_0 \omega \quad (\text{D.28.c})$$

where  $k_0$  is the free space propagation constant,  $\epsilon_r$  is the real part of the relative permittivity,  $\epsilon_i$  is the imaginary part of the relative permittivity and  $n$  is the real index of refraction. Thus the fields expressed in Eqns. (D.24.a,b) satisfy Maxwell's equations as long as the propagation constant  $k$  satisfies the dispersion relation in Eqn. (D.27).

Before continuing to determine the transmission matrices, it is useful to consider an alternative form of the complex propagation constant which will be needed:

$$k = k_r + jk_i \quad (\text{D.29})$$

Equation (D.29) can be substituted into Eqn (D.24.a) to give:

$$E(z, t) = E_0 e^{k_i z} e^{j(\omega t - k_r z)} \quad (\text{D.30})$$

revealing that the imaginary part represents the exponential field gain coefficient. Typically, the known quantities for each material are  $k_0$ ,  $\epsilon_r$ , and the power gain coefficient  $g_{mat}$ . The power gain assumes the growth is proportional to the intensity  $I$ :



$$\frac{\partial I}{\partial z} = g_{mat} I \quad \text{with solution} \quad I(z) = I_0 e^{g_{mat} z}$$

The optical intensity is proportional to the magnitude squared of the electric field,  $EE^*$ , hence we can identify that:

$$k_i = g_{mat} / 2 \quad (D.31)$$

We determine  $k_r$  by squaring Eqn. (D.29) and equating real and imaginary parts with Eqn. (D.27), yielding:

$$k_0^2 \epsilon_r = k_r^2 - k_i^2 = k_r^2 - (g_{mat} / 2)^2$$

which gives:

$$k_r = k_0 \sqrt{\epsilon_r + \left( \frac{g_{mat}}{2k_0} \right)^2} \quad (D.32)$$

Thus the parameters  $k_0$ ,  $\epsilon_r$  and  $g_{mat}$  completely specify the propagation of waves of the type expressed in Eqn. (D.24). For loss, simply substitute  $-\alpha_{mat}$  for  $g_{mat}$ . As can be seen from Eqn. (D.25), the  $E$  and  $H$  fields will not be in phase for complex  $k$ . The polarizations, however, do remain perpendicular for normal incidence. These waves and the boundary conditions at interfaces are used to generate the transmission matrices in the following section.

### D.3.2 Transmission matrix derivation

We wish to calculate the response of an optical system with an arbitrary number of layers whose material properties vary in a discrete fashion and only along one axis, taken here to be the  $z$  axis. The transmission matrix treats the forward and backward traveling wave amplitudes on the left as the dependent

variables with the amplitudes on the right as the dependent variables, shown in Fig. D.5. The expressions for the fields, Eqn. (D.24), are repeated here for reference:

$$E_i^+ = \hat{u}_x E_i^+ e^{j(\omega t - k(z - z_i))} \quad (\text{D.33.a}) \quad H_i^+ = \hat{u}_y H_i^+ e^{j(\omega t - k(z - z_i))} \quad (\text{D.33.b})$$

$$E_i^- = \hat{u}_x E_i^- e^{j(\omega t + k(z - z_i))} \quad (\text{D.34.a}) \quad H_i^- = -\hat{u}_y H_i^- e^{j(\omega t + k(z - z_i))} \quad (\text{D.34.b})$$

where the subscript  $i$  distinguishes the field in each layer in the optical system and

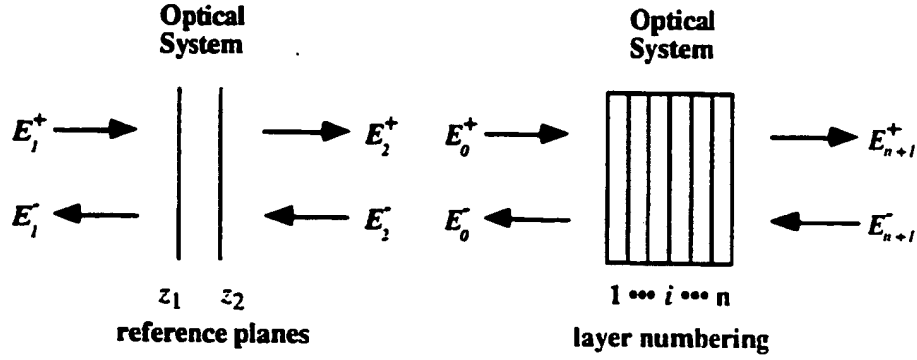


Fig. D.5. Arbitrary multilayer optical system. Input and output fields are defined at the first and last interfaces. Polarizations are shown in Fig. D.4

the forward and backward waves have been identified by a + or - superscript respectively. The value of the electric fields will be calculated on both sides of each interface in the system. The reference plane  $z_i$  is defined as the boundary at which the field was calculated. The transmission matrix can thus be written as:

$$\begin{bmatrix} E_1^+ \\ E_1^- \end{bmatrix} = \begin{bmatrix} T_{11} & T_{12} \\ T_{21} & T_{22} \end{bmatrix} \begin{bmatrix} E_2^+ \\ E_2^- \end{bmatrix} \quad (\text{D.35})$$

where  $E_2$  are the fields on the right and  $E_1$  are the fields on the left. The task at hand is to determine the coefficients for propagation within a medium and the coefficients for scattering at an interface.

Consider first the propagation of the waves in a uniform medium  $i$  of length  $l_i$ . There is no scattering in a uniform medium so the off diagonal elements are zero while the diagonal elements simply account for the phase of propagation. Relating the fields on the left to the fields on the right is found by inserting a length  $-l_i$  in Eqns. (D.33.a) and (D.34.a) and factoring out the phase shift, yielding

$$\mathbf{P}_i = \mathbf{T}_{prop} = \begin{bmatrix} e^{jk_i l_i} & 0 \\ 0 & e^{-jk_i l_i} \end{bmatrix} \quad (\text{D.36})$$

where  $\mathbf{P}_i$  is the transmission matrix for propagation in the  $i^{\text{th}}$  layer. Next consider the transmission matrix for the fields across an interface. Again, we assume the fields on the right (medium 2) are known, and want to find the fields on the left (medium 1). Maxwell's equations (D.22.a) and (D.22.b) can be integrated over a closed rectangles, oriented in the  $xz$  and  $yz$  planes respectively, which enclose the interface. Using Stoke's theorem, the area integral of the curl is converted to a line integral around the rectangle boundary, so that Eqn. (D.22.a) becomes:

$$\oint_{\text{boundary}} \mathbf{E} \cdot d\mathbf{l} = \iint_{\text{area}} -\frac{\partial B}{\partial t} \cdot \hat{u}_y \, dx \, dz \quad (\text{D.37})$$

with a similar equation for the  $\mathbf{H}$  field. Letting the sides parallel to the  $z$  axis go to zero while still spanning the interface results in a zero for the right hand side of Eqn. (D.37). Thus the tangential electric field must be continuous across the interface so that the line integral also goes to zero. Similarly, the tangential  $\mathbf{H}$  field is also continuous across the interface. These boundary conditions can be used to solve for the matrix coefficients.

The transmission matrix for the interface is written as:

$$\mathbf{T}_{int} = \begin{bmatrix} A & B \\ C & D \end{bmatrix} \quad \text{which states} \quad \begin{bmatrix} E_1^+ \\ E_1^- \end{bmatrix} = \begin{bmatrix} A & B \\ C & D \end{bmatrix} \begin{bmatrix} E_2^+ \\ E_2^- \end{bmatrix} \quad (\text{D.38})$$

First consider the case where a field is incident from the left so that there will be no incoming wave from the right and thus  $E_2^- = 0$ . Continuity of the  $E$  field then requires  $E_1^+ + E_1^- = E_2^+$  which can be substituted into the system of Eqns. (D.38) to give:

$$A + C = 1 \quad (\text{D.39})$$

Continuity of the  $H$  field must be satisfied as well. Eqn. (D.25.a) states that the magnitude  $H = \pm kE / \omega\mu_0$ , keeping in mind that the + sign is for positive traveling waves while the - sign is for negative traveling waves. Thus the continuity of  $H$  requires  $H_1^+ + H_1^- = H_2^+$  or equivalently  $k_1 E_1^+ - k_1 E_1^- = k_2 E_2^+$  which, along with  $E_2^- = 0$  can be combined with the system of Eqns. (D.38) to give:

$$A - C = k_2 / k_1 \quad (\text{D.40})$$

Equations (D.39) and (D.40) can be solved to yield:

$$A = \frac{k_1 + k_2}{2k_1} \quad (\text{D.41})$$

$$C = \frac{k_1 - k_2}{2k_1} \quad (\text{D.42})$$

To determine the two remaining unknowns, consider next the case of an incident field from the right so that there will be no incoming wave from the left and thus  $E_1^+ = 0$ . Continuity of the  $E$  field then requires  $E_1^- = E_2^+ + E_2^-$ . These two conditions can be combined with the system of Eqns. (D.38) to give:

$$A - B = AD - BC \quad (D.43)$$

Furthermore, the continuity of  $H$  now requires  $-k_1 E_1^- = k_2 E_2^+ - k_2 E_2^-$  which, along with  $E_1^+ = 0$  can be combined with the system of Eqns. (D.38) to give:

$$(A + B)k_2 = (AD - BC)k_1 \quad (D.44)$$

Equations (D.43) and (D.44) can be solved simultaneously :

$$B = \frac{k_1 - k_2}{k_1 + k_2} A \quad \text{and} \quad D = \frac{BC}{A} + \frac{2k_2}{k_1 + k_2}$$

Inserting the values for  $A$  and  $C$  from above yields:

$$B = \frac{k_1 - k_2}{2k_1} \quad (D.45)$$

$$D = \frac{k_1 + k_2}{2k_1} \quad (D.46)$$

for the remaining coefficients.

With all four matrix elements determined, the interface matrix can now be written as:

$$\mathbf{I}_{i,i+1} = \mathbf{T}_{int} = \begin{bmatrix} \frac{k_i + k_{i+1}}{2k_i} & \frac{k_i - k_{i+1}}{2k_i} \\ \frac{k_i - k_{i+1}}{2k_i} & \frac{k_i + k_{i+1}}{2k_i} \end{bmatrix} \quad (D.47)$$

where  $\mathbf{I}_{i,i+1}$  is the transmission matrix for propagation across the interface between the layer  $i$  and layer  $i+1$ . The transmission matrix for an arbitrary structure of  $n$  layers as shown in Fig.2.5 is constructed by multiplying successive propagation and interface matrices:

$$\mathbf{I}_{0,1} \mathbf{P}_1 \mathbf{I}_{1,2} \mathbf{P}_2 \cdots \mathbf{I}_{i-1,i} \mathbf{P}_i \mathbf{I}_{i,i+1} \cdots \mathbf{P}_{n-1} \mathbf{I}_{n-1,n} \mathbf{P}_n \mathbf{I}_{n,n+1} \quad (\text{D.48})$$

To determine the power transmission and reflection coefficients,  $T_{\text{pow}}$  and  $R_{\text{pow}}$ , for the structure for a wave incident from the left, the time average energy flux per unit area (intensity  $I$ ) in each traveling wave can be calculated using the complex Poynting vector and Eqn. (D.25.a) to eliminate  $H$ . For the simple case of plane waves in non-conducting medium:

$$I = \frac{1}{2} \text{Re}(\mathbf{E} \times \mathbf{H}^*) = \frac{1}{2} \frac{k}{\omega \mu_0} |\mathbf{E}|^2 = \frac{n}{2} \frac{|\mathbf{E}|^2}{\eta_0} \quad (\text{D.49})$$

where  $\eta_0 = 377\Omega$  is the free space impedance. The ratios of the various intensities provide the coefficients in terms of the transmission matrix elements:

$$R = \frac{I_0^-}{I_0^+} = \frac{(E_0^-)^2}{(E_0^+)^2} = \frac{|\mathbf{T}_{21}|^2}{|\mathbf{T}_{11}|^2} \quad (\text{D.50})$$

$$T = \frac{I_{n+1}^+}{I_0^+} = \frac{n_{n+1}}{n_0} \frac{(E_{n+1}^-)^2}{(E_0^+)^2} = \frac{n_{n+1}}{n_0} \frac{1}{|\mathbf{T}_{11}|^2} \quad (\text{D.51})$$

where only the initial and final materials have been presumed lossless. (Note that the *field* reflection coefficient  $\Gamma$  calculated this way requires a minus sign to agree with the conventional definition of the Fresnel coefficient  $r_{12}$  due to our choice of identical orientation for the forward and backward traveling  $\mathbf{E}$  fields) It is interesting to note that if  $\mathbf{T}_{11}=0$ , the reflection and transmission become infinite. This is exactly the lasing condition, outward waves without any incoming waves, and will be used to determine the round trip cavity parameters. In the next section a simple but important problem will be examined using the transmission matrix formalism, clarifying its use while shown the importance of using the complex propagation constants in the interface matrices as well as the propagation matrices.

### D.3.3 Longitudinal enhancement factor

With mirror reflectivities of ~99%, there is a strong standing wave pattern inside a vertical cavity. The gain due to stimulated emission is proportional to the square of the electric field. If there are two counter propagating waves adding in phase, the electric field can be twice its average value. Thus the stimulated emission would be four times the value for a single wave passing through. Effectively, the gain for each wave has been doubled due to this coherent effect. Similarly, losses in thin regions can be minimized by placing them at the standing wave nulls. While this argument seems sensible, the question arises as to how this longitudinal enhancement factor shows up in the transmission matrix equations.

To answer this question, the transmission matrix technique is applied to the simplest of gain structures. Consider a material with gain  $g_{mat}$ , thickness  $l$  and an index  $n = 1$  cladded by passive material with  $n = 1$  as well. The procedure will be to apply the transmission matrix analysis, convert from the  $T$  parameters for the overall structure to  $S$  parameters, and then make the appropriate expansions. The scattering parameters treat the outgoing waves as the dependent variables and the incoming waves as the independent variables. This is ideal for studying coherent effects between opposite traveling waves.

For this simple structure, the transmission matrix consists of two interface matrices around one propagation matrix:

$$\mathbf{T} = \mathbf{I}_{12} \mathbf{P}_2 \mathbf{I}_{23}$$

where the propagation constants are shown in Fig. 2.6. Using Eqns. (D.36) and (D.47), the expression for the transmission matrix is:

$$\mathbf{T} = \begin{bmatrix} \frac{k_1 + k_2}{2k_1} & \frac{k_1 - k_2}{2k_1} \\ \frac{k_1 - k_2}{2k_1} & \frac{k_1 + k_2}{2k_1} \end{bmatrix} \begin{bmatrix} e^{-jk_2 l} & 0 \\ 0 & e^{-jk_2 l} \end{bmatrix} \begin{bmatrix} \frac{k_2 + k_1}{2k_2} & \frac{k_2 - k_1}{2k_2} \\ \frac{k_2 - k_1}{2k_2} & \frac{k_2 + k_1}{2k_2} \end{bmatrix} \quad (\text{D.52})$$

Defining  $C_k \equiv k_1 / k_2$  to simplify, Eqn. (D.52) becomes:

$$\mathbf{T} = \frac{1}{4C_k} \begin{bmatrix} C_k + 1 & C_k - 1 \\ C_k - 1 & C_k + 1 \end{bmatrix} \begin{bmatrix} e^{-jk_2 l} & 0 \\ 0 & e^{-jk_2 l} \end{bmatrix} \begin{bmatrix} 1 + C_k & 1 - C_k \\ 1 - C_k & 1 + C_k \end{bmatrix} \quad (\text{D.53})$$

which can be multiplied together to give the following form:

$$\mathbf{T} = \begin{bmatrix} \cos k_2 l + jB_k \sin k_2 l & jA_k \sin k_2 l \\ -jA_k \sin k_2 l & \cos k_2 l - jB_k \sin k_2 l \end{bmatrix} \quad (\text{D.54})$$

where the coefficients  $A_k$  and  $B_k$  are defined as:

$$A_k \equiv \frac{1/C_k - C_k}{2} \quad (\text{D.55})$$

$$B_k \equiv \frac{1/C_k + C_k}{2} \quad (\text{D.56})$$

$$C_k \equiv k_1 / k_2 \quad (\text{D.57})$$

which specifies the transmission matrix.

The next step is to transform  $\mathbf{T}$  into an  $\mathbf{S}$  matrix. The field scattering matrix elements are defined by:

$$\begin{bmatrix} E_1^- \\ E_2^+ \end{bmatrix} = \begin{bmatrix} S_{11} & S_{12} \\ S_{21} & S_{22} \end{bmatrix} \begin{bmatrix} E_1^+ \\ E_2^- \end{bmatrix} \quad (\text{D.58})$$

The  $\mathbf{T}$  matrix, defined in Eqn. (D.35), gives the fields on the left in terms of the field on the right. The  $\mathbf{S}$  matrix gives the fields coming out in terms of the fields coming in. This is almost identical to the chain scattering matrices and scattering matrices common in microwave theory [6], except that the material impedance has



not been included in the field amplitudes. If one writes out the two systems of equations and rearranges terms, the conversion between the two forms can be made. The result for the conversion of  $T$  into  $S$  is,

$$\begin{bmatrix} S_{11} & S_{12} \\ S_{21} & S_{22} \end{bmatrix} = \begin{bmatrix} \frac{T_{21}}{T_{11}} & T_{22} - \frac{T_{21}T_{12}}{T_{11}} \\ \frac{1}{T_{11}} & -\frac{T_{12}}{T_{11}} \end{bmatrix} \quad (D.59)$$

From Eqns. (D.50) and (D.59) it can be identified that:

$$R = |S_{11}|^2 \quad (D.60)$$

$$T = |S_{21}|^2 \quad (D.61)$$

since  $n_3 = n_1$ . Combining Eqn. (D.54) and (D.59) yields the scattering parameters for our simple system,

$$S = \begin{bmatrix} \frac{-jA_k \sin k_2 l}{\cos k_2 l + jB_k \sin k_2 l} & \frac{1}{\cos k_2 l + jB_k \sin k_2 l} \\ \frac{1}{\cos k_2 l + jB_k \sin k_2 l} & \frac{-jA_k \sin k_2 l}{\cos k_2 l + jB_k \sin k_2 l} \end{bmatrix} \quad (D.62)$$

As a check, note that the scattering matrix is symmetric as would be expected since the optical system is symmetric.

Now that we have derived  $S$  in exact form, we can begin making approximations to reveal the physical behavior of the system. We begin by expanding the propagation constants,  $k_1$  and  $k_2$ , and the coefficients,  $A_k$ ,  $B_k$  and  $C_k$ , to first order in  $g_{mat}/2k_0$ :

$$k_1 = k_0 = 2\pi/\lambda_0$$

$$\begin{aligned}
k_2 &= k_r + jk_i = k_o \sqrt{1 + \left(\frac{g_{mat}}{2k_o}\right)^2} + j\frac{g_{mat}}{2} \\
&\equiv k_o \left(1 + \frac{1}{2} \left(\frac{g_{mat}}{2k_o}\right)^2 + j\frac{g_{mat}}{2k_o}\right) \\
&\equiv k_o \left(1 + j\frac{g_{mat}}{2k_o}\right)
\end{aligned}$$

which gives:

$$1/C_k \equiv k_2/k_1 \equiv 1 + j\frac{g_{mat}}{2k_o} \quad \text{and} \quad C_k \equiv k_1/k_2 \equiv 1 - j\frac{g_{mat}}{2k_o}$$

so that:

$$\begin{aligned}
A_k &\equiv \frac{1/C_k - C_k}{2} \equiv j\frac{g_{mat}}{2k_o} \\
\sin k_2 l &\equiv \sin k_o l \left(1 + j\frac{g_{mat}}{2k_o}\right) \equiv \sin k_o l + k_o l j\frac{g_{mat}}{2k_o} \cos k_o l
\end{aligned}$$

$$A_k \sin k_2 l \equiv j\frac{g_{mat}}{2k_o} \sin k_o l \quad (\text{D.63})$$

likewise:

$$\begin{aligned}
B_k &\equiv \frac{1/C_k + C_k}{2} \equiv 1 \\
\cos k_2 l &\equiv \cos k_o l \left(1 + j\frac{g_{mat}}{2k_o}\right) \equiv \cos k_o l - k_o l j\frac{g_{mat}}{2k_o} \sin k_o l
\end{aligned}$$

$$\begin{aligned}
& \cos k_2 l + j B_k \sin k_2 l \\
& \equiv \cos k_0 l - k_0 l j \frac{g_{mat}}{2k_0} \sin k_0 l + j \left( \sin k_0 l + k_0 l j \frac{g_{mat}}{2k_0} \cos k_0 l \right) \\
& \equiv (\cos k_0 l + j \sin k_0 l) \left( 1 - k_0 l \frac{g_{mat}}{2k_0} \right) \\
& \equiv e^{jk_0 l} \left( 1 - k_0 l \frac{g_{mat}}{2k_0} \right)
\end{aligned}$$

Assuming that  $g_{mat}l \ll 1$ , generally true for vertical-cavity structures, we can express the last equation as:

$$\frac{1}{\cos k_2 l + j B_k \sin k_2 l} \equiv e^{-jk_0 l} \left( 1 + \frac{g_{mat}l}{2} \right) \quad (D.64)$$

Equations (D.63) and (D.64) are valid to first order in  $g_{mat}/2k_0$ . To check the validity, consider typical values of  $\lambda = 1 \mu\text{m}$  and  $g_{mat} = 2000 \text{ cm}^{-1}$ . Then  $g_{mat}/2k_0 = 0.016$  and it is valid to drop higher order terms. Inserting Eqns. (D.63) and (D.64) into Eqn. (D.64) yields:

$$S \equiv \begin{bmatrix} \frac{g_{mat}}{2k_0} \sin k_0 l & 1 + \frac{g_{mat}l}{2} \\ 1 + \frac{g_{mat}l}{2} & \frac{g_{mat}}{2k_0} \sin k_0 l \end{bmatrix} e^{-jk_0 l} \quad (D.65)$$

which is a generally useful form for the scattering parameters of a gain region embedded in passive materials of identical index of refraction (for  $n \neq 1$ , substitute  $k_s = nk_0$  for  $k_0$ .)

Before deriving the longitudinal enhancement factor from the S matrix, Eqn. (D.65), it is useful to make one additional approximation. In the case where  $k_0 l \ll 1$ , as for a quantum well active region, we can use  $\sin x \approx x$  to get:

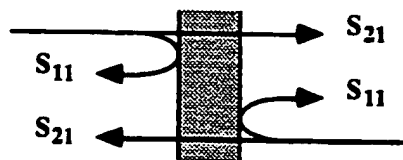
$$S = \begin{bmatrix} \frac{g_{mat}l}{2} & 1 + \frac{g_{mat}l}{2} \\ 1 + \frac{g_{mat}l}{2} & \frac{g_{mat}l}{2} \end{bmatrix} e^{-jk_0 l} \quad (D.66)$$

Using this form it is easy to see how the gain enhancement effect is included in the equations. From the definition of S in Eqn. (D.58),  $S_{11}$  is the field reflection coefficient and  $S_{21}$  is the field transmission coefficient. The structure under analysis is shown in Fig. 2.6 along with two different excitations, each with a normalized intensity of 1. First consider the case where there is only a single incident wave from the left. The power coming out of the two sides are:

$$\text{outward left: } |S_{11}|^2 = (g_{mat}l/2)^2 \quad \text{which is very small. } \sim (0.01)^2$$

$$\text{outward right: } |S_{21}|^2 = (1 + g_{mat}l/2)^2 = 1 + g_{mat}l + (g_{mat}l/2)^2$$

which shows the expected single pass gain of  $g_{mat}l$ . Next consider both waves passing through the gain layer. The power out each side is identical, and now the



$$k_1 = k_0 \quad k_2 \equiv k_0 + j g_{mat}/2 \quad k_3 = k_0$$

Fig. D.6. All three materials are identical except the center layer has gain, introducing reflections which interfere with the opposite traveling wave.

reflection is significant as it is modulating a carrier:

$$\begin{aligned}
 |S_{21} + S_{11}|^2 &= S_{21}^2 + 2S_{21}S_{11} + S_{11}^2 \\
 &= (1 + g_{mat}l/2)^2 + 2(1 + g_{mat}l/2)(g_{mat}l/2) + (g_{mat}l/2)^2 \\
 &= 1 + 2g_{mat}l + (g_{mat}l)^2
 \end{aligned}$$

which shows each wave experienced a gain  $2g_{mat}l$ , effectively double that of the single pass gain! For the extremely short gain lengths of a vertical-cavity laser, this effect is essential for high performance designs. The above analysis shows that it is the reflections due to the *imaginary part* of the index discontinuities which result in a gain enhancement for standing waves.

Returning to the more general scattering parameters, Eqn. (D.65), we can derive an equation for the longitudinal enhancement factor. Consider two incoming waves of equal amplitude but with a phase difference of  $\phi$ . We can thus express the outgoing fields as:

$$\begin{bmatrix} E_1^- \\ E_2^+ \end{bmatrix} = \begin{bmatrix} S_{11} & S_{12} \\ S_{21} & S_{22} \end{bmatrix} \begin{bmatrix} e^{+j\phi/2} \\ e^{-j\phi/2} \end{bmatrix} \quad (D.67)$$

so that the outgoing power, normalized to the incoming power, is given by:

$$\begin{aligned}
 \frac{P_{out}^+}{P_{in}^+} &= (S_{11}e^{j\phi/2} + S_{12}e^{-j\phi/2})(S_{11}^*e^{-j\phi/2} + S_{12}^*e^{j\phi/2}) \\
 &= S_{11}S_{11}^* + S_{12}S_{12}^* + S_{11}S_{12}^*e^{j\phi} + S_{11}^*S_{12}e^{-j\phi}
 \end{aligned}$$

$$\begin{aligned}
&= \left( \frac{g_{mat}}{2k_o} \sin k_o l \right)^2 + \left( 1 + \frac{g_{mat} l}{2} \right)^2 + \frac{g_{mat}}{2k_o} \sin k_o l \left( 1 + \frac{g_{mat} l}{2} \right) 2 \cos \phi \\
&= 1 + g_{mat} l \left( 1 + \frac{\sin k_o l}{k_o l} \cos \phi \right) + \text{higher order terms} \quad (D.68)
\end{aligned}$$

Equation (D.68) shows that the gain enhancement factor is:

$$\xi_{enh} = 1 + \frac{\sin nk_o l}{nk_o l} \cos \phi \quad (D.69)$$

where  $nk_o$  is the real propagation constant,  $l$  is the thickness of the gain region and  $\phi$  is the phase difference between the two counter propagating waves at the center of the gain region. If the two waves arrive in phase, then the  $\cos \phi = 1$  and the enhancement factor varies from a maximum value of two for short lengths to an average value of one as expected for gain regions extending over many wavelengths. If the two waves arrive out of phase, then the  $\cos \phi = -1$  and the enhancement factor approaches zero for very short lengths.

In general, one would like to minimize the amount of gain material needed in a design to keep the threshold current as low as possible. From the above analysis, it becomes clear that the gain material near the standing wave peak is most effective while any material near the nulls provides essentially no optical gain at all. This effect limits practical active region lengths to be less than  $\lambda/4$ , or  $\sim 700 \text{ \AA}$  for GaAs material at a free space wavelength of  $1 \text{ \mu m}$ .

In summary, the transmission matrix technique incorporates the longitudinal enhancement factor as long as the complex propagation constant is used in the interface matrices  $I_{i,i+1}$  given in Eqn. (D.47). As we have seen, it is the reflections due to the complex part of the index discontinuities that result in the gain enhancements. By using a transmission matrix numerical approach to vertical-cavity design, all of the standing wave effects are included in the analysis.

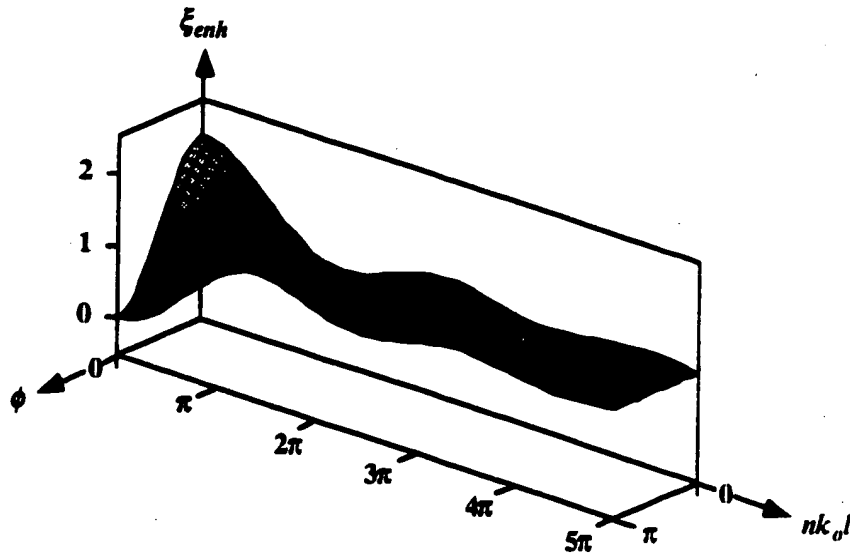


Fig. D.7. Enhancement factor vs. the gain length  $nk_o l$  and the phase difference  $\phi$  between the two counter propagating waves.

#### D.4 Distributed Bragg Reflectors

Distributed Bragg reflectors have proven to be the enabling technology for vertical-cavity lasers. The first application of the transmission matrix technique is therefore the design of the reflectors. The basic concept is reviewed, then extended to include termination on various materials. The section concludes with numerical calculations showing the mirror spectrum for various configurations to provide a feel for the reflectivity dependency on design parameters.

A schematic of a section of a distributed Bragg reflector is shown in Fig. D.8. Alternating layers of high index,  $n_H$ , and low index,  $n_L$ , materials are designed to be a quarter wavelength thick. At the design wavelength, all the reflections will return to the cavity in phase, making it possible to achieve very high reflectivities with dielectric materials. This can be seen in the diagram, where the phase of propagation is shown for the horizontal lines and the phase of

reflection is shown for the vertical lines. Starting at the reference plane, any path followed by the arrows returns to the reference plane in multiples of  $2\pi$ . Thus all reflections must be in phase. The high index material is often GaAs while the low index material could be AlAs.

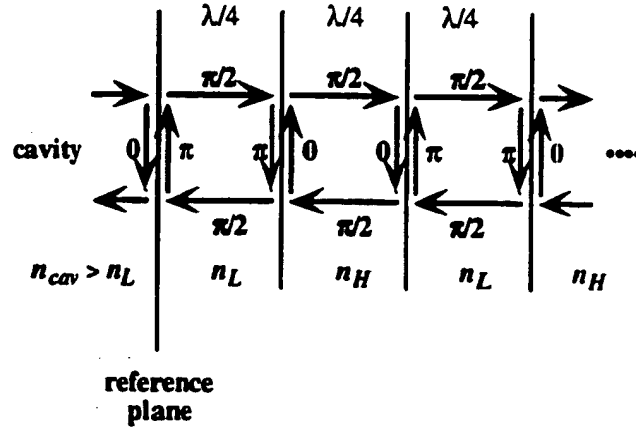


Fig. D.8. Phase diagram showing the design of a distributed Bragg reflector. All reflections return to the reference plane in phase.

The field reflection coefficient for an interface,  $\Gamma$ , can be expressed in terms of the transmission matrix coefficients for an interface:

$$\Gamma \equiv \frac{E_1^-}{E_1^+} = \frac{T_{21}}{T_{11}} \quad (\text{D.70})$$

which can be rewritten in terms of  $k$  or  $n$ :

$$\Gamma = \frac{k_1 - k_2}{k_1 + k_2} = \frac{n_1 - n_2}{n_1 + n_2} \quad (\text{D.71})$$

showing a  $\pi$  phase change for reflections from low to high and no phase change for reflections from high to low. In order to be useful, the mirror must be



terminated on a material. Simplified phase diagrams for air and substrate terminations are shown in Fig. D.9. Since air is the lowest index, the last mirror layer should be  $n_H$ , although one could instead add an extra quarter wavelength of  $n_L$  material.

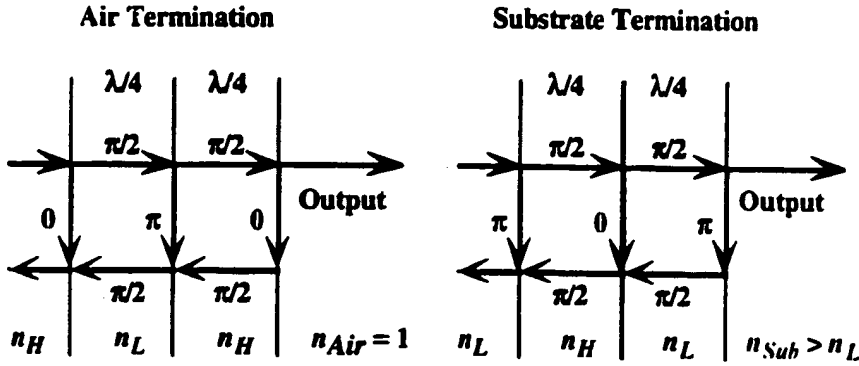


Fig. D.9. Phase diagrams for air and substrate terminations.

In practice, it is preferable to terminate with the GaAs as it is more chemically stable. For the substrate termination, the  $n_L$  layer is last. Output coupling through the substrate requires wavelengths transparent to the substrate material such as InGaAs on GaAs while air termination allows a broader range of operating wavelengths.

An additional termination of interest is the termination on a conductor such as gold or silver. The phase of reflection is neither 0 nor  $\pi$  but something in between, closer to  $\pi$  if it is a good conductor. To determine the phase, Eqn. (D.71) for  $\Gamma$  can be used, where the metal's index is now complex:

$$k_{metal} = k_o(n_c - jk_c) \quad (D.72)$$

$$\Gamma_{metal} = \frac{n_s - n_c + jk_c}{n_s + n_c - jk_c} = \left( \frac{(n_s - n_c)^2 + k_c^2}{(n_s + n_c)^2 + k_c^2} \right)^{1/2} e^{j\phi} \quad (D.73)$$

where the semiconductor propagation constant is  $k_s = n_s k_0$  and  $n_c$  and  $k_c$  are the optical constants of the metal. The phase can be expressed as:

$$\phi = \tan^{-1}\left(\frac{k_c}{n_s - n_c}\right) + \tan^{-1}\left(\frac{k_c}{n_s + n_c}\right) = \pi - \delta \quad (\text{D.74})$$

$$\delta \equiv \tan^{-1}\left(\frac{2k_c n_s}{k_c^2 + n_c^2 - n_s^2}\right) \quad (\text{D.75})$$

#### Metal Termination

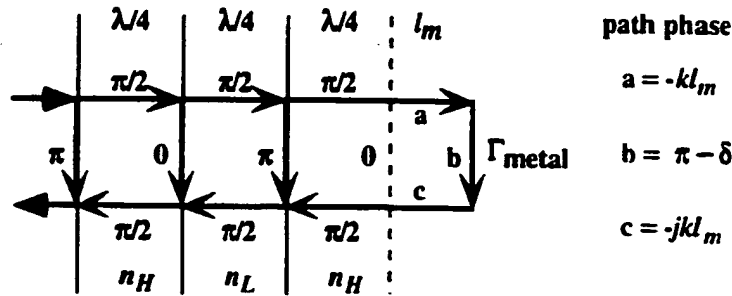


Fig. D.10. Phase diagram illustrating metal termination. As the metal reflection phase is less than  $\pi$ , layer thicknesses must be adjusted for resonance

Equation (D.75) can be derived from Eqn. (D.74) using the trigonometric identities for the tangent of the sum of two angles. The phase condition is diagrammed in Fig. D.10, showing the phase path  $a$ - $b$ - $c$  must return to zero phase. The thickness of the phase matching layer  $l_m$  can thus be determined:

$$-2k_s l_m + \pi - \delta = 0 \quad (\text{D.76})$$

$$l_m = \frac{\pi - \delta}{2k_s} = (1 - \delta/\pi)(\lambda_s/4) \quad (\text{D.77})$$

Equation (D.77) gives the additional thickness, in terms of wavelengths in the material, that should be added to a quarter wave of high index material to terminate on a metal. By reviewing the above analysis, it should be fairly obvious how to terminate the mirrors in other configurations. If it was desired to use a metal termination on the low index material, for example, one would remove the last quarterwave of high index material shown in the figure and simply set the right hand side of Eqn. (D.76) to  $\pi$  instead of 0 and then solve for  $l_m$ , resulting in a negative length so that less than a quarter wave of low index material would be used.

To make things clear, let's calculate the phase matching layer for a gold film on a GaAs layer, assuming  $n_H = 3.52$  and  $\lambda_0 = 1\mu\text{m}$ . First we need the optical constants. For gold at this wavelength, they are  $n_c = 0.174$  and  $k_c = 5.69$ . Equation (D.75) gives  $\delta = 0.352\pi$ . The wavelength in the GaAs is  $\lambda_s = \lambda_0/n_H = 2841\text{\AA}$ . Then Eqn. (D.77) yields  $l_m = 460\text{\AA}$ . Thus the final GaAs layer in the distributed Bragg reflector would have a total thickness of  $(2841\text{\AA}/4) + 460\text{\AA} = 1170\text{\AA}$ . Using the complex coefficients in the final interface matrix, the reflectivity can be calculated as well. The power reflectivity is given by  $\Gamma\Gamma^*$ , where  $\Gamma$  is defined in Eqn. (D.72). For the same problem, the power reflectivity of the GaAs/gold interface is 94.6%, too low to be used alone but very helpful to boost the reflectivity of a mirror stack. One could also use an oxide layer between the GaAs quarter wave layer and the metal for phase matching. For a  $\text{SiO}_2$  layer with  $n = 1.45$ , the oxide layer between the  $n_H$  quarter wave layer and the gold should be  $1150\text{\AA}$  thick. The reflection of the semiconductor-oxide interface reduces the effect of the metal absorption losses, boosting the reflectivity of the GaAs- $\text{SiO}_2$ -gold reflector to 98.7%.

Now that the theory of the transmission matrix analysis and the fundamentals of distributed Bragg reflector (DBR) design have been covered, it is

useful to apply the technique to calculate the reflectivity spectrum of various DBR structures. To make an accurate calculation, it is necessary to include the variation in refractive index with wavelength called dispersion. Our group has used, very successfully, the model of Afromowitz [7] modified to behave smoothly as the wavelength moves above the bandgap (see Appendix A). Randy Geels wrote a user friendly transmission matrix program called Multilayer [4]. The program combines the transmission matrix equations derived above with Afromowitz's dispersion data. Layer thicknesses can be specified either by dimension or in terms of a design wavelength. As well as calculating transmission and reflection coefficients

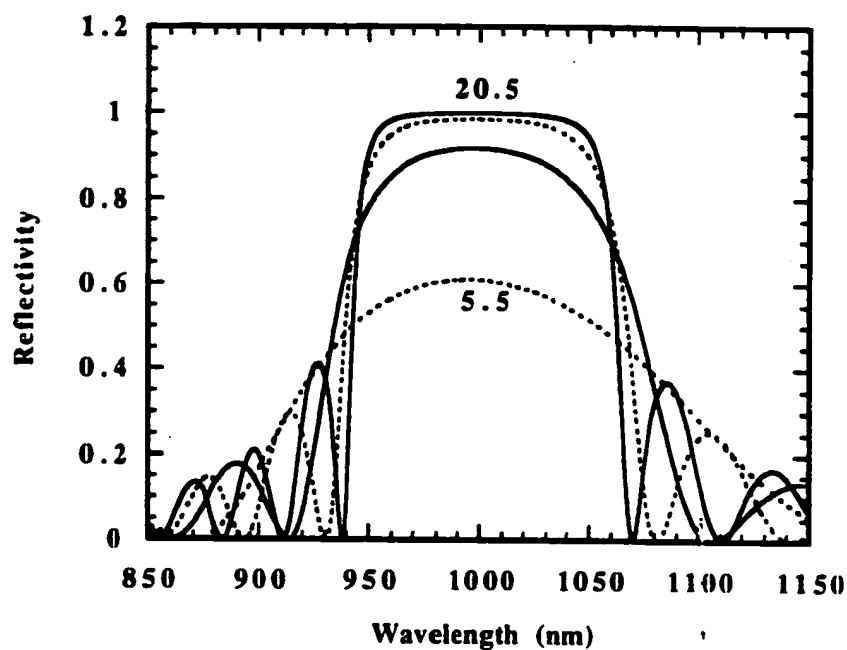


Fig. D.11. Power reflectivity spectrum for GaAs/AlAs distributed Bragg reflectors with 5.5, 10.5, 15.5 and 20.5 periods

vs. wavelength, it will also calculate the standing wave pattern using a partial transmission matrix to calculate the fields at the interfaces and Eqns. (D.33) and (D.34) to generate the fields in between.

The following calculations were made with Multilayer. Figure D.11 shows the calculated reflectivity spectrum for GaAs/AlAs distributed Bragg reflectors with varying numbers of mirror periods, where one period is a AlAs/GaAs pair. Starting from GaAs, the reflection is calculated for 5.5, 10.5, 15.5 and 20.5 periods where the extra "0.5" represents the additional AlAs layer need for termination on a GaAs substrate. As more periods are added, the stop band becomes more defined and flatter with greater interference resonances in the wings. The power reflectivities at the design wavelength of 1000 nm are 60.85%, 91.71%, 98.50% and 99.74% respectively. If an additional 5 periods are added, the calculated reflectivity for a 25.5 period DBR is 99.95%. No absorption losses have been assumed in the calculation. If a uniform absorption loss of  $10 \text{ cm}^{-1}$  is assumed, the reflectivities become 60.81%, 91.64%, 98.41% and 99.87% respectively. The difference between the reflectivities with and without absorption gives a power loss of  $\sim 0.09\%$ , showing a significant effect only at the highest reflectivities.

The power loss can be predicted using the penetration depth in the mirror and the average loss coefficient. The penetration depth is defined as the equivalent depth of a hard mirror which provides the same phase as the linear phase relation at the center of the stop band. The phase of the field reflectivity is plotted in Fig. 2.12. The penetration depth can be determined from the calculated mirror phase by writing its definition and then taking the derivative with respect to wavelength:

$$-2k_s l_p = \phi_{DBR} \quad (\text{D.78})$$

$$l_p = -\frac{1}{2} \frac{\partial \phi_{DBR}}{\partial k} = \frac{1}{2} \frac{\lambda_o^2}{2\pi n_s} \frac{\partial \phi_{DBR}}{\partial \lambda_o} \quad (\text{D.79})$$

The penetration depth can thus be calculated. Using  $n_s = 3.52$ ,  $\lambda_0 = 1000\text{nm}$  and the phase slope of  $1.07^\circ/\text{nm} = 0.0187\text{ rad/nm}$  gives  $l_p = 422\text{ nm}$ . The field penetrates approximately a half micron into the mirrors. The power loss for the field propagating in and back is the  $2l_p\alpha_{\text{mat}}$ . Using a loss of  $10\text{ cm}^{-1}$  gives a

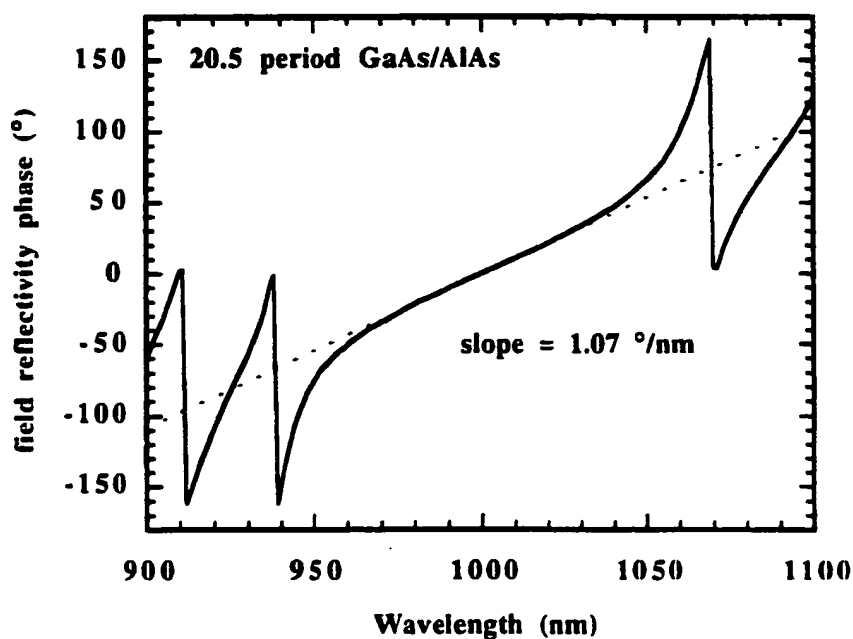


Fig. D.12. Phase for the field reflected from a 20.5 period DBR and the slope at the center of the stop band.

predicted absorption of 0.084%, in agreement with the calculated losses. In practice, the dopants will be distributed to minimize the losses, but the above calculations can provide a relative feel for the effects.

The last topic to be discussed here is the variation of DBR characteristics with changing index discontinuity between the low and high index materials. Using GaAs for the high index and AlAs for the low index provides the maximum index step. This has the advantages of a shorter penetration depth, fewer periods

needed for a desired reflectivity, and a broader stop band. To make this point, the reflectivity spectrum for  $\text{Al}_x\text{Ga}_{1-x}\text{As}/\text{AlAs}$  DBRs are shown in Fig. D.13 where the aluminum mole fraction  $x$  is stepped from 0 to 0.6 while the number of periods has been increased to maintain a 99% reflectivity. The calculation assumes the cavity is GaAs while the mirror is terminated on air, keeping the number of mirror periods to a minimum because of the ~32% semiconductor-air reflection. The most obvious feature is the shrinking width of the stop band. For a sense of scale, consider that a 1% variation in growth would result in a 10 nm shift in the lasing wavelength. The lower index discontinuity designs require extremely accurate growth control and uniformity.

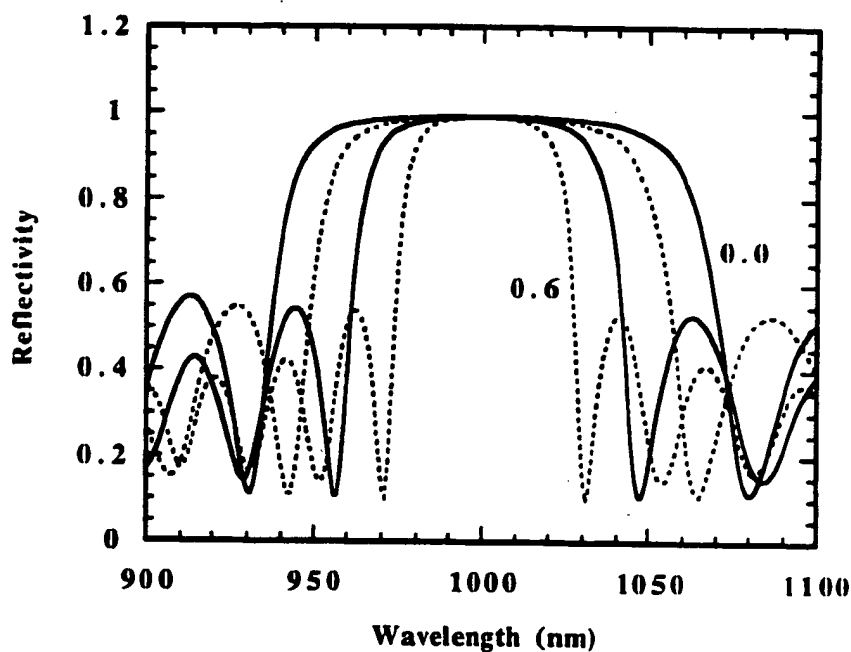


Fig. D.13 Reflectivity spectrum for DBRs terminated on air. The four curves are for  $\text{Al}_x\text{Ga}_{1-x}\text{As}/\text{AlAs}$  mirrors with  $x$  stepped in increments of 0.2. Number of periods adjusted to maintain 99% reflectivity.

More detail on the different structures is listed in Table D.1. The number of periods needed to give 99% reflectivity, the penetration depth and the mirror thickness are listed. Again, the materials have been presumed lossless. The penetration depth shows that the losses of the lower index step mirrors will be more than double that of the binary mirrors while their thicknesses become a major challenge to the grower's patience. These issues are important for vertical-cavity

**Table D.1. Properties of the mirrors shown in Fig. D.13. The reflectivity is from a GaAs/DBR/air configuration.**

$\text{Al}_x\text{Ga}_{1-x}\text{As}/\text{AlAs}$	periods for 99%	penetration depth	mirror thickness
$x = 0.0$	14	$0.420 \mu\text{m}$	$2.18 \mu\text{m}$
$x = 0.2$	17	$0.520 \mu\text{m}$	$2.70 \mu\text{m}$
$x = 0.4$	23	$0.663 \mu\text{m}$	$3.71 \mu\text{m}$
$x = 0.6$	35	$0.984 \mu\text{m}$	$5.74 \mu\text{m}$

laser designs using semiconductor mirrors at shorter or longer wavelengths. Visible wavelength designs use  $x \sim 0.5$  to keep the layers transparent while InP based mirrors have small index steps as well, making the growth and losses of these designs major issues.

This section has presented the fundamental properties and design of distributed Bragg reflector. With the background presented here and accurate index dispersion and loss models, the reader should be able to design a reflector and predict its properties. We are therefore ready to apply the transmission matrix technique to vertical-cavity structures.

### D.5 Round-trip Cavity Parameters

As discussed in the first section of this appendix, the optical properties of a vertical cavity can be conveniently written in terms of the round trip parameters  $G_{th}$ ,  $L$ ,  $T$  and the longitudinal enhancement factor  $\xi_{enh}$ . Using the transmission matrix technique, these parameters can easily be determined.



A cavity is constructed to have a round trip phase in multiples of  $2\pi$  at the Bragg wavelength of the mirror designs which has been chosen to be the design wavelength. As can be seen from Fig. D.8, as long as the cavity index  $n_{cav}$  is greater than the low mirror index  $n_L$ , the reflections of the Bragg wavelength will return with zero phase. Thus the optical path length of the cavity is determined by:

$$\sum_{cavity} k_i l_i = m\pi \quad m = 0, 1, 2, \dots \quad (D.80)$$

or:

$$\sum_{cavity} \frac{l_i}{(\lambda_i/2)} = m \quad m = 0, 1, 2, \dots \quad (D.81)$$

where the index  $i$  stands for the various layers comprising the cavity. Eqn (D.81) states that the cavity must be an integral number of half wavelengths thick. The integer  $m$  represents the number of nodes in the cavity. For  $m$  odd, the two reflections enter the cavity with a  $\pi$  phase difference so there will be a standing wave null in the center of the cavity while for  $m$  even there will be a standing wave maximum in the center. The case of zero thickness represents the placing of the two mirrors back to back. The case of  $m = 1$  is not practical since an active region at the center would be at a null. Thus most vertical-cavity lasers have a cavity thickness of one wavelength or  $m = 2$ . As discussed in Chapter 4, intra-cavity contacted structures often require thicker layers within the optical cavity to reduce the device resistance. At the expense of increase optical losses, the basic  $1\lambda$  cavity can be modified by adding multiple half waves of material where desired, keeping in mind that the active region must still be kept at a standing wave maximum.

A  $1\lambda$  cavity laser structure is shown in Fig. D.14. The active region is made of three InGaAs quantum wells with GaAs barriers cladded by  $Al_{0.5}Ga_{0.5}As$  spacers on each side. The spacer thicknesses have been adjusted to make the optical length of the cavity equal to one wavelength, where the refractive index of the InGaAs has been assumed equal to the index of GaAs for convenience. The mirrors are made of GaAs/AlAs pairs. The output coupler into the top surface has

14 periods while the bottom reflector, terminated on the substrate, has 23.5 periods. Doping profiles are often increased to reduce the heterobarrier resistances at the mirror layer interfaces while keeping the average doping low to minimize optical losses. For now, we'll include this effect by modulating the losses in each mirror layer. The losses for the first and last  $0.03\lambda$  of the  $0.25\lambda$  layers will be five times the loss in the  $0.19\lambda$  center, reflecting a doping of  $5 \times 10^{18} \text{ cm}^{-3}$  at the interfaces and  $1 \times 10^{18} \text{ cm}^{-3}$  elsewhere. For the p-type doping in output coupler the free carrier losses will be assumed to be  $11 \text{ cm}^{-1}$  per  $10^{18} \text{ cm}^{-3}$  hole density while for the n-type doping in the bottom reflector the losses will be  $5 \text{ cm}^{-1}$  per  $10^{18} \text{ cm}^{-3}$  electron density [8]. The spacers are assumed doped with doping setbacks of  $500 \text{ \AA}$  from either side of the active region. The doping setbacks and active region are undoped.

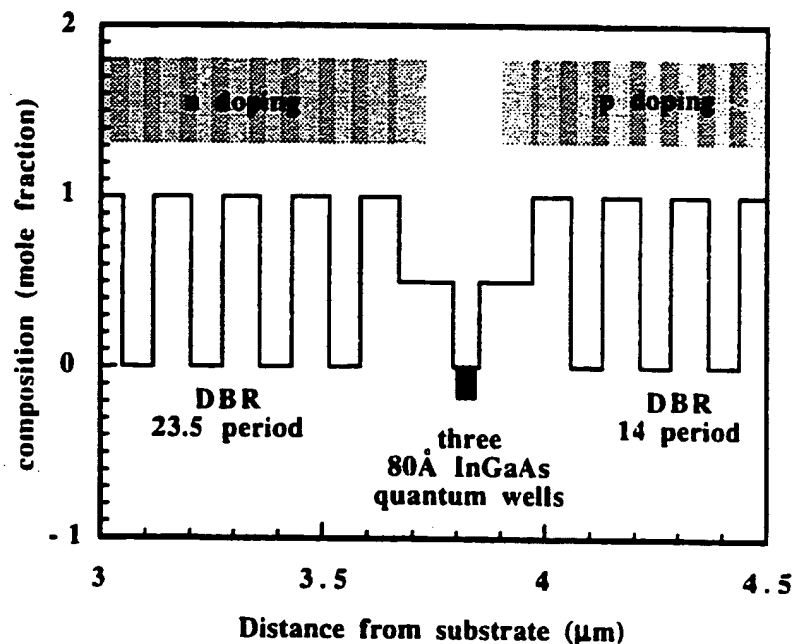


Fig. D.14. Structure of the 11 cavity design used for sample calculations. Positive compositions are for  $\text{Al}_x\text{Ga}_{1-x}\text{As}$  while the absolute of the negative values represent  $\text{In}_x\text{Ga}_{1-x}\text{As}$ .

The threshold gain for such a structure is calculated using the transmission matrix for the entire cavity,

$$\begin{bmatrix} E_1^{in} \\ E_1^{out} \end{bmatrix} = \begin{bmatrix} T_{11} & T_{12} \\ T_{21} & T_{22} \end{bmatrix} \begin{bmatrix} E_2^{out} \\ E_2^{in} \end{bmatrix}, \quad (D.82)$$

which can be rewritten into a field scattering matrix as in Eqn. (D.59)

$$\begin{bmatrix} E_1^{out} \\ E_2^{out} \end{bmatrix} = \begin{bmatrix} \frac{T_{21}}{T_{11}} & T_{22} - \frac{T_{21}T_{12}}{T_{11}} \\ \frac{1}{T_{11}} & -\frac{T_{12}}{T_{11}} \end{bmatrix} \begin{bmatrix} E_1^{in} \\ E_2^{in} \end{bmatrix}. \quad (D.83)$$

Now if we let  $T_{11} \Rightarrow 0$  then there can be out going waves for no incoming waves. This is the lasing condition (!) and is solved by scanning wavelength and gain in the quantum wells to find the zeros of the real and imaginary parts of  $T_{11}$ :

$$\text{Re}\{T_{11}(\lambda, g)\} = 0 \quad (D.84.a)$$

$$\text{Im}\{T_{11}(\lambda, g)\} = 0 \quad (D.84.b)$$

Equation (D.84) can be solved using a two dimensional Newton loop. The roots yield the lasing longitudinal wavelength,  $\lambda_{cav}$ , and associated threshold gain,  $g_{th}$ , for the cavity.

The threshold gain compensates for all the losses. If the threshold gain is also calculated for the case where all the absorption losses are set to zero, the threshold gain is compensating for transmission only. The ratio provides the optical efficiency,

$$\eta_{opt} = \frac{T_1 + T_2}{L + T_1 + T_2} = \frac{T_1 + T_2}{G_{th}} = \frac{g_{th}^{no\ loss}}{g_{th}}. \quad (D.85)$$

If the transmission coefficients for the mirrors  $T_1$  and  $T_2$  are calculated using the transmission matrix, then the round trip losses  $L$  and the longitudinal enhancement factor  $\xi_{enh}$  can be calculated from Eqn. (D.85):

$$L = G_{th} - (T_1 + T_2) = \left( \frac{1}{\eta_{opt}} - 1 \right) (T_1 + T_2) \quad (D.86)$$

$$\xi_{enh} = \frac{T_1 + T_2}{2l_{act} g_{th}^{no\ loss}} \quad (D.87)$$

With  $T_1$ ,  $T_2$ ,  $L$ ,  $g_{th}$  and  $\xi_{enh}$  calculated, the optical properties of the cavity have been determined. The essential steps are the determination of the threshold material gain with and without internal loss and the calculation of the mirror transmission coefficients.

The transmission coefficients and enhancement factor can also be determined graphically from the standing wave pattern of the cavity. The fields are calculated assuming  $E_2^{out} = 1$  and  $E_2^{in} = 0$  as would be the case for excitation from the left. With  $g_{mat} = g_{th}$ , the reflection coefficient becomes infinite and  $E_1^{in} \Rightarrow 0$ , leaving only the outward traveling waves. Thus the fields calculated represent the standing wave pattern in the cavity normalized to the right hand output field. The magnitude squared of the electric field for the design in Fig. D.14 is shown in Fig. D.15. The threshold gain was calculated without and with internal losses. The results were  $1169 \text{ cm}^{-1}$  and  $1510 \text{ cm}^{-1}$  respectively, predicting an optical efficiency of 77%. Details of the standing wave are shown below. On the right, the intensity goes to 1 at the surface. On the left, the intensity of the field emitted into the substrate  $I_1 = 0.03$ . In the center the overlap of the standing wave pattern with the quantum wells is shown. From these plots the mirror transmission coefficients and the enhancement factor can be calculated. To calculate the enhancement factor, the intensity is normalized to its peak value and integrated over the active area:

$$\xi_{enh} = \frac{2}{I_{act}} \int_{active} \frac{I(z)}{I_{peak}} dz \quad (D.88)$$

which returns a value of 2 for very short and 1 for very long active regions. Due to the high reflectivity of the mirrors, the two counter propagating waves at the active region will have equal amplitudes,  $E_{act}$ . The peak intensity can be written in terms of these fields:

$$I_{peak} = |E_{peak}|^2 = |E_{act}^+ + E_{act}^-|^2 = 4|E_{act}|^2 \quad (D.89)$$

The transmission coefficient for the mirrors as seen by the active region are then

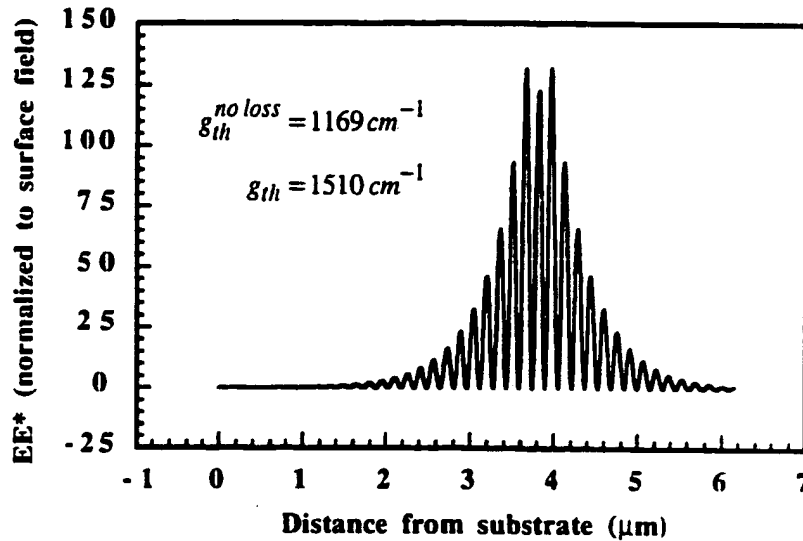


Fig. D.15a. Calculated standing wave pattern for the structure shown in Fig. D.14. The power decays as the fields penetrate the DBRs on either side.

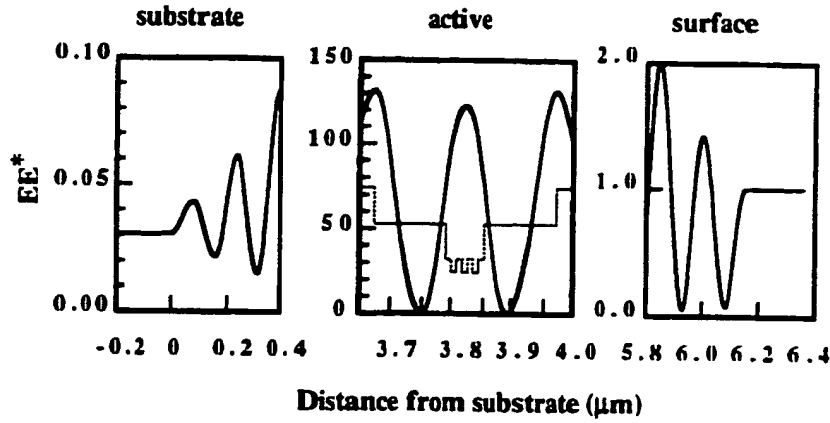


Fig. D.15b. Detail of the standing wave pattern for the structure shown in Fig. D.14. The plots show the important details for analysis.

calculated using Eqn. (D.51):

$$T_2 = \frac{n_2}{n_{act}} \frac{|E_{right}^{out}|^2}{|E_{act}|^2} = \frac{n_2}{n_{act}} \frac{1}{I_{peak}/4} \quad (D.90)$$

$$T_1 = \frac{n_1}{n_{act}} \frac{|E_1^{out}|^2}{|E_{act}|^2} = \frac{n_1}{n_{act}} \frac{I_1}{I_{peak}/4} \quad (D.91)$$

Inserting some numbers should help make the procedure clear. The transmission matrix technique is used to calculate the threshold gain needed by the three 80Å quantum well for the example structure to lase both without internal losses, 1169 cm<sup>-1</sup>, and with losses, 1510 cm<sup>-1</sup>. The standing wave pattern, as shown in Fig. D.15a, is generated to determine the normalized intensity profile. From the detail in Fig. D.15b, the peak intensity  $I_{peak}$  is 123 and the left intensity  $I_1$  is 0.03. The active region index  $n_{act} = 3.51$  while  $n_1 = 3.51$  and  $n_2 = 1$  since they are GaAs and air at a free space wavelength of 1 μm. Inserting these values into Eqns. (D.85), (D.90) and (D.91) give:

$$\eta_{opt} = \frac{1169 \text{ cm}^{-1}}{1510 \text{ cm}^{-1}} = 77.4\%$$

$$T_{right} = \frac{1}{3.51123/4} = 0.926\%$$

$$T_{left} = \frac{3.51}{3.51123/4} = 0.098\%$$

These values can then be inserted into Eqns (D.85), (D.86) and (D.87) and to give:

$$G_{th} = \frac{(0.926\% + 0.098\%)}{0.774} = 1.32\%$$

$$L = \left( \frac{1}{0.774} - 1 \right) (0.926\% + 0.098\%) = 0.299\%$$

$$\xi_{enh} = \frac{(0.00926 + 0.00098)}{2(240 \times 10^{-8} \text{ cm}) 1169 \text{ cm}^{-1}} = 1.82$$

Finally, the cavity's optical properties can be summarized as having a transmission out the top of 0.926%, a transmission out the bottom of 0.098%, round trip losses of 0.299% and a threshold material gain of 1510  $\text{cm}^{-1}$  for a three quantum well active region. These parameters are sufficient to describe the cavity. From this point on, I will assume that once a cavity's structure and material properties such as internal loss and index dispersion have been specified, the round trip cavity parameters can be calculated by the procedure outlined in this section. The beauty of these integrated round trip parameters is that one no longer needs to be concerned with the details of the cavity, only the round trip parameters are needed to quantify and compare alternate designs.

#### D.6 Energy Storage, Quality Factor and Photon Lifetime

From the analysis presented in the previous section, it would appear that the round trip parameters  $G_{th}$ ,  $L$  and  $T$  along with  $\xi_{enh}$  completely characterize the cavity's optical properties. For these parameters, there would be no difference in the properties of a cavity modified by including additional half wavelengths of

lossless material. In other words,  $L$  depends on the  $\alpha l$  product and thus a layer twice as thick with half the loss would seem to be equivalent (I am still assuming a low loss structure). From the point of view of the DC characteristics, this is true. The energy stored in the cavity does increase with increasing length, however, and this will affect the modulation response by increasing the photon lifetime. A simple technique for calculating these parameters uses the quality factor  $Q$ .

The derivation given here follows Jackson [9] and is repeated for the sake of clarity. The quality factor of a resonant cavity with losses is defined as:

$$Q \equiv \omega_0 \frac{\text{Stored energy}}{\text{Power loss}} \quad (\text{D.92})$$

which is equal to  $2\pi$  times the ratio of the stored energy to the power loss per cycle. The resonance frequency  $\omega_0$  is defined as the resonance frequency in the absence of losses. In this analysis we are considering the impulse response of passive system (no gain), and thus energy stored in the cavity,  $U$ , will decay with time. This is expressed using Eqn.(D.92) as:

$$\frac{dU}{dt} = -\frac{\omega_0}{Q} U \quad \text{with solution} \quad U(t) = U_0 e^{-\omega_0 t/Q} \quad (\text{D.93})$$

showing that the decay rate is inversely proportional to  $Q$ . The photon lifetime is thus given by:

$$\tau_{ph} = \frac{Q}{\omega_0} \quad (\text{D.94})$$

Furthermore, note that the energy stored in the cavity can be expressed as:

$$U = \text{power loss} \times \frac{Q}{\omega_0} = \frac{P_{out}^i}{\eta_{opt}^i} \tau_{ph} \quad (\text{D.95})$$



It would be desirable, then, to be able to calculate  $Q$  for a cavity using the transmission matrix technique. To do this, note that Eqn. (D.93) implies that the fields in the cavity decay as:

$$E(t) = \begin{cases} 0, & t < 0 \\ E_0 e^{-\omega_0 t / 2Q} e^{j(\omega_0 + \Delta\omega)t}, & t \geq 0 \end{cases} \quad (\text{D.96})$$

where  $\Delta\omega$  allows for a shift of the resonance frequency. These fields do not have a pure frequency, but a spectrum of frequencies around  $\omega_0 + \Delta\omega$  that can be calculated using the Fourier transform:

$$E(\omega) = \frac{1}{\sqrt{2\pi}} \int_{-\infty}^{+\infty} E(t) e^{j\omega t} dt \quad (\text{D.97})$$

$$E(\omega) = \frac{1}{\sqrt{2\pi}} \int_{-\infty}^{+\infty} E(t) e^{-j\omega t} dt \quad (\text{D.98})$$

inserting Eqn. (D.96) into (D.98) and integrating gives the resonant line shape of the intensity inside the cavity as a function of the frequency  $\omega$ :

$$EE^* \propto \frac{1}{(\omega - \omega_0 - \Delta\omega)^2 + (\omega_0 / 2Q)^2} \quad (\text{D.99})$$

The lineshape has a full width at half maximum of  $\delta\omega = \omega_0 / Q$  so that the quality factor is:

$$Q = \frac{\omega_0}{\delta\omega} \equiv \frac{\lambda_0}{\delta\lambda} \quad (\text{D.100})$$

Thus plotting the resonance in the frequency domain and determining the "half width" will give the quality factor and the associated parameters.

The transmission coefficient spectrum for six calculations are shown in Fig. D.16. The outer curve is for the sample cavity design of section D.2.5. The five curves inside are for structures where an additional lossless one wavelength thick  $\text{Al}_{0.5}\text{Ga}_{0.5}\text{As}$  layer has been added inside the cavity just before one of the mirrors. No additional reflections are introduced, the round trip cavity parameters are identical resulting in identical transmission values at resonance. The off resonance behavior, however, is different reflecting the different quality factors of the cavities. Using the full width at half maximum  $\delta\lambda$  in Eqn. (D.100) yields the quality factors. As can be seen in the figure, the resonances become narrower with

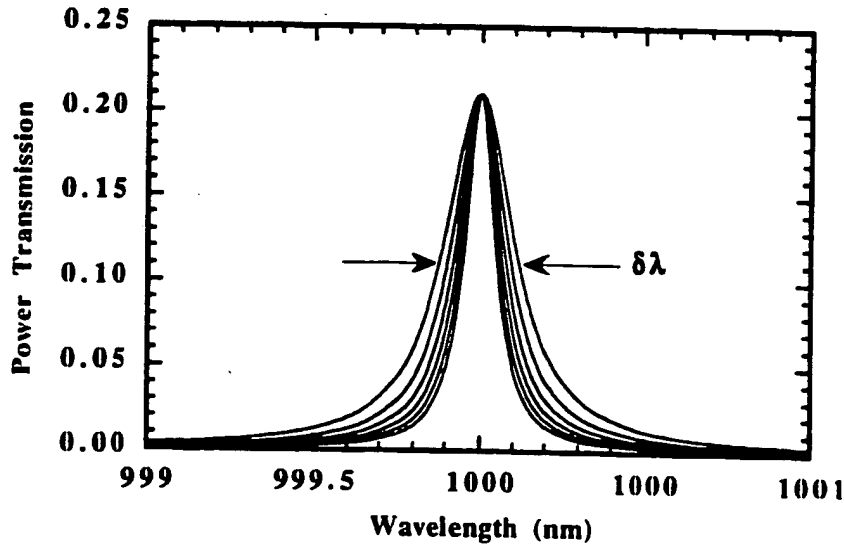


Fig. D.16. Plot of the transmission resonance for the cavity of Fig. 2.14. The broadest curve is for the original design. To generate the narrower curves, additional  $1\lambda$  lossless  $\text{Al}_{0.5}\text{Ga}_{0.5}\text{As}$  spacers were added inside the cavity. The full width at half maximum  $\delta\lambda$  is indicated in the figure.

increasing cavity length. The quality factor for the cavity with  $0\lambda$ ,  $1\lambda$ ,  $2\lambda$ ,  $3\lambda$ ,  $4\lambda$ , and  $5\lambda$  additional lengths are 3960, 4995, 6000, 7027, 8052 and 9141 while the associated photon lifetimes are 2.1, 2.6, 3.2, 3.7, 4.3 and 4.9 ps respectively.

The quality factor is inversely proportional to the losses. With internal and transmission losses, the quality factor for the cavity is 3960. If the transmission spectrum is calculated for the cavity with no internal losses, the full width at half maximum is 0.195 nm which gives a quality factor of 5128. The ratio gives the optical efficiency:

$$\eta_{opt} = \frac{Q_{loss}}{Q_{no\ loss}} \quad (D.101)$$

For the sample structure, Eqn. (D.101) predicts an optical efficiency of 77.2%, in good agreement with Eqn. (D.85). Thus the quality factor as related to the cold cavity linewidth is another method of determining the cavity's optical efficiency.

In summary, the transmission matrix technique has been derived and applied to determine the optical properties of vertical cavities. A sample structure has been analyzed to show the utility of the technique and clarify the procedure. The round trip cavity parameters have been introduced and determined, showing that a cavity's DC characteristics are specified once the round trip parameters of  $L$ ,  $T$  and the longitudinal enhancement factor  $\xi_{enh}$  have been calculated. In addition, the quality factor  $Q$  has been introduced as another cavity parameter that is important for the high frequency response of the lasers.

## References

1. S.W. Corzine, R.H. Yan, and L.A. Coldren, "A tanh substitution technique for the analysis of abrupt and graded interface multilayer dielectric stacks." *IEEE Journal of Quantum Electronics*, 27 (9) pp. 2086-90. 1991
2. S.W. Corzine. *Design of Vertical-Cavity Surface Emitting-Lasers with Strained and Unstrained Active Regions*, Ph.D. Dissertation. University of California at Santa Barbara (1993) ECE technical report #93-09

3. D.I. Babic and S.W. Corzine, "Analytic expressions for the reflection delay, penetration depth, and absorptance of quarter-wave dielectric mirrors." *IEEE Journal of Quantum Electronics*, **28** (2) pp. 514-24. 1992
4. R.S. Geels. *Vertical-Cavity Surface-Emitting Lasers: Design, Fabrication and Characterization*, PhD Dissertation. University of California at Santa Barbara (1991) ECE Technical Report #92-15
5. A. Yariv, Optical Electronics, 3 ed. New York: CBS Collage Publishing, 1985, Chapter 15 covers in-plane semiconductor lasers nicely
6. G. Gonzalez, Microwave Transistor Amplifiers Analysis and Design, Englewood Cliffs, N.J.: Prentice-Hall, Inc. 1984,
7. M.A. Afromowitz, "Refractive Index of  $\text{Ga}_{1-x}\text{Al}_x\text{As}$ " *Solid State Comm.* **15** (59) pp. 59-63. 1974
8. J.W. Scott, R.S. Geels, S.W. Corzine, and L.A. Coldren, "Modeling temperature effects and spatial hole burning to optimize vertical-cavity surface-emitting laser performance." *IEEE Journal of Quantum Electronics*, **29** (5) pp. 1295-308. 1993
9. J.D. Jackson, Classical Electrodynamics, 2cd Edition ed. New York: John Wiley & Sons. 1975,

## Appendix E: Thermal and Electrical Properties of AlGaAs

When considering the specification of a vertical-cavity-laser layer structure, the designer first makes an optical design. The desired threshold current and operating temperature range sets limits on the external efficiency and gain offset to be used. Finally, electrical and thermal properties of the material must be considered to minimize the lasers electrical and thermal resistance. This appendix introduces some of the relevant material properties of  $\text{Al}_x\text{Ga}_{1-x}\text{As}$  to provide the necessary background for designing a high performance laser. In general, the random alloy scattering of the ternary materials makes their thermal impedances higher than the binaries. Similar scattering effects reduce the electrical mobility in the alloys as well. The section begins by discussing the thermal properties and then turns to the electrical properties.

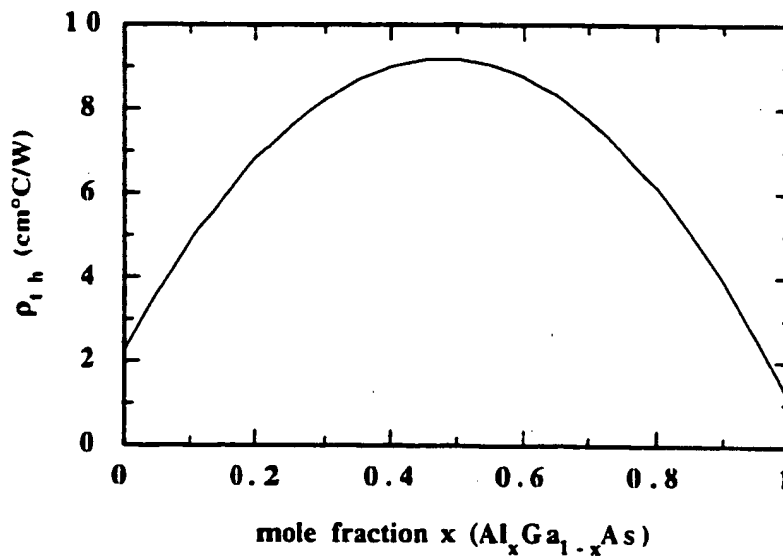


Fig. E.1. Plot of Eqn. (E.1), showing the high increase of the thermal resistance due to random alloy scattering.

An analytic expression for the thermal resistivity of  $\text{Al}_x\text{Ga}_{1-x}\text{As}$  has been given by Adachi [1] which uses a bowing parameter:

$$\rho_{th}(x) = 1/\sigma_{th}(x) = 2.27 + 28.83x - 30x^2 \text{ [cm}^2\text{C/W]} \quad (\text{E.1})$$

This function shows good agreement with the experimental data. To highlight the importance, this function is plotted in Fig. E.1. Incorporating just 10% aluminum into a GaAs material results in a doubling of the thermal impedance. To estimate the junction temperature rise,  $\Delta T_{jcr}$ , of a surface emitting laser the formula for a constant temperature disk on the surface of a semi-infinite substrate of can be used[2]:

$$\Delta T_{jcr} = \frac{(P_{elec} - P_{opt})}{4r\sigma_{th}} \quad (\text{E.2})$$

where  $P_{elec}$  is the input power,  $P_{opt}$  is the light output,  $r$  is the laser radius and  $\sigma_{th}$  is the thermal impedance of the substrate. Using Eqn. (E.2) and the thermal conductivity of GaAs, 0.044 W/cm°C, gives a thermal impedance of 1.1°C/mW for a 10µm-diameter laser. To generate 1mW of output power with a 10% power conversion efficiency requires ~10mW of dissipated power. This dissipated power results in a junction temperature rise of 10°C. Using the impedance of  $\text{Al}_{0.2}\text{Ga}_{0.8}\text{As}$  increases the junction temperature rise @ 1mW output power to 34°C. If we instead consider a 5 µm diameter laser, the rise increases to ~70°C!

The point is that for higher output powers or smaller device diameters, great care must be taken when considering the thermal design of the lasers. If the heat is to be dissipated through the bottom of the laser, then the optimal design will minimized the amount of ternary material between the junction and the substrate. The intra-cavity contacted laser designs discussed in Chapter 3 approaches this limit since the intra-cavity contact layers can be GaAs while the mirrors can be made from the binary AlAs/GaAs materials.

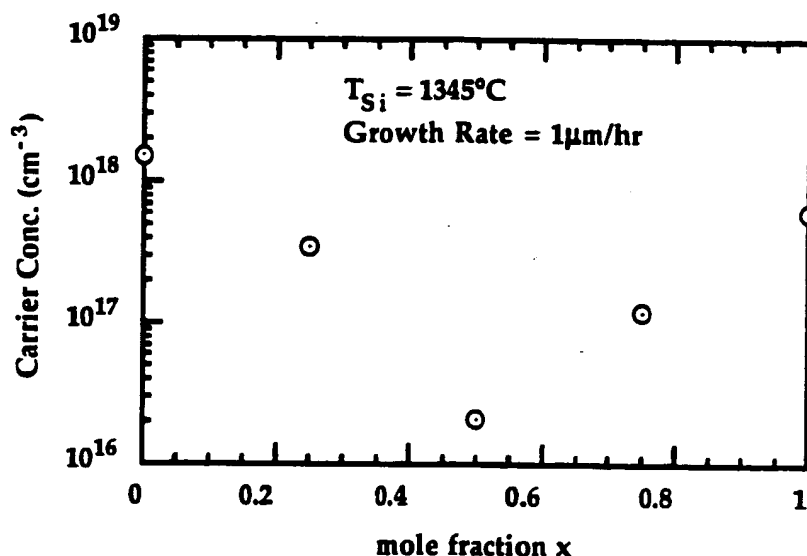


Fig. E.2. Measured electron concentration for varying  $\text{Al}_x\text{Ga}_{1-x}\text{As}$  compositions formed from a  $20\text{\AA}$  period digital alloy. All samples were grown with identical dopant fluxes. Activation energies of the DX center indicate the a sharp drop in carrier concentration should be observed for  $x > 0.28$

Now consider the electrical limitations of AlGaAs. In particular, there are limitations for the incorporation and activation of both p and n-type dopants which result in modified cavity designs. In the case of the n-type doping using Silicon the DX center results in a very low activation for  $x$ -values near or above 30% [3]. To determine the numbers more precisely for our  $20\text{\AA}$  period digital alloys, we made Hall measurements to determine the carrier concentrations for  $x=0, 0.25, 0.50, 0.75$  and  $1.00$  for a constant dopant flux intended to produce an electron concentration of  $1 \times 10^{18} \text{ cm}^{-3}$  in GaAs. The results are shown in Fig. E.2. If one wishes to provide low resistance paths in n-type material it is clear that  $\text{Al}_x\text{Ga}_{1-x}\text{As}$  in the range of  $0.28 < x < 0.8$  should be avoided. This is essentially impossible in the case of vertically contacted structures where the current flows through the distributed Bragg reflectors. For the intra-cavity contacted designs which bypass

the mirror layers the use of an  $x = 0.25$  cladding on the n side of the active region makes it possible to provide a low resistance path to the contacts.

In the case of p-type doping, the DX center does not play a role and it is possible to heavily dope the entire range of AlGaAs alloys. There are, however, limits to the incorporation of dopants during growth due to solid solubility limits. This is highly dependent on the type of dopant and the substrate growth temperature. Our MBE machine uses beryllium as the p-type dopant. At typical growth temperatures of  $-650^{\circ}\text{C}$  the p-type doping densities are limited to levels of  $\sim 7 \times 10^{17} \text{ cm}^{-3}$  for  $x > 0.8$ . Higher fluxes "float" on the surface during growth, becoming incorporated into the crystal once lower aluminum content materials are grown. This results in doping profiles very different than originally designed. UCSB graduate student Matt Peters has spent considerable effort investigating this effect. By growing at lower temperatures, higher dopant levels can be achieved but the optical absorption of the lower temperature material increases considerably. An alternative solution is to use carbon as the p-type dopant. Extensive development of carbon doping has been driven by the desire to produce high doping concentrations in the thin base layer of heterostructure bipolar transistors. Carbon has been found to be stable over time, showing very high doping densities and low diffusion into the emitter regions. Using carbon doping researchers at Sandia National Laboratories have produced very low voltage p-type distributed Bragg reflectors.

To illustrate the importance of these electrical considerations, I draw upon the development of the intra-cavity design. Initial device results showed high drive voltages and corresponding low output powers due to heating. To determine the source of the excess voltage several active regions were grown on conducting substrates. The three different active regions are shown in Fig. E.3. For the test structures, the p contact was made at the top where the upper mirror would begin while the n-type substrate replaced the bottom mirror. In this way it was assured that the current injection would be vertical and uniform. Device 930514h had  $\text{Al}_{0.5}\text{Ga}_{0.5}\text{As}$  cladding layer on both sides of the active region and the AlAs layer.



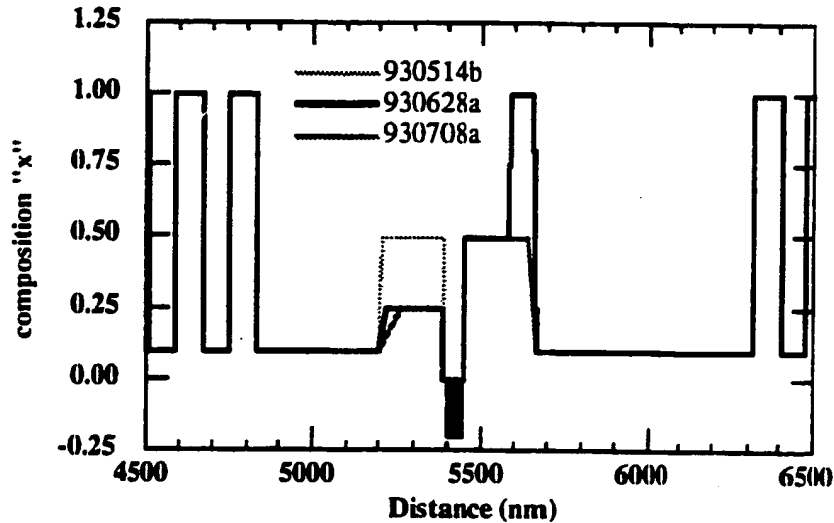


Fig. E.3. Three intra-cavity active region designs. The active regions were grown without mirrors on a conducting n-type GaAs substrate to investigate their electrical properties.

Device 930628a reduced the aluminum content on the n side to 25% to avoid the DX center. Device 930708a eliminated the AlAs layer on the p side to see the effect of the beryllium segregation on the current density-voltage ( $J$ - $V$ ) characteristics. While the AlAs was essential to the device structure by providing a selective etch material for a current constriction, it was important to determine its contribution to the drive voltage. In chapter 6, the design of more advanced intra-cavity structures are discussed which use avoid the use of high Al content materials for current constriction.

To measure the electrical characteristics, circular 30  $\mu\text{m}$  diameter Cr/Zn/Au dot contacts were evaporated onto the surface and etched to form isolated mesas. A Ni/Au/Ge/Au/Ni/Au contact was evaporated on the backside of the substrate and the contacts were alloyed in an rapid thermal anneal. The measured  $J$ - $V$  characteristics are shown in Fig. E.4. In agreement with the measured characteristics of the early intra-cavity devices, the  $J$ - $V$  characteristics of the first test active region displays drive voltages in excess of 5V. This excessive voltage

is attributed to space charge limited flow in the 2000Å wide (unintended) intrinsic region in the n-type  $\text{Al}_{0.5}\text{Ga}_{0.5}\text{As}$  due to DX center compensation. When the Al

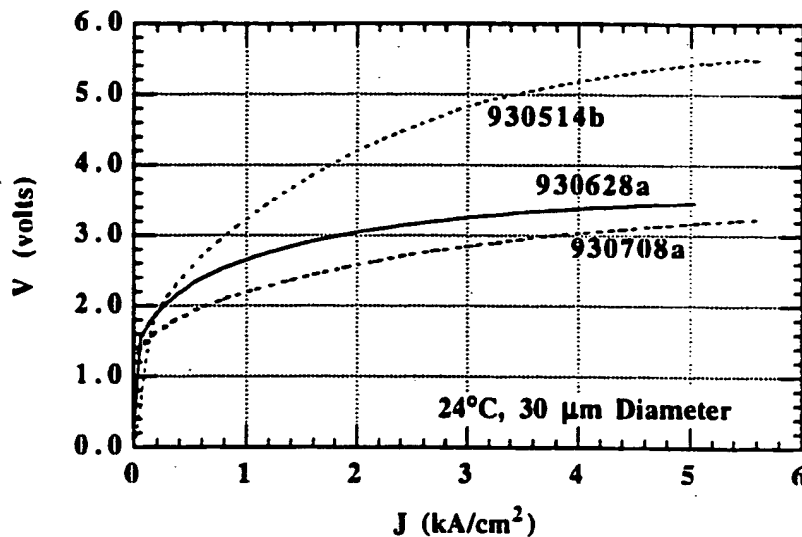


Fig. E.4. Measured voltage vs. current density characteristics for the three active regions shown in Fig. E.3. The drive voltage is greatly reduced by altering the layer structure in the active region.

content is reduced to 25%, the drive voltage drops by 2V! Next the AlAs undercut layer is eliminated, resulting in an additional ~0.5V drop in drive voltage. This final curve, 930708a, gives the  $J$ - $V$  characteristics of the active region alone. The quantum well photon energy is 1.24 eV, and it can be seen that the diode does turn on at the correct voltage. Even so, the drive voltage is near 3V, indicating significant room for improvement in the electrical properties of the active regions used in these lasers.

In summary, the thermal and electrical properties of AlGaAs have been discussed. The thermal impedance of the ternary alloys drive the designer to minimize their use to maximize the heat dissipation properties of the lasers. The electrical properties of the alloys also introduce considerations for the optimal

design of the layer structure for minimizing the series resistance and drive voltage of the lasers. An example set of  $J$ - $V$  characteristics for various modified structures have been presented to emphasize the importance of these considerations to the overall performance of vertical-cavity lasers. By separating the electrical design from the mirror design, intra-cavity contacted structures provide greater flexibility enabling more optimal laser performance.

### References

1. S. Adachi, "GaAs, AlAs and  $\text{Al}_x\text{Ga}_{1-x}\text{As}$ : Material parameters for use in research and device applications" *Journal of Applied Physics*, **58** (3) pp. R1-R29. 1985
2. S.S. Kutateladze and V.M. Borishanski, A Concise Encyclopedia of Heat Transfer, Oxford: Pergamon. 1966.
3. N. Chand, R. Fischer, J. Klem, T. Henderson, P. Pearsall, W.T. Masselink, Y.C. Chang, and H. Morkoc, "Beryllium and silicon doping studies in  $\text{Al}_x\text{Ga}_{1-x}\text{As}$  and new results on persistent photoconductivity." *Journal of Vacuum Science & Technology B*, **3** (2) pp. 644-8. 1985

**THIS PAGE BLANK (USPTO)**